

Alma Mater Studiorum – Università di Bologna

DOTTORATO DI RICERCA IN

CHIMICA

Ciclo XXVIII

**Settore Concorsuale di afferenza: 03/C1**

**Settore Scientifico disciplinare: CHIM/06**

Computational investigation of catalyzed organic reactions: Metal- and  
Organo-Catalysis, Bio-Catalysis and Carbo-Catalysis

**Presentata da: Pietro Giacinto**

**Coordinatore Dottorato**

**Relatore**

**Chiar.mo Prof. Aldo Roda**

**Chiar.mo Prof. Andrea Bottoni**

**Esame finale anno 2016**

*A mio  
padre*

# Contents

<b>AIM OF THE DISSERTATION.....</b>	<b>7</b>
<b>INTRODUCTION.....</b>	<b>9</b>
1.1 INTRODUCTION TO TODAY'S CATALYSIS.....	9
1.2 COMPUTATIONAL CHEMISTRY CONTRIBUTION.....	10
<b>PART I : COMPUTATIONAL METHODS .....</b>	<b>12</b>
<b>1 AN OVERVIEW ON COMPUTATIONAL CHEMISTRY.....</b>	<b>13</b>
1.1 INTRODUCTION.....	13
1.2 MODELLING A MOLECULAR SYSTEM.....	14
<b>2 THE POTENTIAL ENERGY SURFACE (PES).....</b>	<b>14</b>
2.1 REPRESENTATION OF THE PES.....	16
2.2 GEOMETRY OPTIMIZATION ON THE PES.....	19
2.3 CALCULATION OF VIBRATIONAL FREQUENCIES.....	21
<b>3 QUANTUM MECHANICAL METHODS.....</b>	<b>23</b>
3.1 SLATER DETERMINANT AND LCAO APPROXIMATION.....	24
3.2 BASIS SET.....	25
3.3 CORRELATION ENERGY.....	26
3.4 DENSITY FUNCTIONAL THEORY METHOD (DFT).....	28
<b>4 MOLECULAR MECHANICAL METHODS.....</b>	<b>32</b>
<b>5 HYBRID QM/MM METHODS.....</b>	<b>33</b>
5.1 OUR OWN N-LAYER INTEGRATED MOLECULAR ORBITAL AND MOLECULAR MECHANICS: ONIOM.....	34
5.2 INTERACTIONS BETWEEN THE LAYERS, THE ELECTROSTATIC EMBEDDING.....	36
5.3 THE BOUNDARY REGION.....	37
<b>6 SOLVENT EFFECT.....</b>	<b>38</b>
6.1 THE POLARIZABLE CONTINUUM MODEL (PCM).....	38
6.2 THE EFFECTIVE HAMILTONIAN.....	38
6.3 THE CAVITY SHAPE.....	40
6.4 THE ENERGY SOLVATION.....	41

<b>PART II: METAL- AND ORGANO-CATALYSIS.....</b>	<b>43</b>
<b>1 COMPUTATIONAL INVESTIGATION ON ORGANIC CATALYSIS.....</b>	<b>44</b>
1.1 INTRODUCTION.....	44
1.2 COMPUTATIONAL ORGANOMETALLIC CATALYSIS.....	44
<b>2 ORGANO-GOLD CHEMISTRY.....</b>	<b>45</b>
2.1 RELATIVISTIC EFFECTS ON GOLD ATOM.....	46
<b>3 COMPUTATIONAL INVESTIGATION OF THE GOLD(I)-CATALYZED SYNTHESIS OF AZEPINO [1,2-a]INDOLES.....</b>	<b>48</b>
3.1 AZEPINO[1,2-a]INDOLES.....	48
3.2 PRELIMINARY MECHANISTIC INSIGHTS.....	50
3.3 RESULTS AND DISCUSSION.....	53
3.4 COMPUTATIONAL DETAILS.....	59
3.5 CONCLUSIONS.....	60
<b>4 COMPUTATIONAL STUDY OF GOLD(I)-ASSISTED <math>\alpha</math>-ALLYLATION OF ENALS AND ENONES WITH ALCOHOLS.....</b>	<b>61</b>
4.1 $\alpha$ -OXO GOLD CARBENES.....	61
4.2 EXPERIMENTAL RESULTS.....	63
4.2.1 <i>Optimization of the catalyst and reaction conditions</i> .....	63
4.2.2 <i>Application field of the reaction</i> .....	65
4.3 MECHANISTIC INVESTIGATION OF THE REACTION.....	67
4.3.1 <i>Preliminarily mechanistic insights</i> .....	67
4.3.2 <i>DFT computational study of the reaction profile</i> .....	68
4.4 COMPUTATIONAL DETAILS.....	73
4.5 CONCLUSIONS.....	74
<b>5 GOLD(I)-CATALYZED DEAROMATIVE [2+2]-CYCLOADDITION OF INDOLES WITH ACTIVATED ALLENES: A COMBINED EXPERIMENTAL–COMPUTATIONAL STUDY.....</b>	<b>75</b>
5.1 ALLENAMIDES IN CATALYSIS.....	75
5.2 INDOLYL-BASED ALKALOID CHEMISTRY.....	77
5.3 EXPERIMENTAL RESULTS.....	79
5.3.1 <i>Optimization of the catalyst and reaction conditions</i> .....	79
5.3.2 <i>Application field of the reaction with allenamides</i> .....	80
5.3.3 <i>Application field of the reaction with aryloxyallene</i> .....	82

5.4 GOLD-CATALYZED DEAROMATIZATION REACTION: MECHANISTIC STUDY.....	83
5.4.1 <i>Preliminarily mechanistic insights</i> .....	83
5.4.2 <i>DFT computational study of the reaction</i> .....	84
5.5 COMPUTATIONAL DETAILS.....	92
5.6 GOLD-CATALYZED [2+2]-CYCLOADDITION BETWEEN INDOLES AND ELECTRON-RICH ALLENES: ENANTIOSELECTIVE VERSION.....	92
5.7 CONCLUSIONS.....	93
<b>6 COMPUTATIONAL INVESTIGATION OF METAL-FREE ENANTIOSELECTIVE ELECTROPHILIC ACTIVATION OF ALLENAMIDES.....</b>	<b>95</b>
6.1 ORGANOCATALYSIS.....	95
6.1.1 <i>Brønsted acid catalysts</i> .....	95
6.2 ELECTROPHILIC ACTIVATION OF ALLENAMIDES.....	96
6.3 EXPERIMENTAL RESULTS.....	98
6.3.1 <i>Optimization of the catalyst and reaction conditions</i> .....	99
6.3.2 <i>Application field of the reaction</i> .....	99
6.4 DFT INVESTIGATION OF METAL-FREE ENANTIOSELECTIVE ELECTROPHILIC ACTIVATION OF ALLENAMIDES.....	100
6.4.1 <i>Preliminary mechanistic insights</i> .....	100
6.4.2 <i>Computational study of the reaction</i> .....	101
6.5 COMPUTATIONAL DETAILS.....	108
6.6 CONCLUSIONS.....	109
<b>PART III: CARBO-CATALYSIS.....</b>	<b>111</b>
<b>1 CATALYSIS BY CARBON NANOSTRUCTURES.....</b>	<b>112</b>
1.1 INTRODUCTION.....	112
1.2 CARBON NANOTUBES AS NANO-REACTORS.....	113
<b>2 CL(-) EXCHANGE S<sub>N</sub>2 REACTION INSIDE CARBON NANOTUBES.....</b>	<b>115</b>
2.1 REACTIONS INSIDE CNT: CHOOSING THE LEVEL OF THEORY.....	115
2.2 GAS-PHASE CL(-) EXCHANGE S <sub>N</sub> 2 REACTION AND THE EFFECT OF THE CNT CONFINEMENT.....	116
2.2.1 <i>Validation of the DFT benchmarck method</i> .....	116
2.2.2 <i>CNT confined reaction using hybrid methods</i> .....	120
2.3 COMPUTATIONAL DETAILS.....	126
2.4 CONCLUSIONS.....	127

<b>3 CNT-CONFINEMENT EFFECTS ON THE MENSCHUTKIN S<sub>N</sub>2 REACTION.....</b>	<b>129</b>
3.1 INTRODUCTION.....	129
3.2 MENSCHUTKIN S <sub>N</sub> 2 REACTION IN THE GAS-PHASE AND IN SOLUTION. THE EFFECT OF THE CNT CONFINEMENT.....	129
3.2.1 <i>Full QM study of the reaction</i> .....	129
3.2.2 <i>CNT confined reaction using hybrid methods</i> .....	135
3.3 COMPUTATIONAL DETAILS.....	140
3.4 CONCLUSIONS.....	141
<b>4 REGIOSELECTIVE CONTROL OF CNT CONFINED AROMATIC HALOGENATION REACTIONS: A COMPUTATIONAL STUDY.....</b>	<b>143</b>
4.1 INTRODUCTION.....	143
4.2 AROMATIC HALOGENATION REACTIONS IN SINGLE-WALLED CARBON NANOREACTORS.....	144
4.3 RESULTS AND DISCUSSION.....	147
4.3.1 <i>Computed reaction without CNT</i> .....	147
4.3.2 <i>The CNT Confined Reaction</i> .....	153
4.4 COMPUTATIONAL DETAILS.....	158
4.5 CONCLUSIONS.....	158
<b>PART IV: BIO-CATALYSIS.....</b>	<b>160</b>
<b>1 A COMPUTATIONAL INVESTIGATION ON THE CATALYTIC MECHANISM OF TYROSYLPROTEIN SULFOTRANSFERASES.....</b>	<b>161</b>
1.1 INTRODUCTION.....	161
1.2 TYROSYLPROTEIN SULFOTRANSFERASES.....	162
1.3 HUMAN TYROSYLPROTEIN SULFOTRANSFERASE-2.....	163
1.4 RESULTS AND DISCUSSION.....	165
1.4.1 <i>Danan mechanism</i> .....	165
1.4.2 <i>Teramoto mechanism</i> .....	165
1.4.3 <i>The virtual mutagenesis experiment</i> .....	168
1.5 COMPUTATIONAL DETAILS.....	170
1.6 CONCLUSIONS.....	172
<b>REFERENCES.....</b>	<b>173</b>
<b>PUBLICATIONS.....</b>	<b>190</b>

## ***AIM OF THE DISSERTATION***

In this thesis the results of a Computational Organic Chemistry Ph.D. work course ranging from organometallic to metal-free and enzymatic catalysis is discussed. Various energetic and mechanistic aspects of organic reactions in catalysis are the key-issues which are addressed. A multidisciplinary approach allowed the development of several research projects in collaboration with experimental groups and combined experimental-theoretical works were carried out. Notes and comments concerning the theoretical models used and the experimental work carried out by the research groups who cooperated with us, are reported. Commercially available packages for molecular computations have been used to carry out the theoretical investigations.

The thesis comprises four main sections.

The first section (Part I) provides basic information on the computational methods used in the present work. In particular we give a simple description of the methods used to investigate the potential energy surface (PES) (search for stationary points). We provide a short and simple description of the Quantum Mechanical (QM), Molecular Mechanics (MM) and hybrid (QM/MM) methods used along this work. The basic mathematical aspects are briefly treated.

In the subsequent sections (Part II, Part III and Part IV) we focus on different aspects of organic catalysis.

In Part II the results of computational studies on the mechanism of various metal-catalyzed reactions (organometallic catalysis) are presented. In particular we describe organic reactions catalyzed by Gold(I) complexes. These studies are the result of a combined experimental-computational collaboration involving the organic synthesis group of prof. Marco Bandini (Department of Chemistry "G.Ciamician"). We consider some synthetically important processes in organic chemistry. In particular: (i) The *Gold(I)-catalyzed synthesis of Azepino[1,2-a]indoles* (the key-role played by the gold counter-ion and the peculiar 1,3 proton-transfer involved in the process are elucidated. (ii) *[Au(I)]-assisted  $\alpha$ -allylation of enals and enones with alcohols* and (iii) *Gold(I)-catalyzed dearomative [2+2]-Cyloaddition of Indoles with activated allenes*. The purpose of these studies was to discover some general rules to rationalize the role of gold complexes in different classes of organic reactions. Furthermore, at the end of this section we describe a mechanistic investigation of *Metal-Free Enantioselective Electrophilic Activation of Allenamides*, an example of organo-catalysis, thus not involving metal complexes.

In Part III we focus on an emerging and promising area of "metal-free" catalysis, based on carbon nanostructures such as graphite, graphene, graphene oxide, fullerenes and carbon nanotubes (CNTs). This "metal-free" catalysis is usually denoted as Carbocatalysis. In this context simple prototype reactions such as  $S_N2$  chlorine exchange reactions ( $Cl + CH_3Cl$ ) and the Menshutkin  $S_N2$  reaction ( $H_3N + CH_3Cl$ ) occurring inside a CNT are investigated. The energy contributions (electrostatic, van der Waals interactions, polarizability effects, hydrophobic effects) that may influence (speed up or slow down) the course of a reaction inside a CNT, have been elucidated by means of computational methods. In addition to the previous prototype reactions we have examined the mechanism of aromatic halogenation reactions carried out inside a CNT. In particular, we have analyzed the mechanism of the bromination of N-phenylacetamide for which experimental data are available in literature. The regio-selective control exerted by the CNT has been elucidated.

In Part IV the computational approach is used to elucidate the mechanism of an enzymatic reaction (enzyme catalysis). We describe the results obtained in the study of tyrosine O-sulfonation catalyzed by human Tyrosylprotein Sulfotransferases-2 (TPST-2). A QM-based protocol of alanine scanning identifies unequivocally the role of the amino acids involved in the catalysis.



# INTRODUCTION

## 1.1 Introduction to today's Catalysis

Although if we are not aware of this, life on Earth depends on catalysis. Natural chemical transformations essential for cellular functions are too energetically demanding to happen at physiological temperature and pressure, thus nature has developed enzymes, that is protein catalysts that accelerate many key reactions necessary for life. Life is based on countless catalytic processes and we have quickly learned to exploit some of them. The process of alcohol production from sugar, by fermentation, has ancient roots and the origins of this catalytic process are too remote to trace<sup>1</sup>, this emphasizes that the knowledge of chemical catalysis dating from the dawn of humanity. However it was during the era of the industrial and the scientific revolution that the concept of catalysis was deepened and scientifically investigated. This period was marked not only by systematic research and the discovery of new catalytic processes but also by an enhanced perception of chemical reactions.

In the last two centuries the industrialization have altered the human life more than any event or development since its appearance on earth. The Industrial Revolution brought a radical change in the ways and conditions of production of consumer goods and in all sectors of economic and social life and resulted in the most far-reaching changes in the history of humanity. In order to achieve all of this it was necessary to invent thousands of new materials and to find the ways for their fast and cheap production in large quantities. This was and is possible thanks to the use of catalysts in chemical processes. The benefits of these processes were immediately evident and the study and research in the field of chemistry catalysis had a dramatic growth.

In recent years the need for a more sustainable industrialization is becoming more urgent, therefore the scientific research and technological innovation are increasingly turning their gaze towards a greater sustainability. Even in terms of environmental sustainability catalysis plays a leading role. In general, the goal of sustainable chemistry is to develop technologies that use fewer raw materials and less energy, that maximise the use of renewable resources, and minimise or eliminate the use of dangerous chemicals. Even now, many syntheses of chemical products are still carried out via classical organic reactions that are more than 100 years old. These include nitrations,

Friedel-Crafts reactions, and halogenations. The disadvantage of these methods is the occurrence of stoichiometric (frequently even over-stoichiometric) quantities of salts that have to be separated and discarded. They also often require complicated protective group techniques, such as halogenations and dehalogenations that are needed for the regionally specific activation of a functional group. This is why these conventional production processes often generate several metric tons of waste per metric tons of target product. It is therefore clear the need for more innovative and environmentally safe versatile catalytic methods.

However, although the above changes could lead to huge benefits for life on earth, it is not enough: tackling the environmental and energetic crisis issues requires multidisciplinary input from the whole scientific community. Among the various scientific disciplines, computational chemistry can give a highly effective support to the environmental sustainability. We are in an exciting era where computers are becoming more powerful and widely available. This has placed computational methods and computational chemists at the center of the quest to develop solutions to many environmentally challenges.

## **1.2 Computational Chemistry contribution**

The information on the structure and reactivity of organic molecules is usually supplied by so-called physical organic chemistry methods usually based on experimental methods such as thermochemical, kinetic and spectroscopic. In recent decades, however, next to the experimental methods, representing the traditional approach of physical organic chemistry, an enormous development of the computational methods occurred. These methods have allowed the development of a new discipline, the computational organic chemistry. Computational organic chemistry now allows obtaining very accurate and precious information about the structure of organic molecules and their reactivity. Several complex mechanistic and structural issues of experimentally chemical interest can be addressed and clarified providing a complementary set of information that cannot be obtained by experimental techniques, such as transition state structure and electronic properties. The idea of a largely made at the table chemistry is still too bold now. However, computational chemistry has become a key technique used to interpret experimental data that can also be used as an “experimental science”, which investigates events that would not be possible to understand, nor to replicate, at the macroscopic level of a laboratory. Using computational chemistry in the field of chemical catalysis means to combine theory and experiment to understand mechanisms of catalytic

reactions on a molecular level. This knowledge enables to formulate basic guidelines for the design of new and improved catalytic systems, explain different experimental observations and determine the fundamental factors that control the reactivity and selectivity of different catalytic systems.

In the research project reported in this dissertation a computational approach is used in order to rationalize mechanistic aspects in catalytic organic reactions difficult to understand. This can give a relevant contribution to the improvement of reaction performance in the experimental field and shed light on important future developments in the field of catalysis.

# Part I

## Computational Methods

# 1. An Overview on Computational Chemistry

## 1.1 Introduction

Computational chemistry approaches the study of molecules and biomolecular systems by simulating their structure and reactivity numerically solving the physics laws. Computational Chemistry is primarily concerned with the numerical computation of molecular structures, molecular interactions and energetics of chemical transformations. The term computational chemistry is usually used when a mathematical method is sufficiently well developed that it can be automated for implementation on a computer. It uses computers to generate information such as properties of molecules or simulated experimental results. Very few aspects of chemistry can be computed exactly, but almost every aspect of chemistry has been described in a qualitative or approximate quantitative computational scheme. Although not all spectra are perfectly resolved, often a qualitative or approximate computation can give useful insight into chemistry if you understand what it tells you and what it doesn't.

Computational chemistry has become a useful way to investigate materials that are too difficult to find or too expensive to purchase. It also helps chemists make predictions before running the actual experiments so that they can be better prepared for making observations. The quantum and classical mechanics as well as statistical physics and thermodynamics are the foundation for most of the computational chemistry theory and computer programs. This is because they model the atoms and molecules with mathematics. The most important numerical techniques are ab-initio, semi-empirical and molecular mechanics.

The two most common computational approaches are Molecular Mechanics (using the classical physics laws MM) and Quantum Mechanical (based on the laws of quantum mechanics and having as a substantial target the solution of the Schrodinger wave equation). Molecular mechanics (MM), and in particular its more interesting branching, the molecular dynamic (MD) simulation is widely used, since it is applicable to large molecules such as those involved in biochemical processes (proteins, enzymes,...) and it gives information on the dynamic evolution of the system over the time. The insurmountable limit of MD, being a son of MM theory, is that it does not consider electrons explicitly, so that bonds forming and breaking cannot be studied at this

level of theory. The Quantum Mechanical methods are able to treat the electrons which governs the reactions, are much more accurate and more suitable to study the mechanism of a chemical reaction.

Both computational approaches provide the total energy for a given atomic configuration. Thus it is possible to determine the energy change as a function of atomic and molecular motions (Potential Energy Surface: PES).

## 1.2 Modelling a molecular system

The systems that can be considered in molecular modelling<sup>2</sup> range from small isolated molecules to biological macromolecules (like proteins and DNA) and solids. Most molecular modelling studies involves three stages. The first one requires the choice of the theoretical approach (QM or MM) suitable to describe the system under examination. This choice reflects the nature of the system as well as its dimension because sometimes one needs to sacrifice some accuracy to study a larger system or to obtain the results faster. The second stage of a molecular modelling study is the calculation itself, namely the computational procedure chosen to obtain the best geometrical arrangement (the one with the lowest energy), the reaction pathway, the behaviour of systems as a function of time, or the value of various observables useful to rationalize, or even predict, experimental data. The third stage in a molecular modelling investigation can be the accurate analysis of the results and the construction of a semi-quantitative or qualitative interpretative model. This stage is not obvious and not always accomplished.

## 2. The Potential Energy Surface (PES)

A PES is an effective potential function for molecular vibrational motion or atomic and molecular collisions as a function of internuclear coordinates. The concept of a potential energy surface is basic to the quantum mechanical and semiclassical description of molecular energy states and dynamical processes. Given the great mass disparity between nuclei and electrons (a factor of 1838 or more) the concept of PES may be understood by considering electronic motions to be much faster than nuclear motions, therefore electronic and nuclear motions can be separated according to time scales and the consequent introduction of an effective potential energy

surface for nuclear motion. This common assumption for both quantum mechanics (QM) and molecular mechanics (MM) methods is the Born-Oppenheimer (B.O.) approximation.<sup>2c,3</sup> The electrons of a molecule can rapidly adjust to any change of the nuclear positions and the energy of a molecule in its ground state can be considered as function of the nuclear coordinates only. The form of this function (and its accuracy) is determined by the particular method (QM and MM) used. In particular in QM calculations<sup>2b</sup> the energy of electrons is computed for a fixed nuclear configuration and the nuclear term is treated as an additive factor to the electronic energy. On the contrary, in MM calculations<sup>2c</sup> one considers explicitly the motions of the nuclei and the electronic contribution is indirectly taken into account by the potential describing the nuclear interactions. In both cases, it is possible to obtain an energy value for each nuclear configuration and one can build a diagram of the energy as a function of the nuclear coordinates. These diagrams (Figure 1.1), often referred to as Potential Energy Surfaces (PES), are of paramount importance in describing molecular structure and reactivity.

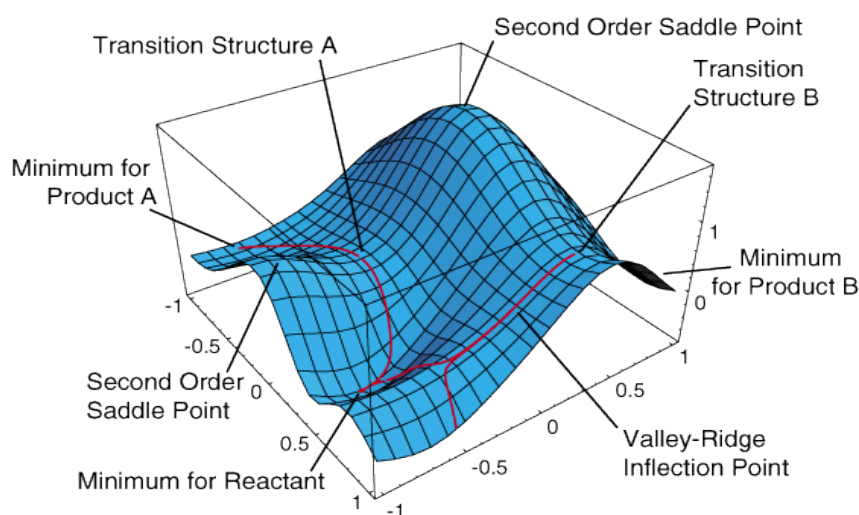


**Figure 1.1**  
Graphical representation of a three-dimensional energy surface

The first step in drawing a PES is the choice of an appropriate coordinate system to describe the configurations of the nuclei. Even if the choice is, in principle, arbitrary only in a few cases it can be useful to adopt a coordinate system different from the Cartesian or Internal ones (two other coordinate systems rarely used are Spherical and Cylindrical coordinates). In the Cartesian coordinate system each atom is described by 3 coordinates that specify its position with respect to an arbitrary point (origin of the coordinate system). Thus, a molecular system of  $N$  nuclei is described by a set of  $3N$  coordinates. Since 3 coordinates must describe the translational motions and 3 the rotational motion of the whole system, the relative positions of  $N$  nuclei can be

determined by  $3N-6$  internal coordinates (or  $3N-5$  if the system, being linear lacks a rotational degree of freedom). The Internal coordinate system can be obtained by choosing  $3N-6$  linearly independent coordinates that coincide with bond lengths, angles (plane angles) and dihedral angles (solid angles) between atoms<sup>2</sup>. Except for diatomic molecules, possessing only one ( $[3*2]-5=1$ ) internal coordinates, the PES of the most common systems are rather complicated and correspond to many-dimensional surfaces (hypersurfaces). Carbonic dioxide ( $\text{CO}_2$ ), a triatomic linear molecule, can be described by four ( $[3*3]-5=4$ ) internal coordinates, and the related PES cannot be visualised as in an unique graphical representation. When the number of internal coordinates is higher than 2, the PES cannot be represented in a single three-dimensional graphic. It is possible to have partial representations of the PES constituted by bi- or three-dimensional (the energy plus one or two coordinates) sections (cross-sections) of the whole surface (in Figure 1.1 and Figure 1.2 a three- and a bi-dimensional cross-section of a multi-dimensional surface are represented).

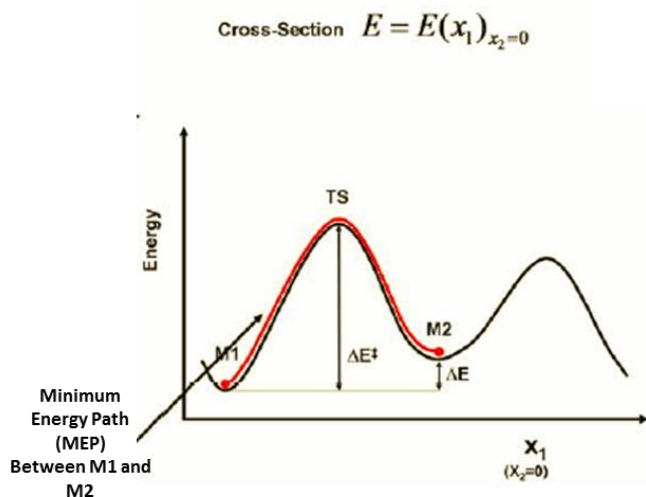


**Figure 1.2**  
bi-dimensional cross-section. The MEP (Minimum Energy Path) connecting the two critical points M1 and M2 is showed.

## 2.1 Representation of the PES

The PES (or a cross-section) can be represented as a diagram where each point corresponds to an unique arrangement of coordinates and, thus, to a particular geometrical structure of the system. Only a few between these structures are interesting and to determine the position of the corresponding points on the PES is usually a challenging task. The PES can be used to study either the structural features of a molecular system or its reactivity. If we consider the energy of the



system as a function (Eq. 2.1) of  $n$  variables (for example the  $3N-6$  internal coordinates), the interesting points (called critical points) are characterized by a null first derivative of the energy with respect to all the  $n$  variables. Only a few of these points have a chemical significance. In particular the points with null first derivatives and all positive second derivatives can be either one of the many local minima or the unique global minimum of the PES. It can correspond to one metastable nuclear configuration or to the most stable configuration, respectively. Points with null first derivatives and negative second derivatives with respect to  $k$  variables are denoted as saddle point of index  $k$ . They have a chemical sense only if  $k=1$  and in this case they correspond to transition structures. An elementary reaction step is described as a transition from one equilibrium state (minimum) to a neighbouring one *via* a single transition state. The reaction mechanism is given by the sequence of steps involved in a chemical process and corresponds on the PES, to the Minimum Energy Path (MEP) connecting the two minima that represent reactants and products, respectively (see Figure 1.2).

**Eq. 2.1**  $E=E(x)$       E function of  $n$  variables

The localization of the critical points is the main target in exploring the PES in both structural and reactivity studies. Should the exact (analytical) shape of the PES be known, the stationary points would be (rather) easily obtained by applying the rules of mathematical analysis. However, the analytical expression of the PES is usually unknown and is rather different for each system. Thus, to locate a point on the unknown PES it is necessary to use an approximate representation of the surface itself. If we consider a bi-dimensional surface where the energy is a function of one variable  $x$  (Eq. 2.2).

**Eq. 2.2**  $E=E(x)$       E function of one variable  $x$

We can represent this function as a Taylor series around a critical point  $x_0$  (Eq. 2.3). This expression contains an infinite number of terms which can be reduced to the first two, by truncating the series after the quadratic term (quadratic approximation). Moreover the first term must be zero because the first derivative at the critical point  $x_0$  is zero; so, by putting  $\Delta x = x - x_0$  we obtain Eq. 2.4.

$$\text{Eq.2.3} \quad E = E^0 + \left(\frac{\partial E}{\partial x}\right)_0 (x - x_0) + \frac{1}{2} \left(\frac{\partial^2 E}{\partial x^2}\right)_0 (x - x_0)^2 + \frac{1}{6} \left(\frac{\partial^3 E}{\partial x^3}\right)_0 (x - x_0)^3 \dots$$

**Eq.2.4**  $E = E^0 + \frac{1}{2} \left( \frac{\partial^2 E}{\partial x^2} \right)_0 \Delta x^2$

If we generalize Eq. 2.3 to a system of n coordinates (Eq. 2.5) we obtain the general Taylor expansion (Eq. 2.6).

**Eq. 2.5**  $E = E(x_1, \dots, x_n)$

**Eq. 2.6**

$$E = E^0 + \sum_i \left( \frac{\partial E}{\partial x_i} \right)_0 (x - x_0) + \frac{1}{2} \sum_{ij} \left( \frac{\partial^2 E}{\partial x_i \partial x_j} \right)_0 \Delta x_i \Delta x_j + \frac{1}{6} \sum_{i,j,k} \left( \frac{\partial^3 E}{\partial x^3} \right)_0 \Delta x_i \Delta x_j \Delta x_k \dots$$

Simplifying to Eq. 2.7

**Eq. 2.7**  $E = E^0 + \frac{1}{2} \sum_{i,j} \left( \frac{\partial^2 E}{\partial x_i \partial x_j} \right)_0 \Delta x_i \Delta x_j$

A most compact representation (Eq. 2.8) can be obtained by means of matrix formalism where G and Δx are used to denote the second derivative (or Hessian) matrix and the displacement vector, respectively (Eq. 2.9).

**Eq. 2.8** 
$$E = E^0 + \frac{1}{2} (\Delta x_1 \dots \Delta x_n) \begin{pmatrix} \left( \frac{\partial^2 E}{\partial x_1^2} \right)_0 & \dots & \left( \frac{\partial^2 E}{\partial x_1^2 \partial x_n^2} \right)_0 \\ \vdots & \ddots & \vdots \\ \left( \frac{\partial^2 E}{\partial x_n^2 \partial x_1^2} \right)_0 & \dots & \left( \frac{\partial^2 E}{\partial x_n^2} \right)_0 \end{pmatrix} \begin{pmatrix} \Delta x_1 \\ \vdots \\ \Delta x_n \end{pmatrix} =$$

$$= E^0 + \frac{1}{2} \Delta \mathbf{x}^T \mathbf{G} \Delta \mathbf{x}$$

**Eq. 2.9** 
$$\mathbf{G} = \begin{pmatrix} \left( \frac{\partial^2 E}{\partial x_1^2} \right)_0 & \dots & \left( \frac{\partial^2 E}{\partial x_1^2 \partial x_n^2} \right)_0 \\ \vdots & \ddots & \vdots \\ \left( \frac{\partial^2 E}{\partial x_n^2 \partial x_1^2} \right)_0 & \dots & \left( \frac{\partial^2 E}{\partial x_n^2} \right)_0 \end{pmatrix}; \Delta \mathbf{x} = \begin{pmatrix} \Delta x_1 \\ \vdots \\ \Delta x_n \end{pmatrix}$$

The Hessian matrix provides both chemical and topological information. It provides an estimate of the coupling between the coordinates adopted to describe the system. The Hessian matrix  $G$  can also give information concerning the nature of the various critical points of a surface. However, to obtain this type of information we must carry out a diagonalization of the matrix  $G$ , that is to transform it into a new different matrix where only diagonal elements are different from zero (diagonal matrix  $H$ ). A matrix  $U$ , satisfying Eq. 2.10, is needed to diagonalize  $G$ , which is a real symmetric matrix.  $U$  is the matrix of eigenvectors and  $U^{-1}$  its inverse (which coincides in this case with its transpose  $U^T$ ). This transformation, which is equivalent to a change of the basis set used to represent the matrix, does not determine any loss of information.

**Eq. 2.10**  $U^{-1}AU = H$

The set of coordinates that makes diagonal the Hessian matrix is usually referred to as “normal coordinates” The matrix  $H$  (Eq. 2.11) is a diagonal  $n*n$  matrix formed by  $n$  *eigenvalues*. If all *eigenvalues* of the Hessian, computed in a given critical point on the PES, are positive, then the point is a minimum of the surface and the corresponding structure describes a chemical species (reactants, products or intermediate). If only one *eigenvalue* is negative, the point is a saddle point of index 1 and corresponds to a transition state. When  $k$  ( $k > 1$ ) negative *eigenvalues* are detected the point is a saddle point of index  $k$  and, as stated above, the corresponding structure is not of chemical interest.

**Eq. 2.11** 
$$H = \begin{pmatrix} h_1 & 0 & \dots & 0 & 0 \\ 0 & h_2 & \dots & 0 & 0 \\ \vdots & \vdots & \ddots & \vdots & \vdots \\ 0 & 0 & \dots & h_{n-1} & 0 \\ 0 & 0 & \dots & 0 & h_n \end{pmatrix}$$

## 2.2 Geometry optimization on the PES

Since the PES complexity rapidly increases with the increasing number of coordinates, a crucial point is the search and location of the various critical points. Efficient algorithms for locating equilibrium and transition structures are now available in modern molecular software. These algorithms are based on the calculation of the first (gradient) and second derivatives (Hessian

matrix) and allow to perform a simultaneous optimisation of the whole set of coordinates. The problem consists in finding a critical points (and the corresponding geometry), given a structure represented by a point on the PES potentially far away from the goal. In general the search algorithm is iterative and the geometry is gradually modified till the wanted critical point is obtained. The fundamental equations to compute the coordinate variations at each step of the search procedure can be derived assuming a quadratic shape of the PES. This can be done after development of a Taylor expansion (see Eq. 2.1) on a generic point of the surface  $x_0$  up to second order. For the one-dimensional case  $E = E(x)$  (Eq. 2.12) can be used to locate a critical point on the surface.

$$\text{Eq.2.12} \quad E = E^0 + \left(\frac{\partial E}{\partial x}\right)_0 + \frac{1}{2}\left(\frac{\partial^2 E}{\partial x^2}\right)_0 \Delta x^2$$

$\Delta x = x - x_0$  is a displacement coordinate and  $E_0$  is the energy value at the point  $x_0$ . Since in a critical point the first energy derivative must be zero, so we can use Equation 2.13 (where the first and second derivative are indicated, respectively with  $g$  and  $G$ ) to determine the critical point  $x$ .

$$\text{Eq.2.13} \quad \frac{\partial E}{\partial \Delta x} = g + G = 0$$

Thus we obtain Equation 2.14 and Equation 2.15 (Newton-Raphson equations) for one variable case.

$$\text{Eq.2.14} \quad \Delta x = x_1 - x_0 = -\frac{g}{G}$$

$$\text{Eq.2.15} \quad x = x_0 - \frac{g}{G}$$

The extension to a  $n$  variable problem can be easily given using a matrix formulation (Equation 2.16).

$$\text{Eq.2.16} \quad x = x_0 - G^{-1}g$$

Should the surface a real quadratic surface, the wanted critical point would be obtained in a single step. However, since in most cases the surface is far from being quadratic, a sequence of motions (sometimes several) on the surface (optimization step) is usually required to locate the critical point. Thus, the most correct and general form of the Newton-Raphson equations is represented by Equation 2.17, where  $\mathbf{x}^{(i+1)}$  is the new position on the surface as computed from the previous one at the  $i^{\text{th}}$  displacement.

$$\text{Eq.2.17} \quad \mathbf{x}^{i+1} = \mathbf{x}^i - \mathbf{G}^{-1}\mathbf{g}$$

Being the calculation of the Hessian matrix computationally expensive, approximate forms of the Newton-Raphson equations (involving approximate Hessian matrices) are usually employed. These methods are often referred to as “quasi-Newton” methods. An example is given in Eq. 2.18, where the Hessian is approximated by a unitary matrix and  $\lambda_i$  is an appropriate scale factor used to modulate the amount of the  $i^{\text{th}}$  displacements on the surface, which always follows the opposite direction of the gradient. In this particular case, where the Hessian is a unit matrix, the method is known as a “steepest descent” method)

$$\text{Eq.2.18} \quad \mathbf{x}^{i+1} = \mathbf{x}^i - \lambda_i \mathbf{g}$$

The “steepest descent” method is far from being accurate but is very fast. It can be efficiently used to decide the first moves on a non quadratic region of the PES, far away from the critical point. Then, in the vicinity of the critical point, the search algorithm can be switched to the Newton-Raphson method or to a more accurate quasi-Newton scheme.

The critical points studied in this work have been determined by an analytical calculation of the gradient by the program series Gaussian09<sup>4</sup>.

### 2.3 Calculation of Vibrational Frequencies

The vibrational states<sup>5</sup> of a molecule are experimentally observed by means of IR (Infra-Red) and Raman spectroscopy<sup>6</sup> and give precious information about molecular structure and environment. However, to achieve this information is often an hard work because it can be difficult to assign each observed peak to a defined molecular motion. The calculation of vibrational frequencies can be of great help in the peak assignment and also in the computation of some

important thermodynamical parameters (molecular enthalpy, entropy and free energy), using some results of statistical mechanics<sup>7</sup>. The simplest description of a vibration is an harmonic oscillator<sup>8</sup> defined by a quadratic (harmonic) potential energy function ( $E_{\text{harm}}$ ) where the energy is a function of the square of the displacement with respect to an equilibrium position ( $x_0$ ), as indicated in Equation 2.19.

$$\text{Eq.2.19} \quad E_{\text{harm}} = k(x - x_0)^2 = k\Delta x^2$$

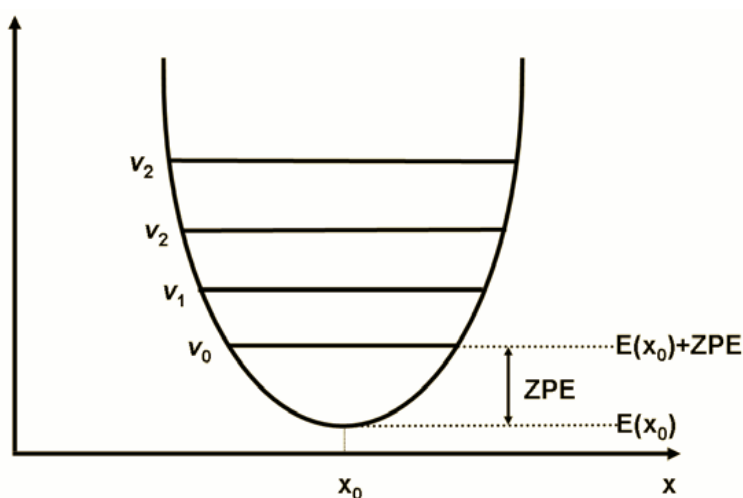


**Figure 1.3**  
Schematic representation of a harmonic potential energy function and first vibrational levels ( $v_0$  to  $v_2$ ). The Zero Point Energy (ZPE) is indicated.

Better results can be achieved by using a more sophisticated potential like the one given using the Morse functional form.

Vibrational frequencies and vibrational energy levels for a molecular system can be directly obtained from the Hessian matrix, which can be computed either analytically (for the most part of the methods used in molecular investigation) or numerically by means of a finite difference procedure applied to analytical first derivatives (a practical task to compute Cartesian numerical frequencies on a given point consists in displacing each atom in the 6 directions of the Cartesian space; this requires a total of  $6N+1$  energy and gradient evaluations,  $N$  being the number of atoms of the system).

A different technique to obtain the vibrational frequencies is bound to the molecular dynamics (MD) (see the next section). The vibrational motions observed in a MD simulation is a superposition of all the normal modes of vibration, so, to obtain the frequencies, it is necessary to apply the Fourier transform to all the motions of the MD motions; the motion corresponding to each peak of the so obtained spectrum is obtained by applying to it an inverse Fourier transform.

The energy value obtained by means of geometry optimization of a stable species coincides with the minimum of the PES. Actually, the system can never reach this energy value because it always maintains some vibrational motion. It is possible to evaluate the energy associated with the lowest vibrational level (Zero-Point energy or ZPE, see Figure 1.3) and sum it to the potential energy to obtain a more accurate value. This is of particular importance when comparing the energy of different critical points of the surface (different conformers or in the investigation of a chemical reaction).

### 3. Quantum Mechanical methods

Chemical bond breaking and forming involve electrons. In order to obtain information about a reaction mechanism, we need to treat explicitly electrons, so we have to face the quantum mechanical theory.

The basic principles are the dual character of the sub-atomic particle, corpuscular and undulatory, and that the particle is not located in a determined spot, but it has a probability of being in this or that point (Heisenberg's indetermination principle).

This probability is described by a wave function which is, in turn, the solution of the Schrödinger equation. The time-independent Schrödinger equation is reported in Equation 3.1, where  $\Psi$  is the wavefunction describing the system,  $E$  is the energy of the system and  $\hat{H}$  is the Hamiltonian operator.

$$\text{Eq.3.1} \quad \hat{H}\Psi = E\Psi$$

The total, non-relativistic Hamiltonian ( $\hat{H}$ ) for a system of charged particles (electron and nuclei) can be written as

$$\text{Eq.3.2} \quad \hat{H} = \sum_a -\frac{1}{2m_a} \nabla_a^2 + \sum_{a<b} \frac{q_a q_b}{|\vec{r}_a - \vec{r}_b|}$$

where  $m_a$  is the mass of the particle  $a$ ,  $\nabla_a^2$  the Laplacian operator for particle  $a$ ,  $q_a$  and  $q_b$  are the charges of  $a$  and  $b$ , and  $\vec{r}_a$  and  $\vec{r}_b$  the positions of  $a$  and  $b$ . According to the B.O. approximation the total Hamiltonian can be split in the nuclear and electronic term to give Equation

3.3 and Equation 3.4, where the indices  $\nu\mu$ , and  $ji$ , indicate the coordinates of nuclei and electrons, respectively. Thus, the total Hamiltonian is written in term of one-, two- and zero-electrons operators.

$$\text{Eq.3.3} \quad \hat{H}_{nucl} = \sum_{\mu} -\frac{1}{2m_{\mu}} \nabla_{\mu}^2$$

$$\begin{aligned} \text{Eq.3.4} \quad \hat{H}_{el} &= \sum_i -\frac{1}{2m_i} \nabla_i^2 + \sum_{\mu,i} \frac{Z_{\mu}}{|\vec{r}_{\mu}-\vec{r}_i|} + \sum_{i<j} \frac{Z_{\mu}}{|\vec{r}_i-\vec{r}_j|} + \sum_{\mu,\nu} \frac{Z_{\mu}Z_{\nu}}{|\vec{r}_{\mu}-\vec{r}_{\nu}|} = \\ &= \sum_i \hat{h}_i + \sum_{i<j} \hat{g}_{ij} + \hat{h}_0 \end{aligned}$$

### 3.1 Slater Determinant and LCAO approximation

As well as for atoms, molecules are expressed as molecular wave function, i.e molecular orbitals (MO) which are usually described by a linear combination of atomic orbitals (LCAO). The Molecular Orbital (MO) theory is an approach to Quantum Mechanics which uses one-electron functions to approximate the electronic wave function. These functions are formed by the product of a spatial part  $\psi_i(j)$  times a spin function  $\alpha(j)$  or  $\beta(j)$ , and are therefore called spinorbitals (the index  $i$  refers to the  $i$ th spatial part, while  $j$  refers to the  $j$ th electron). The antisymmetry property of the wave function is fulfilled using a Slater Determinant<sup>9</sup> composed of spinorbitals:

$$\text{Eq.3.5} \quad \Psi = (n!)^{-1/2} \begin{vmatrix} \psi_1(1)\alpha(1) & \psi_1(1)\beta(1) & \psi_2(1)\alpha(1) & \cdots & \psi_{n/2}(1)\beta(1) \\ \psi_1(2)\alpha(2) & \psi_1(2)\beta(2) & \psi_2(2)\alpha(2) & \cdots & \psi_{n/2}(2)\beta(2) \\ \vdots & \vdots & \vdots & \ddots & \vdots \\ \psi_1(n)\alpha(n) & \psi_1(n)\beta(n) & \psi_2(n)\alpha(n) & \cdots & \psi_{n/2}(n)\beta(n) \end{vmatrix}$$

In the Hartree-Fock (HF)<sup>10</sup> method the total electronic wave function is formed by a single Slater Determinant of the occupied spinorbitals.

Each molecular orbital  $\psi_i$  of a system can be expanded in terms of a set of  $N$  pre-defined one electron functions  $\phi_{pi}$  denoted as basis functions (basis set) according to the Equation 3.6, where the  $c_{ij}$  are the molecular orbital expansion coefficients. When atomic orbitals (AO) are used as basis functions this approach is often referred to as Linear Combination of Atomic Orbital (LCAO) approximation.



$$\text{Eq.3.6} \quad \psi_i = \sum_{j=1}^N c_{ij} \phi_j$$

### 3.2 Basis set

The basis set is formed by atomic orbitals (s, p, d, f,...) which can be described by hydrogen-like wave functions (Slater type orbitals) or by wave functions mathematically expressed as Gaussian functions.

The Slater type orbitals (STOs) are suited in describing the electronic behavior in the molecular space (near and far from the nucleus), but their application in polyatomic systems is problematic, since STOs do not calculate with the necessary precision the polycentric integrals.

The new generation of orbitals developed by Boys<sup>9</sup> and later by Shavitt and Karplus<sup>11</sup>, are known as Gaussian type orbitals (GTOs), and are described by:

$$\text{Eq.3.7} \quad \chi_j^{GTO} = N \cdot x^l y^m z^n e^{-\alpha(x^2+y^2+z^2)}$$

Where N is a normalization constant and  $\alpha$  is the orbital exponent, which is a constant as well. Defining  $L = l+m+n$ , for  $L=1$  the GTO describes a s orbital,  $L=1$  a s orbital and so on. Usually a primitive  $\chi_{GTO}$  gives a good but poor description of the electronic wave function, so the common approach is to use a Gaussian function which is a linear combination of primitive Gaussians  $\chi_{GTO}^s$ :

$$\text{Eq.3.8} \quad \phi_i = \sum_{ij} b_{ij} \chi_j^{GTO}$$

Where  $\phi_i$  is the contracted Gaussian and  $b_{ij}$  is the contraction coefficient. Once the function type (STO or GTO) is chosen, it is important to decide the number of function that form the basis set.

The minimum level of accuracy is given by the minimal basis set, which gives each atom the number of basis functions necessary to place each electron. The basis function can be STO orbitals which are much more exact than GTOs whereas GTOs are less computing-demanding. So, in order

to obtain the same STOs level of description for a minimal basis set, we can use a combination of GTOs to approximate a single STO:

$$\text{Eq.3.9} \quad \phi_i^{STO} = \sum_{ij} b_{ij} \chi_j^{GTO}$$

The most popular minimal basis set is STO-NG, where N refers to the number of Gaussian functions  $\chi_j^{GTO}$  needed to approximate one  $\phi_i^{STO}$ . The STO-NG basis set, unfortunately, is isotropic, so that the description of the three p orbitals is identical and the charge distribution is always spherical, when we know that e.g. ethylene  $\pi$ -orbitals are not spherical at all. The other problem of STO-NG is that it cannot expand or contract itself depending on the chemistry of the system, meaning that the base cannot describe the charge cloud of a carbanion properly.

So the choice of a STO-NG is a compromise between results-accuracy and computing-efficiency.

The STO-NG limitations are overcome by choosing an *extended basis set* for describing the system. The extended basis set describes the external electrons with a greater number of contracted Gaussian functions and *double- $\zeta$*  and *triple- $\zeta$*  basis utilize two or three contracted function respectively to express the external shell electrons. Many other extensions can be added in order to obtain the most correct description of an electron: *split valence* (the electronic valence orbital is split), *polarization* (which describes the uneven charge density motion in respect to the atoms).

### 3.3 Correlation Energy

The Hartree-Fock<sup>10</sup> method is one of the most widely used computational approach for the determination of the wave-function within the molecular orbital model. The wave function is written in the form of a Slater Determinant and the related energy is obtained by minimization of its expression with respect to the molecular orbitals  $\phi_i$ . The wave function of the poly-electronic system orbital (MO) is approximated to a finite summation of mono-electronic functions which are solutions of the Fock's equation. The paradox that the set of input mono-electronic functions are solutions of the same equation is solved by an iterative calculation where the initial function set is approximated to rough molecular orbital.

To solve the HF equation with a wave function constructed using the Slater Determinant and LCAO scheme, in a self consistent way the Roothaan-Hall<sup>12</sup> equations were introduced. The

algorithm used to solve these equations is an iterative approach known as Self Consistent Field (SCF) procedure. Despite the improvements, these theories are all based on the independent-particle model which states that each electron is affected by a mean potential and it does not feel the effective presence of an electron in its same orbital. The energy eigenfunctions (wave-functions) are assumed to be products of one-electron functions (Slater determinants). The effects of electron correlation, beyond that of exchange energy resulting from the anti-symmetry of the wavefunction, are neglected. The missing electronic correlation effects of the HF method, lead to large deviations with respect to experimental results. This error is the Correlation Energy<sup>13</sup> and it arises from:

$$\text{Eq.3.10} \quad E_{\text{corr}} = E - E_{\text{HF}}$$

Where  $E_{\text{HF}}$  is the limit energy calculated by the Hartree-Fock method and  $E$  would be the exact eigenvalue of the Schrödinger equation if it was possible to solve it.

The correlation energy is just a mathematical quantity and it amounts to the 1% of the total energy calculated; it would seem a small error, but its magnitude is the same of many observables.

Considering a N-electron system, the Hamiltonian operator associated to it is:

$$\text{Eq.3.11} \quad \hat{H} = \sum_i h_i + \frac{1}{2} \sum_{ij} h_{ij}$$

Where  $h_i$  is the hydrogen-like mono-electronic Hamiltonian as follows

$$\text{Eq.3.12} \quad h_i = -\frac{1}{2} \nabla_i^2 - \sum_j \frac{Z_j}{r_{ij}}$$

The  $h_{ij}$  in Eq.3.11 represents the reciprocal repulsion between two electrons  $i$  and  $j$  and it tends to infinite when  $r_{ij}$  tends to zero. This effect is known as “Coulomb’s hole” and it is neglected in the Hartree-Fock method because of the *independent-particle* approximation. On the other hand, the method do consider the Pauli’s principle, so that the possibility of finding to parallel electrons in the same position is zero; this means that the electron is characterized by a “Fermi’s hole”.

Since the Hartree-Fock method considers the “Fermi’s hole” but not the “Coulomb’s hole”, the relative correlation error associated to anti-parallel electrons is greater than that associated to parallel electrons. So two main contributes dominate the correlation energy:

- I. Internal or structure dependent correlation energy due to the inappropriateness of the Hartree-Fock model to describe the degeneration o quasi-degeneration of two o more electronic configurations;
- II. External or dynamic correlation energy associated to the motion of the antiparallel electrons.

The dynamic correlation energy in the study of an organic reaction changes a lot during the reactive path and, in particular in the transition state, where there is a superior electron crowding (the electron feel many other electrons around it) so that the dynamic contribution is very important in the case of activation energy calculations, comparisons between reagents and transition states, etc and it is fundamental to introduce it in the calculations.

The calculations that contemplate the *dynamic correlation energy* are called post Hartree-Fock methods and their goal is, as usual, the resolution of the Schrödinger equation. Among them, the Configuration Interaction (CI)<sup>14</sup> method assumes the system wave function  $\psi_i$  as linear combination of diverse Slater determinants, obtained from the ground state determinant by substituting every spin-orbital function with a virtual one; while the Moller-Plesset (MP)<sup>15</sup> model approaches a perturbative calculation which gives, as a result, the different order correction to the energy calculated by the Hartree-Fock method.

The most promising method is the Density Functional Theory (DFT). Here an accurate description of DFT method is discussed since it is the calculation model we adopted for most of the calculations presented in the thesis.

### 3.4 Density Functional Theory Method (DFT)

The density functional theory is based on the Hohenberg-Kohn theorem<sup>16</sup> that states that all the fundamental state proprieties of the system are determined univocally by the electronic density  $\rho(\mathbf{r})$  and that any other electronic density  $\rho'(\mathbf{r})$  gives rise to an higher energy than the real one.

The exact expression  $E[\rho(\mathbf{r})]$  of is not known, since its dependence on  $\rho(\mathbf{r})$  is not available but in 1965 Kohn and Sham<sup>17</sup> developed an approximation of the density functional, which is adopted till today.

The Kohn-Sham equation is the Schrödinger equation of a fictitious system (i.e. Kohn-Sham system) of non-interacting particles that generates the same density of any given system of interacting particles.

Kohn-Sham proposed to start the calculation using a fictitious system of non-interacting electrons that has the same density as the real system for the ground state where the electrons would interact.

The expression of the total energy is a sum of the kinetic contribution ( $T_k$ ), the attractive nucleus-electron contribution ( $E_{Ne}$ ), the Coulombic term ( $J$ ) and the exchange-correlation term ( $E_{xc}$ ):

$$\text{Eq.3.13} \quad E[\rho] = T_k[\rho] + E_{Ne}[\rho] + J[\rho] + E_{xc}[\rho]$$

The definitions for the nucleus-electron attraction ( $E_{Ne}$ ) and the classical electron-electron Coulomb repulsion energies ( $J$ ) are the same as those used in Hartree-Fock theory, and so the two contributions can be deduced by a Hartree-Fock calculation.

The kinetic energy of the electron has a different form in respects to the Hartree-Fock theory, but the Kohn-Sham formalism resolves the problem by defining the  $T_k[\rho]$  as:

$$\text{Eq.3.14} \quad T_k[\rho] = -\frac{1}{2} \sum_i^N \int \phi_i^*(r) \nabla^2 \phi_i(r) dr$$

Where  $\phi_i(r)$  are the Kohn-Sham non-interacting particles wave functions and are the eigen-functions of the Kohn-Sham eigenvalue equation:

$$\text{Eq.3.15} \quad h_i^{KS} \phi_i(r) = \varepsilon_i \phi_i$$

$h_i^{KS}$  Is the Kohn-Sham operator:

$$\text{Eq.3.16} \quad h_i^{KS} = -\frac{1}{2} \nabla^2 - \sum_k^{nuclei} \frac{z_k}{|r_i - r_k|} - \int \frac{\rho(r')}{|r_i - r'|} dr' + V_{xc}$$

$V_{xc}$  is the exchange-correlation functional for one electron and  $E_{xc}$  is the expectation values of the Kohn-Sham Slater determinant:

$$\text{Eq.3.16} \quad V_{xc} = \frac{\partial E_{xc}}{\partial \rho}$$

The last term of Eq.3.13  $E_{xc}[\rho]$  can be split into two terms: exchange (X) and correlation (C) contribution:

$$\text{Eq.3.17} \quad E_{xc}[\rho] = E_x[\rho] + E_c[\rho]$$

These terms take in account the effects of exchange, correlation, correction for self-interaction and the difference of the kinetic energy between the fictitious non-interacting systems and the real one.

Unfortunately their form is unknown, so various DFT models exist to calculate the exchange and correlation functionals: local methods, where only the electron density is used, and generalized gradient corrected methods (or non-local) which use the electron density as well as its gradients.

The Gaussian09<sup>4</sup> series of programs make available exchange  $E_x[\rho]$  and correlation  $E_c[\rho]$  functionals that can be generally expressed as:

$$\text{Eq.3.18} \quad a_1 E(S)_x + a_2 E(HF)_x + a_3 E(B88)_x + a_4 E(local)_c + a_5 E(non - local)_c$$

Where  $E(S)_x$  is the Slater exchange functional,  $E(HF)_x$  the exchange term of Hartree-Fock and are the non-local correction for the exchange functional as suggested by Becke<sup>18</sup>.  $E(local)_c$  is the correlation functional without gradient corrections, while  $E(non - local)_c$  is the non-local corrected correlation functional. One of the fundamental aspect of any computational study at DFT theory level, is the choice of the functional to be used in the calculation. Many functionals are available in literature which are suited for describing different kind of problems.

Since there is no unique functional able to describe the complete molecular system or the full reactive path, the most used are the hybrid functionals.

The most popular functional is B3LYP where  $E(local)_c$  (Eq. 3.18) corresponds to the local correlation functional of Volsko, Wilk e Nusair<sup>19</sup>, while  $E(non - local)_c$  is the Lee-Yang-Parr<sup>20</sup>

functional; the coefficients are those suggested by Becke<sup>21</sup> ( $a_1 = 0.80$ ,  $a_2 = 0.20$ ,  $a_3 = 0.72$ ,  $a_4 = 0.10$ ,  $a_5 = 0.81$  ).

Despite the continuous development of new functionals some problems still affect B3LYP accuracy. Due to deficiencies in the treatment of exchange–correlation the pure dispersion interactions between unbound chemical species are not well reproduced by common functionals. This problem can be treated by adding an empirical correction to the functional, as proposed by Grimme<sup>22</sup>, enhancing the results with no added computational cost. The second problem relates to the poor cancellation between the electron self-interaction present in the Coulomb term and the exchange energy. The third problem is that even the best current exchange–correlation functionals still lead to unacceptably large energy errors for a significant number of “outliers” species<sup>23</sup>, even when dispersion and self-interaction do not appear to be involved and normal bonding is expected to occur.

Although the B3LYP is the most used functional, the disadvantages described above induce:

- A better efficiency for the chemistry regarding atoms of the principal groups rather than for the transition metals;
- Underestimates the activation barrier heights;
- Imprecision for the interactions dominated by the middle-radius correlation energies, as the van der Waals, the aromatic  $\pi$ -stacking interactions and the isomerization energy of alkanes.

Because of this limitations, a new hybrid meta-GGA (adopting the Generalised Gradient Approximation or GGA) exchange–correlation functionals has been developed by Zhao and Truhlar<sup>24,25</sup>. This new functional class is called M06 (Minnesota Functionals) and it was designed to correct the deficits of the DFT by optimizing a number of empirical parameters.

The M06 functionals depend for the local parts on three variables: the spin density, the reduced spin density gradient and the spin kinetic energy density, the Hartree-Fock’s exchange functional is incorporated in the  $E(\text{non} - \text{local})_c$  functional. The two main functionals of Minnesota’s class are called M06 and M06-2X. The M06 functional is parametrized including both transition metals and non-metals, whereas the M06-2X functional is a high-non-locality functional with double the amount of non-local exchange (2X), and it is parametrized only for non-metals<sup>25</sup>. These functionals are among the best at the moment for the study of organometallic and inorganometallic thermochemistry, non-covalent interactions and long-range interactions.

The choice of the functional is, therefore, always not trivial. Careful consideration should be on the system and according to the its characteristics the most suitable functional have to be employed. In this thesis different systems are presented. In the second part organometallic compounds containing transition metals are treated, in the third and fourth are all non-metallic systems. We decided to adopt the M06-2X in non-metallic systems and M06 for the organometallic section.

## 4. Molecular Mechanical methods

The MM approaches allow to compute energy and properties of large molecular system using very simple models. The atoms are handled as charged sphere interacting under the Newton's laws of motion. These spheres are connected by elastic springs along the direction of the chemical bond. The functional form<sup>2</sup> of the MM energy is composed by various terms, each ones taking into account the contribution arising from various bonding (stretching, bending and torsional) and non-bonding interactions (van der Waals, Coulombic). The potential energy of all systems in molecular mechanics is calculated using force fields. A force field refers to the functional form and parameter sets used to describe the potential energy of a system of particles. Force field functions and parameter sets are derived from both experimental work and ab-initio quantum mechanical calculations. "All-atom" force fields provide parameters for every atom in a system, while "united-atom" force fields treat two or more atoms (a fragment of the system) as a single interaction center.

The Molecular Mechanics Force-Field expresses the total energy as a sum of Taylor series expansions for stretches for every pair of bonded atoms, and adds additional potential energy terms coming from bending, torsional energy, van der Waals energy, electrostatics, and cross terms.

$$\text{Eq.4.1} \quad E = E_{\text{str}} + E_{\text{bend}} + E_{\text{tors}} + E_{\text{vdw}} + E_{\text{el}} + E_{\text{cross}}$$

In the Eq.4.1 are expressed simple harmonic potentials (or sometimes more complex functions) to describe bonds, angle bending and torsions. Non-bonded electrostatic and Van der Waals interactions are accounted for on the basis of the charge (or dipole) assigned to the atoms using a simple Coulombic potential and by means of a Lennard-Jones potential (or similar), respectively. The analytic functional form of the equations used to compute energies and forces



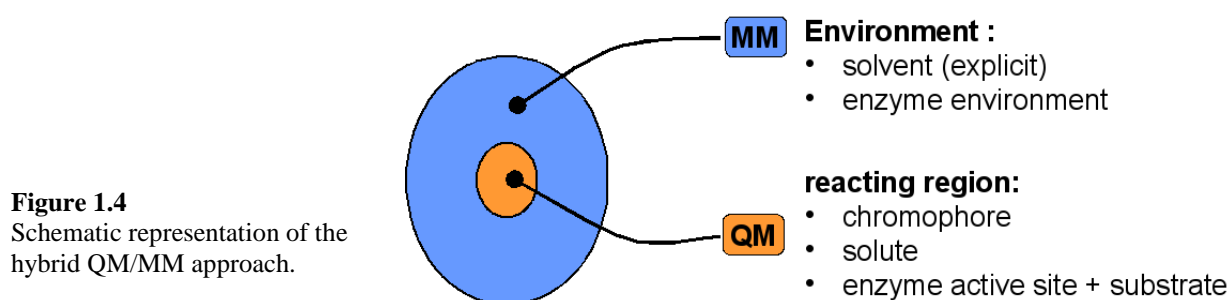
make the MM calculation fast even for large molecules. Anyway, the drawback of these methods is their inability in describing processes involving a change of the “nature” of atoms.

A specific set of parameters is assigned to each couple (or triplet and quartet, for bending and torsions) of atoms. The definition of atoms within MM methods is more complicated than in QM approaches. More precisely to obtain reliable values for MM calculations a new atom definition has been adopted: all atoms in a molecule are classified as different Atom Types not only on the base of the atomic number, but also according to their immediate environment. This lead to the development of different parameters, for instance, for aliphatic and aromatic Carbon atoms, for carbonylic or alcoholic Oxygen atoms, and so on. A particular MM Force Field is defined on the basis of the adopted functional form for the energy expression, of the specific values of the chosen parameters and of the available Atom Types. A commonly used Force Field is the Amber Force Field (AFF)<sup>26</sup>, firstly implemented in the AMBER simulation package but now available in many others as Gaussian09<sup>4</sup>. AFF gives extremely reliable results when used to study proteic<sup>27</sup> or nucleic acid<sup>28</sup> systems, because of its accurate parameterisation focused on bio-molecules. Other common Force field are Universal Force Field (UFF)<sup>29</sup> and DREIDING<sup>30</sup>, both also implemented in the Gaussian09<sup>4</sup> program series employed for the computation of this discussion. Universal Force Field (UFF)<sup>29</sup> was particularly employed in several aspects of carbocatalysis processes investigated here. In the UFF the force field parameters are estimated using general rules based only on the element, its hybridization, and its connectivity. In order to facilitate studies of a variety of atomic associations, this force field using general rules for estimating force field parameters based on simple relations. The angular distortion functional forms in UFF are chosen to be physically reasonable for large amplitude displacements. UFF is more simple and universal with respect to the most popular force fields, that are limited to particular combinations of atoms, for example, those of proteins, organics, or nucleic acids. Other famous force field are Gromacs<sup>31</sup> and Charmm<sup>32</sup> ones, implemented in the homonymous packages.

## 5. Hybrid QM/MM methods

Although they are highly reliable, QM methods are much more expensive than MM ones in terms of computational cost and cannot be used to study very large systems. Thus, a problem arises when studying the chemical reactivity of large molecular systems; in response to this need the last three decades were spent on theoretical studies for the development of new computational methods.

A promising technique is the partitioning of the whole system (called real in the following discussion) in two regions: a small part, containing the atoms involved in the chemical process, is described at QM level, while the remaining atoms are treated at MM level, in order to speed-up the calculation and simulate (although at a lower level) the influence of the environment on the reactive core. This hybrid approach is usually called “QM/MM”<sup>33</sup>.



In the QM/MM general approach the total energy of the whole system,  $E_{QM/MM}$ , is a sum of the energy of the model system by the QM method ( $E_{QM}$ ), the energy of the environment system by the MM method ( $E_{MM}$ ), and the interactions ( $E_{QM-MM}$ ) between the QM model system and the MM environment system (Eq.5.1).

**Eq.5.1**       $E_{QM/MM} = E_{QM} + E_{MM} + E_{QM-MM}$

This scheme is called “additive scheme”<sup>34</sup>, in which the energies of the two systems and the interactions between the two systems are added to obtain the total energy of the whole system. The QM/MM coupling Hamiltonian ( $E_{QM-MM}$ ), the interactions between the “QM” and “MM” systems, generally includes (1) bonded interactions for covalent bond(s) bisecting the QM/MM boundary (i.e., stretching, bending, and torsional contributions), and (2) non-bonded interactions (i.e., van der Waals and electrostatic interactions).<sup>35</sup>

## 5.1 Our own N-layer Integrated molecular Orbital and molecular Mechanics: ONIOM

The QM/MM calculations of this thesis (see part III) are carried out with the multi-layer ONIOM (Our own N-layer Integrated molecular Orbital and molecular Mechanics)<sup>36</sup> scheme developed by Morokuma and coworkers and implemented in Gaussian09<sup>4</sup> series of program.

The ONIOM method (that includes the IMOMM and IMOMO original methods) use a “subtractive” or “extrapolative” scheme approach. As opposed to the additive QM/MM schemes that evaluate  $E_{\text{QM-MM}}$  (Eq 5.1), in the “subtractive” or “extrapolative” method the total energy of the whole (“real”) system is evaluated as the MO (or QM) energy of the model system ( $E_{\text{QM,model}}$ ) plus the MM energy of the real system ( $E_{\text{MM,real}}$ ), and minus the MM energy of the model system ( $E_{\text{MM,model}}$ ):

$$\text{Eq.5.2} \quad E_{\text{ONIOM QM/MM}} = E_{\text{QM,model}} + E_{\text{MM,real}} - E_{\text{MM,model}}$$

The subtractive operation removes the “double-counted” MM contributions<sup>37</sup>, excluding the MM contributions of the part already included in the MO energy. Thus, the energy gradient is also defined and can be used for full geometry optimization of the combined “real” system. The ONIOM extrapolative scheme is not restricted to two layers. Svensson et al.<sup>38</sup> combined the extrapolative two-layer ONIOM schemes to develop a three-layer ONIOM3 method. As shown in Figure 1.5, the entire “real” system can be divided into three systems, “small model”, “intermediate”, and “real”, and three levels of theory, “low”, “medium”, and “high”, can be used. With this three-layer scheme, ONIOM3, the energy of the real system at the high level is approximated as<sup>38</sup>

$$\text{Eq.5.3} \quad E_{\text{ONIOM3(high:medium:low)}} = E_{\text{high,model}} + E_{\text{medium,intermediate}} - E_{\text{medium,model}} + E_{\text{low,real}} - E_{\text{low,intermediate}}$$

Any combination of three levels in the decreasing order of accuracy can be adopted in ONIOM3, typically MO1 is treated at high QM level, the outer is treated at MM level and the intermediate layer (MO2) is treated at a low QM level or semiempirical.

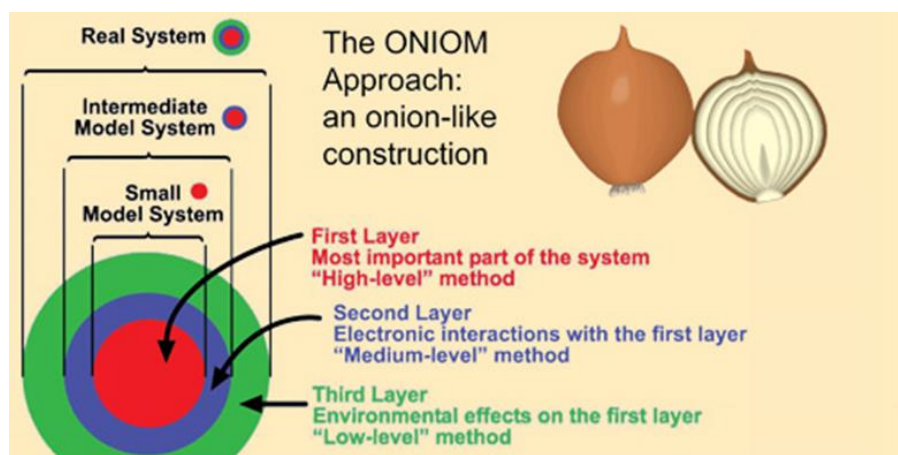


**Figure 1.5**  
Schematic partitions of the whole system by the ONIOM3 method

ONIOM scheme is efficient if an appropriate MM force field is used and if an Electrostatic Embedding (see below) is adopted.

The ONIOM method can be easily expanded and generalized to an n-layer n-level method, however, the implementation has not been made in Gaussian09 for n=4 or larger and it should be considered that in the cases presented here it was enough a two layer ONIOM.

## 5.2 Interactions between the layers, the Electrostatic Embedding

The coupling between the different subsystems (“small model”, “intermediate”, and “real”) is the heart of a QM/MM method. The coupling, in general, must be capable of treating both bonded interactions (bond stretching, bond bending, and internal rotation, sometimes called valence forces) and non-bonded interactions (electrostatic interaction and van der Waals interactions). Various QM/MM schemes have been developed to treat the interactions between the subsystems. As might be expected from its general importance in a myriad of contexts,<sup>39</sup> the electrostatic interaction is the key element of the coupling. If we consider a two-layers system, the treatment of the electrostatic interaction between the high and low layers can be divided into two groups, the group of mechanical embedding and the group of electrostatic embedding<sup>40</sup>. A mechanical embedding (ME) scheme performs QM computations for the high layer in the absence of the low, and treats the interactions between the two models at the MM level. These interactions usually include both bonded (stretching, bending, and torsional) interactions and non-bonded (electrostatic and van der Waals) interactions.

In an electrostatic embedding (EE) scheme the QM computation for the high layer is carried out in the presence of the low layer by including terms that describe the electrostatic interaction between the high and low as one-electron operators that enter the QM Hamiltonian. Because most popular MM force fields have developed extensive sets of atomic-centered partial point charges for calculating electrostatic interactions at the MM level, it is usually convenient to represent the low layer atoms by atomic-centered partial point charges in the effective QM Hamiltonian. The bonded (stretching, bending, and torsional) interactions and non-bonded (van der Waals et al.) interactions between the high and low models are retained at the MM level.

Originally the first ONIOM (MO:MM) method (integrated molecular-orbital molecular-mechanics IMOMM scheme<sup>36,38</sup>) developed by Morokuma and coworkers was a ME scheme.

However, recently, it has been huge advances in the development of electrostatic embedded ONIOM method<sup>41</sup>, thanks to the Vreven et al. work, highlighting the trend of moving from ME to EE in QM/MM methodology. The price to pay for this improvement is more complicated implementation and increased computational cost. To account for the electrostatic influence of the surrounding MM region on the QM layer in our calculations was always employed the Electrostatic Embedding approach.

### 5.3 The boundary region

All the QM/MM method, however, has to overcome a difficult technical problem, which is often a source of significant errors and approximations: the correct description of the boundary region. Thus, the approximations adopted to deal with the interface between the two regions have a fundamental importance for a correct simulation of their reciprocal influence.

In some cases the boundary does not go through a covalent bond: this is the case of a solute (QM level) immersed in a large number of explicit solvent molecules (MM level), or, as in our case, a reactant system (QM level) evolving towards the product inside a Carbon Nanotube (MM level). These case are very easy to handle and do not need special assumptions. However, in many cases, one cannot avoid passing the QM-MM boundary crosswise one (or more) covalent bond(s), like it is for enzymatic systems or a nanostructure representation. Two strategies have been developed to overcome this problem: a) the atom-link approach<sup>42</sup> and b) the modified orbital methods<sup>43</sup>. In the ONIOM scheme implemented in Gaussian09, the atom-link approach is employed<sup>44,37a</sup>. Hydrogen link atoms by default are used: all dangling  $\sigma$  bonds in the model system are capped with hydrogen atoms. This is the simplest and most common boundary approximation, which was used earlier by the Kollman and Karplus groups<sup>45</sup>. However, other monovalent atoms (e.g., fluoride link atom<sup>44b</sup>) can alternatively be used as link atoms to complete the dangling single bond. Likewise, divalent atoms (e.g., oxygen, sulfur) could be used to saturate the dangling double bond (although it is strongly recommended this is avoided, if alternative choices exist)<sup>44b</sup>.

## 6. Solvent Effect

### 6.1 The Polarizable Continuum Model (PCM)

The models based on continuum polarizable stem from simple physical considerations. From the beginning the attention was placed on the microscopic description of only one of the two components of the system: the solute (M). The expression of the energy of classical interaction between M and a simple medium represented by a continuous dielectric obtained by Born and Bell<sup>46</sup> was formally extended by Kirkwood<sup>47</sup> in 1934 without limitations due to the complexity of the system. The fundamental contribution of Onsager<sup>48</sup> in 1936 was to provide an important interpretive tool. Tomasi and coworkers<sup>49</sup> have significantly improved the method, enhancing the mathematical formalism. From the qualitative point of view, the whole body of the solvent is treated as a homogeneous dielectric, in which, it generates a suitable cavity where takes place the solute or the reactive system. The dipole moment of the solute M will induce a second dipole moment in the dielectric. The interaction between the two dipole moments leads to a stabilization of the overall system. Therefore a quantum mechanical treatment that allows to study the wave function of the whole system should be developed. In this way, the dielectric that simulates the mass of the solvent and the cavity housing the reagent system can be correctly described. It is also necessary to ensure that the discussion can easily be achieved in the context of the already available algorithms used for the study of gas-phase reactive systems. The following strategy can be adopted to study a reactive system in solution: the gas-phase reaction surface is first studied, determining the critical points of chemical interest (minima and transition states). Subsequently the solvent effect using the fixed gas-phase geometries is introduced.

### 6.2 The Effective Hamiltonian

The operator which describe a molecular system in solution in the solvation continuum models framework is an effective Hamiltonian. If we consider an infinite set of molecules at a given temperature and pressure which have the typical characteristics of the liquid state. The system is in thermal and mechanical equilibrium, but chemical events within it may take place. This physical system is the starting point for the quantum mechanical formulation of the continuous polarizable model. The formulation of mathematical model is due to Angyan<sup>50</sup> and Tapia<sup>51</sup>. The fixed nuclear

part (by B.O. approximation) of the effective Hamiltonian ( $H_M$ ) for the solute depends on the coordinates of M and  $N_{el}$  ( $q = q_1, \dots, q_{N_{el}}$ ) and the nuclei of  $N_{Nuc}$  coordinates ( $Q = Q_1, \dots, Q_{N_{nuc}}$ ).

$$\text{Eq.6.1} \quad H_M(q, Q) = H_M^{(0)}(q, Q) + V_{int}$$

Where  $H_M^{(0)}$  is the normal gas-phase Hamiltonian, according with the Born-Oppenheimer approximation, and  $V_{int}$  is a potential of interaction that will be defined later. The Schrodinger equation is 6.1.

$$\text{Eq.6.2} \quad H_M(q, Q) \Psi^{(f)}(q, Q) = E^{(f)}(Q) \Psi^{(f)}(q, Q)$$

All relevant information on the effect of the solvent and solute M are contained in the eigenvalue  $E^f$  and the wave function  $\Psi^{(f)}$ . In many cases the distribution of molecular charge ( $\rho_M$ ) is used in place of  $\Psi^{(f)}$ .  $\rho_M$  is the sum between the nuclear charge distribution ( $\rho_{nucl}$ ) and the electron density function ( $\rho_{el}$ ):

$$\text{Eq.6.3} \quad \rho_M(r, Q) = \rho_{nucl}(r, Q) + \rho_{el}(r, Q)$$

$$\text{Eq.6.4} \quad \rho_{nucl}(r, Q) = \sum_{\alpha} Z_{\alpha} \delta(r - Q_{\alpha})$$

$$\text{Eq.6.5} \quad \rho_{el}(q_1) = - \int |\Psi^{(f)}(q, Q)|^2 dq_2 \dots dq_{N_{el}}$$

Where  $Z_{\alpha}$  is a nuclear charge, and the index  $\alpha$  runs over all the nuclei of M. The negative sign in  $\rho_{el}(q_1)$  takes into account the electron charge (-1 in atomic units).  $V_{int}$  contains additional information that can be used in the study of chemical problems. Its definition involves a function of the solvent molecules distribution, mediated by temperature ( $g_s$ ) Eq.6.6.

$$\text{Eq.6.6} \quad V_{int} = V_{int}(q, Q, g_s)$$

Since the solvent must be modeled as a homogeneous dielectric, the form of  $g_s$  is a continuous distribution of the solvent molecules. The formulation of the continuum polarizable model uses a simplified structure of the solute-solvent potential interaction.  $V_{int}$  is reduced to its

classical electrostatic component and  $\epsilon_s$  describes a isotropic linear medium which depend only on the solvent dielectric constant  $\epsilon(T)$ . The effect of the electrostatic polarization is taken into account in Eq.6.7.

$$\text{Eq.6.7} \quad V_{\text{int}} = V_{\sigma}(\mathbf{q}, \mathbf{Q}, \rho_M, \epsilon) = \sum_{\alpha} Z_{\alpha} \Phi_{\sigma}(\mathbf{Q}_{\alpha}) - \sum_i \Phi_{\sigma}(\mathbf{q}_i)$$

$\Phi_{\sigma}(r)$  is the value of the electrostatic field generated by the polarized dielectric at  $r$  point. The contribution to the total energy  $E^{(f)}$  by solute-solvent interaction is therefore expressed by the following integral all over the space (Eq.6.8):

$$\text{Eq.6.8} \quad W_{\text{MS}} = \int \Psi^{(f)*} V_{\sigma} \Psi^{(f)} d\mathbf{q}_1 \dots d\mathbf{q}_{N_{\text{el}}} = \int \rho_M(\mathbf{r}) \Phi_{\sigma}(\mathbf{r}) d\mathbf{r}^3$$

$V_{\sigma}$  is one-electron operator. Typically, the evaluation of  $W_{\text{MS}}$  does not take long computation. The quantum problem is treated with standard techniques. The most common method is Hartree-Fock where  $V_{\sigma}$  is simply added to the Fock operator.

### 6.3 The cavity shape

In the polarizable continuum model the shape and dimensions of the cavity are critical factors for the success of the method. An ideal cavity should perfectly reproduce the shape of the solute molecule. Therefore, when the cavity is too large the solvent effect is underestimated; otherwise if it is too small errors in the estimation of the energy of interaction of  $\rho_M$  portion to the cavity boundaries are made. A cavity that does not have the appropriate shape introduces serious errors in estimating the effect solvent.

In the solvation continuum models the molecular cavity is the portion of space within the surrounding medium that is occupied by the solute molecule. The molecular surface is indeed the boundary between these two areas. The easiest way to build the cavity is to use a sphere or an ellipsoid with radius or axes dimension described like parameter or parameters. This very simple approach is still in use cause of the availability of exact analytical solution of electrostatic equations. The most common way to define molecular cavities is to interlock a set of spheres each



centered on the atoms of the solute. Once molecular cavity is built there are several way to define the molecular surface:

1. The Van der Waals surface (VWS) is a molecular surface obtained by interlocked spheres centered on each atom and having as radius the corresponding van der Waals radius. This definition is particularly useful when the cavitation energy contribution has to be studied.
2. The solvent-accessible surface (SAS)<sup>52</sup> is an extension of the VWS, in fact it is defined as the surface identified by a rolling spherical solvent probe on the van der Waals surface. The probe dimension depends on the molecular solvent properties and nature. This method is usually utilized when short range interactions have to be computed.
3. The solvent-excluded surface (SES)<sup>53</sup> has similar character of the SAS procedure but it defines a surface where only the contact point between the cavity and the probe are included. So, this method, defines a smoothed surface across which no solvent molecule can move in. The volume enclosed in the SES but not in the VWS is called solvent-excluded volume.

In the Gaussian09 series of programs some of these methods are available to construct the cavity around the solute molecules. The first algorithm, called PCM (Polarized Continuum Model) is based on the original work of Tomasi, Miertus and Scrocco<sup>54</sup> in which the cavity is constructed penetrating spheres of Van der Waals radius centered on atoms opportunely tuned. This method keeps constants the phase-gas molecular orbitals calculated and optimizes the shape of the cavity. In the second algorithm an Electronic Isodensity Surface (IPCM isodensity PCM) of the molecule is used. This method using the gas-phase molecular orbitals first calculated computes the isodensity surface through a SCFcycle. The newer method but also more computationally expensive (limited to the small systems) is SCIPCM (Self Consistent IPCM) which is an innovation of IPCM. The cavity is still calculated via a isodensity surface of the solute molecule, the difference is in the iterative process computing the cavity and the molecular orbitals with a self-consistent method.

## 6.4 The Energy Solvation

The solvation process is accompanied by a free energy exchange with the environment, and this value is obtained by summation of the free energy contribution of each interaction term.

Including the thermal motions of the molecular framework in solution, the formal equation that provide the total free energy in solution is:

$$\mathbf{Eq.6.9} \quad G^{(M)} = G_{\text{cav}} + G_{\text{el}} + G_{\text{dis}} + G_{\text{rep}} + G_{\text{tm}}$$

Computationally speaking the formation of each term has the name "Charging Process" (CP). Each CP is based on several iteration finalized to minimize the residual coupling between an appropriate parameter and a potential function. In the PCM formalism only the first term is evaluated separately whereas the others three CP are unified and described by Schrodinger solution. The CP related to  $G_{\text{cav}}$  makes an empty cavity inside the continuum with a proper shape and size to host the solute. Only the nuclear relative position and atomic parameters are used in this route and no electronic properties of solute are involved. The calculations are performed at a given temperature  $T$  and solvent density  $\rho$ . This term represents the reversible work spent to build the cavity against the cohesion liquid forces and it could be computed with several methods<sup>55</sup>. In the actual PCM codes the standard methods is that proposed by Pierotti<sup>56</sup> in according to a suggestion given by Claverie<sup>57</sup>. The parameter characterizing the solvent cavity is the solvent equivalent radius and the expression for the free energy term is analytical for spherical shape cavity and semi-analytical for the cavities built with atomic solute.

Part II  
Metal- and  
Organo-Catalysis

# 1. Computational investigation on organic catalysis

## 1.1 Introduction

In chemical synthesis, catalysis is a phenomenon, in which a relatively small amount of a material, called catalyst, increases the rate of a chemical reaction. Interacting with the reactants, the catalyst enters into the reaction cycle, but is regenerated in its last step and therefore is not consumed in its course, ideally remaining unchanged after its completion. Thus, the amount of product obtained with the given amount of catalyst is theoretically unlimited, in practice usually very large. The accelerating effect of a catalyst is achieved through interactions with the substrates, which lowers energy activation barrier. The vastness of this topic is significant and consequently there are many specific areas that can be examined. The structure and size of catalysts can be very different as they can consist of single metal atoms surrounded by organic ligands, small simple organic molecules (homogeneous catalysts), clusters of a few dozen metals, oxide, carbide, or nitride atoms or metal particles of up to 10 nm or more in diameter (heterogeneous catalysts).

## 1.2 Computational Organometallic catalysis

Computational chemistry has been considerably advancing in the last decades and it now allows analyzing catalytic reactions with the detail and accuracy required to satisfactorily compare computational results with experiments and to understand why a catalyst performs better than others. Computational catalysis efforts have historically focused on the study of both homogeneous catalysts and heterogeneous catalysts. Both classes of systems are readily treated with computational approaches discussed in Part I and are highly relevant to experimentally studied catalysts.

In this second part (Part II), results of the study of different organometallic and organocatalyzed reactions are presented. In particular our project focused on gold homogeneous catalysis as part of a combined experimental-computational collaboration with the experimental group directed by Prof. Marco Bandini (Department of Chemistry "G.Ciamician"). One of the purposes of the study was to rationalize the role of gold complexes in different classes of organic reactions. At the end of this section, a mechanistic investigation of a metal-free enantioselective

electrophilic activation of allenamides as an example of an organocatalytic reaction in which an organic complex replaces the gold catalyst.

## 2. Organo-Gold chemistry

Once reputed an inert and catalytically inactive element<sup>58</sup>, gold has recently gained attention as a catalyst. With hundreds of papers being published each year, this rapidly-evolving field is carrying significant advances in organometallic catalysis. The first examples of the gold extraordinary efficiency came to the attention of the scientific community when, independently, Haruta et al. investigated the low-temperature oxidation of CO<sup>59</sup> and Hutchings the hydrochlorination of ethyne to vinyl chloride<sup>60</sup>, both heterogeneous reactions. For the first time these studies showed gold to be the best catalyst for organic reactions, in stark contrast to the common thought on the poor activity of gold<sup>61</sup>. Consequently gold became a hot topic in chemistry and its use has proved equally to be effective as heterogeneous or homogeneous catalyst. In the recent years great progress have been made in developing efficient and selective homogeneous Au-catalyzed transformations.<sup>62</sup> An important contribution was given by Hashmi and coworkers with a series of comprehensive reviews outlining the progression of Au-catalyzed reaction development,<sup>61,63</sup> and a number of more focused reviews providing further insight into particular aspects of Au catalysis. The most frequently used gold complexes are Au(I) and Au(III)<sup>64</sup>. These gold salts can promote some chemical transformations at room temperature with reaction times of minutes, in contrast with other metal-catalyzed reactions that require higher temperatures and much longer reaction times.<sup>65</sup> Given the increasing need for environmental sustainability, the Au-catalysis has spurred growing interest in investigation of the chemical and catalytic reactions.<sup>66</sup> Among the different reactions that use homogeneous Au-catalysts there are the addition of both inter- and intramolecular nucleophilic of double and triple C-C bonds to give new bonds CE (E = C, N, O, S), the activation of C-H bonds and rearrangement reactions of various cyclic derivatives. The best characteristic that makes gold an extremely interesting metal in catalysis is the propensity of Au to activate carbon-carbon  $\pi$ -bonds as electrophiles.<sup>61,62,63</sup> The electron rich alkynes and alkenes typically interact with electrophilic reagents like halogens in organic synthesis or electrophilic metal centers like gold (in the oxidation states I or III).<sup>67</sup> In this interaction the alkene or alkynes high energy occupied  $\pi$ -orbitals interact with the *d* orbitals of the metal. The alkyne (and sometimes the

less reactive alkenes) can be activated towards nucleophilic attack through coordination to the electrophilic gold complexes. This coordination withdraws electron density from the multiple bond, enhancing its electrophilicity and thus making the attack of weak nucleophiles possible.

This gold behavior is due to its electronic configuration and the involvement of its relativistic effects.<sup>68</sup>

## 2.1 Relativistic effects on Gold atom

Schrödinger's equation correctly predict the atomic orbital energy levels for hydrogen but is unable to account for the fine structure of the hydrogen atomic spectrum, in which the bands are split, it does not consider that the effective mass of an electron depends on the velocity by which it moves. In the heavy elements where the electrons attain relativistic speeds, approaching that of light ( $c$ ), more general relativistic considerations are required, that are not taken into account by the Schrodinger equation. In 1928 Dirac developed a new equation considering special relativity, and thus capable of describing “relativistic effects”, i.e. any phenomenon resulting from the need to consider the value of the velocity significant with respect to the speed of light.

The first consequence of the Dirac equation is that mass increases towards infinity as a body's velocity approaches  $c$ . Mathematically can be expressed as  $m = m_0/[1 - (v/c)^2]$ , where  $m$  is the corrected mass,  $m_0$  is non-relativistic (rest) mass, and  $v$  is velocity. For a given atom, the average radial velocity of the 1s electrons is  $V_r = Z$ , where  $Z$  is the atomic number. The expression  $v/c$  can therefore be calculated as  $Z/137$  (137 atomic units (a.u.) =  $c$ ).

There are three major phenomena that result from relativistic effects. In non-relativistic calculations,  $c = \infty$  and  $v/c$  therefore approaches 0, so no mass correction need to be applied to the particles under consideration. In situations in which  $c$  is considered to be 137 a.u., the mass of an electron will increase considerably. Because the Bohr radius of an electron orbiting a nucleus is inversely proportional to the mass of the electron, this increase in mass corresponds to a decrease in radius. This relativistic contraction of the 1s orbital also applies to all other s and p orbitals. Thus, the p and s electrons are closer to the nucleus and have greater ionization energies. Practically, this contraction is only significant for elements in which the 4f and 5d orbitals are filled (Figure 2.1). The second manifestation of relativistic effects is indirect; electrons occupying the d and f orbitals are better shielded by the electrons in the contracted s and p orbitals and therefore see a weaker

nuclear attraction. The third effect of a relativistic treatment is spin–orbit coupling, which accounts for the fine splitting in the hydrogen atomic spectrum noted above.<sup>68a</sup>

Among the experimental observations conventionally explained by relativistic effects is the colour of Au. The golden colour is due to excitation of the 5d electrons to the Fermi level, which occurs with a bandgap of 2.38 eV; blue visible light is therefore absorbed.

In silver, by contrast, the bandgap is much larger and no visible light is absorbed. The smaller bandgap in Au is due to the relativistic contraction of the 6s and 6p orbitals and the expansion of the 5d orbitals. In Au complexes, the relativistic contraction of the 6s and 6p orbitals (which explains the strong stability of the metallic state) and the simultaneous expansion of the 5d orbitals increase  $\pi$ -acidity and electronic delocalization (i.e. backbonding) explaining the characteristic reactivity of gold complexes and their affinity with the  $\pi$  electrons of olefins and alkynes. Another important phenomenon due to the distortion from the expected electronic structure, is the aurophilicity,<sup>68c</sup> that represents the tendency for Au-Au interactions to be stabilizing on the order of hydrogen bonds. [Au(I)] complexes generally adopt a linear, bicoordinate geometry.<sup>68d,e</sup> The practical consequence of the limited coordination geometry in [Au(I)] complexes is the general need to abstract only one ligand from the neutral complex to obtain the cation catalytic species.

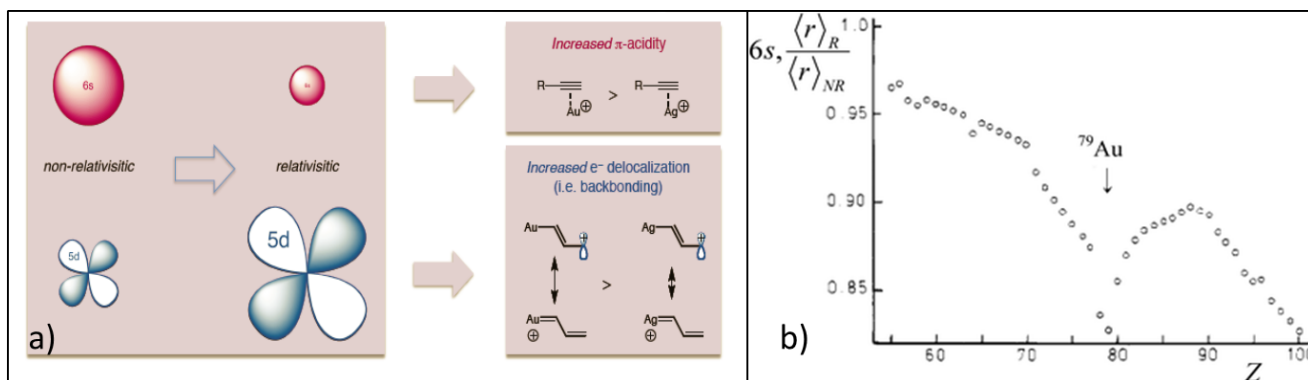


**Figure 2.1**

Relativistic consequences effects due to the gold electron configuration.

### 3. Computational investigation of the Gold(I)-Catalyzed Synthesis of Azepino[1,2-a]indoles<sup>69</sup>

#### 3.1 Azepino[1,2-a]indoles

Indole is one of the most abundant heteroaromatic compounds found in nature and is ranked third (after benzene and pyridine) among the prevalent architectures found in bioactive molecules.<sup>70</sup> Indoles have an extremely interesting history in both medicinal and natural product chemistry. Interest has been driven toward it by the vast physiological activity this class of structures exhibits and its broad ranging chemical reactivity.<sup>71</sup> As a part of our ongoing interest in gold-catalyzed synthesis of the indole architectures, we turned our attention to the azepinoindole scaffold, which is commonly encountered in biologically active compounds<sup>72</sup>.

More specifically, we have considered azepino[1,2-a]indoles, which feature a fused seven-membered ring through the N1–C2 connection. These indoles-derivatives possess many pharmacological properties. As a matter of fact, azepino[1,2-a]indoles display potent activity against the non-structural 5B (NS5B) RNA dependent RNA polymerase of the hepatitis C virus (HCV).<sup>73</sup> This enzyme is a key component of the viral replicase complex and its function is essential for proliferation of the pathogen.<sup>74</sup>

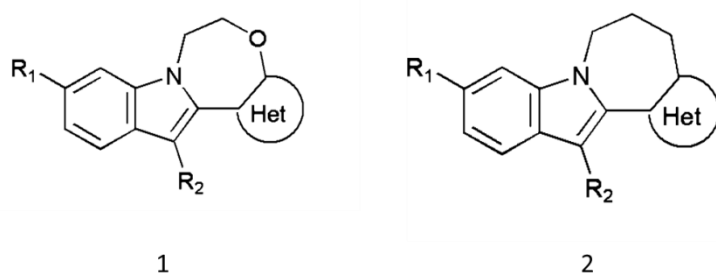


**Figure 3.1**  
Examples of pharmacologically active azepino[1,2-a]indoles as effective inhibitors of HCV NS5B polymerase.

Furthermore many azepino-indoles are used in the treatment of psychiatric disorders by modulation of receptors for central nervous system neurotransmitters. The most commonly prescribed CNS medications worldwide are those that affect the function of serotonin (5-HT). Among the identified sub-types of the 5-HT receptor, the 5-HT<sub>2C</sub> sub-type has received considerable attention as a potential therapeutic target for several indications, including anxiety, epilepsy, schizophrenia, and obesity.<sup>75</sup> The search for agents with high selectivity for this site has



revealed that indole-based derivatives agonists possess 5-HT<sub>2C</sub> selectivity of 5–10 fold relative to 5-HT<sub>2A</sub>. In particular azepinoindole-based agonists showed remarkable efficacy for the treatment of anxiety (Figure 3.2).<sup>76</sup>

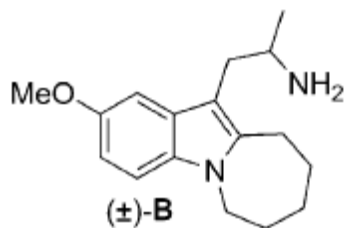
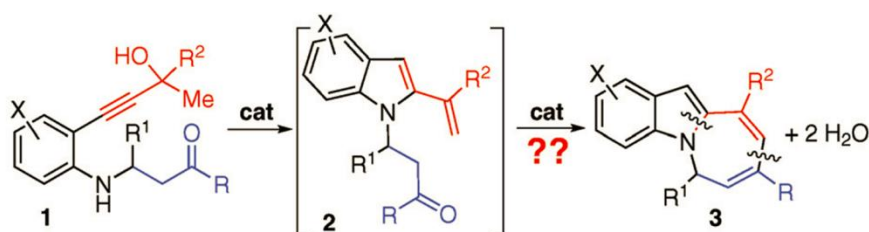


**Figure 3.2**

Example of pharmacologically active azepino[1,2-a]indole as modulators for CNS neurotransmitter receptors.

This family of important indolyl alkaloids are accessible synthetically by metal catalysis<sup>77</sup> or, more generally, by stepwise synthetic sequences that start from a preformed indolyl nucleus<sup>78</sup>. However, catalytic methods that simultaneously address synthesis and derivatization of indoles are still far from common.<sup>79</sup> Some leading metal-assisted examples deal principally with the construction of the pyrrolyl ring with a final C3-functionalization through alkylations<sup>80</sup> or cross-coupling reactions.<sup>81</sup> Among them, gold(I) catalysis has played a major role<sup>82</sup> in generating chemical diversity under mild and selective conditions.

In the case of azepino-indole species, although the metal-catalyzed synthesis of these derivatives has recently been documented,<sup>83</sup> stepwise synthetic sequences starting from a preformed indolyl nucleus are generally necessary to build up the polycyclic system.<sup>84</sup>



Yields up to 96%  
(17 examples)

cat: [Au(*i*Pr)Cl]/AgOTf

**Figure 3.3**

Gold-assisted synthesis of azepino[1,2-a]indoles; reaction scheme.

Recently, our cooperating experimental research group has documented a gold(I)-assisted cascade reaction (one-pot) for the synthesis of azepino[1,2-a]indoles.<sup>85</sup> The gold(I)catalysis (optimal conditions: catalyst=[Au(IPr)Cl]/AgOTf (IPr=1,3-bis(2,6-diisopropylphenyl-imidazol-2-ylidene) in refluxing toluene delivers a collection of functionalized azepino[1,2-a]-indoles **3** starting from readily accessible amino-propargylic alcohols **1** (figure 3.3). Interestingly, two molecules of water are the only stoichiometric byproduct of the whole transformation.<sup>86</sup>

### 3.2 Preliminary mechanistic insights

In the reaction scheme of Figure 3.3 the suitability of 2-(propargylic-alcohol)-anilines **1** in providing nucleophilic 2-vinylindole intermediates **2** through a gold mediated hydroamination/dehydration sequence is the baseline point of our study.<sup>87</sup> At this stage, a complementary (electrophilic) group (such as carbonyl)-tethered to the aniline nitrogen atom was thought to allow the second cyclization reaction to take place, producing a N1-C2 fusion to the indole core.

The tertiary propargylic alcohol (+/-)-**4a** and 2-vinyl-indole **2a**, are isolated in the presence of less active catalysts and characterized. Their active role during the course of the reaction was proved unambiguously by subjecting them to optimal catalytic conditions, under which comparable results in terms of chemical yields (75–77% **3**) with respect to **1a** were obtained (Figure 3.4).

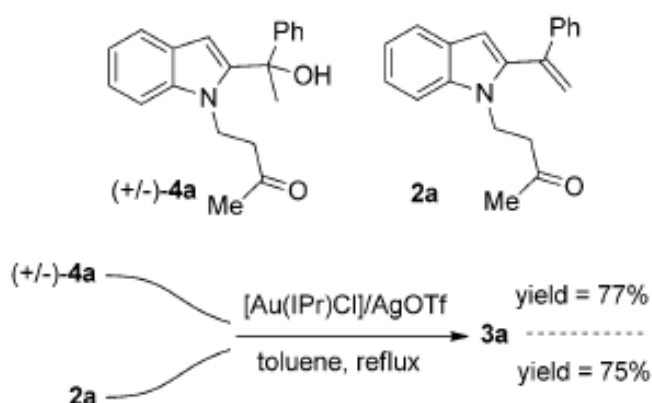


**Figure 3.4**

Role of compounds (+/-)-**4a** and **2a** in the course of the reaction.

Therefore, the initial steps of the catalytic cycle are the following:

- (i) gold-assisted hydroamination of the C-C triple bond,<sup>88</sup>
- (ii) subsequent protodeauration of the resulting indolyl-3-gold intermediate,<sup>89</sup>

- (iii) acid-catalyzed dehydration of the tertiary alcohol 4a to release the isolated 2-vinylindole 2a.

Conversely, the mechanism of the final ring-closing process (2→3 in figure 3.3) is still obscure.<sup>90</sup> In the final ring-closing stage, the lower efficiency of highly electrophilic cationic phosphite-gold complexes with respect to carbene analogs indicates that the hypothesis of a standard Prins mechanism can be ruled out. Moreover, intriguing outcomes resulted from labeling experiments performed on [D<sub>2</sub>]-2a ([Au(IPr)(OTf)] 5 mol%, toluene, reflux). In particular, a complete proton-deuterium exchange (H/D>25:1) was observed during the process [D<sub>2</sub>]-2a→[H]-3a (Figure 3.5), which accounts for a C=C gold insertion as a plausible chemical event to lead to a vinyl-gold complex I.<sup>91</sup>

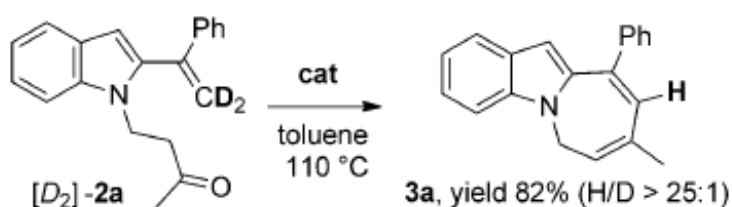


**Figure 3.5**

Role of compounds (+/-)-4a and 2a in the course of the reaction.

This result can be explained assuming that:

- (i) After formation of I, both methylene H atoms in 2a (or both D atoms in [D<sub>2</sub>]-2a) move from the vinylic carbon to form a water molecule which is successively expelled;
- (ii) The hydrogen atoms H<sub>a</sub> and H<sub>b</sub> (in blue in Figure 3.6) must originate from the substrate itself.

Within this conjectural mechanistic scheme the alkenyl-gold species I is the key nucleophile leading to the seven membered ring through an intramolecular condensation with the ketone group.<sup>92</sup>

A schematic representation of this hypothesis is given in Figure 3.6.

Another crucial point is to determine the role of the counterion. The nature of the counterion was demonstrated to be essential in controlling both kinetics and chemoselectivity of the overall cascade process,<sup>93</sup> electing OTf(·) as the optimum one. Important issues are still open: (1) how does the gold complex activate the substrate? (2) what is the nature of the hypothesized intermediate I? (3) what is the role played by the OTf<sup>-</sup> counter-ion? (4) how does the final proton transfer (leading to 3) take place?

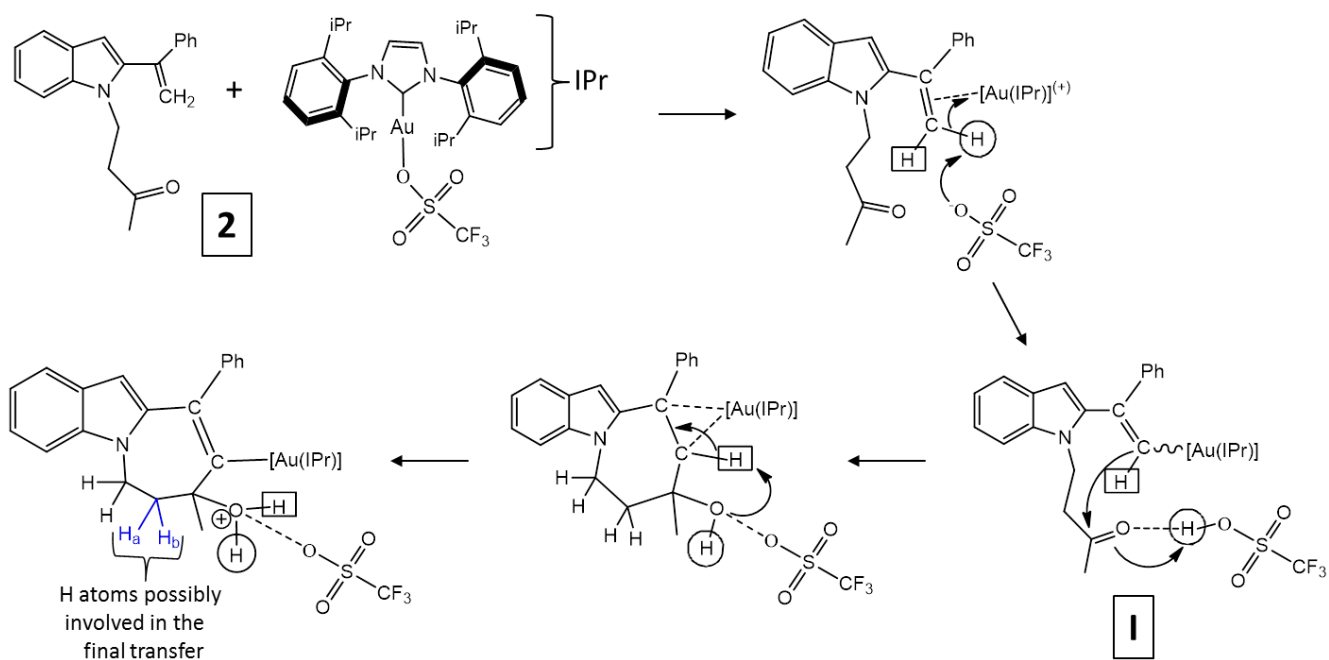


**Figure 3.6**  
A mechanistic hypothesis for the final ring-closing process (2 → 3).

We carried out a DFT computational investigation on the transformation **2**→**3** in order to fully elucidate the mechanism issue. The model-system simulates the experimental catalytic system affording the best yields and consists of the 2-vinyl-indole derivative and the [Au(IPr)OTf] catalyst in which the two isopropyl groups of the carbene ligand (Figure 3.6) have been replaced by methyl groups (IDM = 1,3-dimethyl-imidazol-2-ylidene) [Au(IDM)OTf].<sup>94</sup>

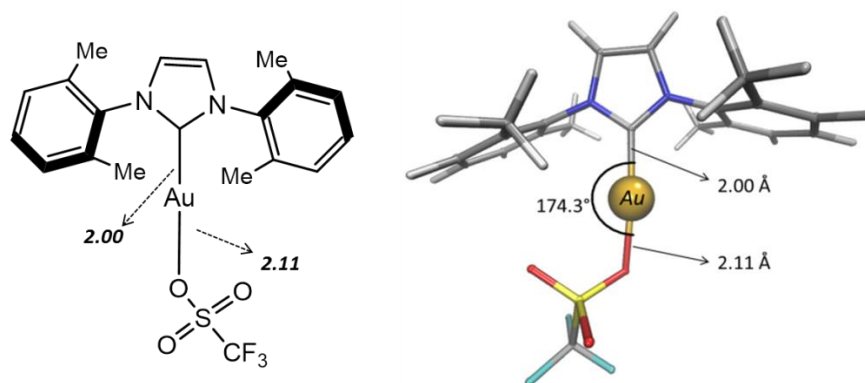


**Figure 3.7**  
2D and 3D representations of the [Au(IDM)(OTf)] catalyst. Bond length are in Angstrom.

### 3.3 Results and discussion

The computations carried out revealed a rather complex multi-step mechanism for the transformation **2** → **3**. A schematic representation of the corresponding reaction surface is given in Figure 3.8.

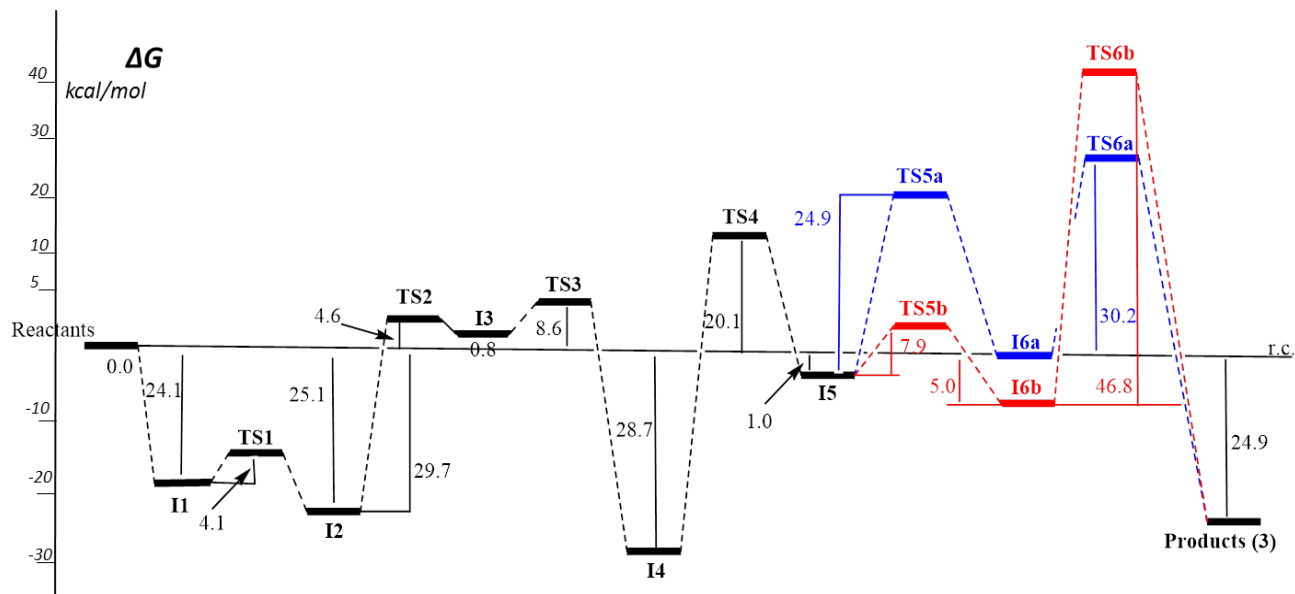


**Figure 3.8**

Reaction profile for the transformation **2a**→**3a**. Free energy values  $\Delta G$  are in kcal/mol. Reactants correspond to the 2-vinyl-indole derivative and gold complex [Au(IDM)OTf].

The initial interaction between the gold catalyst and 2-vinyl-indole<sup>95</sup> leads to a long-range complex **I1** (24.1 kcal mol<sup>-1</sup> more stable than reactants) where the OTf anion is still bonded to the metal (Figure 3.9).

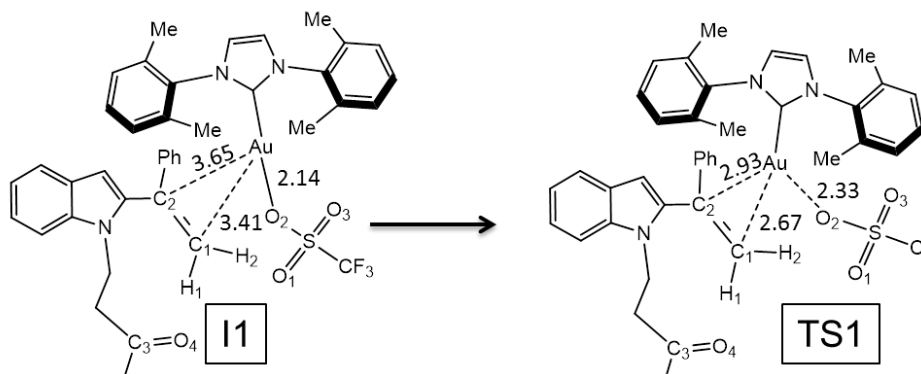


**Figure 3.9**

A schematic representation of intermediate **I1** and transition state **TS1**. Bond lengths are in Ångstroms.

The I2 gold complex (Figure 3.10) is obtained by overcoming a rather small barrier of TS1 (4.1 kcal mol<sup>-1</sup> Figure 3.9). C<sub>1</sub>-C<sub>2</sub> double bond reported in I2 replaces triflate as a ligand ( $\eta^2$  complex). Subsequently, the anion OTf assists the deprotonation of the methylene carbon C1. This is evident in TS2 (Figure 3.10) where the triflate group clasps the hydrogen H<sub>2</sub> and accompanies its “travel” to oxygen O<sub>4</sub> by overcoming a free energy barrier of 29.7 kcal mol<sup>-1</sup>: the hydrogen H<sub>2</sub> is approximately half way between C<sub>1</sub> and O<sub>1</sub>, the H<sub>2</sub>-C<sub>1</sub> and H-O<sub>1</sub> distances being 1.41 and 1.23 Å, respectively.

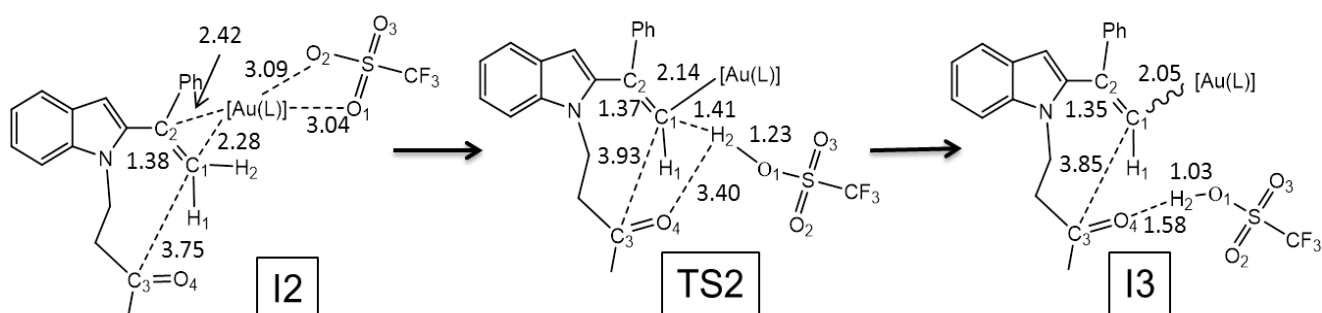


**Figure 3.10**

A schematic representation of intermediates I2 and I3 and transition state TS2. Bond lengths are in Å (L=IDM).

The final result is the delivering of one triflic acid molecule (HOTf) and the formation of an alkenyl-gold intermediate I3 (the hypothesized intermediate I in Figure 3.6) characterized by a carbon-gold  $\sigma$  bond (Figure 3.10). In I3 a strong hydrogen bond involving the carbonyl group C<sub>3</sub>O<sub>4</sub> and H<sub>2</sub> (O<sub>4</sub>-H<sub>2</sub> distance = 1.58 Å) maintains HOTf in the proximity of the reacting molecule. The enhanced acidity of the methylene H atoms, due to the initial  $\eta^2$ -coordination (I2) of the cationic gold group, certainly contributes to the formal Csp<sup>2</sup>-H activation event.

The next transformation involves the formation of the seven-membered ring that characterizes the product (step I3  $\rightarrow$  TS3  $\rightarrow$  I4 figure 3.11). The intramolecular cyclization occurs in two steps, in which the pivotal role of the *in situ* formed HOTf in assisting the process and controlling the chemoselectivity clearly emerges. Firstly, HOTf enhances the nucleophilic character of C1, which condenses on the carbonyl moiety affording the ring closing (TS3, Figure 3.11). Furthermore, HOTf fulfills a “folding effect”<sup>96</sup> on the substrate by forcing the two reactive sites (C<sub>2</sub> and C<sub>3</sub>) of the molecule to stay close during the ring-closing event. The “folding effect” clearly appears in TS3 (Figure 3.11) where, in addition to the O<sub>4</sub>...H<sub>2</sub> hydrogen bond, HOTf is involved in two additional important interactions: the H<sub>1</sub>...O<sub>2</sub> H-bond (H<sub>1</sub>...O<sub>2</sub> distance = 2.51 Å) and the gold-

oxygen interaction ( $\text{Au}\dots\text{O}_3$  distance = 3.41 Å). The “assistance” by HOTf certainly contributes to lower the activation barrier (8.6 kcal mol<sup>-1</sup>). In the resulting intermediate I4 (Figure 3.11) H<sub>2</sub> is definitely bonded to the carbonyl oxygen O<sub>4</sub>, the C<sub>1</sub>-C<sub>3</sub> bond is completed (1.53 Å) and the gold atom is again η<sup>2</sup> coordinated to the C<sub>1</sub>-C<sub>2</sub> double bond.

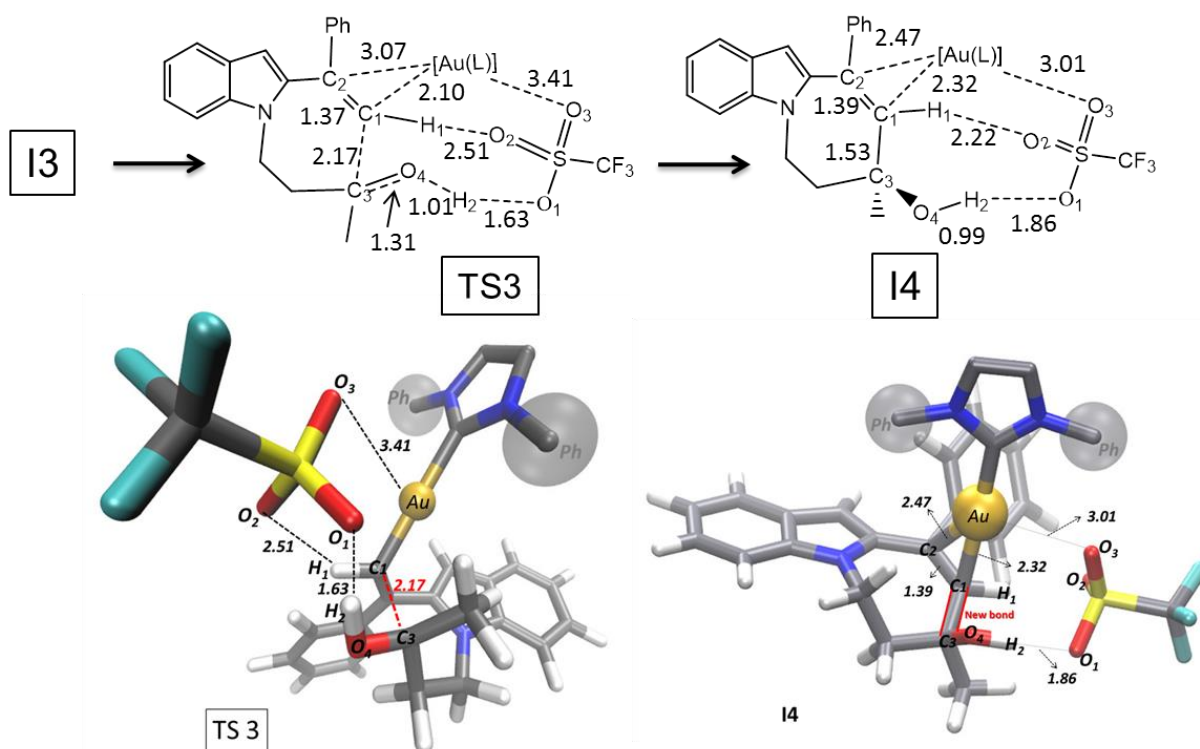


**Figure 3.11**

A 2D and 3D representation of intermediate I4 and transition states TS3. Bond lengths are in Ångströms (L = IDM).

The η<sup>2</sup>-complex transforms back to a σ-complex moving H<sub>1</sub> from C<sub>1</sub> to the hydroxyl group bonded to C<sub>3</sub>. The process is again assisted by the triflate (TS4, Figure 3.12) and by the gold metal ( $\text{Au-H}_1$  = 1.91 Å). In particular, the triflate, which, acting as a proton shuttle, “accompanies” the proton along its path from C<sub>1</sub> to the hydroxyl oxygen O<sub>4</sub>: H<sub>1</sub> is approximately half way between C<sub>1</sub> and O<sub>4</sub> and simultaneously interacts with the triflate oxygen O<sub>2</sub> ( $\text{H}_1\dots\text{O}_2$  distance = 2.63 Å). The final result is the formation of a “masked” water molecule (bonded to C<sub>3</sub>), where the hydrogen H<sub>2</sub> is almost shared between the “water” oxygen O<sub>4</sub> and the triflate oxygen O<sub>1</sub> (intermediate I5 in Figure 3.12).

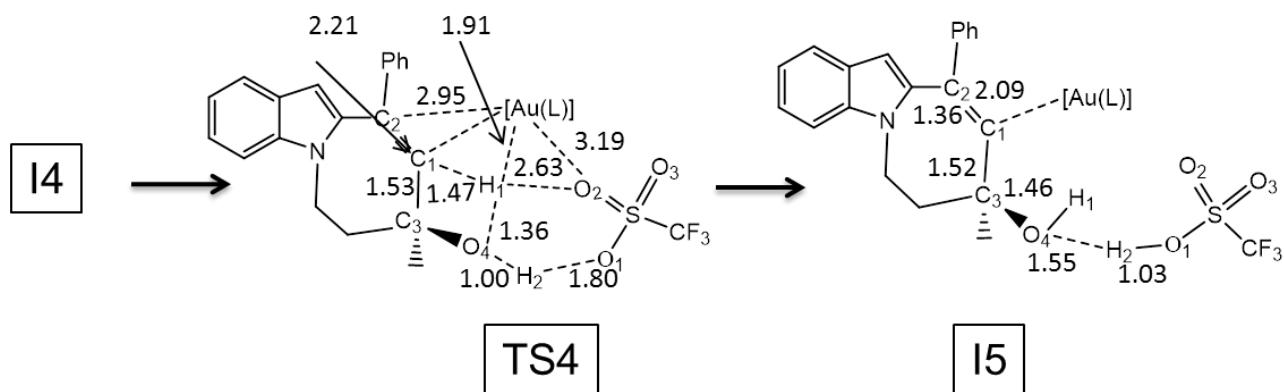


**Figure 3.12**

A schematic representation of intermediate I5 and transition state TS4. Bond lengths are in Å (L=IDM).

Importantly, the two water hydrogens originate from carbon C<sub>1</sub>, in agreement with the proposed mechanistic scheme of Figure 3.6, which would explain the experimental evidence of proton/deuterium exchange. The formal positive charge is now mainly located on O<sub>4</sub> and this certainly contributes to increase the energy of the system (only 1.0 kcal mol<sup>-1</sup> below reactants).

Two reaction paths, *path a* and *path b* (schematically represented in Figure 3.13, with a schematic 2D representation of the two intermediates I6a and I6b) mainly differing in the coordination mode of the gold atom with the substrate, originate from I5. The two paths involving two kinetic steps are:

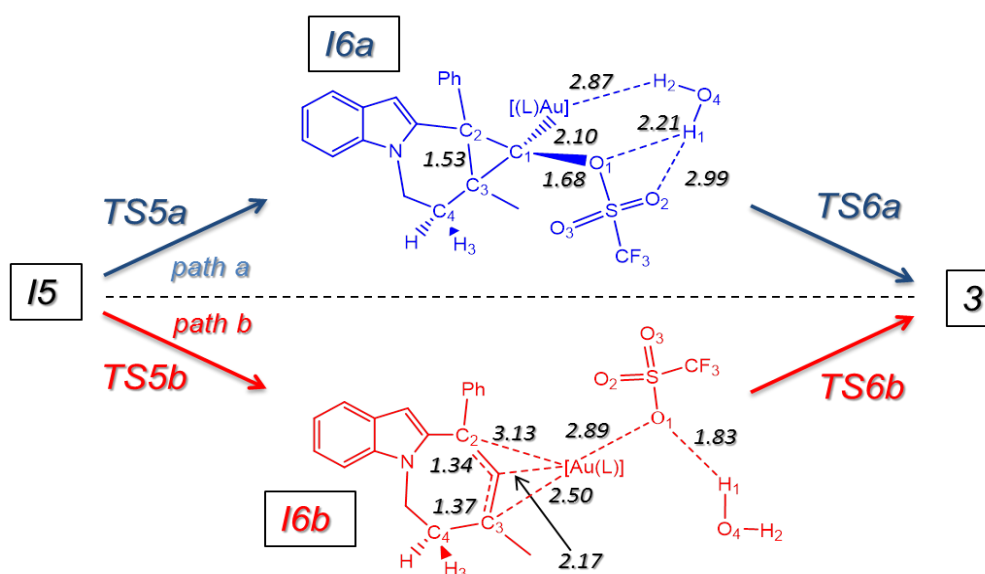


**Figure 3.13**

Representation of two reaction paths originate by I5, *path a* (blue) and *path b* (red), and their relatives intermediates I6a and I6b. Bond lengths are in Å (L=IDM).



The corresponding transition states (TS5a, TS6a, TS5b, and TS6b) are depicted in Figure 3.14. Along the favored *path a*, C<sub>2</sub> behaves as a nucleophile and gives rise to a new bond with C<sub>3</sub> (transition state TS5a), which leads to the C<sub>1</sub>-C<sub>2</sub>-C<sub>3</sub> cyclopropane structure (intermediate I6a) and determines the definitive expulsion of the water molecule (dehydration). This process, which has an activation free energy of 24.9 kcal mol<sup>-1</sup> (TS5a), is assisted by the gold atom and by the triflate group, which interacts with the leaving water through the hydrogen bond H<sub>1</sub>⋯O<sub>1</sub> (H<sub>1</sub>⋯O<sub>1</sub> = 1.99 Å in TS5a). The σ bond between the gold atom and carbon atom C<sub>1</sub> is maintained in the transformation I5→I6a, which is characterized by a strong OTf(-)⋯C<sub>1</sub> contact (C<sub>1</sub>⋯O<sub>1</sub> = 1.68 Å) and is degenerate to reactants. The partial carbenic character of C<sub>1</sub> in I6a (the σ Au-C<sub>1</sub> bond pair is mainly localized on it) allows the final structural rearrangement, in which H<sub>3</sub> moves from C<sub>4</sub> to C<sub>1</sub> by overcoming a free energy barrier of 30.2 kcalmol<sup>-1</sup> (transition state TS6a).

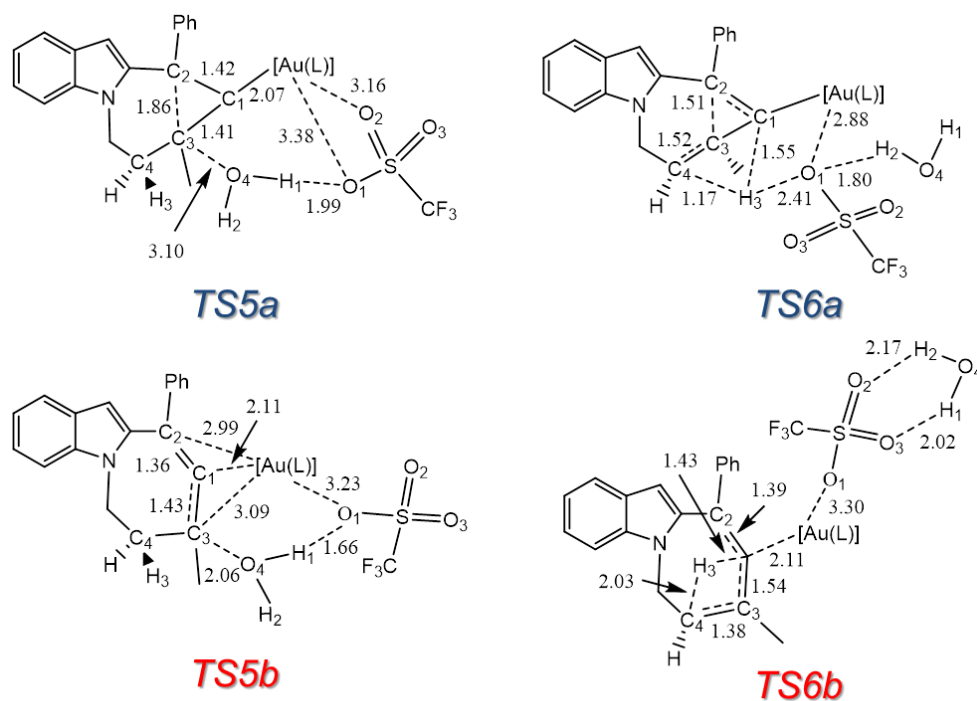


**Figure 3.13**

Representation of two reaction paths originate by I5, path a (blue) and path b (red), and their relatives intermediates I6a and I6b. Bond lengths are in Å (L=IDM).

This barrier is consistent with the experimental conditions (toluene heated to reflux at 110 °C, 4 h). Interestingly, the structure of I6a is flexible enough to allow a significant decrease of the C<sub>1</sub>⋯C<sub>4</sub> distance (which varies from 2.80 Å in I6a to 1.87 Å in TS6a), which makes the H<sub>3</sub> transfer much easier (see 3D representation in Figure 3.14).

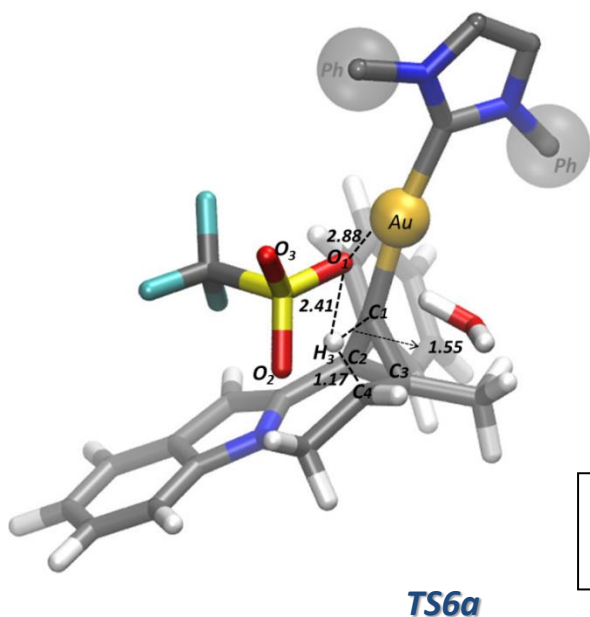


**Figure 3.14**

3D representation of favoured transition state of the final proton transfer TS6a. Bond lengths are in Å (L=IDM).

This proton transfer is again assisted in the transition region by the triflate ion through a hydrogen bond that involves H<sub>3</sub> and a triflate oxygen atom (O<sub>1</sub>, O<sub>1</sub>⋯H<sub>3</sub> = 2.41 Å). Simultaneously, the opening of the cyclopropane ring allows the formation of the C<sub>2</sub>=C<sub>1</sub> bond in the final product 3.

Along the alternative reaction channel (*path b*) the gold atom is η<sup>3</sup> coordinated, which prevents the formation of the cyclopropane ring. Because of the η<sup>3</sup> coordination involving C<sub>1</sub>, C<sub>2</sub> and C<sub>3</sub>, C<sub>1</sub> and C<sub>4</sub> cannot move close enough (TS6b in Figure 3.13) to help the transfer of the H<sub>3</sub> proton. The large C<sub>1</sub>...C<sub>4</sub> distance (C<sub>1</sub>...C<sub>4</sub> = 2.62 Å in TS6b) and the absence of the triflate assistance determine a significant increase of the free energy barrier (46.8 kcal mol<sup>-1</sup>) that should be surmounted to form the final product. Thus, *path b* can be ruled out on energy grounds, TS6b being the highest in energy transition state (41.7 kcal mol<sup>-1</sup> above reactants).

The endoergonicity of the reaction (see the energetic profile in Figure 3.8) is undoubtedly underestimated by our calculations, which refer to the initiation catalytic step in which only one water molecule is present. It is thus plausible to think that, as the reaction proceed, and more water molecules are produced, they would group and form stabilizing interactions that are not taken into account in our calculations thus lowering the energy of the product.

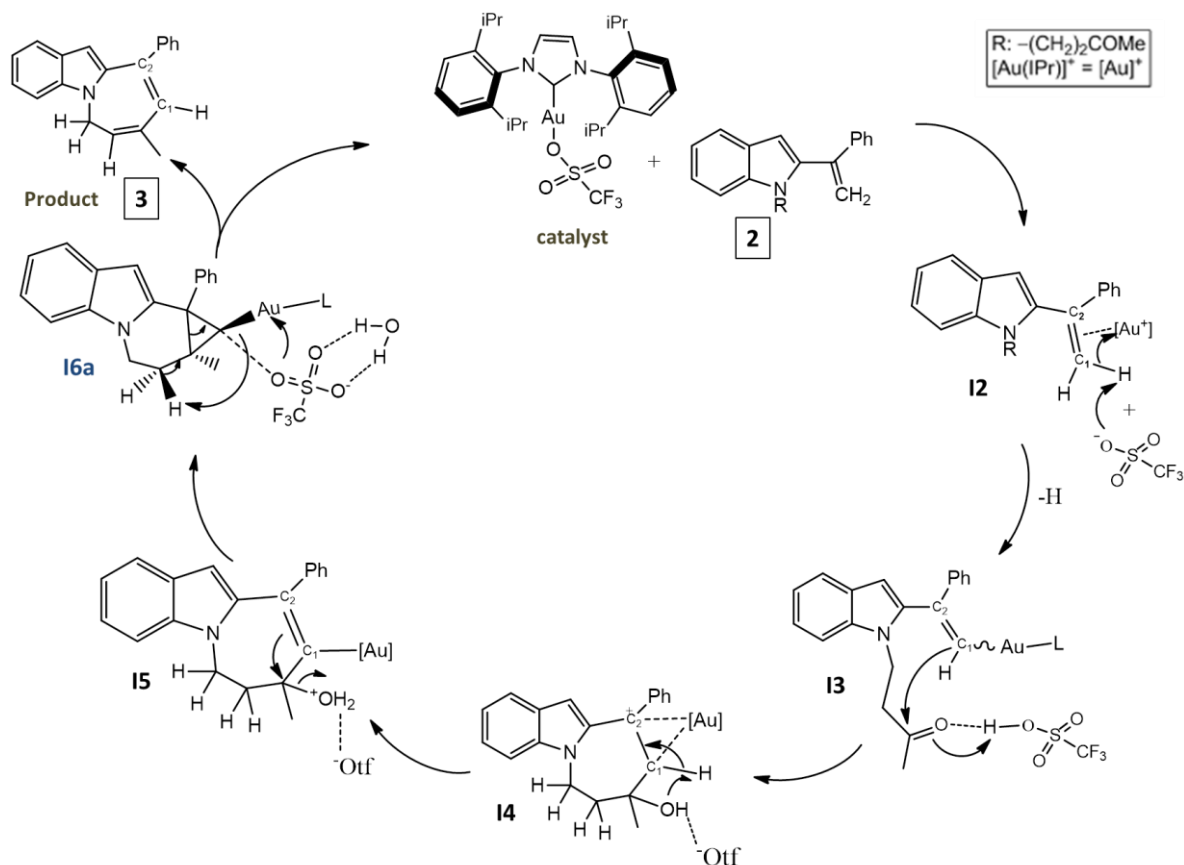


**Figure 3.15**

Schematic representation of the complete catalytic cycle obtained for the final ring-closing process examined

Finally in Figure 3.15 we can define the favored mechanism of the last stage catalytic cycle revealed by our computations.

### 3.4 Computational Details

In this work the DFT computations were performed by using the Gaussian09 series of programs.<sup>4</sup> The M06 functional proposed by Truhlar and Zhao<sup>24,25</sup> was used in all computations. This functional can provide a reliable description of transition metals and medium-range  $\pi$ - $\pi$  interactions at the same time.<sup>97</sup> The DZVP basis set, which is a local spin density (LSD) optimized basis of double-zeta quality, was used for all atoms except the gold atom,<sup>98</sup> which was described with the LANL2DZ basis set.<sup>99</sup> The geometries of the various critical points on the potential surface were fully optimized with the gradient method available in Gaussian09, and harmonic vibrational frequencies were computed to evaluate the nature of all critical points and entropy contributions to free energy. The solvent effects were taken into account during optimization using the polarizable

continuum model (PCM) approach.<sup>100</sup> A value of 2.38 (toluene) for the dielectric constant  $\epsilon$  was employed.

### 3.5 Conclusions

The results that we have reported in this computational investigation shed light on the mechanism of the last stage (ring closing 2→3) of the gold(I)-catalyzed synthesis of azepino[1,2-*a*]indoles. The catalytic cycle of this final step that we have found is depicted in Figure 3.15. In particular, we have demonstrated that the gold catalyst activates the substrate through the formation of a carbon-gold  $\sigma$  complex. This nucleophilic alkenyl-gold species, which corresponds to the hypothesized intermediate I in Figure 3.6 (I3 on the computed reaction surface), undergoes the ring-closing process with the “assistance” of triflic acid. Thanks to this “assistance” (which consists of the activation of the carbonyl group C<sub>3</sub>O<sub>4</sub> and the “folding effect” exerted on the two reactive carbon atoms C<sub>2</sub> and C<sub>3</sub>), the barrier for the nucleophilic attack is rather low (only 8.6 kcal mol<sup>-1</sup>). The triflate group “assistance” is also essential in the second stage of the transformation in which a second proton transfer leads to the formation of a water molecule that is subsequently expelled (dehydration). The gold coordination mode adopted in the last stage of the process ( $\sigma$ -bonded gold atom vs.  $\eta^3$ -coordination) differentiates the two final reaction channels. The  $\sigma$ -bonded gold atom of the favored *path a* allows the formation of a cyclopropane ring, which makes the C<sub>1</sub>⋯C<sub>4</sub> distance short enough to complete the final 1,3-proton transfer easily. This final step undoubtedly shows that the hydrogen atom finally bonded to the diene moiety in 3 originates from the substrate itself. Once again the triflate moiety plays a key role as a proton shuttle, which follows the proton migration from C<sub>4</sub> to C<sub>1</sub>.

## 4. Computational study of Gold(I)-Assisted $\alpha$ -Allylation of Enals and Enones with Alcohols<sup>101</sup>

### 4.1 $\alpha$ -Oxo Gold Carbenes

Some of the most versatile aspects of gold catalysis involve the generation of gold carbene intermediates, which occur through the approach of an electrophile to the distal end of the alkenyl gold moiety, and their diverse transformations thereafter. Also  $\alpha$ -oxo metal carbene/carbenoids are highly useful intermediates in organic synthesis and can undergo various synthetically challenging yet highly valuable transformations such as C-H insertion, ylide formation, and cyclopropanation reactions.<sup>102</sup> This family of activated [Au]-C(sp<sup>2</sup>) species is commonly accessible through initial gold-promoted [3,3] rearrangement of the corresponding propargylic carboxylates, followed by inter- as well as intramolecular electrophilic interception.<sup>103</sup> Alternatively, hydrolysis of the oxocarbenium adducts has been postulated to deliver the corresponding  $\alpha$ -gold(I) enals/enones **I** during oxidative cross-coupling reactions (Figure 4.1).<sup>104</sup>

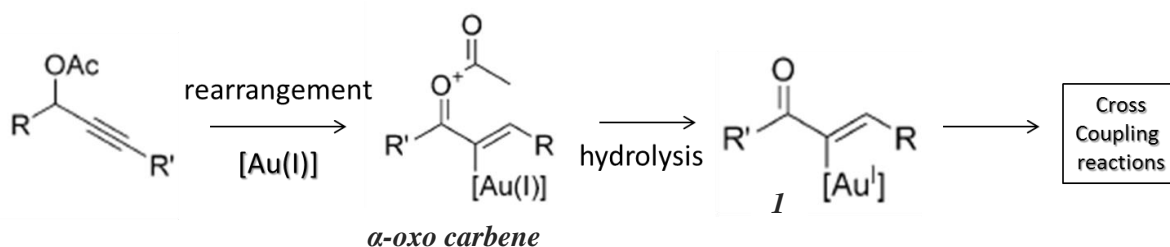


**Figure 4.1**

Classical approach to the in situ generation of  $\alpha$ -[Au(I)]-substituted enals and enones.

The studies of Faza and López on [Au(I)]-catalyzed oxidative cross-coupling in silico revealed the presence and role of  $\alpha$ -gold(I) enone species in the [Au(I)]-based redox transformation.<sup>105</sup> In this context, our cooperating experimental group has recently reported the NMR spectroscopic identification of an analogous  $\alpha$ -gold(I) enal adduct **I'** upon treatment of the complex [Au(P(2,4- tBu<sub>2</sub>C<sub>6</sub>H<sub>3</sub>O)<sub>3</sub>)(tfa)] (tfa = trifluoroacetate)<sup>106</sup> with the allenamide **a**<sup>107</sup> in wet CDCl<sub>3</sub> or CD<sub>2</sub>Cl<sub>2</sub> (Figure 4.2).<sup>108</sup>

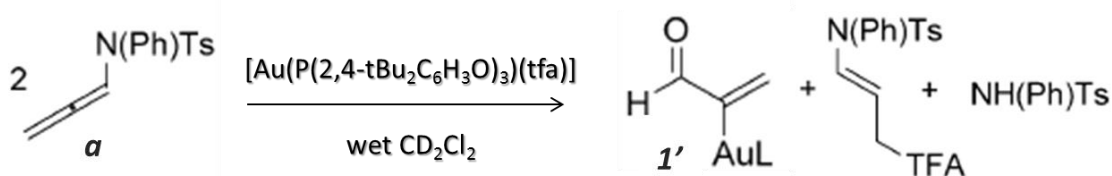


**Figure 4.2**

Alternative approach to  $\alpha$ -[AuI] enals intermediate ( $L=P(2,4\text{-tBu}_2\text{C}_6\text{H}_3\text{O})_3$ ). TFA=trifluoroacetate, Ts=p-toluenesulfonyl.

On the basis of this alternative approach (Fig. 4.2) to  $\alpha$ -[AuI] enals, and in conjunction with our interest in the gold(I)-catalyzed manipulation of amino derivatives, we have carried out a combined experimental-computational study in order to develop and rationalize the first gold(I)-catalyzed  $\alpha$ -allylation of unsaturated carbonyl moieties exploiting the intrinsic nucleophilic character of  $\alpha$ -gold(I) enal 1'-type adducts.<sup>101,109</sup> This reaction, developed by us, also has an important value in terms of sustainability, in addition to the already well-known advantages of Gold complexes in this field we selected environmentally desirable allylic alcohols<sup>110</sup> as potential alkylating agents (Figure 4.3).

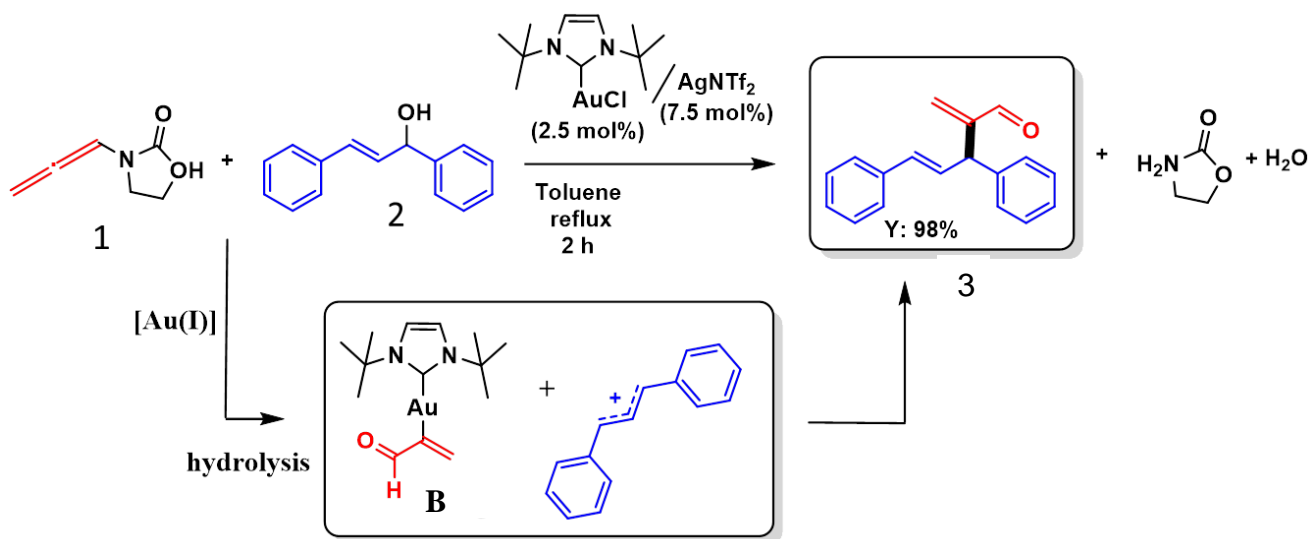


**Figure 4.3**

Working hypothesis for the gold(I)-assisted  $\alpha$ -allylation of  $\alpha,\beta$ -unsaturated carbonyl compounds.

The most applications in gold catalysis of allenamide are often the condensation of nucleophilic species with the metal-activated allenyl unit.<sup>111</sup> Conversely, the proposed alternative approach in our case would involve the electrophilic trapping of the organogold intermediate derived from the hydrolysis of a gold–allenamide adduct.<sup>112</sup>

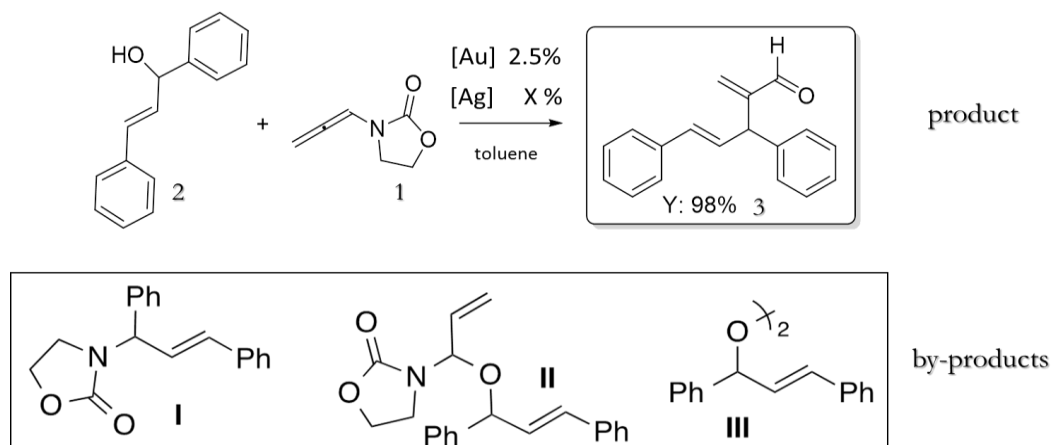
## 4.2 Experimental results

The intermolecular  $\alpha$ -allylic alkylation of enals and enones is carried out by condensing variously substituted allenamides with allylic alcohols. The catalysis, exerted cooperatively by [Au(ItBu)NTf<sub>2</sub>] and AgNTf<sub>2</sub>, allowed the synthesis of a range of densely functionalized  $\alpha$ -allylated enals, enones and acylsilanes in good yields under mild reaction conditions. The model substrates employed (allenamide **1** and the secondary alcohol **2**) are shown in figure 4.3.

### 4.2.1 Optimization of the catalyst and reaction conditions

The model substrates were initially subjected to various reaction conditions in order to get the best reaction performance in terms of yield and rate (Table 4.1). First attempts with [Au(P(2,4-tBu<sub>2</sub>C<sub>6</sub>H<sub>3</sub>O)<sub>3</sub>)(tfa)] (2.5 mol%) led to the formation of the desired product **3** (Fig. 4.3) in modest yield (28%) and also to the concomitant formation of by-products in varying amounts (Table 4.1, entry 1). Among them, the condensation product derived from the oxazolidinone and **2** (compound II), was present in high enough amounts to be isolated. These early results, and the presence of II supports our working hypothesis of the initial electrophilic activation of the allenyl group by the metal. The isolation of II as the major reaction product could be attributable to the highly electrophilic gold species used and that more  $\sigma$ -donating ligands could result in a more nucleophilic organogold(I) intermediate, thereby, hopefully, enabling **3** to be obtained in higher extent. Carrying on in the analysis of experimental results, higher yields of **3** were obtained by moving from phosphite- to phosphine-based gold catalysts. In this context, *in situ* formed [Au(PPh<sub>3</sub>)(NTf<sub>2</sub>)] [Au(JohnPhos)(NTf<sub>2</sub>)] and pre-formed [Au(XPhos)(NTf<sub>2</sub>)] provided **3** in comparable amounts (entries 2-4). Then, gold-NHC (NHC = N-heterocyclic carbene) complexes [Au(IPr)(NTf<sub>2</sub>)] and [Au(ItBu)(NTf<sub>2</sub>)] were tested and lead to very promising results (entries 5 and 6).<sup>113</sup> Intriguingly, when we carried out the reaction by *in situ* cation formation (IPrAuCl with AgNTf<sub>2</sub>) a marked improvement in chemical yield was observed (yield = 96%, entry 8). The higher performance might be due to the presence of an excess of AgNTf<sub>2</sub> with respect to the gold source, so the impact of the [Au:Ag] ratio on the final reaction outcome (entries 8-11) is investigated. In particular, optimal chemo-selectivity was found by utilizing a 1:3 [Au:Ag] (2.5:7.5 mol%) ratio, providing **3** in nearly quantitative amount (97%, entry 10 and 99% entry 13). This optimization classifies the present gold catalysis as a “silver-assisted” transformation.<sup>114,115</sup> A peculiarity distinguishing carbene-based from

other phosphorus-based gold species is the complete suppression of the formation of by-product III, which was not detected in the product mixture.



Entry	[Au]/[Ag] ([mol%])	T[°C]/t[h]	Yield of 3[%]	Yield of I/II/III [%]
1	[Au(P(OtBu)2Ph)3](TFA)] / - (-)	110/4	28	-/40/50
2	[Au(PPh3)Cl]/AgNTf2 (2.5)	110/4	60	35/-/25
3	[Au(JohnPhos)Cl]/AgNTf2 (2.5)	110/4	61	32/-/-
4	[Au(XPhos)(NTf2)] / - (-)	110/4	61	30/-/18
5	[Au(IPr)(NTf2)] / - (-)	110/4	70	53/-/-
6	[Au(ItBu)(NTf2)] / - (-)	110/2	84	44/-/-
7	[Au(IPr)Cl]/AgNTf2	110/4	96	36/-/-
8	[Au(IPr)Cl]/AgNTf2 (2.5)	110/4	68	55/-/-
9	[Au(IPr)Cl]/AgNTf2 (5)	110/4	89	41/-/-
10	[Au(IPr)Cl]/AgNTf2 (7.5)	110/4	97	35/-/-
11	[Au(IPr)Cl]/AgNTf2 (10)	110/4	35	40/-/-
12	[Au(IPr)(NTf2)] / AgNTf2 (5)	110/4	96%	-/-/-
<b>13</b>	<b>[Au(ItBu)Cl] / AgNTf2 (7.5)</b>	<b>25/24</b>	<b>99</b>	<b>34/-/-</b>
14	[Au(ItBu)Cl]/AgNTf2 (7.5)	110/4	94	37/-/-
15	[Au(IAd)Cl]/AgNTf2 (7.5)	110/4	65	57/-/-
16	[Au(IPr*)Cl]/AgNTf2 (7.5)	110/4	71	53/-/-
17	-/AgNTf2 (2.5)	110/4	50	-/35/11
18	--	110/4	NR	-/-/-

**Table 4.1**

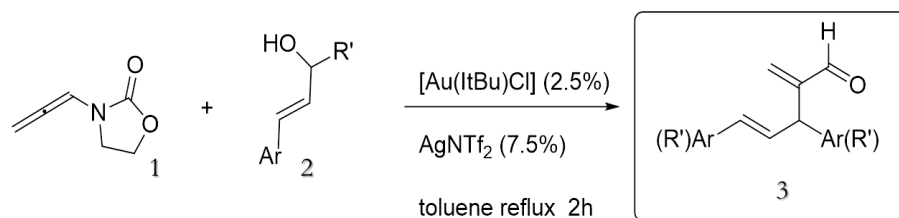
Optimization of the reaction conditions for the  $\alpha$ -allylic alkylation of arylaldehyde. All the reactions were carried out in anhydrous conditions (1:2:[Au]cat = 1: 1.5:0.025). Isolated yields after flash chromatography and referred to the initial amount of alcohol.

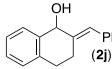


This stresses the higher selectivity of NHC-based catalysts towards promoting the cross-condensation with respect to “homo-coupling” processes. Notably, the use of AgNTf<sub>2</sub> alone led to the formation of a complex product mixture (entry 17), and no reaction was observed in the absence of catalytic species (entry 18).

#### 4.2.2 Application field of the reaction

Once optimized the reaction conditions and the catalyst, the scope of the process was examined by conducting the cross-condensation of a range of allylic alcohols **2** and allenamide **1** (Table 4.2) using the best conditions obtained (a 1:3 [Au:Ag] (2.5:7.5 mol%) ratio with [Au(ItBu)Cl] /AgNTf<sub>2</sub> catalyst, entry 13 table 4.1).



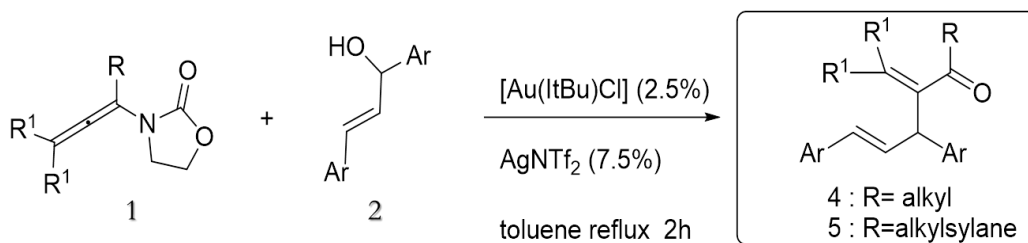
Entry	R (1)	Ar/R' (2)	Yield [%] (3)
1	H (1)	Ar/R' = <i>p</i> -MeC <sub>6</sub> H <sub>4</sub> (2b)	95 (3ab)
2	H (1)	Ar/R' = <i>o</i> -MeC <sub>6</sub> H <sub>4</sub> (2c)	94 (3ac)
3	H (1)	Ar/R' = <i>m</i> -MeOC <sub>6</sub> H <sub>4</sub> (2d)	55 (3ad)
4	H (1)	Ar/R' = <i>p</i> -FC <sub>6</sub> H <sub>4</sub> (2e)	94 (3ae)
5	H (1)	Ar/R' = <i>p</i> -ClC <sub>6</sub> H <sub>4</sub> (2f)	94 (3af)
6	H (1)	Ar/R' = <i>o</i> -ClC <sub>6</sub> H <sub>4</sub> (2g)	86 (3ag)
7	H (1)	Ar/R' = <i>p</i> -BrC <sub>6</sub> H <sub>4</sub> (2h)	84 (3ah)
8	H (1)	Ar/R' = <i>o</i> -BrC <sub>6</sub> H <sub>4</sub> (2i)	84 (3ai)
9	H (1)	 (2j)	88 (3aj)
10	H (1)	Ar = Ph / R' = <i>p</i> -ClC <sub>6</sub> H <sub>4</sub> (2k)	45 (3ak)

**Table 4.2**

Scope of the formal  $\alpha$ -allylation of acrylaldehyde. All the reactions were carried out in anhydrous conditions. Isolated yields after flash chromatography and referred to the initial amount of alcohol. Product 3aj was isolated as a 4:1 mixture of regioisomers; the major isomer featured an exocyclic C=C bond.

A substantial substituent tolerance at the allylic substrate was noted, as the introduction of both electron-withdrawing and electron-donating groups at the aryl groups (i.e. *ortho*-, *meta*- and *para*-position) provided the corresponding  $\alpha$ -allylated acrylaldehydes in good yield (55-95%, Table 2, entry 1-8). Differently substituted allylic alcohols, such as cyclohexen-2-ol and (E)-pent-3-en-2-ol were also tested, but unfortunately they were found to be unreactive under the optimized conditions. Decomposition the allylic alcohol **2** was observed, with the formation of the corresponding compound of type **III** (Table 4.1) as the main side product.

Additionally, asymmetrically substituted allylic alcohols **2i** and **2k** were tested, delivering the desired products **3aj** and **3ak** in moderate to good yields (45-88%) as a mixture of regioisomers. These data point to a possible  $S_N1$ -type mechanism involved in the C-C bond forming event.



Entry	R/R <sup>1</sup> ( <b>1</b> )	Ar ( <b>2</b> )	Yield [%] ( <b>3</b> )
1	Bn/H ( <b>1b</b> )	C <sub>6</sub> H <sub>5</sub> ( <b>2a</b> )	52 ( <b>4ba</b> )
2	Bn/H ( <b>1b</b> )	<i>p</i> -MeC <sub>6</sub> H <sub>4</sub> ( <b>2b</b> )	57 ( <b>4bb</b> )
3	Bn/H ( <b>1b</b> )	<i>p</i> -FC <sub>6</sub> H <sub>4</sub> ( <b>2e</b> )	65 ( <b>4be</b> )
4	Bn/H ( <b>1b</b> )	<i>p</i> -ClC <sub>6</sub> H <sub>4</sub> ( <b>2f</b> )	48 ( <b>4bf</b> )
5	Bn/H ( <b>1b</b> )	<i>p</i> -BrC <sub>6</sub> H <sub>4</sub> ( <b>2h</b> )	50 ( <b>4bh</b> )
6	<i>p</i> -FC <sub>6</sub> H <sub>5</sub> CH <sub>2</sub> /H ( <b>1c</b> )	C <sub>6</sub> H <sub>5</sub> ( <b>2a</b> )	63 ( <b>4ca</b> )
7	<i>p</i> -FC <sub>6</sub> H <sub>5</sub> CH <sub>2</sub> /H ( <b>1c</b> )	<i>p</i> -MeC <sub>6</sub> H <sub>4</sub> ( <b>2b</b> )	40 ( <b>4cb</b> )
8	<i>p</i> -FC <sub>6</sub> H <sub>5</sub> CH <sub>2</sub> /H ( <b>1c</b> )	<i>p</i> -FC <sub>6</sub> H <sub>4</sub> ( <b>2e</b> )	46 ( <b>4ce</b> )
9	Me/H ( <b>1d</b> )	C <sub>6</sub> H <sub>5</sub> ( <b>2a</b> )	50 ( <b>4da</b> )
10	H/Me ( <b>1e</b> )	C <sub>6</sub> H <sub>5</sub> ( <b>2a</b> )	36 ( <b>4ea</b> )
11	SiMe <sub>3</sub> /H ( <b>1f</b> )	C <sub>6</sub> H <sub>5</sub> ( <b>2a</b> )	77 ( <b>5a</b> )
12	SiMe <sub>3</sub> /H ( <b>1f</b> )	<i>p</i> -ClC <sub>6</sub> H <sub>4</sub> ( <b>2b</b> )	70 ( <b>5b</b> )
13	SiMe <sub>3</sub> /H ( <b>1f</b> )	<i>p</i> -FC <sub>6</sub> H <sub>4</sub> ( <b>2e</b> )	57 ( <b>5e</b> )

**Table 4.3**

Formal  $\alpha$ -allylation of enones and acyl-silanes. Reactions were carried out with 0.1 mmol of **1** under nitrogen in dry toluene (1/2 1 :1.5). Isolated yields after flash chromatography and referred to the initial amount of alcohol.

The scope of the methodology was further tested by applying the best reaction conditions to  $\alpha$ -allylated allenamides **1b-e** (Table 4.3). Simply performing chemical manipulation at the C(1)-position of the starting allene would also allow direct access to allylation of keto-derivatives. Gratifyingly, a range of  $\alpha$ -allylated enones (**4**, entries 1-9, Table 4.3) was isolated in moderate to good yields (40-65%) regardless of the nature of the  $\alpha$ -substituent or electronic-properties of the allylic alcohol. Importantly, the methodology could also be extended to the  $\alpha$ -allylation of  $\alpha,\beta$ -unsaturated acylsilanes (entries 10-12) that represent a well-known class of highly synthetically flexible organic compounds. For these, isolated yields ranging from 57 to 77% were isolated under optimum conditions. It should be emphasized that the introduction of a substituent at the  $\alpha$ -carbon of the allenyl unit of **1** enhanced significantly the overall reactivity of the  $\pi$ -system towards the allylation reaction, allowing the temperature to be lowered to rt and the reaction time shortened to a few minutes.

The method could also be extended to the  $\alpha$ -allylation of  $\alpha,\beta$ -unsaturated acyl silanes **5** (Table 3, entries 11–13), which are a well-known class of synthetically versatile building blocks. The products of these reactions were obtained in 57–77% yield (reflux, 2 h). Additionally, the  $\gamma,\gamma$ -disubstituted allenamide **1e** (entry 10 table 4.3) was treated with **2** under the optimized conditions. The corresponding enal **4ea**, featuring a tetra-substituted C=C double bond, was isolated in moderate yield (36%; Table 4.3, entry 10).

## 4.3 Mechanistic investigation of the reaction

### 4.3.1 Preliminarily mechanistic insights

The large scope of the reaction examined requires a clarification of the mechanistic aspects. The transformation poses several mechanistic questions: What is the role of the excess silver? What is the reaction profile of the C-C bond-forming event? and What is the nature of the nucleophilic species? among others. Insights into the C-C bond-forming step come from the isolation of products **3aj** and **3ak** as a mixture of regioisomers (entries 9,10, Table 2). Accordingly, a  $S_N1$ -type mechanism, involving stabilized allylic carbocations could be invoked.<sup>116</sup>

Experiments toward the elucidation of the role of  $AgNTf_2$  are preliminarily carried out. Firstly, it should be mentioned that,  $AgNTf_2$  alone (2.5 mol%) does promote the reaction but with moderate chemoselectivity (entry 18, Table 1). The presence of an excess of Lewis acid could both

promote the activation of the allylic alcohol (*i.e.* formation of the allylic carbocation) and/or converting the ether **III** into a chemically active alkylating form. To support this, **2** was refluxed in the presence of catalytic amount of AgNTf<sub>2</sub> in toluene for 2 h. The corresponding ether **III** was isolated in high yield (88%) along with the disproportionation products **6a** and **9a** in a 9% combined yield (Figure 4.4).<sup>117</sup> Moreover, when **III** was used as starting material in combination with water (1 eq. and AgNTf<sub>2</sub>) and **1** (2 eq. [Au(<sup>t</sup>Bu)(NTf<sub>2</sub>)]/AgNTf<sub>2</sub>), **6a/7a** and the desired product **3** were isolated in high conversion (90%) and 40% yield, respectively. All these evidences support key role the played by the silver salt in activating **2** and “recycling” **III** towards the nucleophilic trapping. In the absence of AgNTf<sub>2</sub>, only trace amounts of ether **III** were detected when **2** was heated at reflux in toluene for 4 h. The water for the hydrolysis of the immonium intermediate could be derived from the silver-assisted dehydrative dimerization of **2** to give **III**. The addition of activated molecular sieves seriously eroded the performance of the catalytic system.

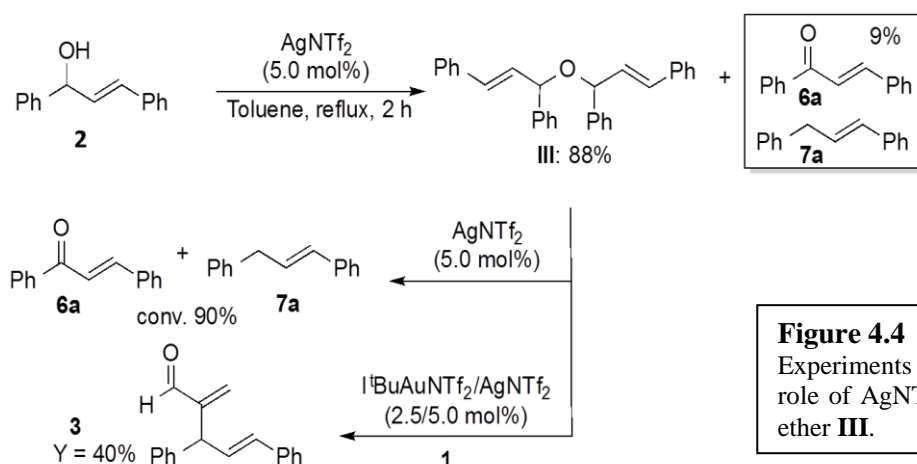


**Figure 4.4**

Experiments in support of the proposed role of AgNTf<sub>2</sub> in the activation of **2** and ether **III**.

### 4.3.2 DFT computational study of the reaction profile

In this study, to address the above mechanistic questions, we perform a computational DFT investigation for the model reaction profile of the gold(I)-assisted  $\alpha$ -allylation of  $\alpha,\beta$ -unsaturated carbonyl compounds described in Figure 4.3. Our work consisted of two main parts. Initially is directed towards the formation of the postulated organogold intermediate **B**-type (Figure 4.3) via hydrolysis of the gold activated allenyl unit (Figure 4.5). In the second part the key C-C forming step was investigated by condensing the diphenyl-allyl cation and the alkenyl gold species to obtain the final product (Figure 4.5). The first chemical event (**M0**→**M1**) involves the replacement of the

NTf<sub>2</sub> anion by the allenamide **1a** leading to the cationic gold **M1** in which the metal center is η<sup>2</sup>-coordinated to the C2=C3 bond of the allenyl unit.<sup>108</sup>

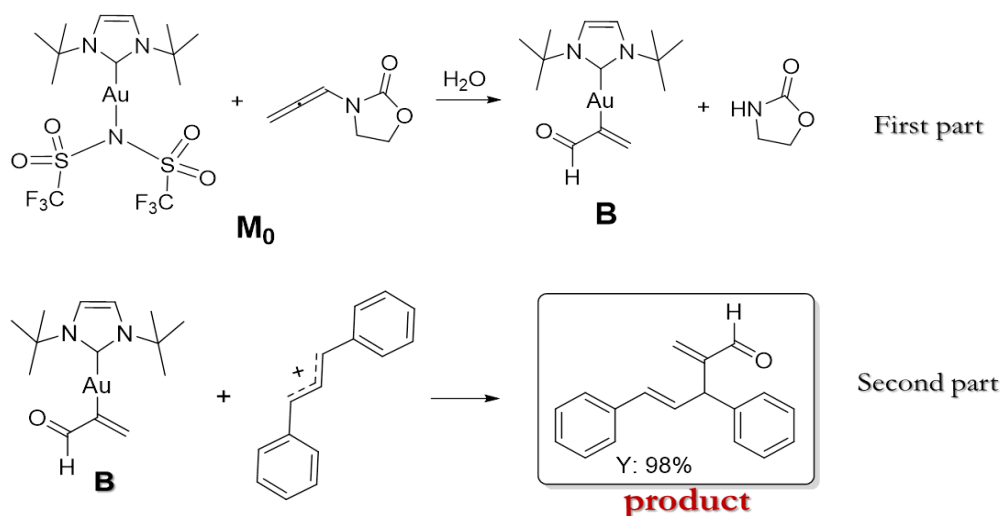


**Figure 4.5**

Schematic representation of our working goals.

A free energy barrier of 9.1 kcal mol<sup>-1</sup> is overcome passing through a tri-coordinated gold **TS1**. This energy barrier accounts for the impossibility to detect the rapid formation of intermediate **B**-type by mixing [Au(<sup>t</sup>Bu)(NTf<sub>2</sub>)] and **1** in wet CD<sub>2</sub>Cl<sub>2</sub> or CDCl<sub>3</sub>. In **M1**, the initial allene motif is almost completely preserved, although the Au-C2 σ-bond structure partly contributes to the description of the system (Au-C2 = 2.15 Å and Au-C3 = 2.55 Å).

Accordingly, N1-C3 shows a slight double bond character, being 1.35 Å long. In a subsequent step, a water molecule performs a nucleophilic attack on C3 (transition state **TS2**, 11.3 kcal mol<sup>-1</sup> above **M0**) promoting the allenamide hydrolysis. In **M2**, C3 changes its hybridization to sp<sup>3</sup> and the gold atom has completely switched its coordination mode, being σ-bonded to C2 (Au-C2 = 2.07 Å). Hence, the positive charge is now formally on H7 that although being shared with N2 (H7-N2 = 1.51 Å), is still firmly bonded to O2 (H7-O2 = 1.07 Å). This is probably the main reason of the high energy of **M2**, which lies 8.2 kcal mol<sup>-1</sup> above **M0**. Simultaneously, H6 is strongly interacting with O1 (H6-O1 = 1.85 Å). The hydrolysis is finally accomplished through a **TS3** (8.4 kcal mol<sup>-1</sup> above **M0**) featuring an oxazolidinone-assisted intramolecular proton transfer (H6 migrates from O2 to O1), delivering the predicted organogold intermediate (Au-C2 = 2.08 Å) depicted in **M3**.

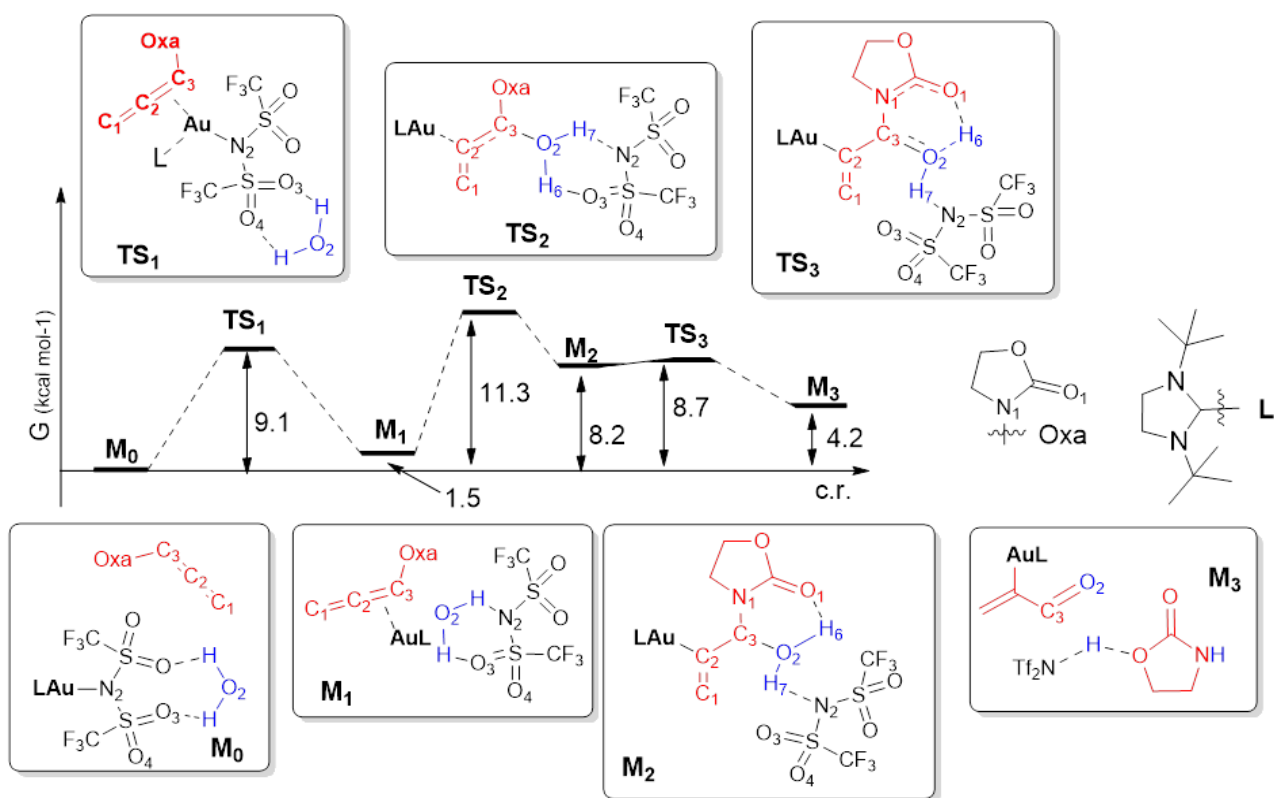


**Figure 4.6**

Computational mechanistic investigation: reaction profile and structures for the formation of  $\alpha$ -[Au]-enal species.

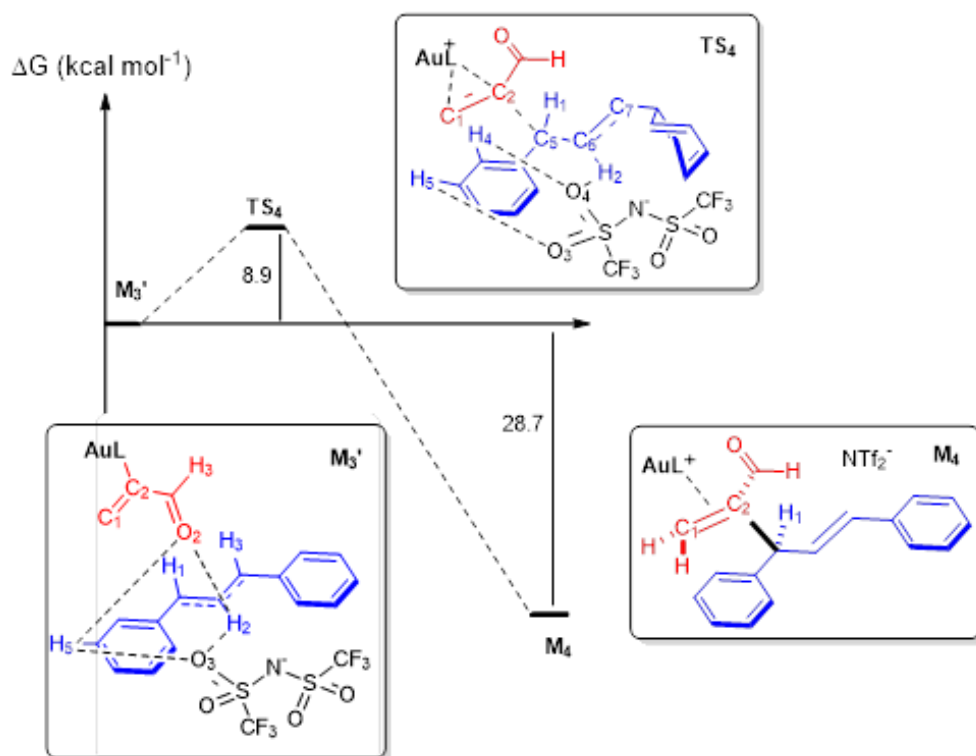


**Figure 4.7**

Computational mechanistic investigation: reaction profile and structures for the C-C bond-forming step.

Subsequently, the key C-C forming step was investigated by condensing the diphenyl-allyl cation and the alkenyl gold species, (Figure 4.7). **M3'** shows a gold species with a *gauche* conformation (dihedral O1-C3-C2-C = 60°) with the carbonyl oxygen atom pointing towards the fully delocalized diphenyl carbocation (C5-C6 and C6-C7 = 1.38 Å).

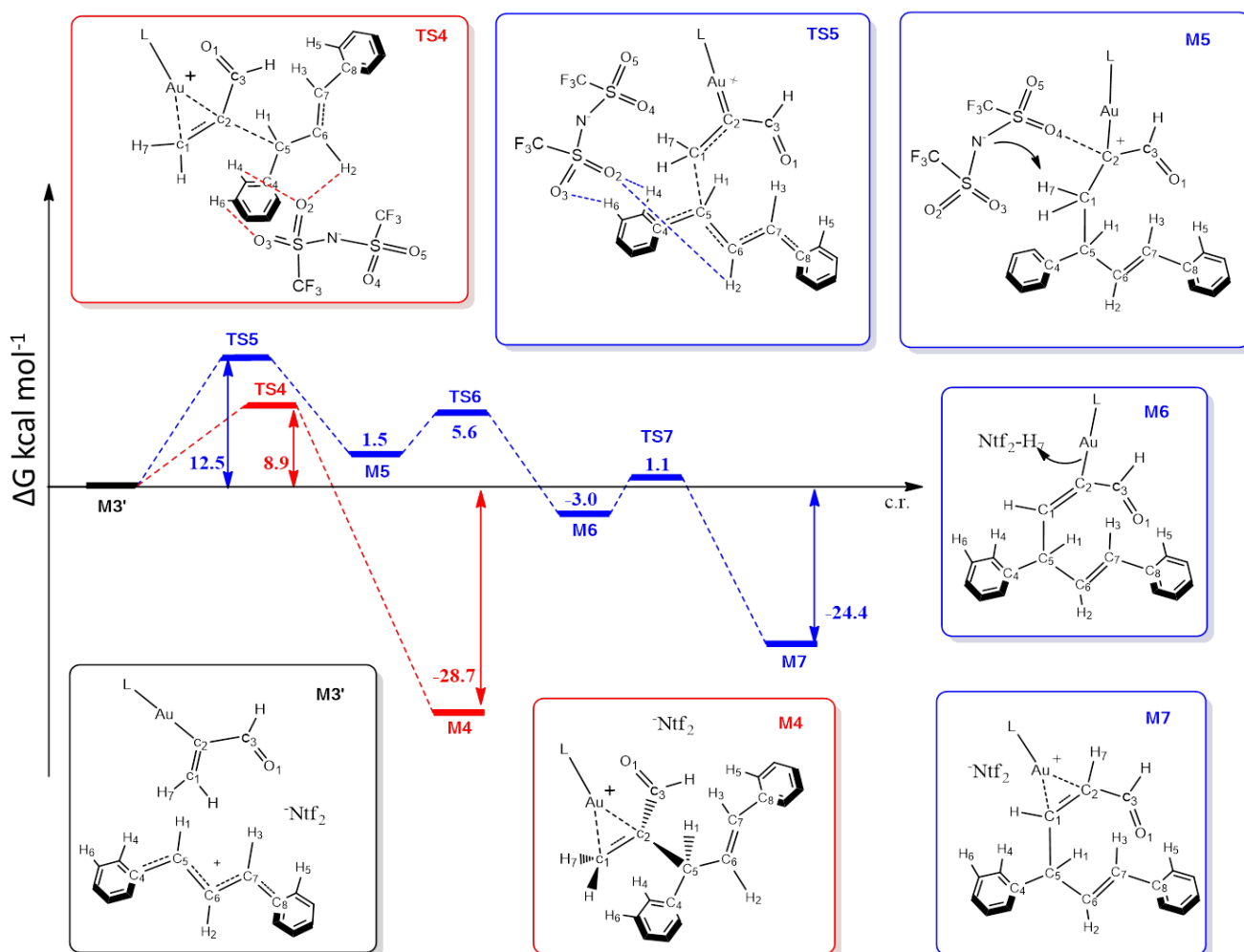


**Figure 4.8**

A comparison between the two possible reaction paths for the formation of the C-C bond: attack of C2 on C5 (red) and attack of C1 on C5 (blue).

The bistriflimide is located in proximity of the carbocation through two unconventional hydrogen bonds (O2-H2 = 2.06 Å and O2-H5 = 2.22 Å). In the following step the [C1=C2-Au] motif approaches the benzylic carbon C5, resulting in the formation of a new C-C bond (C2-C5). The transition state, **TS4**, lies 8.9 kcal mol<sup>-1</sup> higher than **M3'** and it is reactant-like. Here, despite the evident pyramidalization of C5 atom (hybridization sp<sup>2</sup> → sp<sup>3</sup>), the C2-C5 distance is still quite large (2.20 Å), whereas, as expected, the C1-C2 bond retains a double bond character (1.35 Å).

Concomitantly, the C1 methylene groups is rotating (H8-C1-C2-Au dihedral is  $51^\circ$  in **TS4** from  $2^\circ$  in **M3'**) in order to expose the  $\pi$ -electronic density to the gold atom, as it is changing its coordination mode  $\sigma$  (**M0**) to  $\eta^2$  in the final product **M4**. This adduct features a new C2-C5 bond ( $1.52 \text{ \AA}$ ) and results considerably more stable than **M0** and particularly **M3'** ( $24.5$  and  $28.7 \text{ kcal mol}^{-1}$ , respectively).

Additionally, we investigated the attack of C1 on C5, but we found that this process is highly disfavoured, the free energy barrier being  $13.5 \text{ kcal mol}^{-1}$ .

The reaction profile for this alternative reaction channel is reported in Figure 4.8 (blue profile). Accordingly to the computational evidence, the product associated with this path has never been experimentally observed.

Analogous calculations with  $\text{AgNTf}_2$  as the catalytic agent were carried out in order to support the experimental results on the key role of the silver salt in activating **2** and explain the lower chemoselectivity observed using  $\text{AgNTf}_2$  alone ( $7.5 \text{ mol}\%$ ) (Table 1, entry 17). Accounting for the experimental results observed the reaction with  $\text{AgNTf}_2$  led to significantly higher energy barriers (Figures 4.9 and 4.10).

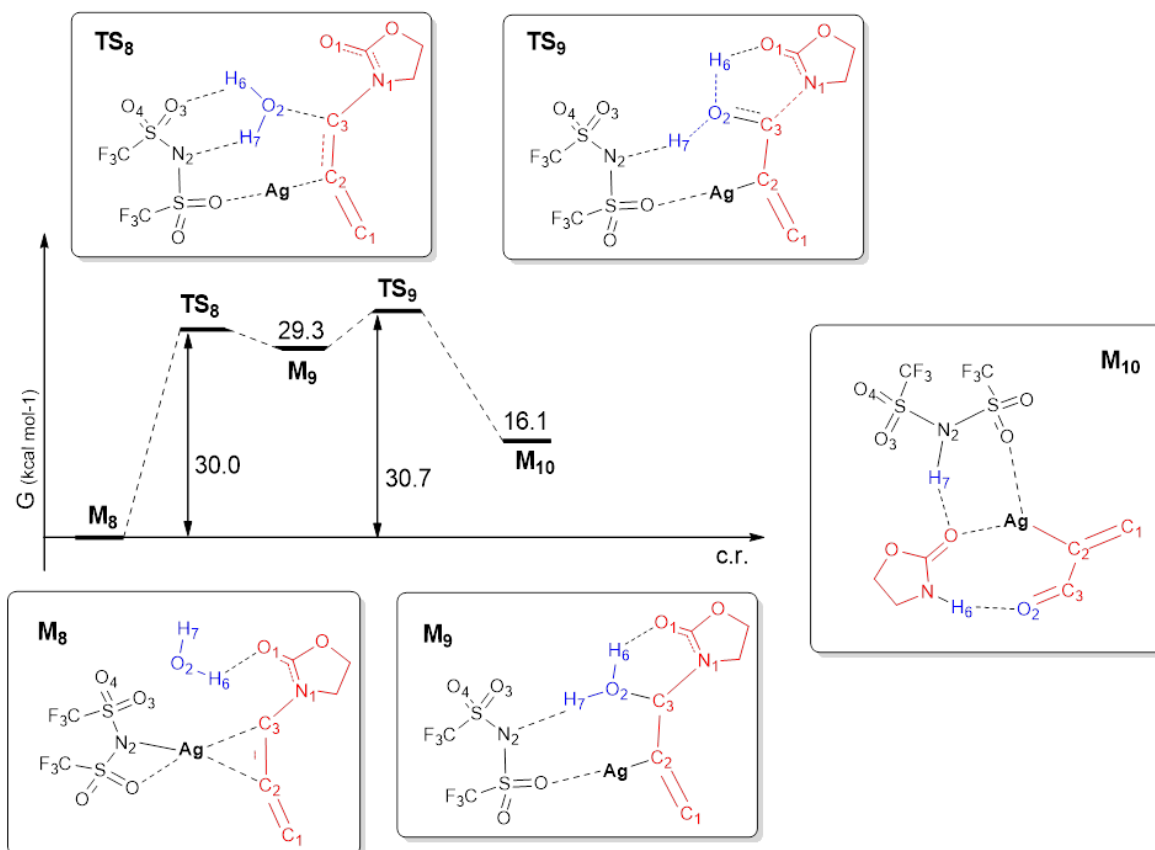


**Figure 4.9**

Computational mechanistic investigation: the formation of  $\alpha$ -[Ag]-enal species.



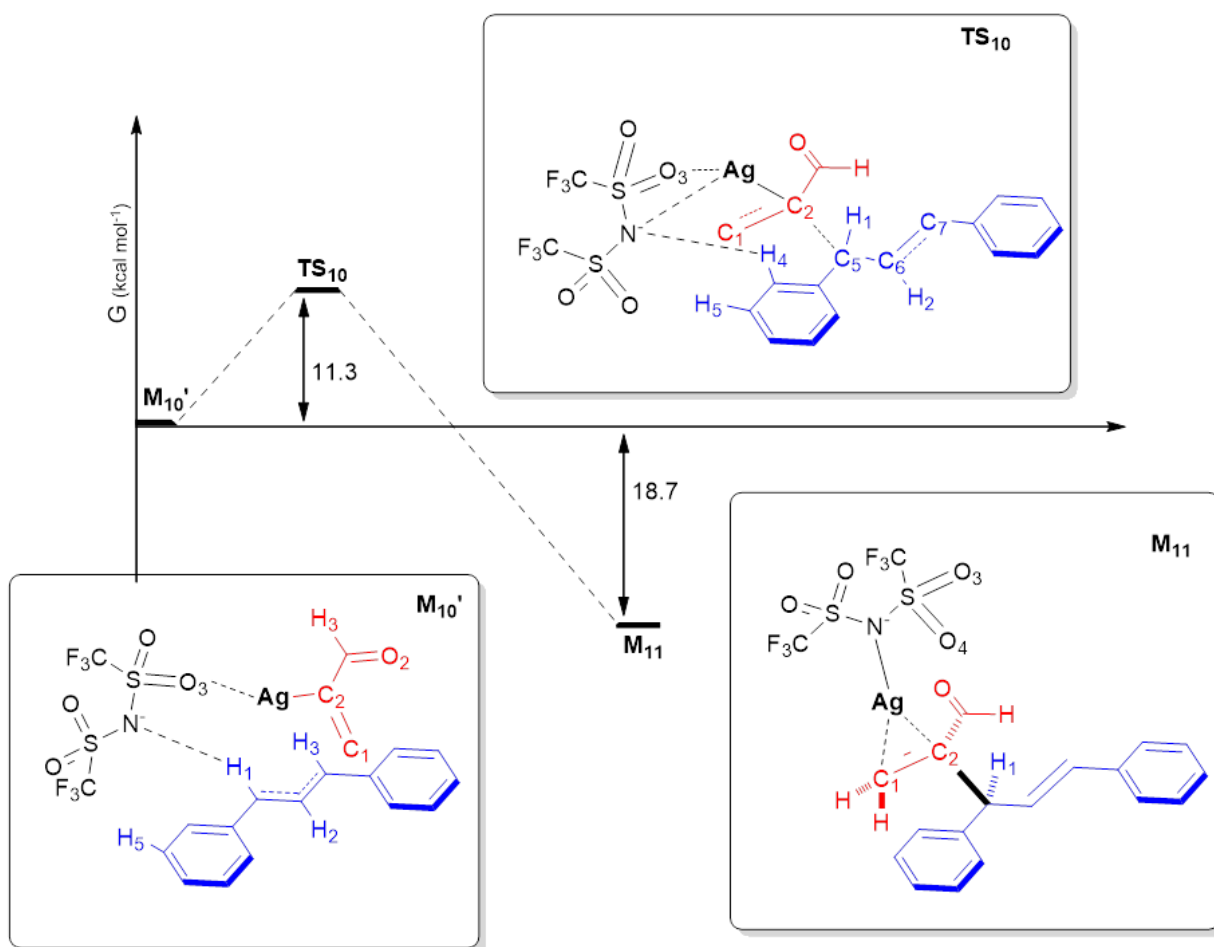


**Figure 4.10**

Computational mechanistic investigation: the C-C bond-forming step with silver catalyst.

Although the coexistence of a background reaction involving the spontaneous condensation of the unactivated allenamide **1** with allylic cationic species cannot be completely excluded, this reaction pathway seems non-competitive with the gold-assisted pathway in terms of chemoselectivity. Indeed, when a “naked” allylic carbocation generated in situ was directly treated with **1**,<sup>118</sup> the corresponding enal **3** was obtained in only 40% yield along with a large amount of unknown by-products.

#### 4.4 Computational details

DFT computations were performed by using the Gaussian09 series of programs.<sup>4</sup> The M06 functional proposed by Truhlar and Zhao<sup>24,25</sup> was used in all computations. This functional can

provide a reliable description of transition metals and medium-range  $\pi$ - $\pi$  interactions at the same time.<sup>97</sup> The 6-31+G\* basis set, included in the Gaussian package, was used for all atoms except the gold and silver atoms, which were described with the LANL2DZ basis set.<sup>99</sup> The geometries of the various critical points on the potential surface were fully optimized with the gradient method available in Gaussian 09, and harmonic vibrational frequencies were computed to evaluate the nature of all critical points and entropy contributions to free energy.

#### 4.5 Conclusions

We have disclosed a gold(I)/silver(I)-co-catalyzed  $\alpha$ -allylation of unsaturated carbonyls with allylic alcohols providing rapid access to substituted enals, enones and acylsilanes. The cooperative action of gold and silver salts was elucidated via experimental as well as computational studies. The synthetic flexibility of the targeted compounds was shown quite versatile and efficient. Finally, it should be mentioned that the present methodology represents a valuable synthetic alternative to the well-known Baylis-Hillman (BH) reaction<sup>119</sup> for the  $\alpha$ -functionalization of  $\alpha,\beta$ -unsaturated carbonyls, that has found sporadic application in allylic alkylation procedures. Studies addressing the enantioselective variant of the present protocol are currently under investigation.

## 5. Gold(I)-Catalyzed Dearomative [2+2]-Cycloaddition of Indoles with Activated Allenes: A Combined Experimental–Computational Study<sup>120</sup>

### 5.1 Allenamides in Catalysis

In the recent decades, allenes and their derivatives have progressively increased their interest in organic synthesis field becoming one of the most powerful and versatile synthetic building blocks.<sup>121</sup> Among these, allenamides, are electron deficient allenamine equivalents that can participate in a range of cycloaddition events giving rise to novel heterocycles and diverse molecular architectures contained within natural products. As we already saw in the previous research project the applicability of this functional group is very wide. The allenamide subunit can be employed, amongst other things, in radical cyclizations<sup>122</sup>, acid and metal catalyzed cyclizations<sup>123</sup>, palladium mediated transformations<sup>124</sup>, base catalyzed heterocyclizations<sup>125</sup>, Gold mediated transformations<sup>126</sup> and ruthenium-catalysed aminoallylations<sup>127</sup>. Allenamides are functionally derived from allenamines,<sup>128</sup> which along with structurally related systems such as allenol ethers<sup>129</sup> and allenyl sulfides,<sup>130</sup> can be classified as heteroatom-substituted allenes. The  $\pi$ -donating ability of nitrogen atom makes allenamines more electron-rich than simple allenes, thereby predisposing them to electrophilic activations. Electronic considerations can be made through delocalization of the nitrogen lone pair toward the allenic moiety as demonstrated in the resonance form of allenamines. Accordingly, highly regioselective transformations can be achieved with consecutive addition of electrophiles and nucleophiles (Figure 5.1).<sup>121b</sup>

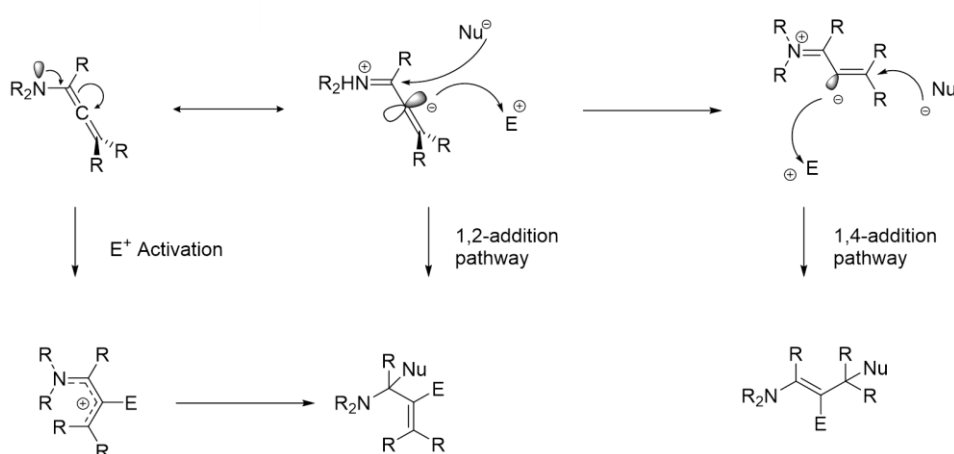
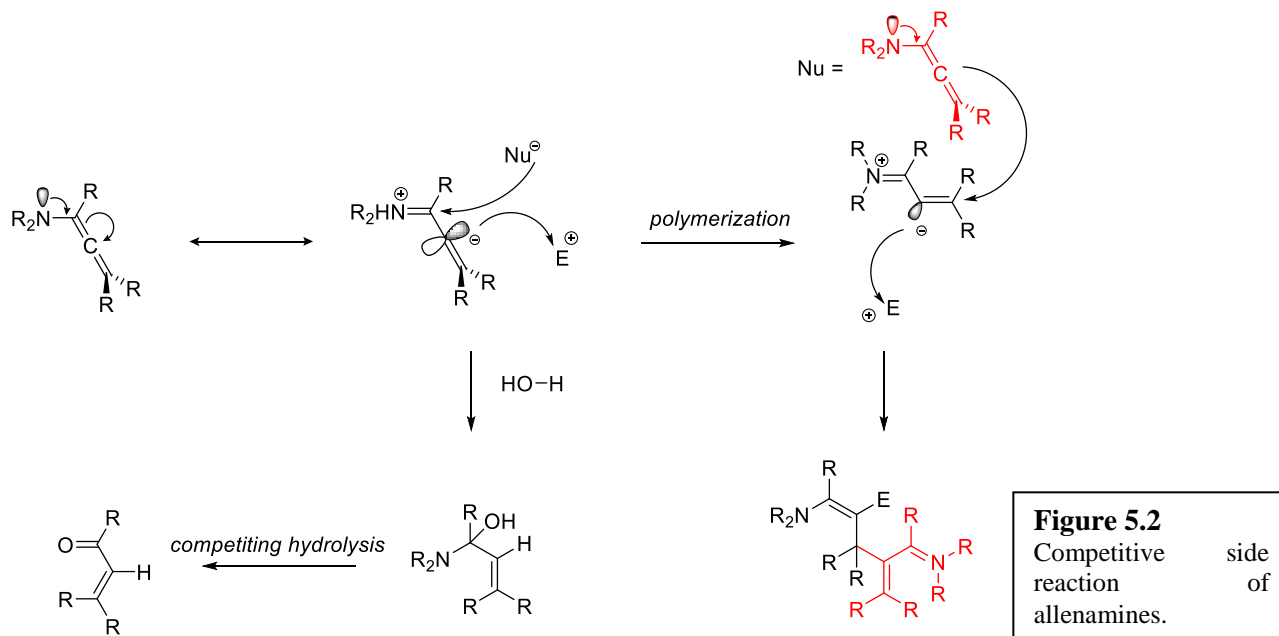
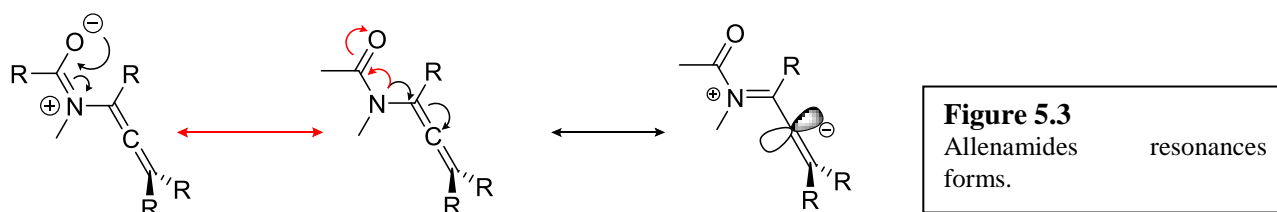


**Figure 5.1**  
Allenamines Reactivity

The allenamines offers a wide number of other advantages over simple allenes, however, allenamines are also highly sensitive toward hydrolysis with a tendency to polymerize even at low temperatures (Figure 5.2), thereby creating serious difficulties in their preparation and experimental handling.<sup>131</sup>



Consequently, the great potential of chemistry of nitrogen-substituted allenes could only be partially realized. Therefore, efforts to identify an allenamine-equivalent should be of high significance if it can strike the right balance between stability and reactivity. On the basis of these considerations allenamides should represent ideal candidates as a stable allenamine-equivalent. Delocalization of the nitrogen lone-pair in the carbonyl group should decrease its donating ability toward the allenic moiety, thereby leading to improved stability (Figure 5. 3)<sup>121b</sup>



They are becoming proven allenamine-equivalents that can be employed in a diverse array of stereoselective and intramolecular reactions that were not possible with traditional allenamines. They represent the ideal platform for pushing the limit of synthetic potential of nitrogen-substituted allenes.

Many of the transformations that allenamides can undergo, give rise to structurally diverse heterocycles as well as complex molecular architectures reminiscent of natural products and biologically relevant substrates, all from relatively simple precursors.

As well as any other olefin, allenamides reactivity includes the reactions of additions, aldol additions,  $\alpha$  and  $\gamma$  hydrogen substitutions, metal catalyzed or not cyclizations and cycloadditions.

In the literature there are many examples that show the allenamides as the ideal partner for cycloadditions, either intramolecular or intermolecular; most of the examples exhibits a catalytic activation of the allenic moiety while sporadic are the reactions that proceed without metals or Brønsted acids.<sup>121,123,125</sup>

## 5.2 Indolyl-based alkaloid chemistry

The indole scaffold probably represents one of the most important structural subunits for the design of new drug candidates. The demonstration that many alkaloids contain the indole nucleus, the recognition of the importance of essential amino acid tryptophan in human nutrition and the discovery of plant hormones served to bring about a massive search on indole chemistry. This has ensured the discovery of a vast number of biologically active natural and synthetic products, with a wide range of therapeutic targets, such as anti-inflammatories, phosphodiesterase inhibitors, 5-hydroxytryptamine receptor agonists and antagonists. The intrinsic molecular diversity of synthetic and natural occurring compounds belonging to this family continues to inspire developments in organic synthesis. To this aim, catalysis is the ultimate forefront in this area with a large portfolio of reliable metal- and metal-free methodologies available.<sup>132</sup>

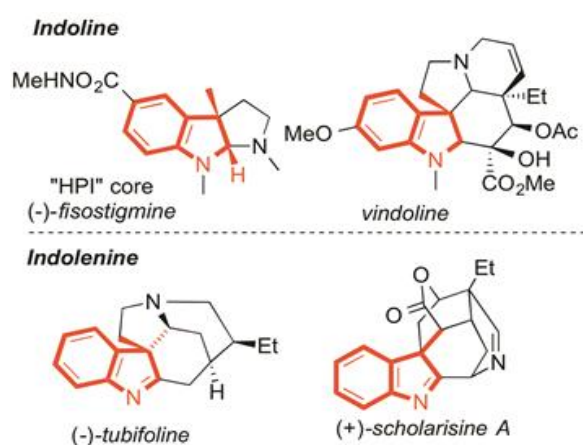


**Figure 5.4**

Collection of natural products featuring polycyclic C(2),(3)-fused indoline and indolenine scaffolds.

Partially dearomatized C(2),C(3)-polycyclic fused indoline and indolenine motifs are widely diffused molecular architectures in indole alkaloids, featuring stereochemically defined all carbon quaternary stereocenters at the C(3)-position.<sup>133</sup> A collection of titled compounds is reported in Figure 5.4.

Among the numerous catalytic methodologies available, the enantioselective C(2),C(3)-annulation of indoles by cycloaddition reactions is gaining growing credit in terms of chemical efficiency. Based on these methodologies, densely functionalized C(2),C(3)-fused cyclopropa-([2+1]),<sup>134</sup> cyclopenta-([3+2])<sup>135</sup> and cyclohexa-indoline cores ([3+3])<sup>136</sup> have been prepared in a stereochemically defined manner.

C2,C3-indolincyclobutanes<sup>137</sup> have found less attention in literature. As a matter of fact, besides the elegant intramolecular approach reported by Zhang,<sup>138a</sup> the cyclobutyl-fused indole species was isolated only in low yields via condensation of allenamides with indoles proposed by Lopéz, and Mascareñas.<sup>138b</sup> Additionally, Xie and co-workers very recently documented the dearomative [2+2]-cycloaddition between o-carboryne and N-silylated indoles under thermal conditions.<sup>139</sup>

In this context, gold catalysis<sup>140</sup> offers unique opportunities due to the peculiar attitude of this coinage metal in promoting cycloaddition transformations via electrophilic activation of  $\pi$ -systems.<sup>141,142</sup>

Recently, our cooperating experimental group documented the first enantioselective gold-catalyzed synthesis of C(2),C(3)-indolincyclobutanes by formal [2+2]-cycloaddition reactions between N-protected indoles and allenamides (Figure 5.5).<sup>143</sup>

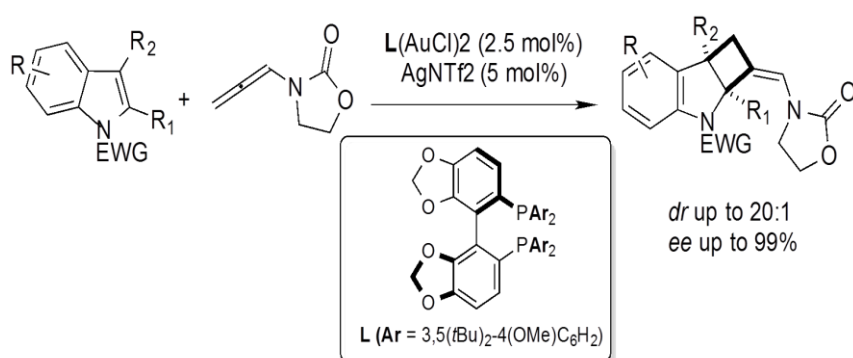


**Figure 5.5**

Preliminary results on the gold-catalyzed asymmetric [2+2]-cycloaddition of indoles and allenamides.

In conjunction with our research interests focused on gold(I)-assisted reactions of indole and allenamide derivative, will now be presented a comprehensive investigation on the dearomative formal [2+2]-cycloaddition reaction between 2,3-disubstituted indoles and allenamides to give

densely functionalized 2,3-cyclobutyl-indolines. In particular, the gold-catalyzed racemic and enantioselective condensations of allenamide/aryloxyallenes with a range of N-substituted indoles will be discussed. Also in this case is presented a combined experimental/computational work, the section that my research group dealt was a detailed DFT computational investigation to obtain a mechanistic insight on the the high chemo- regio- and stereoselectivity experimentally observed.

## 5.3 Experimental results

### 5.3.1 Optimization of the catalyst and reaction conditions

With the aim of optimizing the synthesis of indolyl-2,3-cyclobutyl derivatives via cycloaddition reactions between electron-rich allenes and indoles, initially are screened a range of [Au(I)] complexes in the model reaction comprising the 2,3(Me)<sub>2</sub>-indole **1a** and the allenamide **2**. In parallel, a survey of reaction conditions elected DCM as the best reaction media (other reaction media furnished lower isolated yields of **4a**: CH<sub>3</sub>CN=21%, THF=17%, toluene=15%, DCE (80 C°)=22%). Initial attempts afforded the partially dearomatized indolenine **5a** and the nitrogen-allylated indole **6a** as main byproducts of the process.

From the collection of results summarized on Table 5.1, clearly emerged the attitude of [JohnPhosAu(NCMe)]SbF<sub>6</sub><sup>144</sup> in promoting the cycloaddition, providing the [2+2]-adduct **4a** as the major product (entry 6, yield = 49%) under mild reaction conditions (CH<sub>2</sub>Cl<sub>2</sub>, rt, 16 h).

Based on these results it can be assumed that the introduction of an electron-withdrawing group at the N-(1)-position of the indole could have significant effects on the reaction mechanism and its energetics by preventing the undesired N-alkylation (**6a**) and by increasing the electrophilic character of the intermediate immonium derivative.<sup>145</sup> The experimentalists proved that, N-(Boc)-2,3-(Me)<sub>2</sub>- indole **1b** is a competent reaction partner providing the desired diastereomerically pure cyclobutyl derivative **4b** in 60, 73 and 89% yield at room temperature, -20 and -40 C°, respectively (entries 7–9 of Table 5.1). The increase of isolated yields at lower temperatures can be rationalized in terms of minimization of gold-promoted self-condensation of **2** (i.e., dimerization or polymerization).

Entry	[Au(I)] (5 mol%)	Yield 4 (%)	Yield 5a (%)	Yield 6a (%)
1	JackiePhosAuNTf <sub>2</sub>	< 5 (4a)	22	33
2	Ph <sub>3</sub> PAuNTf <sub>2</sub>	6 (4a)	18	75
3	XPhosAuNTf <sub>2</sub>	19 (4a)	--	--
4	JohnPhosAuTFA	< 5 (4a)	77	< 5
5	XPhosAuTFA	8 (4a)	70	< 5
6	[JohnPhosAu(NCMe)]SbF <sub>6</sub>	49 (4a)	5	7
7 <sup>[a]</sup>	[JohnPhosAu(NCMe)]SbF <sub>6</sub>	40 (4a)	--	--
8	[JohnPhosAu(NCMe)]SbF <sub>6</sub>	60 (4b)	--	--
9 <sup>[a]</sup>	[JohnPhosAu(NCMe)]SbF <sub>6</sub>	73 (4b)	--	--
10	[JohnPhosAu(NCMe)]SbF <sub>6</sub>	89 (4b)	--	--

[a] T = -20 °C, t = 5 h. [d] T = -40 °C, t = 16 h.

**Table 5.1**

Optimization of the reaction conditions for the racemic variant of the formal [2+2]-cycloaddition reaction. All the reactions were carried out under nitrogen atmosphere (**1**:**2**:**[Au]** = 1.2:1:0.05). The Isolated yields are after flash chromatography.

Concerning the stereochemical aspects, optimal conditions provided the *cis*-C(2),C(3)-fused tricyclic compounds in high diastereomeric ratio (d.r.=20:1). Furthermore, the *exo*-C=C double bond was exclusively obtained in the *Z* configuration.

### 5.3.2 Application field of the reaction with allenamides

Once optimized the reaction conditions and the catalyst, the scope of the process was examined by reacting a range of *N*-protected-2,3-disubstituted indoles (**1c-q**) under the elected conditions and a summary of results is depicted in the Figure 5.6.

Interestingly, the presence of C5- and C7-membered cycles fused at the C(2)/C(3)-positions of the pyrrolyl ring were positively tolerated providing the corresponding tetra- and pentacyclic compounds **4c-k** from moderate to excellent yields (41-95%). Additionally, indoles carrying acyclic C(2)/C(3) substituents (**1l-q**) performed similarly furnishing the cycloadducts **4 c-k** in high yield.



This screening enabled us also to shed light on the tolerance towards substituents on the benzene ring. Here, while electron-donating (i.e. Me, OMe) and moderately electron-withdrawing groups (i.e. Br) proved competence in the process, the strong EWG NO<sub>2</sub> group (C(5), **1m**) completely suppressed the kinetics of the transformation. Finally, the Boc-protecting group was also successfully replaced by Cbz (**1l**) with an untouched isolated yield (95%).

To be also mentioned that, the 2,3-disubstitution pattern at the indole core proved to be mandatory for the reaction course. As a matter of fact, while *N*Boc-indole and *N*Boc-3-Me-indoles provided dimerization products of **2** as main outcomes, *N*Boc-2-Me-indole furnished the desired [2+2]-cycloadduct only in 18% yield.

Stereochemically, optimal conditions provided the *cis*-fused tricyclic compounds in high diastereomerically form (*dr* = 20:1). Additionally, the *exo*-carbon carbon double bond was formed exclusively in *cis* configuration. Both molecular skeleton and the stereochemical aspects were finally substantiated by obtaining the x-Ray structure of (+/-)-**3i** via slow evaporation from a solution of AcOEt.

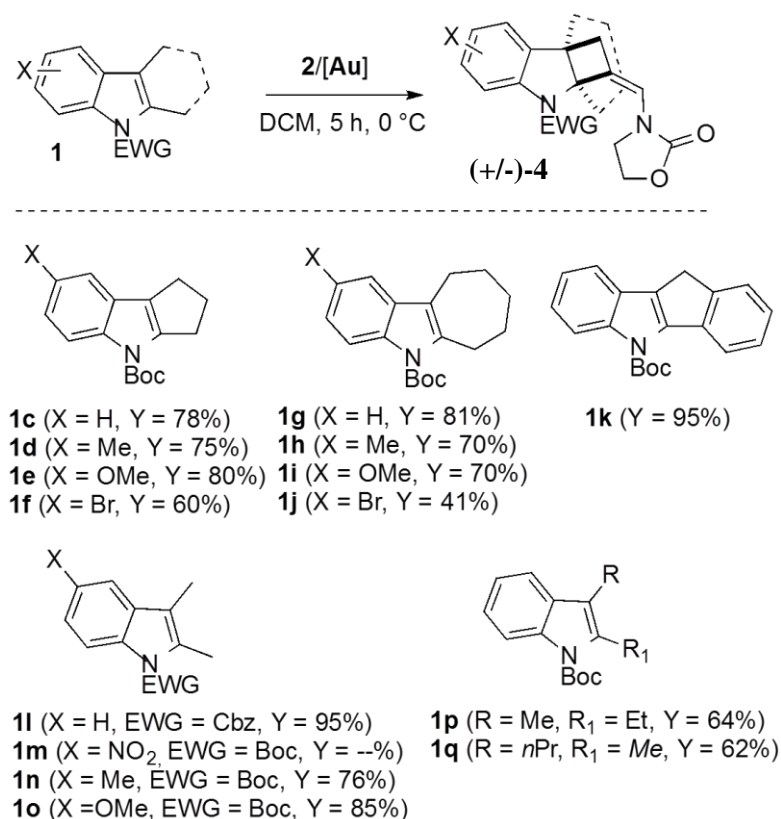


**Figure 5.6**

Substrate scope of the dearomative [2+2]-cycloaddition between indoles and the allenamide **2**.

[Au(I)]: [JohnPhosAu(NCMe)]SbF<sub>6</sub> (5 mol%). Y = Yield

### 5.3.3 Application field of the reaction with aryloxyallene

Aryloxyallenes are an important class of electron-rich allenes derivatives that found extensive applications in organic chemistry, with particular concern to cycloaddition reactions and additions of nucleophiles.<sup>146</sup> Analogously to the afore-describe allenamides, the nucleophilic addition to the  $\gamma$ -carbon would lead to a formal allylation reaction with the concomitant installation of a synthetically versatile aryloxy moiety.

Despite this undoubted synthetic interest, to best of our knowledge, this family of unsaturated compounds has never been employed in dearomative processes up to now. In order to assess the expandability of the methodology to aryloxyallene, a range of allenyl derivatives (**3a-f**) was synthesized via a conventional two-step procedure (propargylation of the corresponding phenol followed by base-assisted isomerization) and subjected to the dearomative cyclization in the presence of **1b** ( $[\text{JohnPhosAu}(\text{NCMe})]\text{SbF}_6$ ). Electron-“neutral” and electron-poor arenes were employed in order to guarantee synthetically acceptable stability of the corresponding allenes. Aryloxyallenes featuring electron-rich arenes proved to rapidly self-polymerize even at low temperatures and turned out to be unsuitable for the present protocol.

Entry	[Au] (x mol%)	<b>3</b> (Ar)	Yield <b>7</b> (%)
1	5	<b>3a</b> (Ph)	75
2	1	<b>3b</b> ( $\beta$ -naphth)	83
3	5	<b>3c</b> ( <i>p</i> BrC <sub>6</sub> H <sub>5</sub> )	96
4	5	<b>3d</b> ( <i>p</i> NO <sub>2</sub> C <sub>6</sub> H <sub>5</sub> )	81
5	5	<b>3e</b> ( <i>p</i> F, <i>o</i> BrC <sub>6</sub> H <sub>4</sub> )	83
6	5	<b>3f</b> ( <i>p</i> , <i>o</i> Cl <sub>2</sub> C <sub>6</sub> H <sub>4</sub> )	95

**Table 5.2**

Gold catalysed dearomative [2+2]-cycloaddition between **1a** and aryloxyallenes **6**. All the reactions were carried out under nitrogen atmosphere (1:2:[Au] = 1.2:1:0.05). Isolated yields are after flash chromatography. *Dr* > 20 :1.

The synthetic procedure turned out to be extraordinarily adaptable to a variety of aryloxyallenes. Accordingly, a range of racemic methylene cyclobutanes **7** (Table 5.2) was isolated as a single stereoisomer in good to excellent yields (75–96%) under mild reaction conditions ([Au]: 1–5 mol%, DCM, 08C, 4 h).

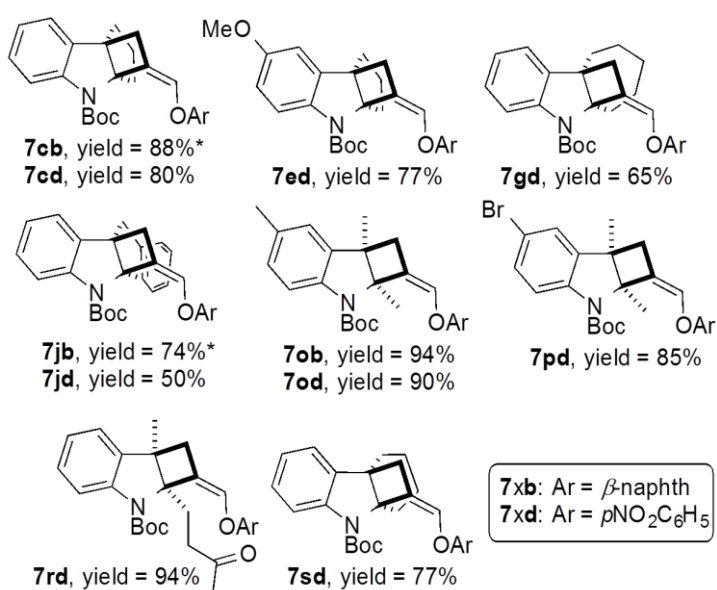


**Figure 5.7**

Formal [2+2]-cycloaddition between N-Boc-indoles and aryloxyallenes (1/3/([JohnPhosAu(NCMe)]SbF<sub>6</sub>)=1:2:0.05, DCM, 0 °C, 16 h). \*: 1 mol% of catalyst was used. All the compounds were obtained in racemic manner.  
 7xb: Ar=2-naphth; 7xd: Ar=pNO<sub>2</sub>C<sub>6</sub>H<sub>4</sub>.

Subsequently, the substrate scope was further investigated by condensing differently substituted N-Boc-indoles and allenes **3b** and **3d**. The results reported in Figure 5.7 emphasize the efficiency of the above-described gold-catalyzed methodology in providing densely functionalized tricyclic fused indolinyl scaffolds **7**.

In particular, the reaction proved to be not significantly affected by the presence of substituents (including either carbon- or heteroatom-based groups) at the indole N(1), C(2), C(3) and C(5) positions. The isolated yields ranged between 50 and 94% and the decrease of the catalyst loading to 1 mol% did not at all affect the chemical outcome. The molecular architectures of **7** were unambiguously determined via X-ray analysis of cyclobutyl derivative **7pd**.

## 5.4 Gold-catalyzed dearomatization reaction: mechanistic study

### 5.4.1 Preliminarily mechanistic insights

The interest for the reaction mechanism originates from intriguing experimental evidences on the classic cycloaddition reaction among allenamide **2** and NBoc-indole **1b**. Here, when the condensation was carried out at higher temperatures (i.e. rt or 40 °C), a second product was formed that became predominant in the latter case (yield = 35%). Crystallographic analysis showed that this product has the structure of the regioisomeric indoline-cyclobutyl ring **4b'**, corresponding to a reverse approaching orientation (with respect to **4b**) of the two reaction partners (Figure 5.8).

Additionally, when **4b** was treated in the presence of the gold complex in hot DCM (40 °C), **4b'** was again isolated along with some decomposition products.

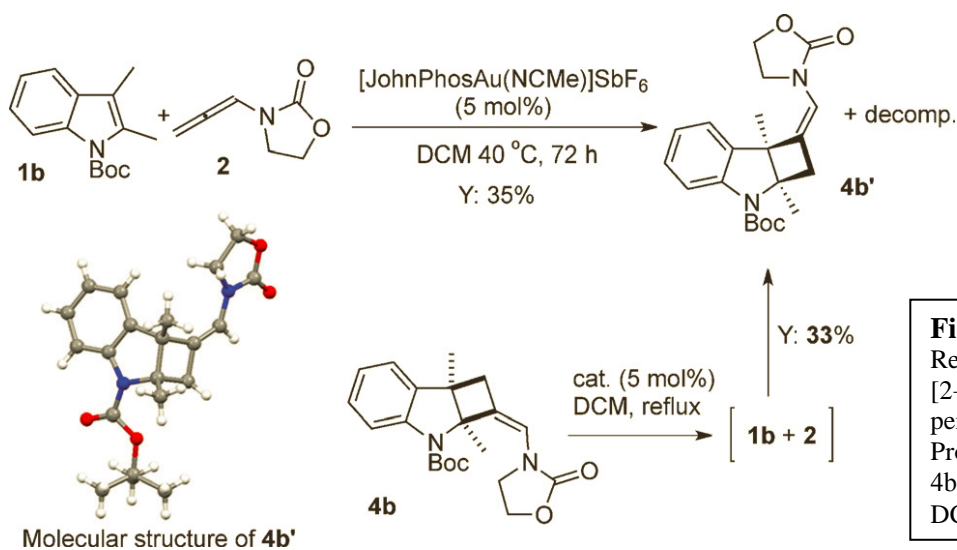


**Figure 5.8**  
Regiodivergent outcome of the [2+2]-cycloaddition when performed in refluxing DCM. Proving the interconversion of **4b** into **4b'** in hot DCM.

This evidence seems suggesting **4b** and **4b'** as the kinetic and thermodynamic products of the present reaction, respectively.

Once again, as in previous research projects, the question on which we will focus is the mechanistic study of the reaction. In the light of the experimental results presented above even in this case the overall mechanistic picture still posed important and unsolved interrogatives such as: 1) What is the coordination/activation mode of the gold catalyst with the allenamides? 2) Is the mechanism concerted or step-wise? 3) What is the rationale for the recorded regio- and stereochemistry? In particular, why does the ring closure occur without affecting the stereochemistry of the exocyclic double bond (Figure 5.9)? 4) Are the “kinetic” and “thermodynamic” adducts the results of two separate reaction channels coexisting on the reaction surface?

#### 5.4.2 DFT computational study of the reaction

In order to answer the described questions determine a computational work based on computational calculations we performed. Relying on the proposed mechanism of the indole alkylation catalysis with allenamides promoted by  $[\text{Au}(\text{I})]$ , a mechanistic model for the cycloaddition reactions was proposed.

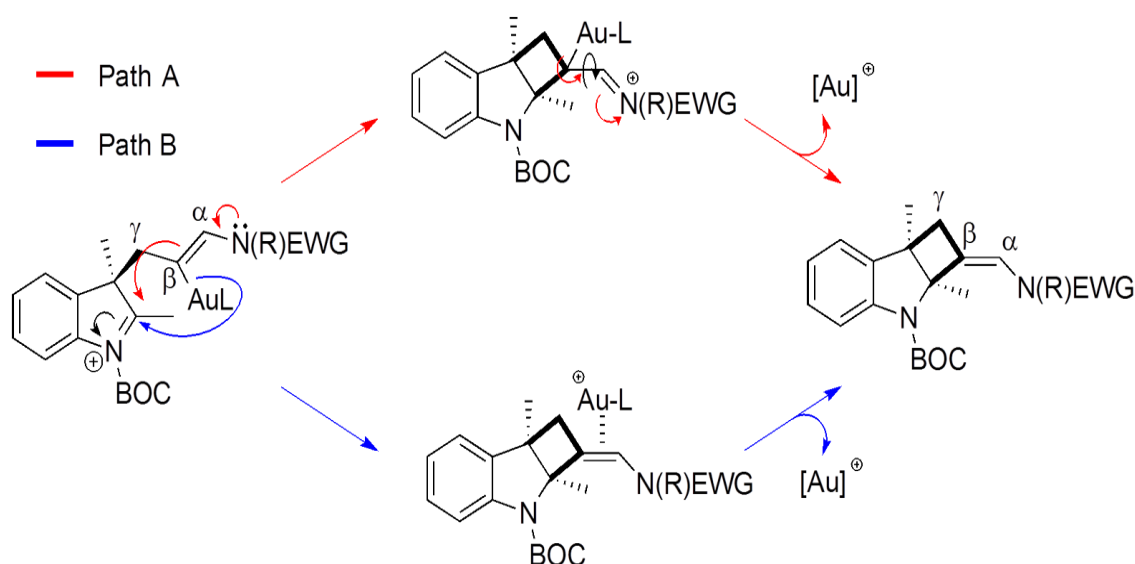


**Figure 5.9**  
Hypothetical mechanisms for the ring-closing step.

We used a DFT approach and a model system formed by **1b** and **2** activated by the [AuI] cation bonded to the JohnPhos ligand ([JohnPhosAu<sup>+</sup>]) to determine i) if the ring closing mechanism occurs without affecting the stereochemistry of the exocyclic double bond or not and ii) the possible reaction pathways for the production of the "kinetic" and "thermodynamic" adducts.

First we examined how the cationic gold complex governs the electrophilic activation of allenamide **2**.<sup>147</sup> We found that the interaction of the metal with the cumulated diene involves an equilibrium between three different complexes M1( $\pi$ ), M2( $\sigma$ ), M3( $\pi$ ) showing  $\eta^2$ ,  $\eta^1$  and  $\eta^2$  coordination to [Au(I)], respectively. Both  $\eta^2$  complexes (M1( $\pi$ ) and M3( $\pi$ )) are more stable than M2( $\sigma$ ) (2.9 and 3.4 kcalmol<sup>-1</sup>, respectively; a 3D representation of the three complexes is given in Figure 5.10).

The perturbation of the  $\pi$ -system caused by the interaction with the gold complex is evidenced by a slight increase of the C-C bond lengths in M1( $\pi$ ) and M3( $\pi$ ) and the increase of the corresponding positive charge density on  $\alpha$  and  $\gamma$  carbons. The reaction surface for the cycloaddition shown in Figure 5.9 involving indole **1b** and allenamide **2** complexed with [Au(I)] (reactants) is reported in Figure 5.11 examining the reaction pathways for the achievement of the "kinetic" and "thermodynamic" reaction products separately.

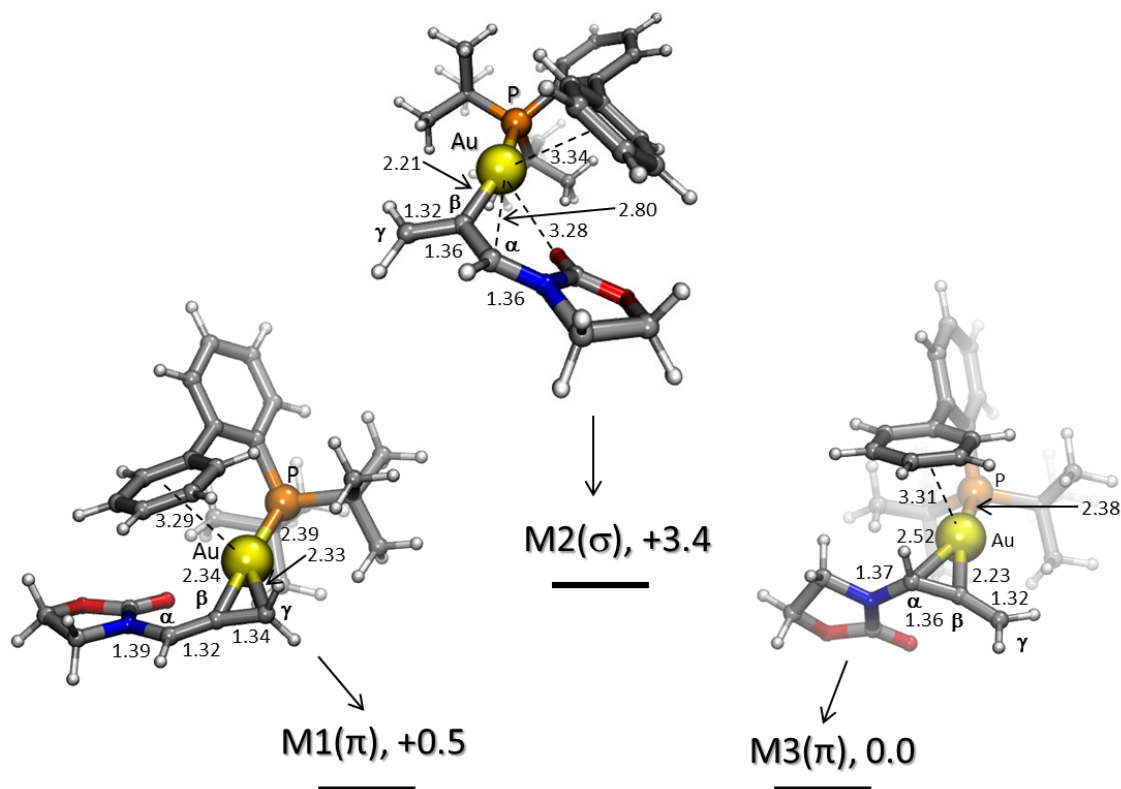


**Figure 5.10**

A schematic 3D representation of the allenamide-[AuI] complexes. Total energy values [kcalmol<sup>-1</sup>] are relative to M3(π). Bond lengths are given in Å.

In Figure 5.11 a schematic representation of the corresponding reaction patterns is also given. Additionally, two-dimensional representation for each point of the structure of the various critical points located along the two pathways are given in Figure 5.12 (more detailed 3D representations in Figure 5.13).

The approach of the two reacting species initially leads to the formation of an encounter complex M0 (12.9 kcalmol<sup>-1</sup> more stable than reactants), where the indole ring plane and the plane of the metal allyl cation are facing each other, the C(3)-C $\gamma$  and C(2)-C $\gamma$  distances being 2.87 and 3.00 Å, respectively. Interestingly, in the encounter complex the preferred coordination of the gold cation is  $\eta^1$  and not  $\eta^2$  as found in the isolated allenamide-[JhonPhosAu<sup>+</sup>] species. The higher stability of the  $\sigma$ -type complex ( $\eta^1$ ) can be reasonably ascribed to the stabilizing interaction between the electron-rich indole  $\pi$ -system and the positive charge localized on the  $\alpha$  allenamide carbon (0.3 is the net computed charge on C $\alpha$ ).

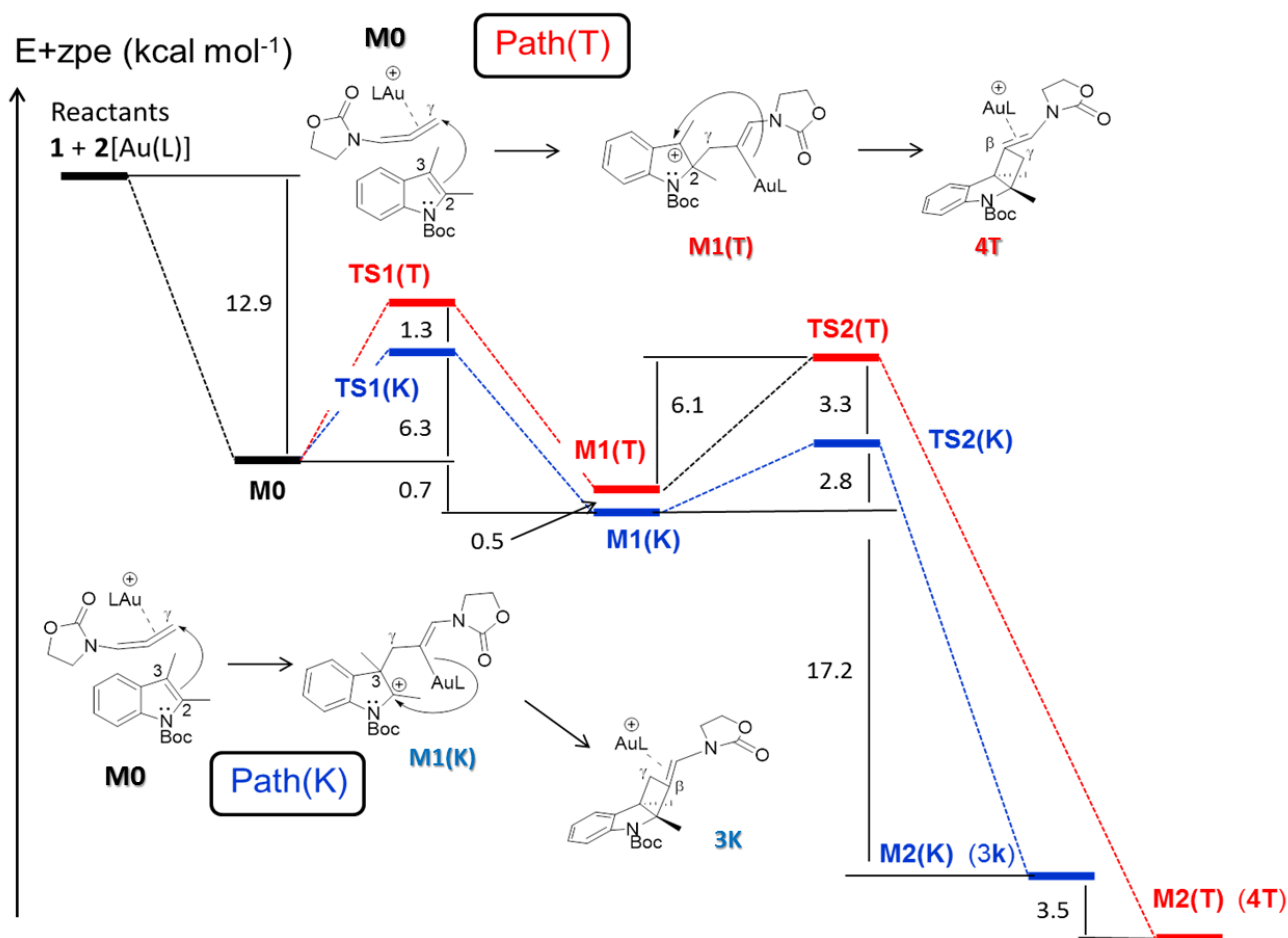


**Figure 5.11**

The two computed reaction profiles **Path(K)** and **Path(T)**. The total energy values ( $E$ , kcalmol<sup>-1</sup>) include ZPE corrections.

Two reaction paths (both consisting of two steps) originate from **M0** and lead to different regioisomers corresponding to opposite approaching orientations of the reacting species. These regioisomers should correspond to the hypothesized thermodynamic and kinetic products **4b'** and **4b** represented in Figure 5.8 (the former being 3.5 kcal mol<sup>-1</sup> more stable than the latter). We denote the two paths leading to **4b'** and **4b** as **Path(T)** and **Path(K)**, respectively. Along **Path(K)** (kinetic pathway) the transition state **TS1(K)** (6.3 kcalmol<sup>-1</sup> above **M0**) corresponding to the rate-determining step of the process, describes the attack of C(3) on C $\gamma$  and leads to the formation of the indoleninic intermediate **M1(K)**, 13.6 kcalmol<sup>-1</sup> more stable than reactants.

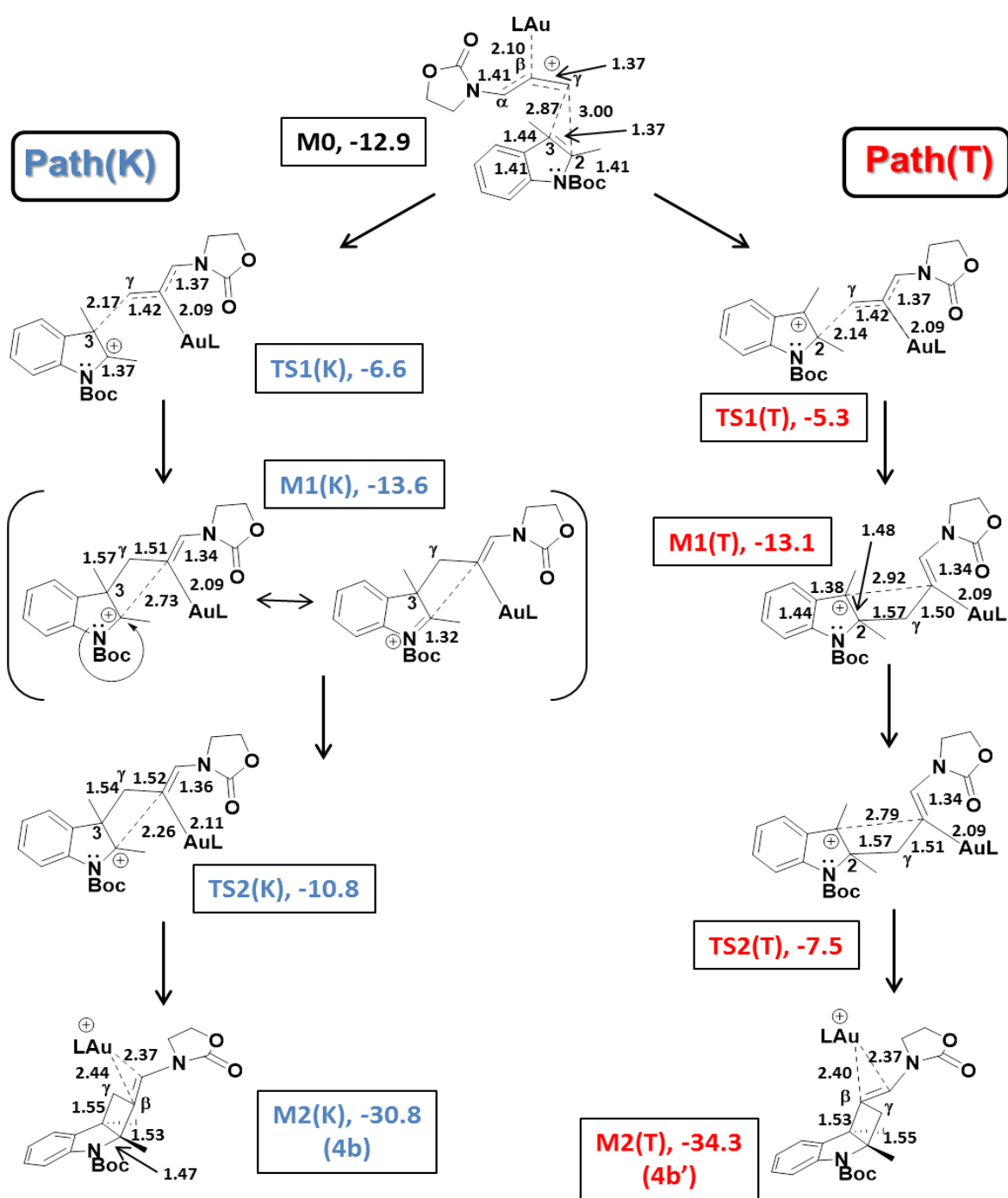


**Figure 5.12**

A schematic representation of the structures of the critical points located along **Path(K)** and **Path(T)**. Energies [kcalmol<sup>-1</sup>] are relative to reactants and include ZPE corrections. Bond lengths are given in Å.



The newly forming bond is 2.17 Å in TS1(K) and becomes 1.57 Å in M1(K) where the bond formation is completed. Here the distance C(2)-C $\beta$  (that identifies the second bond required to obtain the final product) is 2.73 Å. The  $\sigma$ -coordination of the gold atom as found in M0 is conserved in TS1(K) and M1(K). The variation of the N-C(2) bond length along the transformation M0→TS1(K)→M1(K) (1.41, 1.37, 1.32 Å, respectively) indicates that the formation of the new C(3)-C $\gamma$  bond is brought about by the indole nitrogen lone pair through an enaminic-type electronic shift (see M1(K) structure in Figures 5.12 and 5.13). A rather low activation barrier (2.8 kcalmol<sup>-1</sup>) must be overcome (transition state TS2(K)) to close the ring. The structure of TS2(K) is similar to that of the previous intermediate M1(K): the most important difference is the decrease of the C(2)-C $\beta$  distance (the incipient C-C bond), which becomes 2.26 Å. Importantly, the C $\alpha$ -C $\beta$  bond length remains approximately constant on passing from M1(K) to TS2(K) (1.34 and 1.36 Å, respectively). This suggests that the formation of the C(2)-C $\beta$  bond involves the [Au]-C $\beta$  heterolytic bond breakage (path B in Figure 5.8) rather than the enamidic fragment (N-C $\alpha$ -C $\beta$ ) electrons (path A in Figure 5.8). Thus, the ring-closing process does not affect the nature of the C $\alpha$ -C $\beta$  exocyclic double bond, which maintains its Z-configuration generated from the initial outer-sphere nucleophilic attack of the indole on the gold-activated allenamide.

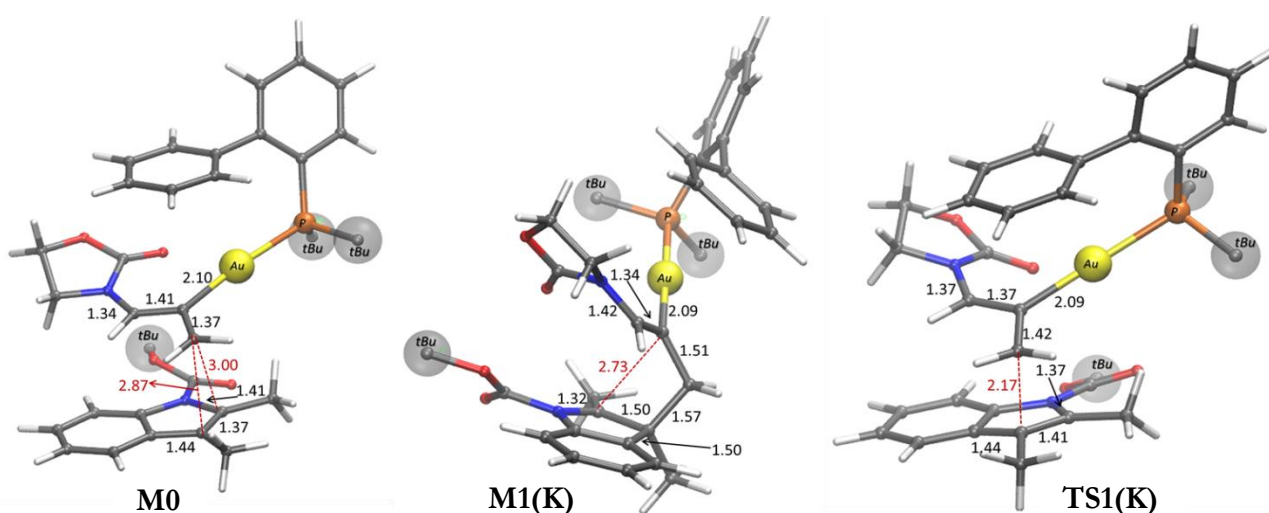


**Figure 5.13**

Detailed 3D representation of the structures of the critical points located along Path(K) and Path(T). Bond lengths are in Å.

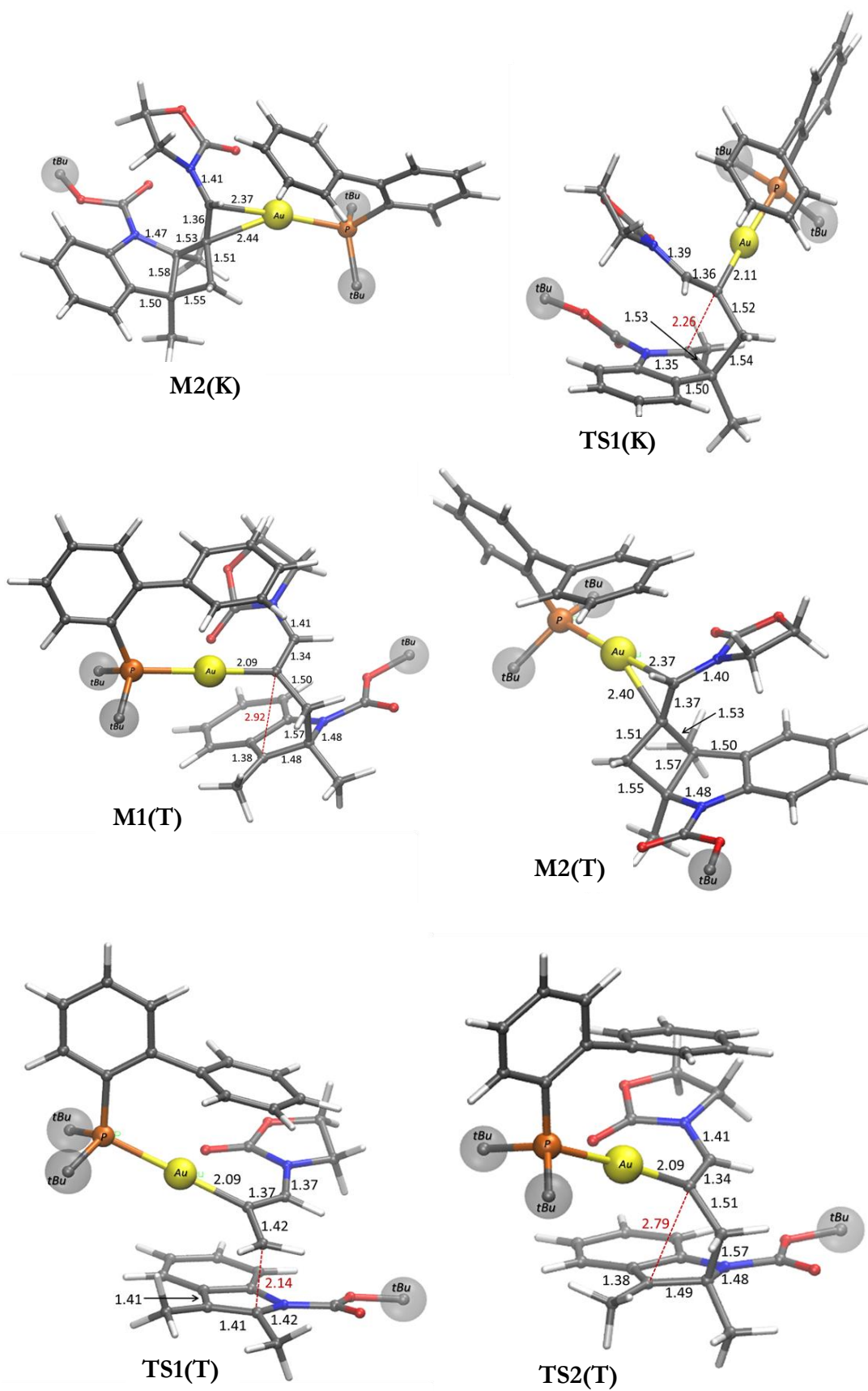


**Figure 5.13 (Continued)**

Detailed 3D representation of the structures of the critical points located along **Path(K)** and **Path(T)**. Bond lengths are in Å.

The final M2(K) product complex (the **4b** regioisomer) is 30.8 kcalmol<sup>-1</sup> more stable than reactants. In this complex the gold atom gets away from C $\beta$  (C $\beta$ -Au distance=2.44 Å) and moves much closer to C $\alpha$  (2.37 Å), thus reactivating a  $\eta^2$  coordination with the exocyclic double bond. Notably, the N-C2 distance (indole moiety) increases from 1.32 to 1.47 Å along the transformation M1(K)  $\rightarrow$  M2(K). This points out the disappearance of the formal charge on the immonium ion (characterizing the indoleninic intermediate M1(K)) and the repositioning of the lone-pair on the nitrogen atom in M2(K). Also, it demonstrates the importance of the protecting group *Boc* that assists the cycloaddition process by displacing electron density from N-C(2).

Along Path(T) (thermodynamic pathway) the first transition state TS1(T) describes the nucleophilic attack of C2 on C $\gamma$  (the new incipient C2-C $\gamma$  bond is 2.14 Å) and corresponds again to the rate determining step of the process. TS1(T) is 7.6 kcal mol<sup>-1</sup> higher than M0 (1.3 kcalmol<sup>-1</sup> above TS1(K)) and leads to M1(T), the indoleninic dearomatized intermediate, where the new C2-C $\gamma$  bond formation is completed (1.57 Å). The dearomatization process occurring in the passage M0  $\rightarrow$  M1(T) and involving the delocalization of the benzene  $\pi$ -electrons on indole is evidenced by the gradual increase in the indole moiety of the C2-C3 (from 1.37 to 1.48 Å) and C4-C5 (from 1.41 to 1.44 Å) distances and a simultaneous shortening of C3-C4 bond (from 1.44 to 1.38 Å). The transition state for the subsequent ring-closing step (transition state TS2(T), 3.3 kcal mol<sup>-1</sup> above TS2(K)) has an intrinsic activation energy of 6.1 kcal mol<sup>-1</sup>. The values of the computed bond lengths again indicate that the ring-closing process involves the C $\beta$ -[Au] electrons. The stability of the resulting product M2(T) (34.3 kcal mol<sup>-1</sup> below reactants) can be reasonably ascribed to the restoring of the aromaticity of the indolinic ring. As observed for M2(K) the coordination mode of the gold cation [Au(I)] again becomes  $\eta^2$ . It is reasonable to believe that the energetic gap among these two adducts is due to the steric hindrance between the Boc and the oxazolinonic groups. In M2(K) these two groups are rather close, but this steric hindrance is partially cancelled in the thermodynamic adduct M2(T) (compare M2(K) and M2(T) in 3D structures of Figure 5.13).

A comparison between the two reaction profiles clearly indicates that the two transition states for indole dearomatization (rate determining step in both cases) are close enough (the two activation barriers differ by 1.3 kcalmol<sup>-1</sup>) to explain why, when the reaction is performed at 0C°, small amounts of the thermodynamic product are observed and only through a rigid kinetic control (- 40 C°) it is possible to avoid the formation of the regioisomer **4b'**. The energy difference between TS1(K) and TS1(T) can be plausibly ascribed to the different indole dearomatization ability associated with the attack of C(3) and C(2) on the allenamidic carbon C $\gamma$ . The energy cost is higher

in the latter case where a loss of aromaticity of the entire system (also involving the benzene ring) occurs. Otherwise, when the attack proceeds from C(3) the loss of aromaticity is confined to the heterocyclic portion.

## 5.5 Computational details

All the reported DFT computations have been carried out using the software Gaussian 09 series.<sup>4</sup> The M063 functional proposed by Truhlar and Zhao was used in all computations. This functional has been demonstrated to provide a better estimate of  $\pi$ - $\pi$  interactions and reaction energetics<sup>4</sup> with respect to the mostpopular DFT Becke's three-parameter exchange functional B3LYP.<sup>24,25,97</sup> According to a locally dense basis set (LDBS) approach, the model system has been partitioned into different regions, which were assigned basis sets of different accuracy. All the atoms of the t-Bu groups of the gold ligand (JohnPhos) and of the BOC protecting group have been described by 3-21G\* basis set, while the rest of system (except the metal center)<sup>98</sup> has been described by more accurate basis set 6-31G\*. Gold atom has been described by the widely used effective core potential (ECP)-type (with pseudopotential) LANL2DZ<sup>99</sup> basis set. The geometries of the various critical points on the potential energy surface were fully optimized with the gradient method available in Gaussian 09. For each stationary point, harmonic vibrational frequencies computations have been performed to determine the nature of the various critical points. The solvent effects have been taken into account during optimization, using the Polarizable Continuum Model (PCM) approach.<sup>100</sup> A value of 8.93 was employed for the toluene dielectric constant  $\epsilon$ .

## 5.6 Gold-catalyzed [2+2]-cycloaddition between indoles and electron-rich allenes: enantioselective version

In the light of the results provided by our computational study for the reaction mechanism of the [2+2]-cycloaddition of indoles, an enantioselective version of the cycloaddition reactions is further documented as a powerful tool for a direct access to stereochemically defined dearomatized indolyl-based scaffolds.<sup>148</sup> As a matter of fact, several metal- and metal-free stereoselective methodologies have been developed with the site-selective functionalization of the C(2)- and C(3)-positions of the indole core. Interestingly, despite the enormous interest towards the development of efficient catalytic methodologies to polycyclic fused indolines, enantioselective protocols to access

C(2)/(3)-cyclobutylindoline compounds were still unreported until our recent contribution on the stereoselective gold catalyzed formal [2+2]-cycloaddition reaction. In particular, the use of in situ formed (*R*)-DTBM-segphos(AuOTf)<sub>2</sub> (2.5–5.0 mol%) enabled the enantioselective preparation of tricyclic indoline scaffolds in straightforward manner by condensing a range of *N*-Boc-indoles and **2** (DCM, -60 °C). Excellent levels of regio-, diastereo- (d.r.>20:1) and enantioselection (ee up to 98%) were obtained for differently substituted indoles with allenamide **2** Figure 5.14. Moreover, the efficiency of the stereoselective gold-catalyzed intermolecular [2+2]-cycloaddition between aryloxyallenes and *N*-Boc indoles was investigated. Among the screened chiral ligands, again (*R*)-DTBM-segphos furnished the highest levels of chemical and optical yields (CH<sub>2</sub>Cl<sub>2</sub>, 0°C, cat.= 2.5 mol%) in the model reaction (3+1 Figure 5.14) in combination with AgNTf<sub>2</sub> as the gold-activator.<sup>149</sup> Aryloxyallenes **3** were generally found less reactive than that allenamide **2** in the enantioselective variant and higher reaction temperatures (i.e., 0°C/-20°C) were required in order to access synthetically acceptable reaction kinetics.

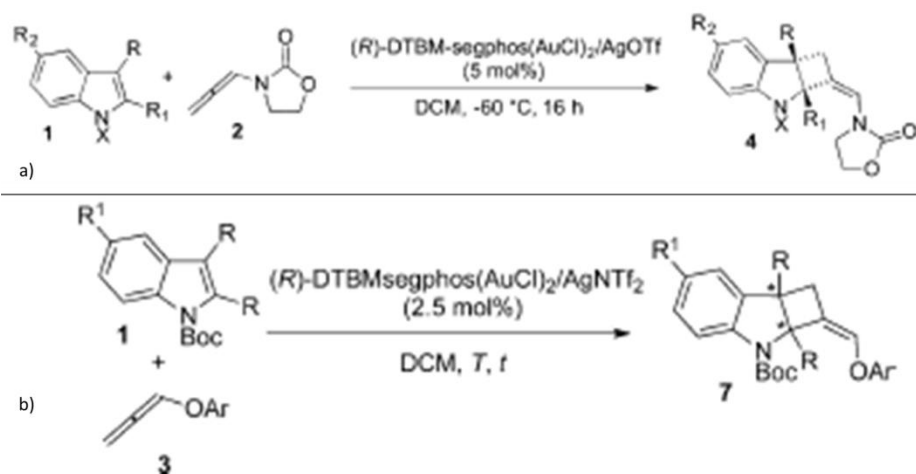


**Figure 5.14**

Gold-catalyzed enantioselective cycloaddition between indoles and allenamide **2** (a) aryloxyallenes **3** (b)

## 5.7 Conclusions

A comprehensive investigation of the gold-catalyzed dearomative cycloaddition reaction of indoles with electron-rich allenes is documented by means of experimental and computational tools. Commercially available ([JohnPhosAu(NCMe)]SbF<sub>6</sub>) showed competence in performing the chemo-, regio- and diastereoselective formal [2+2]-cycloaddition between a wide range of

substrates under mild conditions. A portfolio of densely functionalized C(2),C(3)-fused cyclobutylindolines (**4/7**) is accessible in a straightforward manner. Additionally, the use of chiral C(2)-symmetric DTBM-segphos enabled the control of the stereochemical profile of the dearomatization reaction in a convenient manner (ee up to 95% with aryloxyallenes and 99% with allenamide **2**). Our DFT computations have clearly demonstrated that the mechanism for the formal gold-catalyzed cycloaddition among allenamide **2** and N-Boc-indole **1b** proceeds through a polar non-concerted mechanism involving two kinetic steps. Two different reaction pathways (Path(K) and Path(T), both consisting of two steps) originate from an initial encounter complex and provide the two regioisomers experimentally observed, that is, **4b** obtained under kinetic conditions and **4b'** obtained under thermodynamic conditions. In both cases the first step is rate determining and corresponds to a dearomatization process. The ring closure occurring in the second step involves the heterolytic rupture of the  $\sigma$  [Au]-C $\beta$  bond and not the electrons of the exocyclic C $\alpha$ =C $\beta$  double bond, which maintains its original Z-configuration in agreement with the experiments. The energy cost for the dearomatization process is higher along the thermodynamic pathway (attack from the C(2)-indole position) where the loss of aromaticity involves the entire system (indole and benzene ring). This cost decreases when the attack proceeds from C(3)- and the dearomatization is confined to the indole moiety. The energy difference between the two dearomatization transition states is not very large (about 1.3 kcalmol<sup>-1</sup>). This explains why at 0C° small amounts of the thermodynamic product **4b'** are observed and only under severe kinetic conditions (-40C°) it is possible to avoid the formation of this regioisomer.

## 6. Computational Investigation on Metal-Free Enantioselective Electrophilic Activation of Allenamides

### 6.1 Organocatalysis

In the wide field of catalysis, in these last decades, organocatalysis has played a leading role. Today organocatalysis is one of the most popular research topics in advanced organic chemistry. Until a few decades ago asymmetric catalysis involved metal-based chiral catalysts almost exclusively, and offered a wide range of oxidations, reductions,  $\sigma$ -bond insertions,  $\pi$ -bond activations and Lewis-acid-catalyzed reactions. However, some organometallic systems can be expensive, toxic and/or sensitive to air and moisture. Therefore organocatalysis represents a novel synthetic philosophy and mostly an alternative to the prevalent transition metal catalysis.

An “organocatalyst” is a low molecular weight organic molecule, which, in substoichiometric amounts, catalyzes a chemical reaction. Organocatalysis has several advantages not only for what concerns its synthetic value but also for economic and environmental reasons. As a matter of fact, the major benefit in organocatalysis is the absence of metal. An organocatalyst can be a Lewis base, Lewis acid, Brønsted base, and Brønsted acid. In the specific context of this work, we have employed an asymmetric Brønsted acid catalysis, in particular chiral phosphoric Brønsted acid-type catalysts.

#### 6.1.1 Brønsted acid catalysts

Asymmetric Brønsted acid catalysis is one of the most successful subfields of organocatalysis.<sup>150</sup> These organocatalysts are capable of activating the widest range of functional groups. Compared to Lewis acids, Brønsted acids are generally easier to handle and are usually stable to oxygen and water.

In 2004 independent reports by Akiyama<sup>151</sup> and coworkers, and Uraguchi-Terada<sup>152</sup> represented a new turning point in organocatalysis, by describing relatively strong BINOL-derived phosphoric acids as efficient catalysts for carbon-carbon bond forming reactions. During the last five years the development of novel BINOL phosphate-catalyzed reactions has been continuously studied and enabled great progress in recent years.<sup>153</sup>

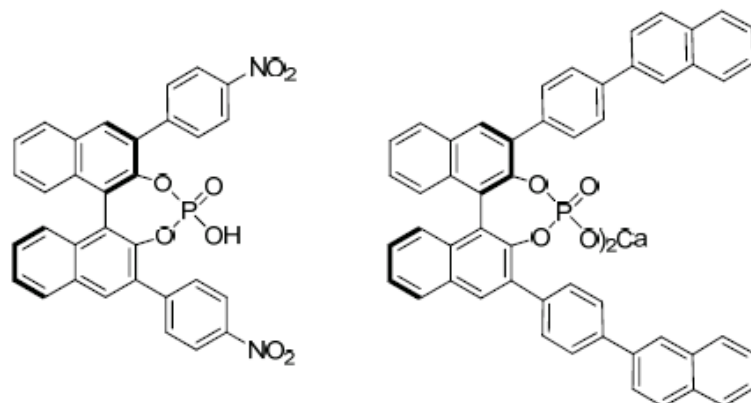


**Figure 6.1**  
Akiyama and Uraguchi-Terada  
Phosphoric acid catalysts.

Several research groups reported the application of BINOL phosphates in numerous highly enantioselective transformations.<sup>153</sup> In most cases, the key aspect of catalysis is the bifunctional character (Brønsted acid/Lewis base) of the phosphoric acid moiety.

## 6.2 Electrophilic Activation of Allenamides

The use of metal-free non-covalent interactions for the direct activation of carbon-based unsaturated  $\pi$ -systems has been rarely treated so far. As a matter of fact, the attention has been mainly focused on asymmetric organocatalytic reactions via hydrogen bonding activation and Brønsted acid activation of carbonyl compounds and imines. Recently, Toste and co-workers<sup>154</sup> reported the efficiency of chiral dithiophosphoric acids as Brønsted acids in promoting the enantioselective intramolecular nucleophilic addition to 1,2-/1,3-dienes. Moreover, Terada and co-workers<sup>155</sup> documented the suitability of BINOL-based phosphoric acids in delivering the enantioselective addition of azalactones to 3-vinylindoles.

In this context, our cooperating research group, lately presented a chiral BINOL phosphoric acid catalyzed (1–10 mol%) dearomatization of indoles through electrophilic activation of allenamides (ee up to 94%).<sup>156</sup> To address this stereochemical manipulations of C-C  $\pi$ -systems by metal-free activation, bifunctional allenamides as valuable scaffolds to access chemical diversity was employed.<sup>157</sup> We have already shown, in our gold(I)-catalyzed studies, how these “electron-rich”  $\pi$ -systems are very important in organic synthesis in metal-assisted electrophilic activation. In particular, the coordination of a positively charged transition-metal chiral complex ( $L^*MX$ ) to the allenamide delivers an intermediate **a** that can undergo an  $\alpha$  or  $\gamma$  nucleophilic condensation with several nucleophilic substrates (Figure 6.2a). An important example is the enantioselective



cycloaddition reactions involving allenamides with the active participation of chiral gold complexes as promoters.<sup>158</sup> A conceptually analogous activation mode occurs when the metal is replaced by a proton in a chiral Brønsted acid organocatalysis. The chiral Brønsted acid can activate an achiral substrate by protonating it. A conjugate base remains to provide the chiral environment for the subsequent bond-forming step that can yield an optically active product. In most cases, the proton is actually ‘shared’ to a varying extent between the two species through hydrogen-bonding interactions. This new activation model represents a challenge for catalyst design. The principles of tuning the ligand chiral environment of metal centers can no longer be applied; instead, it is the interaction between the conjugate base and conjugate acid that is key to achieving high levels of enantioselectivity in the product.<sup>153k</sup>

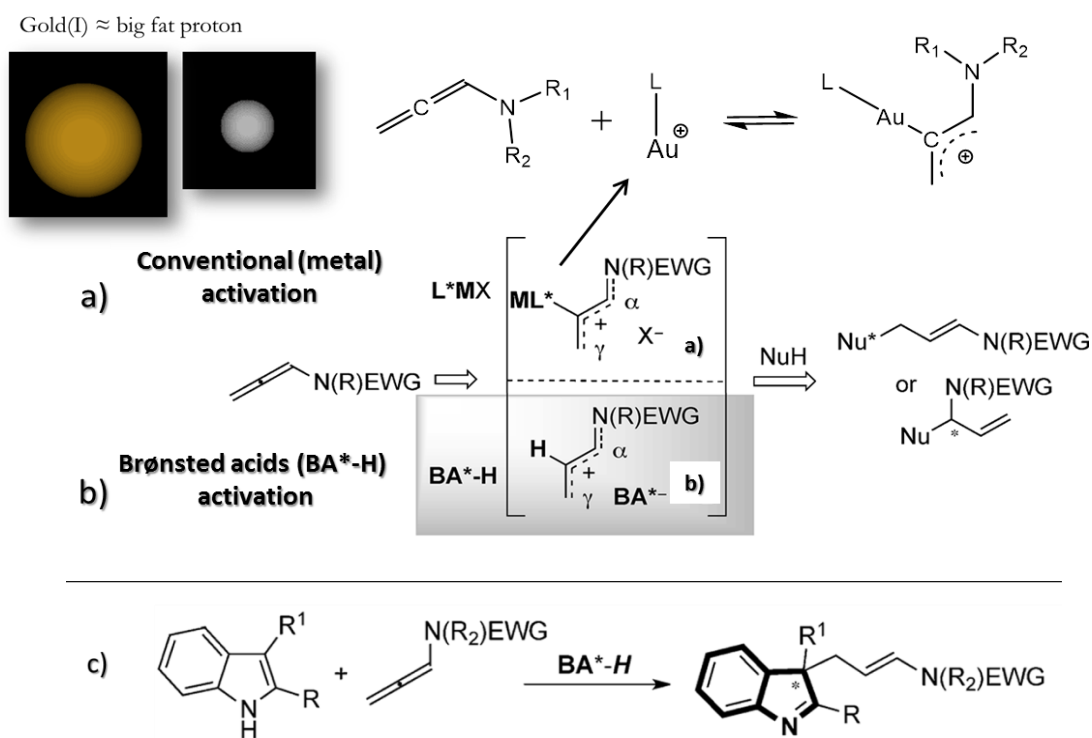


**Figure 6.2**

a) Conventional electrophilic activation of allenamide metal-dependent b) “unconventional” (metal-free) electrophilic activation of allenamides in asymmetric synthesis. c) Inter-molecular enantioselective dearomatization of N(H)-free indoles Brønsted acid catalysed, general reaction.

In this direction, chiral Brønsted acids can be used as effective promoting agents for the stereochemical electrophilic activation of allenamides exploiting the isolobal analogy often interconnecting [Au(I)] species and the proton.<sup>159</sup> As described above, the interaction between a

chiral anion and the substrates (activated  $\alpha,\beta$ -unsaturated iminium species **BA**<sup>\*</sup> and a nucleophile) (Figure 6.2b) can result in a stereochemically-controlled process.<sup>156</sup>

### 6.3 Experimental results

To verify the feasibility of the previous hypothesis, the C3-site-selective intermolecular enantioselective dearomatization of N(H)-free indoles (Figure 6.2c) is considered as the benchmark process.<sup>160</sup> Recently, our cooperating research group reported a work on the key role of the gold counterion in controlling both reactivity and regioselectivity in the condensation of indoles with allenamides that could support the present enantioselective metal-free variant.<sup>161</sup>

The basic transformation, selected as the model reaction, is the condensation of 2,3-dimethylindole (**1a**) and readily available N-phenyl-N-sulfonyllallenamide (**2a**) (see scheme in figure 6.3).

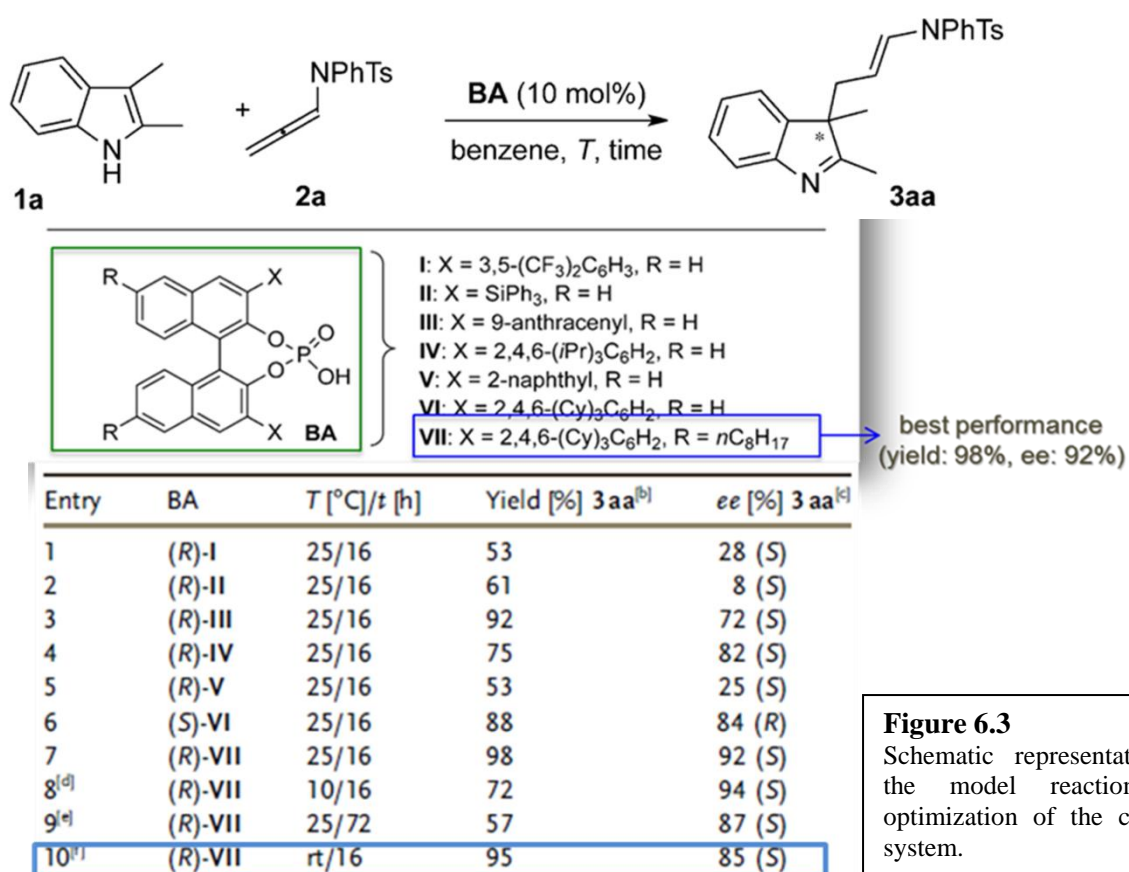


**Figure 6.3**  
Schematic representation of the model reaction and optimization of the catalytic system.

### 6.3.1 Optimization of the catalyst and reaction conditions

The model substrates were initially subjected to various reaction conditions. A range of chiral BINOL-based phosphate catalysts (I–VII, 10 mol%) was screened at room temperature in anhydrous benzene as the reaction media in order to select the best performing catalyst.

The resulting screening reported in Figure 6.3 of differently substituted chiral BINOL phosphoric acids suggests important conclusions about the impact of the BA\* structure on the course of the stereochemical reaction. The ligand (S)-C<sub>8</sub>-TCyP (VII) performed exceptionally in the model reaction, providing the indolenine **3aa** in quantitative yield and 92% ee of (*S*) isomer (entry 10).<sup>162</sup>

### 6.3.2 Application field of the reaction

The efficiency of the BINOL-based phosphoric acid C<sub>8</sub>-TCyP (VII) (Figure 6.3) in the regio- and stereoselective dearomatization of indoles offered the opportunity to extend the methodology to a widely range of enantiomerically enriched 3,3-disubstituted indolines.<sup>163</sup> The application field of the catalytic methodology was investigated testing a range of 2,3-disubstituted indoles (**1b–p**) to dearomatization under the optimized catalytic conditions (VII=1–10 mol%, benzene, 16/72 h, rt). The chemical and stereochemical outcomes are summarized in figure 6.4.

All the products obtained show a high degrees of stereoselectivity. Indoles carrying cyclic C(2,3)-fused substituents (**1b–d**) delivered the desired indolenines **3ba–3da** in moderate to good yields and excellent enantiomeric excess up to 93%. Saturated aliphatic as well as benzylic organic residues at the C3-position of the indole (**1e–h**) provided high enantioselectivity (ee 87–93%). For C2-Et- and C2-nPr-substituted indoles (**1n–p**) afforded the corresponding dearomatized compounds in acceptable yields (69–77%) and ee (87–92%). Therefore several substituents at the indolyl substructure are well tolerated and the validity of the method was verified. A range of differently C5-substituted indoles (**1i–m**) was treated with allenamide **2a** in the presence of **VII**. Synthetically acceptable levels of enantioselectivity were achieved with ee up to 92% in the case of 5-Fand 5-MeO indole derivatives.

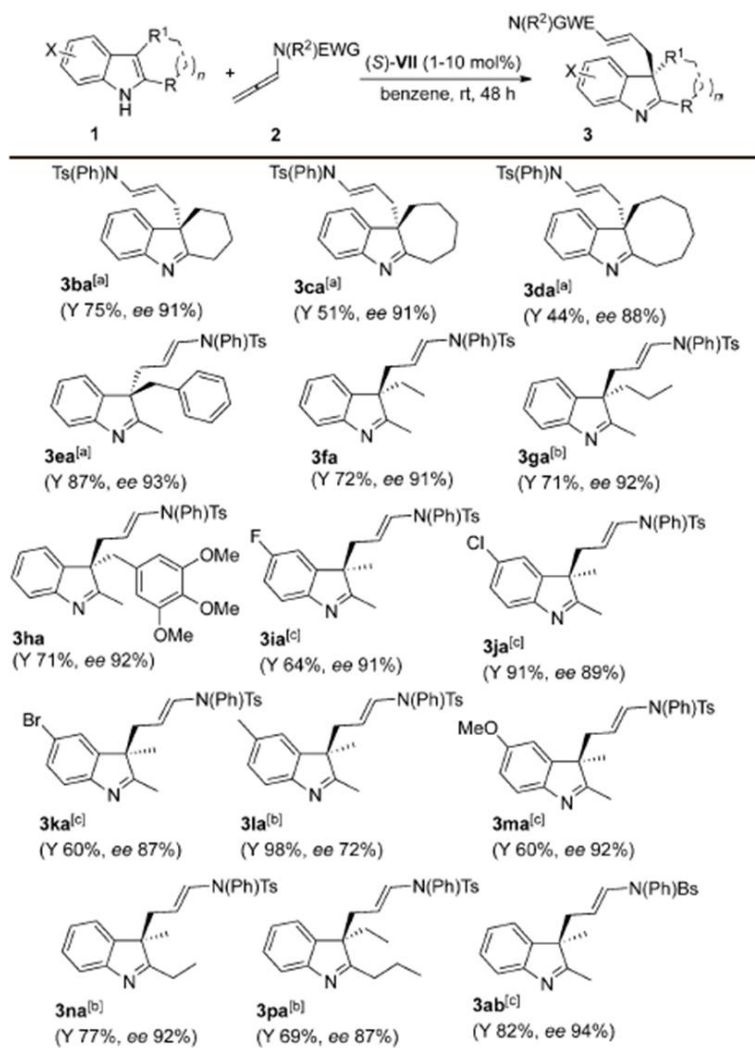


**Figure 6.4**

Representative collection of indolyl scaffolds available through the enantioselective dearomatization of indole procedure.

[a] (R)-VII was used. [b] Catalyst loading 5 mol%, time 72 h. [c] Catalyst loading 1 mol%, time 72 h. Ts = p-toluenesulfonyl, Bs = benzenesulfonyl.

## 6.4 DFT investigation of Metal-Free Enantioselective Electrophilic Activation of Allenamides

### 6.4.1 Preliminary mechanistic insights

The regiochemical preference of the indole nucleophilic attack is by the C3 with respect to the N1 analogues on the  $\gamma$  position of the allenamide (see reaction model in Figure 6.3). The first mechanistic issue concerns what happens after the selective protonation of the allenamide **2** (Figure 6.5a). Two mechanistic schemes are possible. In the former (Figure 6.5a), the indole attacks the  $\gamma$ -position of the protonated  $\alpha,\beta$ -unsaturated iminium intermediate and in a concerted fashion transfers a proton from the nitrogen atom to the phosphoryl oxygen atom restoring the catalyst.

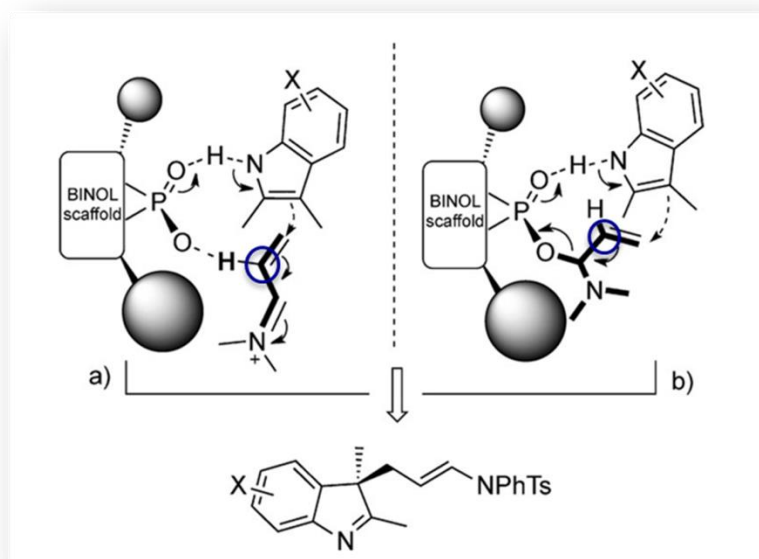


**Figure 6.5**

Possible activation modes: noncovalent (a), and covalent (b) BA–allenamide interactions.

The enantio-discriminating step of the process could be “regulated” by hydrogen bond interaction of the basic site on the phosphoryl oxygen atom controlling the approaching trajectory of the heterocycle (acid/base dual function catalysis). The latter possible pathway (Figure 6.5b) involves a covalent interaction between the catalyst and the  $\alpha$ -carbon of allenamide that takes place before the indole nucleophilic attack. Subsequently, the indole attacks the activated allenamide with a  $\text{S}_{\text{N}}2'$ -type mechanism<sup>154,164</sup> and, at the same time, a proton is being passed to the catalyst, which regenerates. Both hypothetical approaching trajectories do not affect the overall stereochemistry obtained in the final product. Further aspects of the catalytic mechanism are still obscure: 1) how is the stereochemical control carried out?; 2) what is the specific role of chiral Brønsted acids?

#### 6.4.2 Computational study of the reaction

With the purpose of elucidating the above-mentioned mechanistic issues and the origin of the enantioselectivity, we carried out a detailed DFT computational investigation on this enantioselective dearomatization process. In particular, we determined two reaction mechanisms, which lead to the two possible enantiomeric products. The model-system used in the calculations consists of dimethyl-indole (**1a**) and N-phenyl-N-sulfonyllallenamide **2a** together with the commercial available chiral catalyst (S)-C<sub>8</sub>-TCyP (figure 6.6) in which the two alkyl chains C<sub>8</sub>H<sub>17</sub> on BINOL structure were replaced by methyl groups.

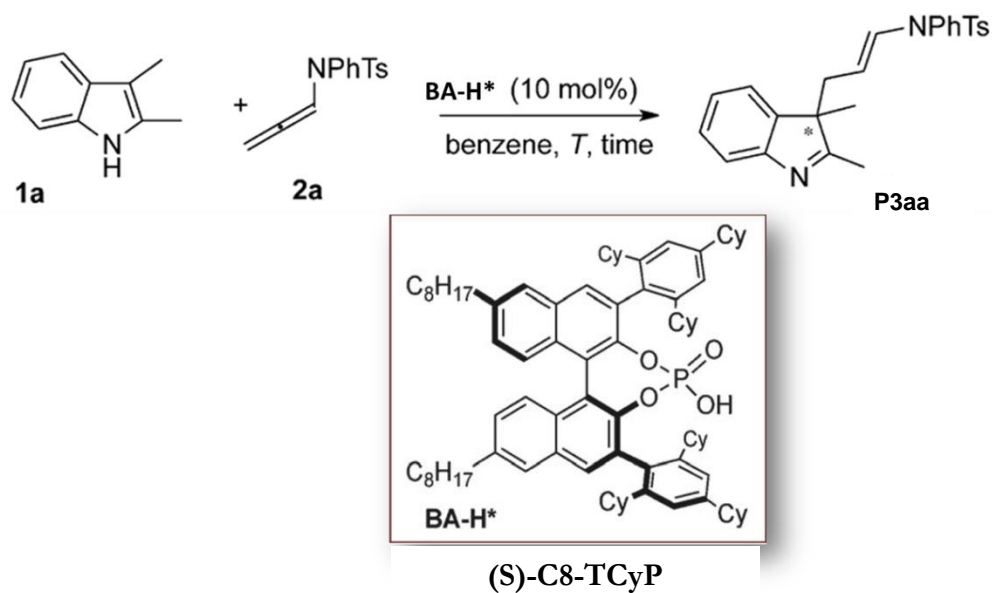


**Figure 6.6**  
Model reaction for the Metal-Free Enantioselective Electrophilic Activation of Allenamides

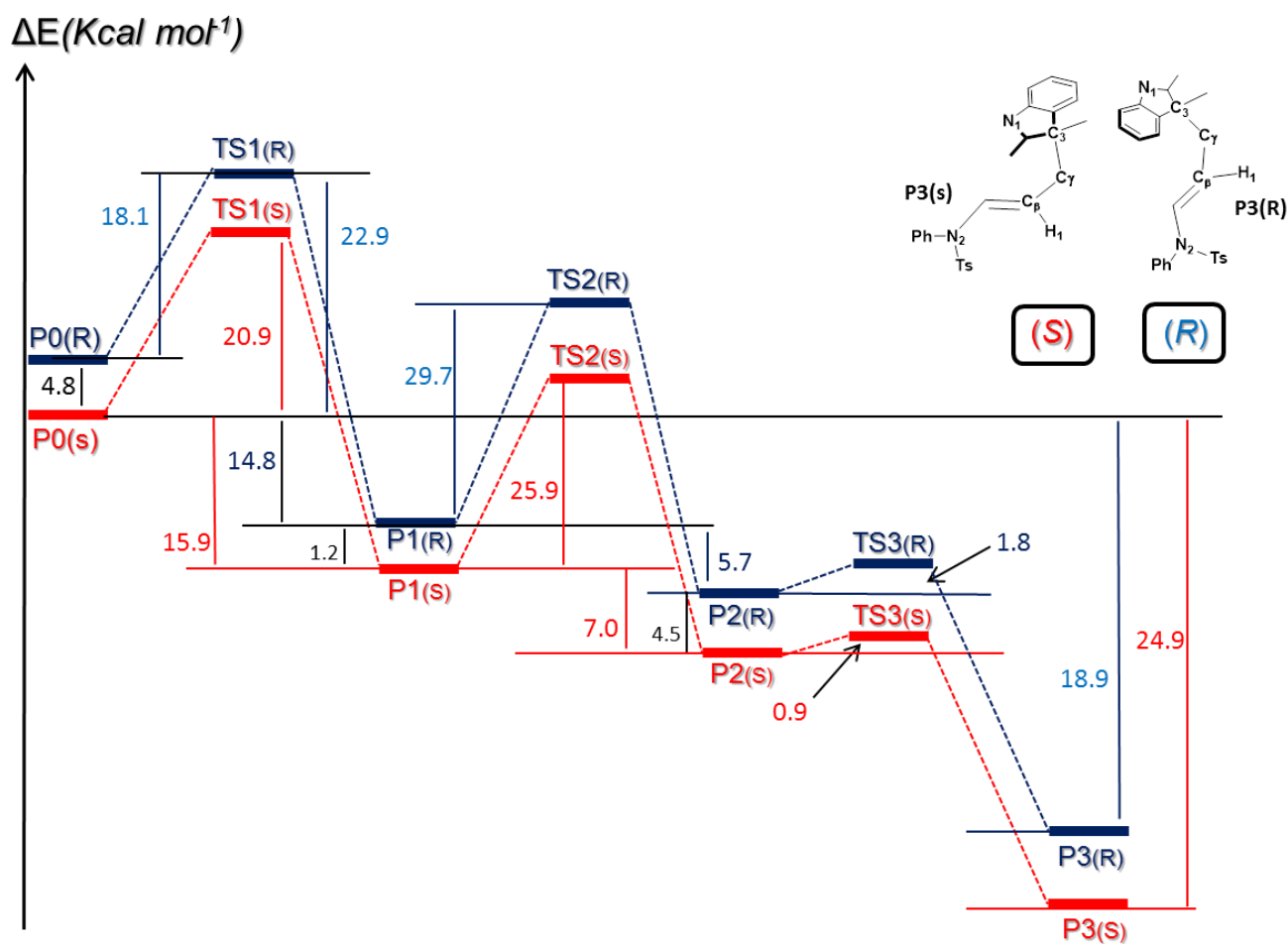


**Figure 6.7**  
The two computed reaction profiles for the **(R)**(blue) and **(S)**(red) enantiomers. The total energy values are in kcal mol<sup>-1</sup>

The reaction energy profile is reported in Figure 6.7. The two reaction channels (red and blue) correspond to the stereoselective profiles leading to the **P3aa(S)** and **P3aa(R)** enantiomeric products. In both cases, our computations revealed a multistep mechanism for the transformation of **2a**→**P3aa(S)/(R)**.

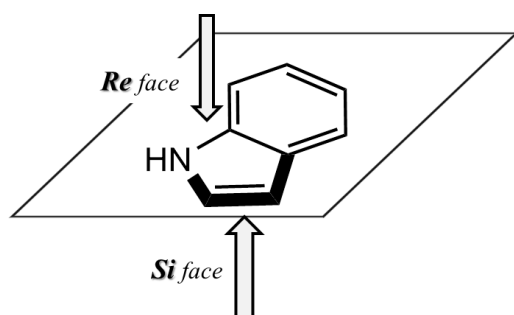


**Figure 6.8**  
*Re* and *Si* Faces of the indolic species.

The approach of the reacting species initially leads to the formation of the first catalyst–substrates adduct **P0**. On the basis of how the reactant approaches the chiral catalyst a particular arrangement characterizes the two rigid isomers **P0(S)** and **P0(R)**, which represent the starting complexes for the two reaction channels leading to the **P3aa(S)** and **P3aa(R)** isomers, respectively.

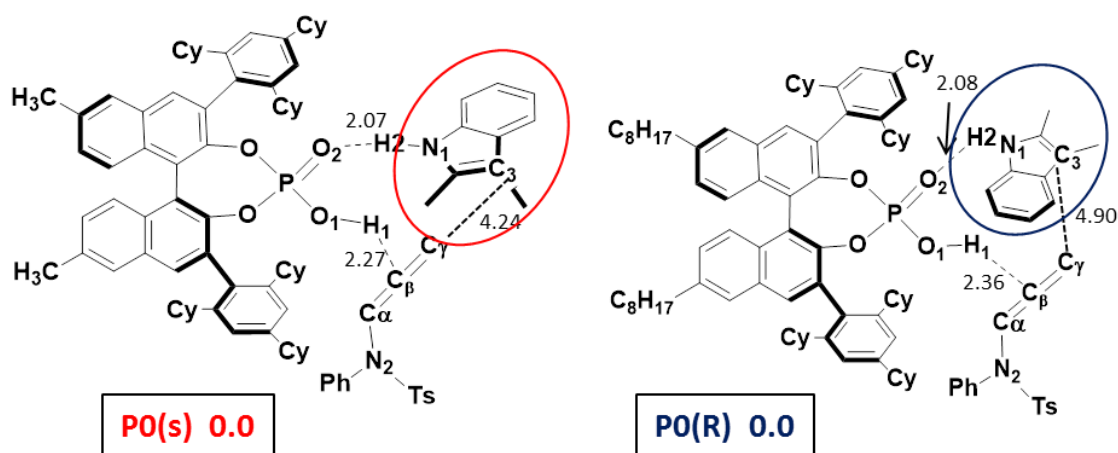


**Figure 6.9**  
Schematic representations of the **P0(S)** starting complex of the dearomatization process. Bond lengths are given in Å.

A schematic representation of the starting complexes **P0(S)** and **P0(R)** is given in figure 6.9. In **P0(S)**, which has been found to be 4.8 kcal·mol<sup>-1</sup> more stable than **P0(R)**, the *Re-face* (Figure 6.8) of the indolic substrate is sterically shielded by the chiral catalyst while leaving free the *Si-face* available for approaching the underlying allenamide. It is interesting to note that the two substrate molecules interact with the catalyst, as if they were inside an enzyme active site. As a matter of fact,

they enter into a pocket featuring the phosphate at end and completely surrounded by the cyclohexyl groups in such a way that the initial above-described arrangement is retained throughout the entire reaction profile. In **P0(R)**, the substrate molecules adopt the opposite arrangement: the indole *Re-face* is facing the activated allenamide on which the nucleophilic attack will be performed to eventually yield the **P3aa(R)** enantiomer.

As mentioned above, the key point for the transfer of chirality is represented by the formation of covalent and non-bonding interactions between the chiral catalyst and the substrates in the reaction environment. In this context, this enzyme-like global arrangement that forces the reactants to maintain rigid relative positions is certainly crucial for the high stereoselectivity of this chiral BINOL-based phosphate catalysts. In particular, the hydrogen bond O2-H2 (2.07 Å in **P0(S)** and 2.08 Å in **P0(R)**) and the strong interaction between H1 and the electron-rich allene system (C $\beta$ -H1 2.27Å in **P0(S)** and 2.36Å in **P0(R)**, Figure 6.9) in the starting complexes keep close catalyst and substrate by providing a proximity effect similar to that of an enzyme.

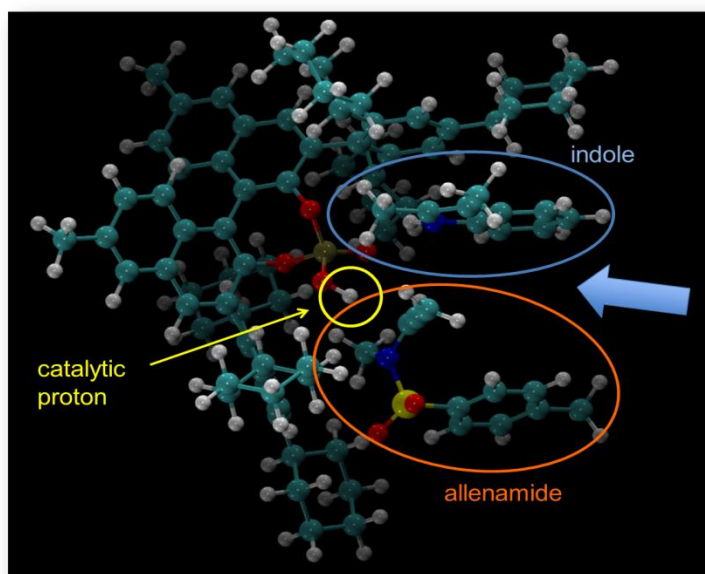


**Figure 6.10**

Detailed three-dimensional representation of **P0(S)** the catalytic center hosts substrates as if they were entering the active site of an enzyme

The first step of the reaction is the activation of the allenamide through the transfer of the phosphate acidic catalytic proton and the asynchronous yet concerted formation of the C $\alpha$ -O1 bond. The structures of the critical points of this step along both the (*S*) and (*R*) profiles are schematically represented in figure 6.11. The proton-transfer takes place beyond the transition states **TS1(R)/(S)**



corresponding to the rate-determining step of the process for both (*S*) and (*R*) pathways. Along the (*S*) path, an energy barrier of 22.9 kcal·mol<sup>-1</sup> (**TS1(*S*)**), must be overcome to obtain a quite stable covalent intermediate **P1(*S*)** (-15.9 kcal·mol<sup>-1</sup>) characterized by a covalent bond C $\alpha$ -O1 (1.46 Å). As the proton is being transferred from O1 to the C $\beta$  of the allenamide, a positive charge starts appearing on the adjacent C $\alpha$  (the net computed ESP charges on C $\alpha$  goes from -0.04 in **P0(*S*)** to +0.02 in **TS1(*S*)**). This electrophilic carbon atom is attacked by the negative charge, which is simultaneously developing on the phosphate O1 (net computed ESP charges on O1 goes from -0.20 in **P0(*S*)** to -0.72 in **TS1(*S*)**) a distance O1-C $\alpha$  of 3.12 Å in **TS1(*S*)** was found. The result is the formation of a covalent intermediate (**P1(*S*)**), in which the allenamide has been protonated and thus activated and linked to the catalyst through a covalent bond (O1-C = 1.46 Å). An analogous mechanism was found along the (*R*) path. However, **TS1(*R*)** lies 2 kcal·mol<sup>-1</sup> above **TS1(*S*)** (22.9 kcal·mol<sup>-1</sup>) and **P1(*R*)** is slightly less stable than **P1(*S*)**.

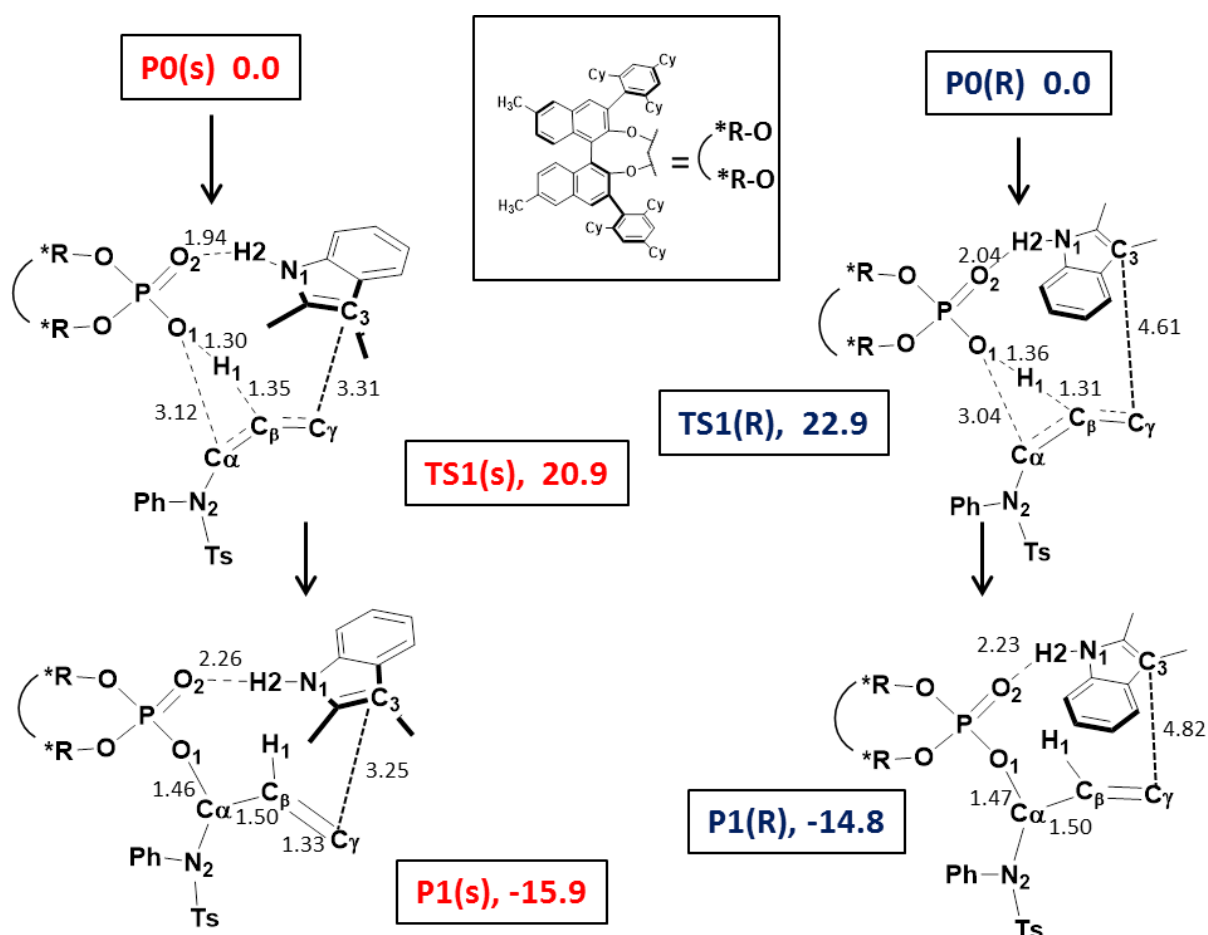


**Figure 6.11**

Schematic representations of the intermediates **P1(*s*)** and **P1(*R*)** and transition states **TS1(*s*)** and **TS1(*R*)**. Bond lengths are given in Å.

The covalent intermediates **P1(S)/(R)**, found in this first step, allow us to discard the hypothetical Michael-type addition supported in the 6.4.1 section (Figure 6.5a). Our computations have rather confirmed a  $S_N2'$ -type mechanism (hypothesized in 6.4.1 section Figure 6.5b) described in **P1(S)/(R)**→**TS2(S)/(R)**→**P2(S)/(R)** step for both enantiomeric channels (Figure 6.12), in which the formation of the C $\gamma$ -C3 bond with the consequent dearomatization and creation of the new stereogenic center on C3 occurs (Figure 6.12). It is important to note that this step determines the stereochemistry of the final product. As the nucleophilic site C3 on the indolic species attacks the electrophilic C $\gamma$  carbon atom, the double bond formally passes from C $\gamma$ -C $\beta$  to C $\beta$ -C $\alpha$  and consequently the C $\alpha$ -O1 bond breaks. In this step, the indole loses its aromaticity, but the system lowers its energy as a new, strong C-C bond is being formed.

The values of the computed intrinsic activation barriers, which are 29.7 and 25.9 kcal·mol<sup>-1</sup> for **TS2(R)** and **TS2(S)** respectively, once again indicates that the (*S*) path is favored. This difference could be ascribed to the different arrangement the indole group which results in a strongest hydrogen bond network in **TS2(S)** (O2-H2 = 1.78 Å) than in **TS2(R)** (O2-H2 = 2.95 Å and O2-H2 = 2.96 Å). The newly forming bond C $\gamma$ -C3 is 2.42 Å in **TS2(S)** and becomes 1.56 Å in **P2(S)** where the bond is completely formed. Very similar values are found in the (*R*) path where C $\gamma$ -C3 passes from 2.37 Å in **TS2(R)** to 1.56 Å in **P2(R)**. During this step, the final proton-transfer, in which H2 moves from N1 to O2 leading to the final products and catalyst regeneration has not occurred yet. This means that a positive charge (counterbalanced by the negative catalyst) is delocalized on the indole system, which is thus found to be able to accommodate it very efficiently. Two similar transition states associated to very low activation barriers (0.9 kcal·mol<sup>-1</sup> in the **TS3(S)** and 1.8 kcal·mol<sup>-1</sup> in the **TS3(R)**) connect **P2(S)** and **P2(R)** with the corresponding final enantiomeric products **P3aa(S)** and **P3aa(R)**. The stability of the final product **P3aa(S)** (24.9 kcal mol<sup>-1</sup> below the starting complex) is once again favored over its (*R*) isomer **P3aa(R)** (18.9 kcal mol<sup>-1</sup> below the starting complex). It is reasonable to believe that the energetic gap between these two adducts is once again due to the best fit of (*S*) product in the chiral catalyst pocket.

Comparison of the two reaction profiles clearly indicates the profile (*S*) as favored during the whole course of the reaction (Figure 6.9) according with the experimental result which show a 92% ee of (*S*) isomer (Figure 6.3, entry 10) for the our model reaction. This is probably due to the rigid arrangement of the substrate molecules in the chiral catalyst pocket that results in a stronger hydrogen bonding network and non-bonding interactions associated to the geometric disposition associated to the (*S*) pathway.

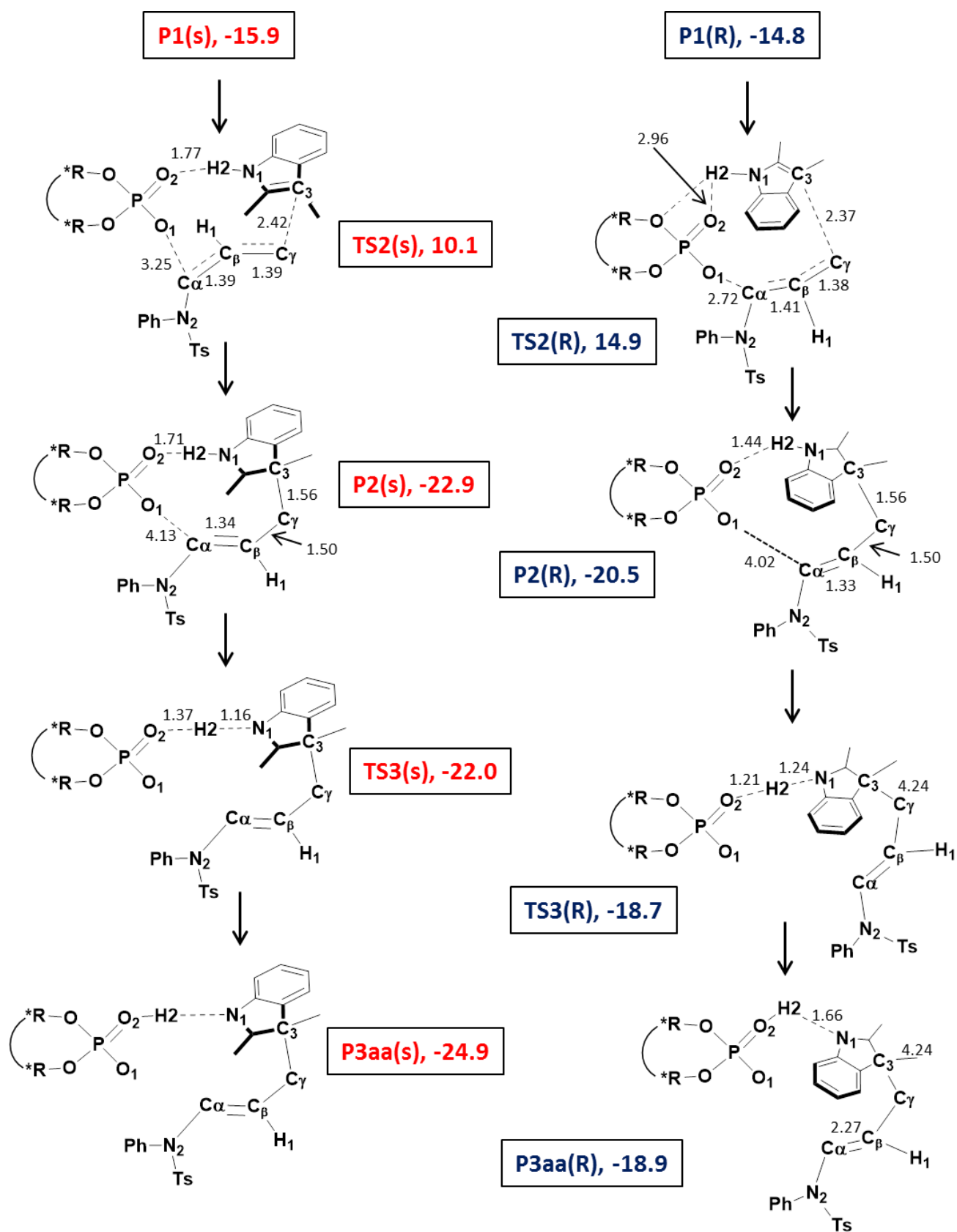


**Figure 6.12**

Schematic representations of the intermediates P2(s) and P2(R), transition states TS2(s), TS2(R), TS3(s), TS3(R) and the two stereoisomeric products P3aa(s) and P3aa(R) related to dearomatization step and final proton transfer. Bond lengths are given in Å. Energy in kcal mol<sup>-1</sup>

The main conformational difference between the two reaction channels observed in the course of reaction, is represented by the position of the indole ring plane, which is related to the enantiotopic plane that performs the nucleophilic attack onto the electrophilic activated allenamide: *Si* face or *Re* face that correspond to the (*S*) or (*R*) pathway respectively. The opposite face interacts with the C-H protons of the cyclohexyl of the chiral catalyst in both (*S*) and (*R*) path. However, in the case of path (*S*) these interactions are stronger, as the cyclohexyl is closer to the indole phenyl moiety. This is especially interesting in the stereochemically determining step (**TS2**(*R*)/(*S*)) where the difference between the indole and C-H of the cyclohexyl overlying interactions are substantial (see distances in Figure 6.13) contributing to lowering the **TS2**(*S*) energy (3.8 kcal mol<sup>-1</sup> below **TS2**(*R*)). This conformation is retained during the whole course of the reaction and contributes to stabilize the intermediates and transition state on the (*S*) pathway.

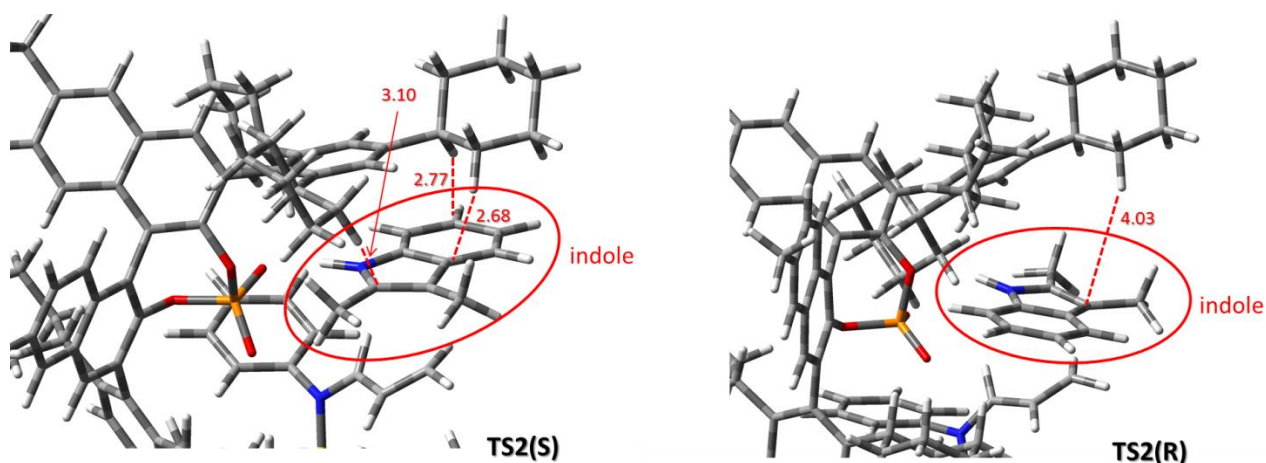


**Figure 6.13**

Representations of the interactions between the C-H of the cyclohexyl ligand moiety of the catalyst and the shielded face of the indole in **TS2**(*S*) and **TS2**(*R*). Distances are in Å.

## 6.5 Computational details

The DFT computations were carried out using the software Gaussian 09 series.<sup>4</sup> The M06-2X functional proposed by Truhlar and Zhao was used in all computations. According to a locally dense basis set (LDBS) approach, the model system has been partitioned into different regions, which were assigned basis sets of different accuracy. The molecules directly involved in the reaction (indole **1a** and allenamide **2a**) and the atoms of the central substructure of the BA\*-H

catalyst (phosphate and BINOL moiety Figure 6.14) were treated with 6-31G\* basis set.<sup>25</sup> The other region includes all remaining atoms which were described by the 3-21G\* basis set.<sup>25</sup>

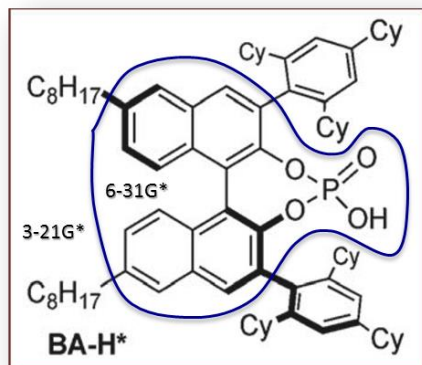


**Figure 6.14**

Partitioning scheme of the BA\*-H catalyst regions described with different accuracy basis sets.

The geometries of the various critical points on the potential energy surface were fully optimized with the gradient method available in Gaussian 09. For each stationary point, harmonic vibrational frequencies computations have been performed to determine the nature of the various critical points.

## 6.6 Conclusions

We have been carried out a detailed computational investigation on the organocatalytic enantioselective dearomatization of indoles by means of a metal-free electrophilic activation of allenamides. In particular, we have considered the reaction between dimethyl-indole **1a** and N-phenyl-N-sulfonylallenamide **2** catalyzed by the commercially available chiral BINOL-based Brønsted acid (S)-C<sub>8</sub>-TCYP. This process has experimentally proved to furnish excellent results: indolenine **3aa** in quantitative yield and 92% ee of (*S*) isomer (Figure 6.3, entry 10).

Our computations have clearly localized two enantiomeric pathways, which we called (*S*) and (*R*) (Figure 6.7) pathways, both consisting of three steps, originating from initial encounter complexes **P0(S)** (path(*S*)) and **P0(R)** (path(*R*)) and delivering the two enantiomers **3aa(S)** and **3aa(R)** respectively. In both cases the first step is rate determining and corresponds to the Brønsted acid-based activation of the allenamide **2** by the phosphate acidic proton. The second step involves the stereochemically determining step with the formation of the newly stereogenic center on C3 corresponding to the dearomatization process. Our computations suggest that this process occurs, in both cases again, through a S<sub>N</sub>2'-type mechanism after the formation of the covalent intermediates **P1(S)/(R)** rather than the hypothetical Michael-type addition supported in the 6.4.1 section (Figure

6.5a). The final proton-transfer, in which H2 moves from N1 to O2 leading to the final products (*R*) and (*S*), occurs in a subsequent final step, characterized by two very low activation barriers (0,9 kcal·mol<sup>-1</sup> in the **TS3(S)** and 1.8 kcal·mol<sup>-1</sup> in the **TS3(R)**).

In agreement with the experimental result indicating the (*S*) isomer as the predominant stereoisomer (92% ee, Figure 6.3, entry 10) the enantiomeric profiles documented by our calculations clearly show that the pathway leading to the (*S*) isomer lies at lower energy along the whole reaction profile. The resulted energy gap between the enantiomeric intermediates and transition state depend on the structural arrangement of the chiral catalyst-substrate adduct which determines better non-bonding interactions in (*S*) channel. The main conformational difference between the two reaction channels is represented by the approach-mode of the indole ring plane with respect to a cycloxylic moiety of the chiral catalyst. On the (*S*) profile the interactions between C-H protons of the cyclohexyl and the phenyl plane ring of the indole are stronger. Moreover, also the hydrogen bond network in the stereochemistry-determining transition states (**TS2(S)** and **TS2/(S)**) favors the (*S*) profile.

Improved understanding of the reaction mechanism and interactions between the chiral catalyst and the substrates would allow research groups to develop highly powerful methodologies. This study can lay the foundation to establish some mechanistic general rules towards the knowledge of the nature of enantioselectivity for this kind of systems and the design of new and more efficient organocatalysts.

# Part III

## Carbo-Catalysis

# 1. Catalysis by Carbon Nanostructures

## 1.1 Introduction

The majority of the catalysts employed in homogeneous and heterogeneous catalysis are based on metals, both noble<sup>165</sup> and base metals.<sup>166</sup> As discussed in previous sections, because of the growing need of sustainability, developing catalysts based on alternative resources has increasingly become essential. Economic considerations, since costs of some precious metals are considerably higher, could be further made to highlight the disadvantages of metal-based catalyst. For these reasons, there is much interest in developing metal-free catalysts; next to the most famous organocatalysis, seen in the previous session, catalysis by carbon nanostructures, also called “*carbocatalysis*” are among the most important examples of this tendency to reduce the dependency on metals. The most viable strategy for future industrial catalysis in the development of “metal-free” catalysts, is currently dominated by carbon-based materials. These materials include carbon black, activated carbon, fullerene, graphite/graphene, carbon nanotubes, and nanodiamond<sup>167</sup> (Figure 1.1).

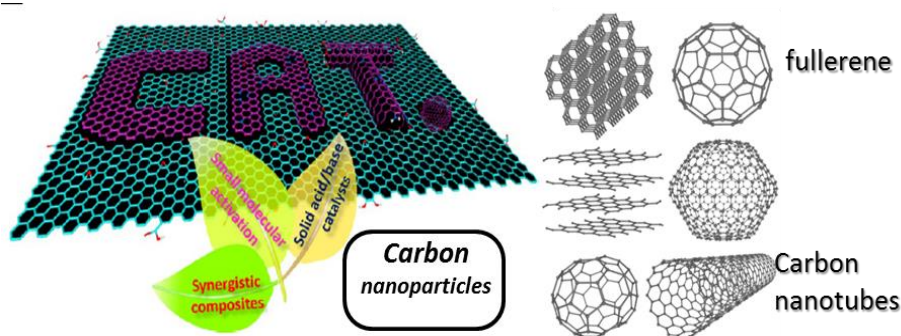


**Figure 1.1**  
Schematic illustration of some nanocarbon.

The elemental composition in carbocatalysts contains predominantly carbon that is performing as active component. In this sense, carbocatalysts are different from organocatalysts, which are constituted by organic molecules rather than carbonaceous materials. All of these carbon-based materials have found extensive use as supports for catalytically active transition metals and base-metal nanoparticle.<sup>168</sup> In this type of applications the role of carbon is to fixing the metal on a large surface area and maybe in the best case also adsorb reactants near the metal particles. In the



case of carbocatalysts the key point is to incorporate the active sites into the carbon nanostructure by suitable modifications, making metals unnecessary.

The use of metal-free heterogeneous carbons as catalysts in organic reactions is old and dates back to at least the 1930s, with Kutzelnigg and Kolthoff which independently demonstrated the ability of the activated charcoals to catalyzing the aerobic oxidation of ferrocyanide to ferricyanide.<sup>169</sup> However, in the last decades, the interest of research towards these materials has greatly increased also due to the discovery of countless fields of application in which can be used. Among the most important features they possess electrical and thermal conductivity, as well as a mechanical strength and lightness that conventional materials cannot match.<sup>170</sup> With the diversity of their structure, these characteristic values can be achieved over an extremely wide range of conditions. For these reasons, they are extensively studied in applications going from photonics and optoelectronics to biotech and nanomedicine, advanced electrodes, and polymer composites.<sup>171</sup>

In this third part of dissertation will be studied some simple reactions carried out inside carbon nanotubes trying to rationalize the energy contributions (electrostatic, van der Waals interactions, polarizability effects, hydrophobic effects) that may influence the course of a reaction inside a CNT.

## **1.2 Carbon Nanotubes as nano-reactors**

The confinement of guest molecules inside host containers offers an innovative way to control the reactivity of the guests, manipulate reaction pathways, and govern the outcome of chemical reactions. During the past decade the course of reactions of molecules encapsulated within various nanoreactors, such as crown ethers, cyclodextrins, calixarenes, cucubiturils, cavitands, carcerands, supramolecular/coordination cages such as metal-organic frameworks (MOF), and purely inorganic three-dimensional frameworks (zeolites), has been shown to be drastically altered by confinement.<sup>172</sup> Changes in the thermodynamic properties of the reacting mixture and in the reaction energy surface are critically determined by the host.<sup>173</sup> These modifications are ascribed to geometrical constraints when the host inner volume is comparable to the guest's size and to selective adsorption of reacting molecules on the host surface. If we exclude the processes that involve formation and breaking of chemical bonds with the host, the confinement effects affecting the course of chemical reactions can be classified as: (i) shape-catalytic effects, i.e., the effects of the shape of the confining material and/or the consequent reduced host space and (ii) physical

effects, i.e., the influence on the potential surface of dispersion and electrostatic interactions between the substrate and the confining material. Carbon nanotubes (CNTs) are containers that easily embed molecules.<sup>174</sup> These nanostructures can be visualized as rolled-up graphene sheets that form cylindrical tube-shaped structures. The number of graphene sheets defines the carbon nanostructure: single-wall (SWCNT's), double-wall (DWCNT's) and multi-wall (MWCNT's) nanotubes can be distinguished. The CNT diameter is the most important parameter determining whether or not a molecule can be trapped inside a CNT. The adjustable size of the CNT cavity can control the alignment and orientation of the guest molecules inside the tube.<sup>174</sup> As a general rule for successful encapsulation, the nanotube internal diameter must be at least 0.6 nm wider than that of the guest molecule. Once encapsulated, the behavior of the guest molecule is greatly affected by confinement. Importantly, the CNT is not just a passive container since, in many cases, it acts as an effective template to control the structural arrangement of the guests.<sup>174</sup> A reasonable consequence of these features is to extend CNT applications one step further, beyond their simple use as nanocontainers and toward the idea of their exploitation as nanoscale reaction vessels or nanoreactors.<sup>174c</sup> CNTs may represent nanocontainers and nanoreactors with several potential advantages over existing systems. Being formed by trivalent sp<sup>2</sup> carbon atoms held together by strong covalent bonds, CNTs exhibit an extremely high thermal (up to 700 °C in air and up to 2800 °C in vacuum) and mechanical (tensile strength of 63 GPa and elastic moduli on the order of 1 TPa) stability, higher than that exhibited by any other molecular or supramolecular nano-containers. Since the walls of CNTs have very low chemical reactivity, some aggressive chemical processes can be contained within CNTs.<sup>174c</sup> Thanks to these properties, it is possible to carry out reactions inside CNTs under a wider range of conditions with respect to existing nanoreactors. Several theoretical studies have explored the effects of confinement in CNTs on hydrogen bond ability,<sup>175</sup> isomerization processes,<sup>176</sup> proton transfer,<sup>177</sup> molecular decomposition,<sup>178</sup> and several other reactions.<sup>179</sup> Recently, experimental studies confirmed that the regioselectivity and rate of metal-catalyzed reactions are affected by confinement inside carbon nanostructures by modifying the redox properties of transition metals and consequently their catalytic performance.<sup>170,180</sup>

## 2. Cl(−) Exchange S<sub>N</sub>2 Reaction inside Carbon Nanotubes<sup>181</sup>

### 2.1 Reactions inside CNT: choosing the level of theory

Computational chemistry can play a key role to understand the factors (electrostatics, van der Waals, polarizability effects, hydrophobic effects, ...) affecting the course of a chemical process inside a tube and can be used as a predictive tool to design the best host to control the rate and the outcome of a chemical reaction. Among the various quantum mechanical (QM) methods, DFT is the only one that can be satisfactorily applied to the study of reactions involving large systems such as nanotubes. However, even DFT methods have restrictions imposed by the system size and cannot be easily applied when very long and multiwall tubes are used and large endohedral reacting systems are involved. A solution is the use of hybrid methods, which allow us to study large systems by dividing them into two (or more) regions, which are described at different levels of theory and accuracy. Usually, a high-level calculation is performed on the small internal region (inner layer), while the effects of the remaining region(s) (outer layer(s)) are described at a lower level of theory (typically molecular mechanics (MM) or, alternatively, QM semiempirical methods). In the case of CNTconfined processes, the inner layer usually corresponds to the reacting endohedral system (the guest), and the outer layer is made up by the tube (the host). Both a careful choice of the computational layers<sup>182</sup> and an accurate benchmark study, to decide the level of theory suitable for the outer layer(s), are crucial. The requirement to decide the most appropriate level of theory can be its ability of reproducing the results of an accurate full QM DFT investigation. Since a benchmark study of this type is not available in the literature, in the present paper we have examined, in the light of the previous discussion, the reaction between chloride anion Cl(−) and chloromethane (CH<sub>3</sub>Cl), which can be considered as an archetypical model of S<sub>N</sub>2 and chemical reactions in general. This S<sub>N</sub>2 reaction occurring in the gas phase and inside a (6,6) carbon nanotube was investigated by Halls and Raghavachari. In their work, they carried out DFT calculations with the popular B3LYP hybrid functional to determine critical point structures and reaction energetics.<sup>179a</sup> They reported that the nanotube confinement enhances the barrier height of the reaction by 6.6 kcal/mol.<sup>179a</sup> Very recently, Ravinder and Subramanian repeated these computational studies within pristine and Stone–Wales defective boron nitride nanotubes (BNNTs) and CNTs, using (8,0) and (9,0) tubes.<sup>179e</sup>

Here we investigate again both the gas-phase and CNT-confined reaction using a more accurate DFT functional (M06-2X). Then, using the hybrid ONIOM methodology,<sup>41</sup> we examine various approaches where the reacting system is described with the M06-2X functional and the tube with different semiempirical QM methods or MM force-field methods. Furthermore, we established the minimum tube length needed to provide a reliable model system for the confined reaction, and we identified the key factors affecting structure and energetics of the reaction, examining various CNT model systems differing in the tube radius.

## 2.2 Gas-Phase Cl(−) Exchange S<sub>N</sub>2 Reaction and the Effect of the CNT Confinement

### 2.2.1 Validation of the DFT benchmarck method

A preliminary DFT theoretical study using the M06-2X functional was carried out on the chloride exchange S<sub>N</sub>2 reaction occurring in the gas phase. The reaction profile of this reaction is well-known: the approaching nucleophile Cl(−) forms a preliminary complex I (more stable than reactants Rx) followed by a transition state TS for the configuration inversion (see Figure 2.1). The M06-2X functional provided an intrinsic barrier of 13.2 kcal mol<sup>−1</sup> (difference between preliminary complex and transition state) which compares very well to the experimental value of 13.0 kcalmol<sup>−1</sup> and computational benchmark results<sup>183</sup> and represents a significant improvement with respect to the B3LYP value of 8.7 kcal mol<sup>−1</sup>.<sup>184</sup> The B3LYP functional not only systematically underestimates the intrinsic barrier height but also fails to locate correctly the transition state for Walden inversion, which is found below the energy of the separated reactants.<sup>184</sup>

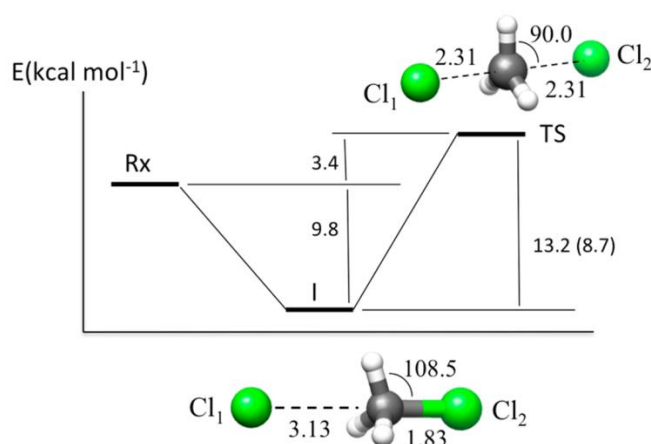


**Figure 2.1**

Reaction profile (kcal mol<sup>−1</sup>) and structure (Å and degrees) for the preliminary complex I and transition state TS computed at the M06-2X level for the gas-phase chloride exchange S<sub>N</sub>2 reaction. The value in parentheses is the intrinsic barrier computed at the B3LYP level.

On the contrary, the M06-2X computed central barrier (difference between reactants and transition state) is  $3.4 \text{ kcal mol}^{-1}$ , in quite good agreement with experimental studies and “gold standard” calculations (coupled cluster CCSD and CCSD(T) methods, basis sets of up to spdfgh quality, extrapolations to the one-particle basis set limit, contributions of inner-shell correlation, scalar relativistic effects, and first-order spin-orbit coupling) which showed that the central barrier for the  $\text{Cl}(-) + \text{CH}_3\text{Cl}$  reaction is of the order of  $3 \text{ kcal mol}^{-1}$ .<sup>183,184</sup>

Also, since the M06-2X functional is able to reproduce accurately  $\text{C-H}\cdots\pi$ <sup>185</sup> and  $\text{Cl}\cdots\pi$ <sup>186</sup> interactions computed at higher levels of theory (such as CCSDT and MP2), it is well-suited to investigate the  $\text{S}_{\text{N}}2$  reaction inside the tube.

The reaction was reinvestigated inside a (6,6) carbon nanotube, using the M06-2X functional and without imposing any geometry constraints on the nanotube and the endohedral reacting system. The length of the model CNT was  $12.4 \text{ \AA}$ , identical to that used by Halls et al.<sup>179a</sup> in their computations with the B3LYP functional. Our results are in qualitative agreement with those obtained by these authors: the reaction is highly disfavored when carried out within the CNT, the M06-2X intrinsic barrier being  $17.9 \text{ kcal mol}^{-1}$ .

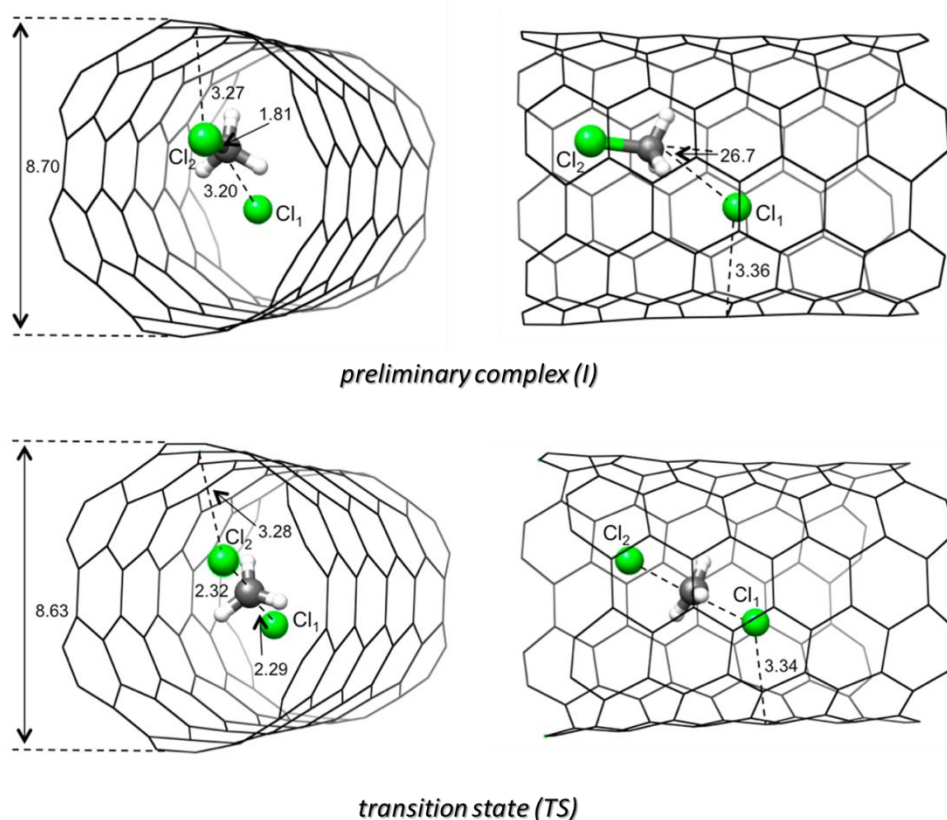


**Figure 2.2**

Schematic representation of the preliminary complex I and transition state TS computed at the M06-2X level for the CNT-confined chloride exchange  $\text{S}_{\text{N}}2$  reaction. In the two perspectives it is evident that the nonsymmetric arrangement of the endohedral reacting system is with respect to the tube axis. Geometrical parameters are given in  $\text{\AA}$  and degrees.

An interesting aspect should be emphasized. The full geometry optimization adopted in our model leads to a distortion of the carbon nanotube framework caused by the interactions between the reacting system and the nanotube electron density.

After formation of the preliminary complex the section of the CNT becomes an ellipse (Figure 2.2) whose major axis is 8.70 Å (the radius of the empty tube is 8.2 Å). This value becomes 8.63 Å in the transition state. Since in their computations Halls and co-workers<sup>179a</sup> kept frozen the nanotube structure, we reinvestigated the confined reaction without geometrical constraints at the B3LYP level. We observed in this case only a small distortion of the nanotube, the major axis of the ellipse being only 8.3 Å. The intrinsic activation barrier in this case was 12.1 kcal mol<sup>-1</sup>. The more pronounced structural changes found with M06-2X can be explained by the ability of this functional to describe weak non-bonded interactions between the reacting system and the electron cloud of the surrounding nanotube. The carbons of the CNT can interact with the three C–H bonds (C–H··· $\pi$  interactions) and the two chlorine atoms (Cl··· $\pi$  interactions). C–H··· $\pi$  interactions are well-known stabilizing interactions featuring, for instance, T-shaped structures between aromatic rings.<sup>187</sup> Cl··· $\pi$  interactions have been recognized to play a key role in determining crystal packing and protein–ligand complexes. High-level ab initio computations using chloro-hydrocarbon model systems provided an estimate of about 2.0 kcal mol<sup>-1</sup> for the Cl··· $\pi$  interaction energy and an average distance between Cl and the benzene carbon atoms of about 3.6 Å.<sup>188</sup> Interestingly, to maximize the Cl··· $\pi$  interactions, the best arrangement found by the reacting system inside the nanotube is not symmetric with respect to the tube axis: even if the substrate carbon is approximately on the tube axis, the reaction coordinate Cl<sub>1</sub>···C···Cl<sub>2</sub> forms in the transition state an angle of about 30° with the tube axis, and the two chlorine atoms interact with opposite sides of the tube wall (Figure 2.2).

Since both Cl<sub>1</sub> and Cl<sub>2</sub> and the three C–H bonds can simultaneously interact with the tube wall, the energetic effects on the reaction surface are the result of a complex interplay between C–H··· $\pi$  and Cl··· $\pi$  interactions. To figure out the role of the various interactions in determining the increase of the activation energy, we have examined the shortest distance (Figure 2.2) and the average distance between each of the two Cl atoms and the tube carbon atoms in the intermediate I and transition state TS (Cl<sub>1</sub>···C(wall) and Cl<sub>2</sub>···C(wall) parameters reported in Table 2.1). These values are in good agreement with the average distance of 3.6 Å available in the literature.<sup>188</sup>

<i>Entry</i>			<i>I</i>	<i>TS</i>
1	Cl <sub>1</sub> ···C(wall)	shortest distance	3.34	3.32
		average distance	3.45	3.47
2	Cl <sub>2</sub> ···C(wall)	shortest distance	3.27	3.27
		average distance	3.58	3.58
3	H <sub>1</sub> ···C(wall)	shortest distance	2.48	3.11
		average distance	2.95	3.39
4	H <sub>2</sub> ···C(wall)	shortest distance	3.03	3.03
		average distance	3.40	3.42
5	H <sub>3</sub> ···C(wall)	shortest distance	3.08	3.03
		average distance	3.48	3.42

**Table 2.1**

Minimum and Average Values (Å) of the Distances between the Wall Carbon Atoms and the Chlorine and Hydrogen Atoms of the Reacting Endohedral System

Both the shortest and average values of Cl<sub>1</sub>···C(wall) and Cl<sub>2</sub>···C(wall) remain almost constant from I to TS suggesting that the change of the corresponding Cl···π interactions is not large enough to significantly affect the activation barrier with respect to the gas phase.

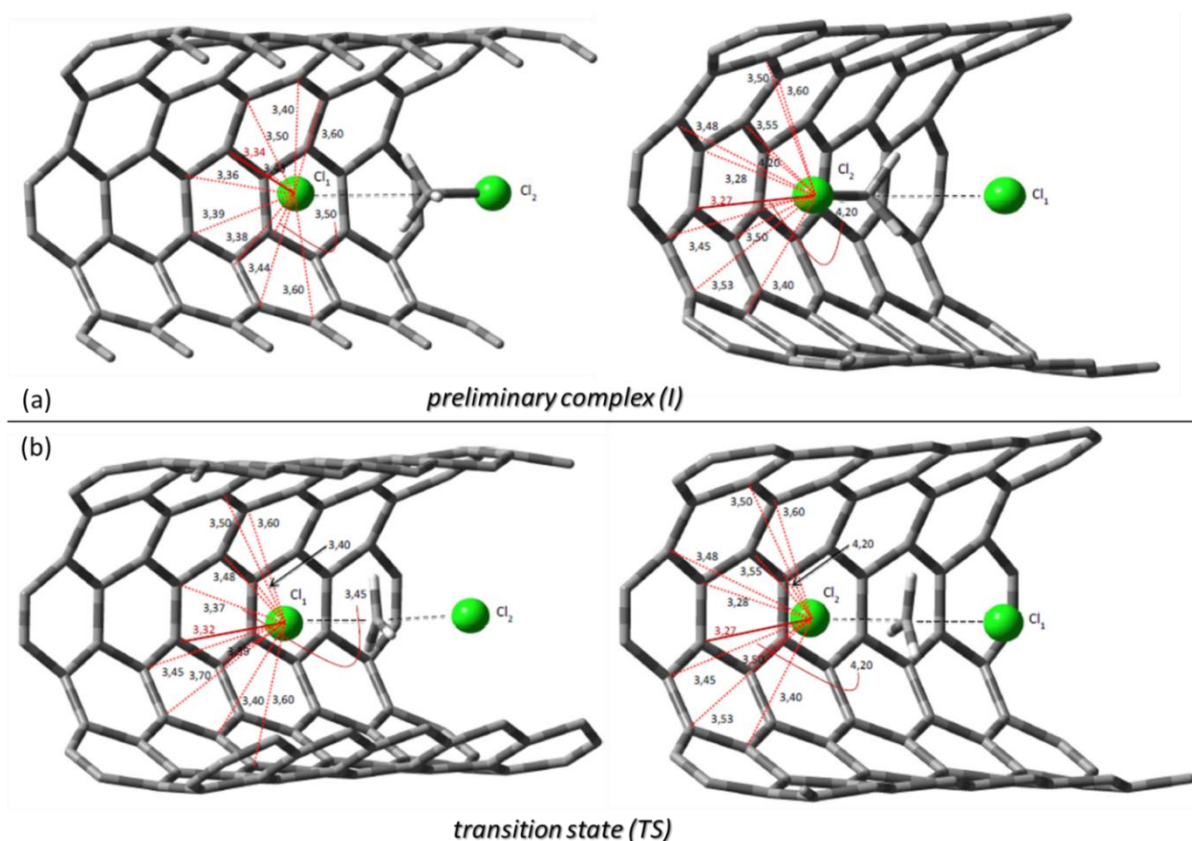


**Figure 2.3**

Cl<sub>1</sub>...C(tube) and Cl<sub>2</sub>...C(wall) distances (Ångstroms) computed (a) in the preliminary complex I and (b) in the transition state TS at the M06-2X level.

A similar analysis carried out for the distances between the three hydrogen atoms and the wall shows that in one case ( $H_1$ ) the  $H_1 \cdots C(\text{wall})$  distance significantly increases in the transition state with respect to the preliminary complex, suggesting a lower stabilizing effect of the  $C-H \cdots \pi$  interactions in the former case.

The resulting different stabilization of the two critical points results in the increase of the activation barrier of the CNT-confined reaction with respect to the gas phase. A schematic representation of the various  $Cl \cdots \pi$  interactions is given in Figure 2.3. The action mechanism of the  $C-H \cdots \pi$  interactions can be easily understood if we compare the structure of I and TS. In both cases the  $Cl \cdots \pi$  interactions behave like a molecular glue which fastens the two chlorine atoms to the wall. However, in the intermediate I  $Cl_1$  weakly interacts with the substrate carbon, which is free to move toward the wall to maximize the  $C-H \cdots \pi$  interactions. The approaching of the  $C-H$  bonds to the tube wall is much more difficult in the transition state where  $Cl_1$  and  $Cl_2$  are equally bonded to the central carbon which has not enough freedom to move closer to the wall.

### 2.2.2 CNT confined reaction using hybrid methods

The above QM DFT computations were used as a benchmark to evaluate the accuracy of various hybrid methods in which the reacting system was always described at the M06-2X/6-31+G\* level, while either a semiempirical (Am1, PM3, and PM6) or MM (UFF, Dreiding, Amber) approach was employed for the carbon nanotube.

The results are summarized in Table 2.2 where we have reported for I and TS the distance ( $Cl_1 \cdots C$ ) between the nucleophile ( $Cl(-)$ ) and the substrate carbon, the breaking  $C-Cl_2$  bond, the distance between the approaching chloride and the closest carbon of the tube wall ( $Cl_1 \cdots C(\text{wall})$ ), and the value of the intrinsic activation barrier  $E_a$ . The length of the CNT was the same as that used in the previous full QM computations. The best agreement with the QM computations (entry 1) was obtained using the UFF force field to describe the CNT (entry 5). We denoted this computational approach as M06-2X/UFF. At this level we computed a barrier of  $18.1 \text{ kcal mol}^{-1}$ , which is very close to the M06-2X value of  $17.9 \text{ kcal mol}^{-1}$ . Also, the M06-2X/UFF geometrical parameters are in satisfactory agreement with those of the full QM computations. This result suggests that a hybrid method where the whole tube is described by the MM UFF potential can provide a reliable description of the CNT-confined reaction.



<i>Entry</i>			$Cl_1 \cdots C$	$C \cdots Cl_2$	$Cl_1 \cdots C(\text{wall})$	$E_a$
1	M06-2X	<i>I</i>	3.20	1.81	3.34	<b>17.9</b>
		<i>TS</i>	2.31	2.29	3.31	
2	M06-2X/AM1	<i>I</i>	3.19	1.81	3.59	<b>17.2</b>
		<i>TS</i>	2.29	2.29	4.03	
3	M06-2X/PM3	<i>I</i>	3.19	1.81	4.04	<b>17.3</b>
		<i>TS</i>	2.30	2.30	4.08	
4	M06-2X/PM6	<i>I</i>	3.19	1.81	2.88	<b>13.4</b>
		<i>TS</i>	2.30	2.30	2.95	
5	M06-2X/UFF	<i>I</i>	3.08	1.82	3.41	<b>18.1</b>
		<i>TS</i>	2.30	2.29	3.39	
6	M06-2X/Dreiding	<i>I</i>	3.08	1.82	3.51	<b>14.5</b>
		<i>TS</i>	2.30	2.30	3.52	
7	M06-2X/Amber	<i>I</i>	3.07	1.82	3.46	<b>14.3</b>
		<i>TS</i>	2.30	2.29	3.44	

**Table 2.2**

Geometrical Parameters  $Cl_1 \cdots C$ ,  $C \cdots Cl_2$ , and  $Cl_1 \cdots C(\text{wall})$  (Å) and Activation Barriers  $E_a$  (kcal mol<sup>-1</sup>) computed with different hybrid approaches.

To obtain a more exhaustive description of the confinement effects, we examined at the M06-2X/UFF level various CNT models differing in the tube length. Longer nanotubes allow us to consider additional interactions (neglected in the first model) between the reacting system and the far away carbons of the tube wall. The values reported in Table 2.3 show that the computed activation barrier increases with the increase of the tube length and the associated increasing number of  $Cl \cdots \pi$  and  $C-H \cdots \pi$  interactions.

Since, as we have previously shown, the former interactions are almost constant when we compare *I* and *TS*, the increase of the barrier associated with longer tubes must be due to the increasing number of  $C-H \cdots \pi$  interactions that further stabilize the preliminary intermediate. However, their importance rapidly decreases when we move away from the reaction center, and their effect becomes negligible for tube length longer than 24.4 Å, as suggested by the trend of the barrier that asymptotically approaches a limit value of 19.9 kcal mol<sup>-1</sup> (Figure 2.4).

Entry	CNT lenght		$Cl_1 \cdots C$	$C \cdots Cl_2$	$E_a$
1	12.4	I	3.12	1.82	18.1
		TS	2.30	2.29	
2	17.1	I	3.19	1.81	18.7
		TS	2.29	2.29	
3	24.4	I	3.13	1.81	19.9
		TS	2.32	2.29	
4	39.1	I	3.08	1.81	19.9
		TS	2.32	2.29	

**Table 2.3**

Geometrical Parameters  $Cl_1 \cdots C$  and  $C \cdots Cl_2$  (Å) and Activation Barriers  $E_a$  (kcal mol<sup>-1</sup>) Computed for Various (6,6) CNT Models of Different Length (Å) at the M06-2X/UFF Level

Thus, these computations represent a rough estimate of the minimum length of a (6,6) CNT model system needed to provide a reliable description of a real CNT-confined S<sub>N</sub>2 reaction.

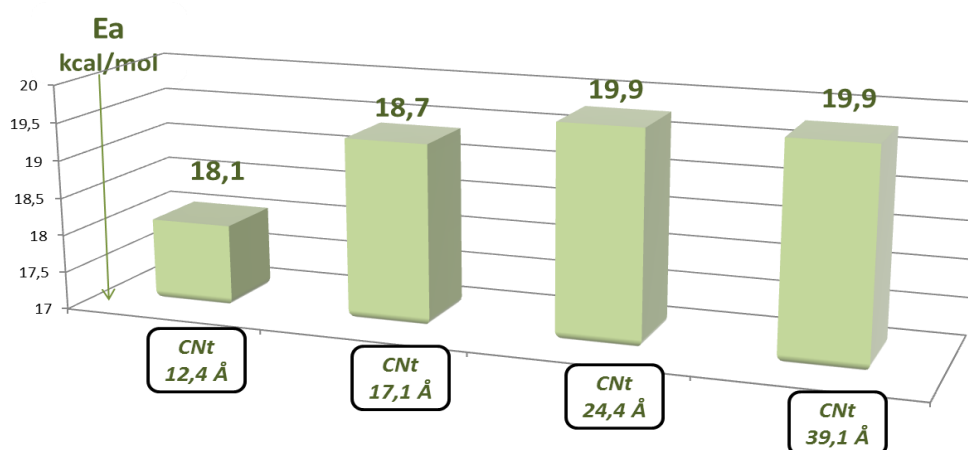


**Figure 2.4**

Diagram showing the variation of the activation barrier as a function of the tube length. Activation Barriers  $E_a$  (kcal mol<sup>-1</sup>) Computed for Various (6,6) CNT Models of Different Length (Å) at the M06-2X/UFF Level

From our previous discussion it is evident that  $Cl \cdots \pi$  and  $C-H \cdots \pi$  interactions are the key factor determining the structure of the reacting system inside the tube. Since it is conceivable that the relative importance of these interactions in I and TS can be significantly affected by a change of the tube radius, in principle, different CNT sizes could lead to an increase/decrease of the activation barrier. To elucidate the actual effect of the tube size on the reaction energetics, we examined at the

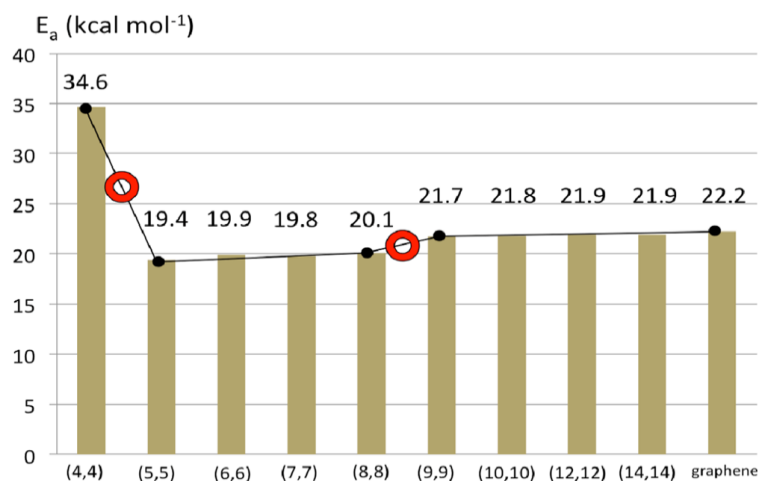
M06-2X/UFF level various CNT model systems with different radius: (4,4), (5,5), (7,7), (8,8), (9,9), (10,10), (12,12), (14,14) and, as a limit case, a graphene sheet. In all cases a tube length of 24.4 Å was used. The results summarized in Table 2.4 and Figure 2.5 show that the activation barrier  $E_a$  is very large for narrow tubes (34.4 kcal mol<sup>-1</sup> in the (4,4) case), and it suddenly decreases (19.4 kcal mol<sup>-1</sup>) for a (5,5) tube and does not change significantly when the tube radius grows till the (8,8) case (20.1 kcal mol<sup>-1</sup>). A more significant growth of  $E_a$  is observed for larger tubes.

Entry	CNT size		$Cl_1 \cdots C$	$C \cdots Cl_2$	$Cl_1 \cdots C(wall)$	$E_a$
1	(4,4)	<i>I</i>	3.03	1.72	2.90	<b>34.6</b>
		<i>TS</i>	2.68	2.51	2.93	
2	(5,5)	<i>I</i>	3.10	1.80	3.27	<b>19.4</b>
		<i>TS</i>	2.31	2.30	3.39	
3	(6,6)	<i>I</i>	3.13	1.81	3.32	<b>19.9</b>
		<i>TS</i>	2.32	2.29	3.40	
4	(7,7)	<i>I</i>	3.13	1.81	3.18	<b>19.8</b>
		<i>TS</i>	2.31	2.28	3.35	
5	(8,8)	<i>I</i>	3.33	1.81	3.25	<b>20.1</b>
		<i>TS</i>	2.34	2.27	3.25	
6	(9,9)	<i>I</i>	3.15	1.81	3.16	<b>21.7</b>
		<i>TS</i>	2.30	2.65	3.16	
7	(10,10)	<i>I</i>	3.02	1.82	3.20	<b>21.8</b>
		<i>TS</i>	2.30	2.30	3.20	
8	(12,12)	<i>I</i>	3.18	1.81	3.18	<b>21.9</b>
		<i>TS</i>	2.36	2.25	3.22	
7	(14,14)	<i>I</i>	3.19	1.1	3.20	<b>21.9</b>
		<i>TS</i>	2.32	2.29	3.25	
7	Graphene sheet	<i>I</i>	3.16	1.83	3.18	<b>22.2</b>
		<i>TS</i>	2.33	2.28	3.30	

**Table 2.4**

Geometrical Parameters  $Cl_1 \cdots C$ ,  $C \cdots Cl_2$ , and  $Cl_1 \cdots C(wall)$  (Å) and Activation Barriers  $E_a$  (kcal mol<sup>-1</sup>) Computed for Various CNT Models of Different Size at the M06-2X/UFF Level (Constant Tube Length of 24.4 Å).  $aCl_1 \cdots C(wall)$  is the shortest distance between the approaching chlorine and the wall carbons.

The value computed for a (9,9) tube is  $21.7 \text{ kcal mol}^{-1}$ , and this value remains almost constant for larger tubes:  $21.9$  and  $22.2 \text{ kcal mol}^{-1}$  are, respectively, the activation barriers found for a (14,14) tube and in the limit case of an infinite radius represented by a graphene sheet. The two discontinuity points in the trend of  $E_a$  are evidenced in the diagram of Figure 2.5.



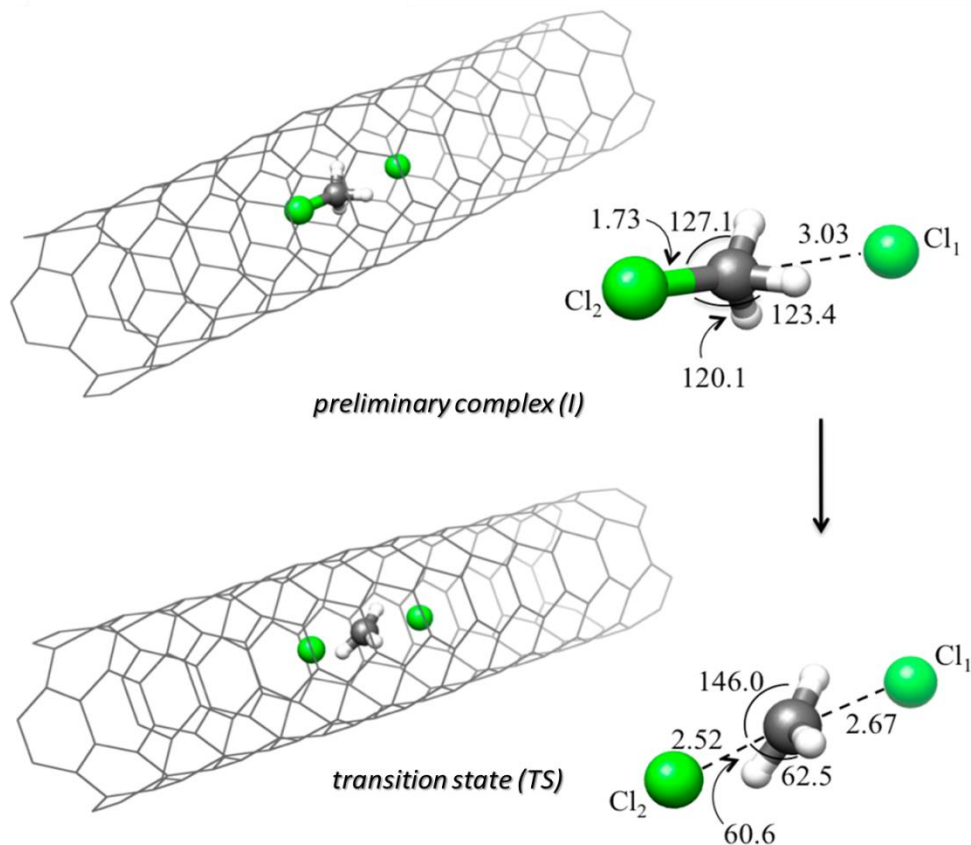
**Figure 2.5**

Diagram showing the variation of the activation barrier as a function of the tube radius. Two discontinuity points corresponding to the change (4,4) → (5,5) and (8,8) → (9,9) are evidenced.

These results can be easily understood. The arrangement of the reacting system is strongly affected by the tube radius and the consequent augmented (or reduced) volume inside the tube. The available volume is lacking for small (4,4) tubes, as evidenced by the shorter values of the  $\text{Cl}_1 \cdots \text{C}(\text{wall})$  distance reported in Table 2.4. To avoid too short distances between the hydrogen atoms and the tube wall (which could make the non-bonded  $\text{C}-\text{H} \cdots \pi$  interactions repulsive), the tetrahedral carbon structure of the intermediate I changes shape, and the  $\text{H}-\text{C}-\text{Cl}_2$  angles become significantly larger than the “ideal” value of  $109.5^\circ$ , as shown in Figure 2.6: the reported angles are  $127.1^\circ$ ,  $120.1^\circ$ , and  $123.4^\circ$ . The structural distortion becomes even stronger in TS where the central carbon cannot attain the usual planar structure approximately orthogonal to the reaction coordinate (see again Figure 2.6). This causes a strong destabilization of TS and a consequent very large activation barrier ( $34.6 \text{ kcal mol}^{-1}$ ).

The sudden decrease of the barrier observed for a (5,5) tube ( $19.4 \text{ kcal mol}^{-1}$ ) occurs because the augmented volume allows an arrangement of the reacting system similar to that previously described in the (6,6) case. Since no significant structural changes are observed for (7,7) and (8,8) CNTs, where the two Cl atoms again stick to the tube wall on opposite sides with respect to the tube axis, the activation barrier is not significantly affected. When the volume inside the tube further

grows ((9,9) and (10,10) tubes) various structural arrangements of the reacting system with respect to the tube wall become possible. The minimum energy structures of I and TS found for a (10,10) CNT are shown in Figure 2.7.



**Figure 2.6**

Schematic representation of the preliminary complex I and transition state TS computed at the M06-2X/UFF level for the chloride exchange  $S_N2$  reaction in a (4,4) tube. The pictures highlight the strong structural distortion caused by the confinement. Geometrical parameters are given in Å and degrees.

The two chlorine atoms act again as a molecular glue and fasten the reacting system to the tube wall in such a way that the reaction coordinate is now orthogonal to a plane cutting the tube along the axis. As described in detail for the (6,6) CNT, the  $Cl \cdots \pi$  interactions do not change significantly on passing from I to TS as suggested by the values of the shortest distances between the wall carbon atoms and  $Cl_1$  and  $Cl_2$  (3.35 and 3.31 Å in the complex and 3.45 and 3.35 Å in the transition state). Since a more significant variation features the distance between the wall and one hydrogen atom (3.04 and 3.23 Å in I and TS, respectively), it is reasonable to consider again the  $C-H \cdots \pi$  interactions as the key factor that stabilizes the intermediate and determines the increase of the barrier (21.8 kcal mol<sup>-1</sup> for a (10,10) CNT). The structural arrangement of the reacting system

remains approximately the same for larger tubes and for the graphene sheet in agreement with the almost constant value of the barrier.

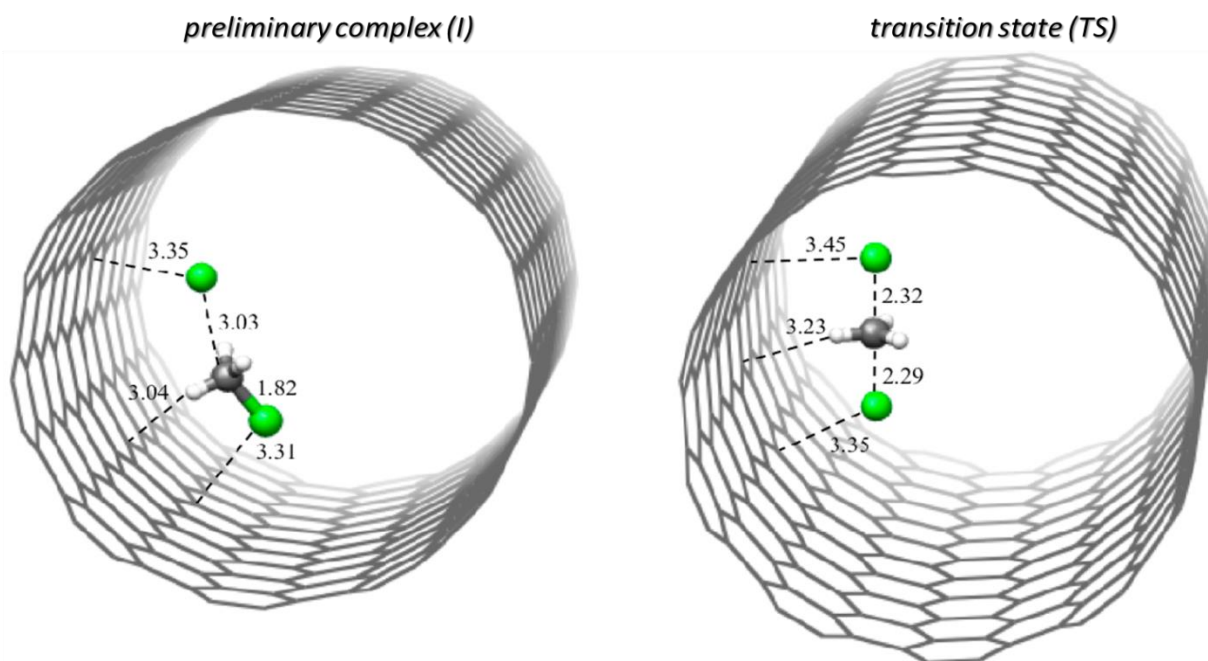


**Figure 2.7**

Schematic representation of the preliminary complex I and transition state TS computed at the M06-2X/UFF level for the chloride exchange  $S_N2$  reaction in a (10,10) tube. In the transition state the reaction coordinate is orthogonal to a plane cutting the tube along the main axis. Geometrical parameters are given in Å and degrees.

## 2.3 Computational details

Nanotubes were built using the Nanotube Builder plugin, as implemented in VMD.<sup>189</sup> All reported computations were carried out with the Gaussian09<sup>4</sup> series of programs. In the full QM DFT calculations the B3LYP<sup>19,20,21</sup> and M06-2X<sup>24,25</sup> functionals were used. The nanotube was described with 3-21G\* basis set,<sup>190</sup> while for the reactive system the 6-31+G\* basis set was used.<sup>191</sup> ONIOM calculations<sup>41</sup> were performed considering mechanical and electrostatic embedding.<sup>41</sup> The inner layer (high-level layer) consisted of the reacting system, i.e., Cl(-) and CH<sub>3</sub>Cl. These were described at the DFT level using the M06-2X functional and the 6-31+G\* basis set. The outer layer (lowlevel layer) was formed by the nanotube and was described using semiempirical (AM1,<sup>192</sup> PM3,<sup>193</sup> PM6<sup>194</sup>) or molecular mechanics (MM) (UFF,<sup>29</sup> DREIDING,<sup>30</sup> AMBER<sup>26</sup>) methods. In the MM calculations partial atomic (point) charges were used to compute the electrostatic interactions.

These charges were calculated using the QEq formalism.<sup>195</sup> The structure of the various critical points (minima and saddle points) was fully optimized. Frequency calculations were carried out at the same level of theory to check the nature of critical points.

## 2.4 Conclusions

In this paper we have examined the confinement effects of various CNTs (differing in the tube radius) on a model reaction, i.e., the CNT-confined chloride exchange  $S_N2$  reaction for methyl chloride. Either full QM DFT calculations based on the M06-2X functional or hybrid methods have been used. This study can provide useful information that can help to define reliable computational approaches to investigate real processes occurring inside nanotubes. The results of our study can be summarized as follows:

(i) In our benchmark we chose DFT computations based on the M06-2X functional as a QM reference because this functional provides for the gas-phase Cl(-) exchange reaction an intrinsic barrier of 13.2 kcal mol<sup>-1</sup>, in good agreement with the experimental value. This result is much more satisfactory than that obtained with the more popular B3LYP functional, which is 8.7 kcal mol<sup>-1</sup>.

(ii) Investigation of the reaction inside a (6,6) CNT with the M06-2X functional provides results in qualitative agreement with those obtained by other authors using the popular B3LYP functional:<sup>179a</sup> the confined reaction is disfavored, the intrinsic barrier being 17.9 kcal mol<sup>-1</sup>.

(iii) The augmented barrier, with respect to the gas phase, can be ascribed to a complex interplay between Cl $\cdots\pi$  and C-H $\cdots\pi$  interactions (these are the interactions of the two Cl atoms and the C-H bonds of the substrate with the carbon atoms of the tube wall). The computed geometrical parameters indicate that, while the Cl $\cdots\pi$  interactions remain approximately constant in I and TS, the importance of the stabilizing C-H $\cdots\pi$  interactions significantly decreases from I to TS with a consequent increase of the barrier. We have compared the Cl $\cdots\pi$  interactions to a “molecular glue” fastening the two chlorine atoms to the wall in both the intermediate and transition state. However, in the former case, one Cl atom only weakly interacts with the substrate carbon, and this has enough freedom to move closer to the wall to maximize several stabilizing C-H $\cdots\pi$  interactions. This motion is not possible in the transition state where both chlorine atoms are equally bonded to the central carbon.

(iv) A hybrid method where the endohedral reacting system (QM region) is described with the M06-2X functional and the nanotube with the MM UFF force field (M06-2X/UFF approach) satisfactorily reproduces the results of the full QM M06-2X computations.

(v) We used the M06-2X/UFF approach to examine in detail the confinement effects on the reaction potential surface. To this purpose we examined various CNT model systems differing in the tube length but with the same radius, i.e., (6,6) tubes. We observed that the barrier increases with the increase of the tube length to reach the asymptotic value of  $19.9 \text{ kcal mol}^{-1}$  for tube length larger than  $24.4 \text{ \AA}$ . This value represents the minimum length of a (6,6) CNT model system that can emulate the CNT confined SN2 reaction and provides useful suggestions to build reliable model systems for other SN2 reactions and, in general, different chemical processes.

(vi) To obtain an exhaustive description of the confinement effects on the SN2 reaction we examined various CNT model systems with different radius: (4,4), (5,5), (7,7), (8,8), (9,9), (10,10), (12,12), (14,14) tubes and, as a limit case, a graphene sheet. In all cases, we fixed the tube length at  $24.4 \text{ \AA}$ . We found that the activation barrier  $E_a$  is very large for small tube radii ( $34.4 \text{ kcal mol}^{-1}$  in the (4,4) case). This large barrier is due to the reduced volume inside the tube causing a strong structural distortion in the transition state. Since the augmented volume inside a (5,5) tube is enough to avoid this distortion, the barrier suddenly decreases and remains approximately constant (about  $20 \text{ kcal mol}^{-1}$ ) for tubes in the range (5,5) to (8,8).

A growth of the activation barrier was observed for a (9,9) tube, and the value again remained approximately constant (about  $22 \text{ kcal mol}^{-1}$ ) for larger tubes all the way to the limit case of a graphene sheet. This finding can be explained by the new structural arrangement of the reacting system within the larger volume available inside the tube. The reacting system is now flattened on the tube wall, and the reaction coordinate is orthogonal to a plane cutting the tube along the main axis. Again the increased barrier can be ascribed to the  $\text{C-H}\cdots\pi$  interactions, which are more stabilizing in the intermediate than in the transition state.



### 3. CNT-Confinement Effects on the Menshutkin $S_N2$ Reaction

#### 3.1 Introduction

Relying on the results just discussed above on the  $Cl^{(-)}$  exchange  $S_N2$  reaction inside CNT, in the present work we use the same computational approach (full QM and hybrid QM/MM) to investigate the prototype Menshutkin reaction  $H_3N + H_3CCl = H_3NCH_3^{(+)} + Cl^{(-)}$  and the effect of the CNT confinement. The Menshutkin reaction is a special kind of  $S_N2$  reaction where the reactants are uncharged, but the products are characterized by a net charge separation.<sup>196</sup> It converts with good yields a tertiary amine to a quaternary ammonium salt by reaction with an alkyl halide. The reaction speeds up with polar aprotic solvents and higher reaction temperatures.<sup>196,197</sup> The reaction was studied in the gas-phase and in solution using either an implicit PCM approach<sup>198</sup> or explicit water molecules.<sup>199</sup> More recently the CNT-confined Menshutkin reaction was investigated by Schlegel and Hall using a DFT/B3PW91 approach.<sup>200</sup> They showed that the reaction is accelerated by CNT that behaves like a low-dielectric solvent. We chose the simplest Menshutkin reaction since it represents a good model-system to investigate the effects of CNTs on chemical processes involving the developing of charge separation along the reaction pathway and is suitable to carry out an accurate benchmark on the level of theory needed for an accurate description of this type of chemical transformations.

#### 3.2 Menshutkin $S_N2$ Reaction in the Gas-Phase and in Solution. The Effect of the CNT Confinement

##### 3.2.1 Full QM study of the reaction

The reaction profile for the gas-phase prototype Menshutkin  $S_N2$  reaction ( $H_3N + H_3CCl = H_3NCH_3^{(+)} + Cl^{(-)}$ ) computed with the M06-2X functional is an asymmetric double-well potential (Figure 3.1) very similar to that obtained by Schlegel and Halls using the B3PW91 hybrid density functional.<sup>200</sup> The first minimum is a reactant dipole complex (**RC**) corresponding to the alignment of the dipole moments of the approaching reactant molecules and lying  $2.9 \text{ kcal mol}^{-1}$  lower than separated molecules. This is a rather common feature for gas-phase reactions involving dipolar reactants. The second minimum is an ion pair product complex (**PC**) which is  $31.2 \text{ kcal mol}^{-1}$  higher

than **RC**. The transition state is late along the reaction path: its structure and energy are near to that of **PC** (only 3.4 kcal mol<sup>-1</sup> higher) and the corresponding activation barrier is 34.6 kcal mol<sup>-1</sup>, a value rather close to that computed by Schlegel (32.7 kcal mol<sup>-1</sup>).<sup>200</sup>

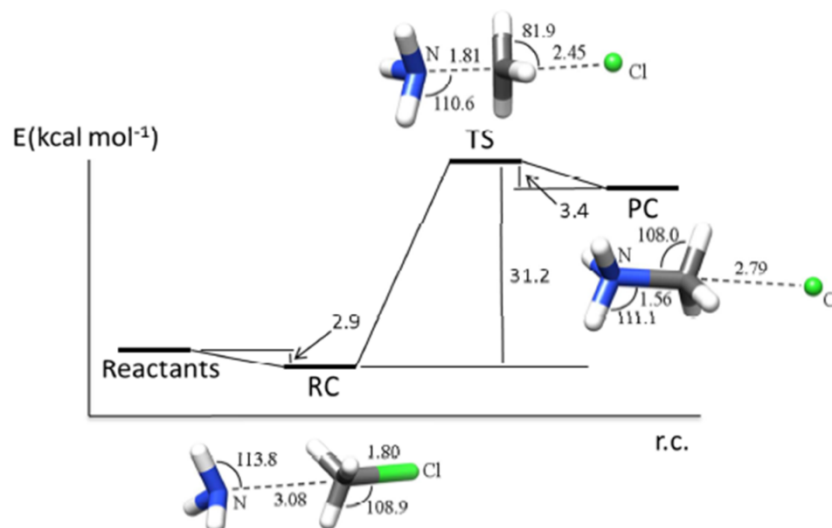


**Figure 3.1**

Reaction profile (kcal mol<sup>-1</sup>) and structure of **RC**, **TS** and **PC** (bond lengths in ångströms and angles in degrees) for the gas-phase Menshutkin SN2 reaction computed at the M06-2X level.

The most important geometrical parameters are reported in Figure 3.1. In addition to gas-phase we computed the reaction profile in benzene and water using an implicit PCM approach.<sup>100</sup> The corresponding reaction profiles are reported in Figure 3.2, a and b respectively. The solvent significantly lowers the activation barrier  $E_a$  and the reaction energy  $\Delta E$ .

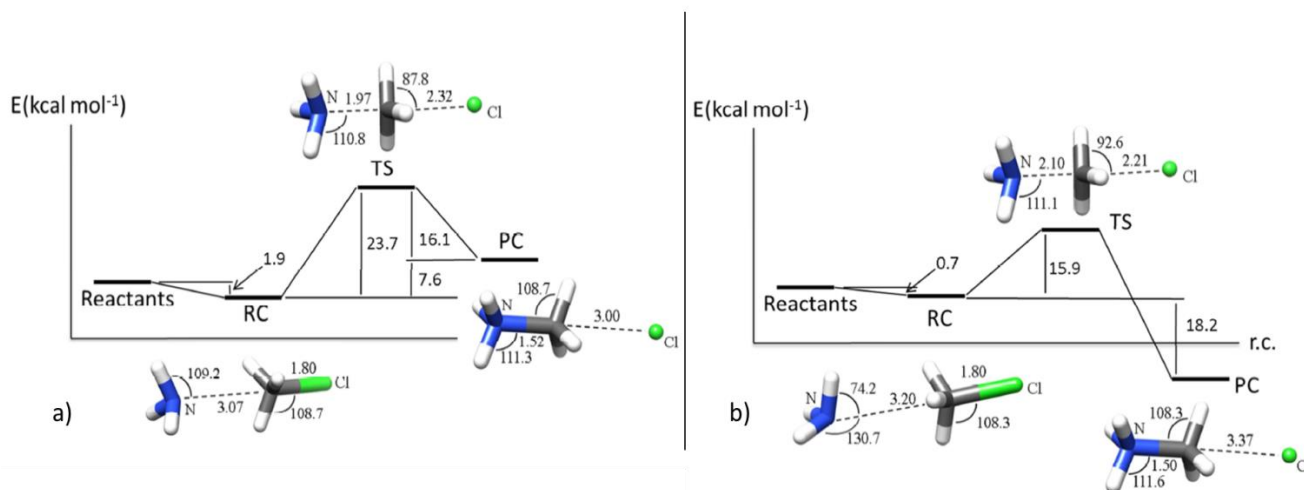


**Figure 3.2**

Reaction profile (kcal mol<sup>-1</sup>) and structure of **RC**, **TS** and **PC** (bond lengths in ångströms and angles in degrees) for the Menshutkin SN2 reaction in benzene **a**) and water **b**) computed at the M06-2X level.

In benzene and water  $E_a$  becomes 23.7 and 15.9 kcal mol<sup>-1</sup> in agreement with the increasing solvent polarity. The effect is even stronger on the product complex **PC** (characterized by a net charge separation) and causes remarkable changes on the reaction energy  $\Delta E$ : the reaction remains endothermic in benzene ( $\Delta E = 7.6$  kcal mol<sup>-1</sup>) and becomes exothermic in water ( $\Delta E = -18.2$  kcal mol<sup>-1</sup>).

We re-investigated the reaction inside a (6,6) carbon nanotube, using the M06-2X functional and without imposing any geometry constraints on the nanotube and the endohedral reacting system. The length of the model-CNT was 12.08 Å and its diameter 8.08 Å, close enough to the values that characterize the (9,0) model-CNT (7.12 and 11.37 Å) used by Schlegel and Halls in their B3PW91 computations. The effect of the CNT on the relative energy of the three critical points **RC**, **TS** and **PC** is remarkable: **PC** is now 13.5 kcal mol<sup>-1</sup> above the initial complex **RC** and the activation barrier decreases to 25.7 kcal mol<sup>-1</sup>. Thus, the reaction is significantly accelerated and becomes much less endothermic. The strong catalytic effect exerted by CNT, that resembles that of a non-polar solvent (see above), was similarly demonstrated by Schlegel computations, but in that case the reaction became exothermic.

Some interesting aspects of our computations should be emphasized. The full geometry optimization adopted in our model leads to a distortion of the carbon nanotube framework caused by the interactions between the reacting system and the nanotube electron density. This distortion could not be observed by Schlegel who kept frozen the CNT structure during geometry optimization. After formation of the preliminary complex the section of the CNT becomes an ellipse (see Figure 3.3) whose major axis is 8.61 Å (the diameter of the empty tube is 8.08 Å). This value becomes 8.40 Å in the transition state and 8.41 Å in the product complex.

Non-conventional weak interactions between C-H, N-H and Cl of the endohedral system and the electron cloud of the surrounding nanotube can explain the speedup of the reaction (catalytic effect), the reduced endothermic character of the process and the structural distortion of the tube. The carbons of the CNT can interact with the three C-H bonds (C-H... $\pi$  interactions), the three N-H bonds (N-H... $\pi$  interactions) and the chlorine atom (Cl... $\pi$  interactions) of the endohedral system. All these non-covalent, weak interactions are well known: they are prevalent in large biological systems and play a key role in chemical and biological recognition processes.<sup>201</sup> In particular, C-H... $\pi$  interactions are stabilizing interactions featuring, for instance, T-shaped structures between aromatic rings.<sup>202</sup> N-H... $\pi$  interactions, first observed in structures of haemoglobin-ligand complexes, have been recognized to be rather common in many protein crystal structures.<sup>202c</sup>

Similarly Cl... $\pi$  interactions are important in determining crystal packing and protein-ligand complexes.<sup>203</sup>

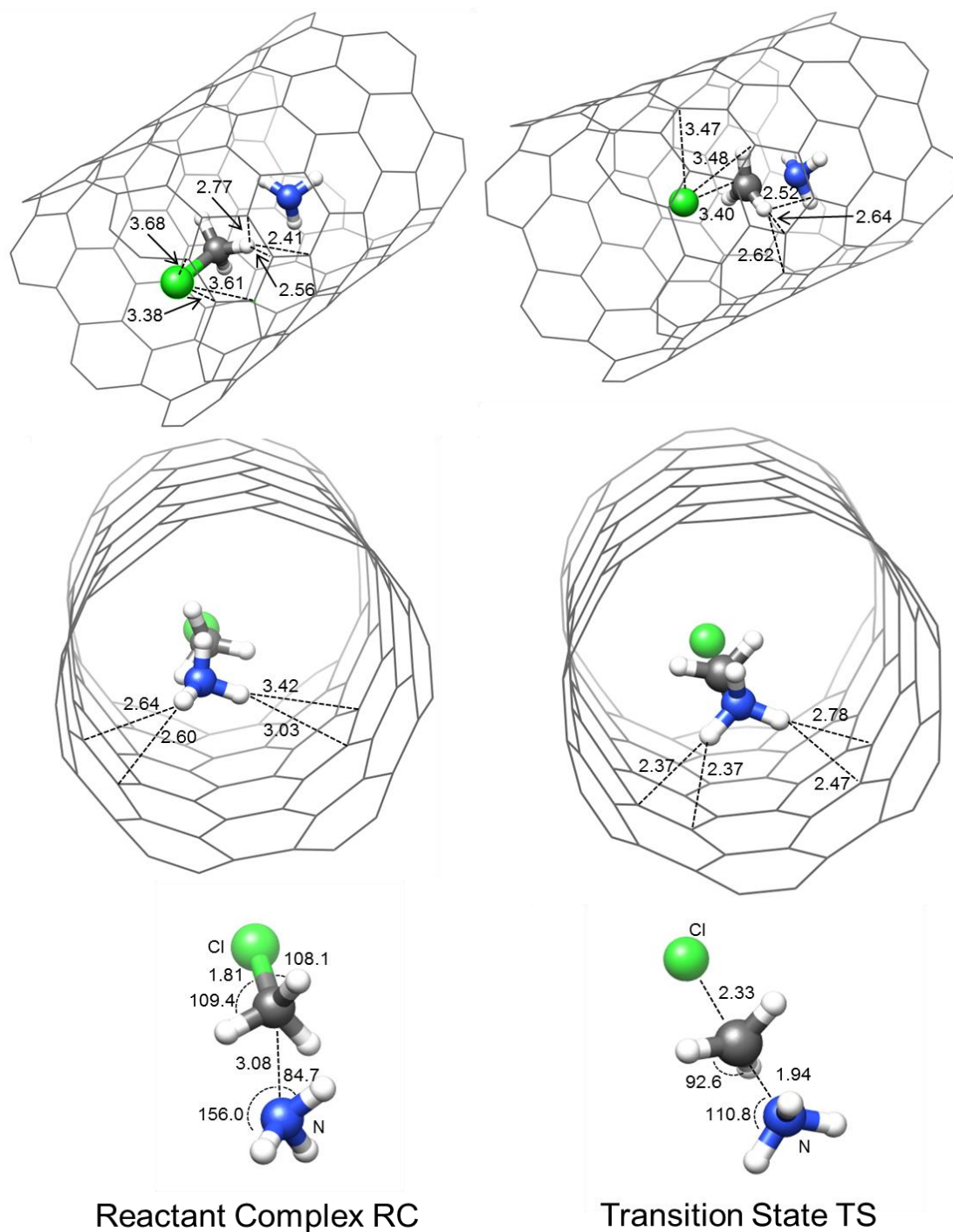


**Figure 3.3**

CNT-confined Menshutkin  $S_N2$  reaction: a schematic representation of the preliminary complex **RC** and transition state **TS** computed at the M06-2X level. At the bottom of the figure we have hidden the tube structure and we have represented only the reacting system. Geometrical parameters are given in Å and degrees.

High-level *ab-initio* computations using various model-systems were carried out during the last decade to evaluate structural features and energetics of these non-covalent interactions.<sup>204</sup> The M06-2X functional used in our computations provides a reliable description of these interactions, similar to that obtained at higher levels of theory (such as CCSDT and MP2).<sup>204</sup>

Our computations showed that the reacting system is not symmetrically arranged along the tube axis. This is particularly evident in the **RC** complex where the angle between the ternary axis of ammonia (which only weakly interacts with H<sub>3</sub>CCl, the N...C distance being 3.08 Å) and the tube axis is 47.7°. As a result the NH<sub>3</sub> molecule orients itself to maximize the interactions of two N-H bonds with the tube wall. To obtain a rough estimate of these interactions we computed the average distances between the three nitrogen-bonded H atoms and the tube carbon atoms (for each hydrogen considered the five shortest H...C(tube) distances). The average distances for H<sub>1</sub> and H<sub>2</sub> (the two hydrogens closest to the wall) are 2.74 and 3.06 Å. The average N-H...CNT distance that characterizes H<sub>3</sub> is much larger i.e. 3.46 Å. In Figure 3.3, for a better understanding of these contacts, we report the two shortest distances between H<sub>1</sub> and H<sub>2</sub> and the tube carbon atoms: 2.60 and 2.64 Å for H<sub>1</sub> and 2.97 and 2.78 Å for H<sub>2</sub>. In the transition state, the interaction of the NH<sub>3</sub> fragment with H<sub>3</sub>CCl becomes stronger (the N...C distance is 1.94 Å). This increases, in turn, the ammonium ion character of nitrogen and, consequently, the positive charge on the hydrogen atoms: the average charge of the three hydrogens varies from 0.44 in **RC** to 0.47 in **TS**. Since NH<sub>3</sub> is now strongly anchored to H<sub>3</sub>CCl, the distortion of the system is restrained and the three fragments remain approximately aligned. Also, the augmented positive charges of the hydrogens make possible stronger interactions with the CNT. To optimize these interactions the entire system moves, as much as possible, toward the tube wall allowing a simultaneous stronger interaction of two N-H bonds with the π-electron cloud, as evidenced by the average N-H...CNT distances of H<sub>1</sub> and H<sub>2</sub> that become 2.62 and 2.72 Å, respectively. As a consequence of the repositioning of the system, H<sub>3</sub> is now, on average, more distant from the tube wall (3.99 Å). To describe more completely the arrangement of the reacting system inside the tube and to compare **TS** to **RC**, we reported in Figure 3.3 the two shortest N-H...CNT distances for H<sub>1</sub> (2.37 and 2.37 Å) and H<sub>2</sub> (2.47 and 2.78 Å). On the whole the stabilizing effect of the N-H...π interactions increases from **RC** to **TS**.

A different trend was found for the C-H...π interactions. In this case the average C-H...CNT distances of the three carbon-bonded H atoms are 3.28, 2.64 and 3.17 Å in **RC**, which become 2.84, 2.59 and 3.77 Å in **TS**. It is evident that in the first case this interaction becomes more stabilizing,

in the second case its effect does not significantly change, and in the third case it becomes less stabilizing, suggesting that on the whole the stabilization due to C-H... $\pi$  interactions is approximately the same in **RC** and **TS**. A similar trend was found for the Cl... $\pi$  interactions, the average Cl...CNT distance being 3.49 Å in **RC** and 3.47 Å in **TS**, which indicates an approximately constant stabilizing effect: it is worth outlining that these values satisfactorily agree with those obtained in high level *ab-initio* computations carried out on chlorohydrocarbon model systems.<sup>204</sup>

In conclusion, the overall augmented stabilizing effect of N-H... $\pi$  contacts seems to be responsible for the decrease of the activation barrier and the consequent catalytic effect of CNT. In the last decade the importance of these interaction for the recognition and binding of carbon nanostructures by proteins was demonstrated.<sup>205</sup>

A similar analysis performed for the product complex **PC** shows that the NH... $\pi$  interactions are also responsible for the reduced endothermicity of the reaction with respect to the gas phase.

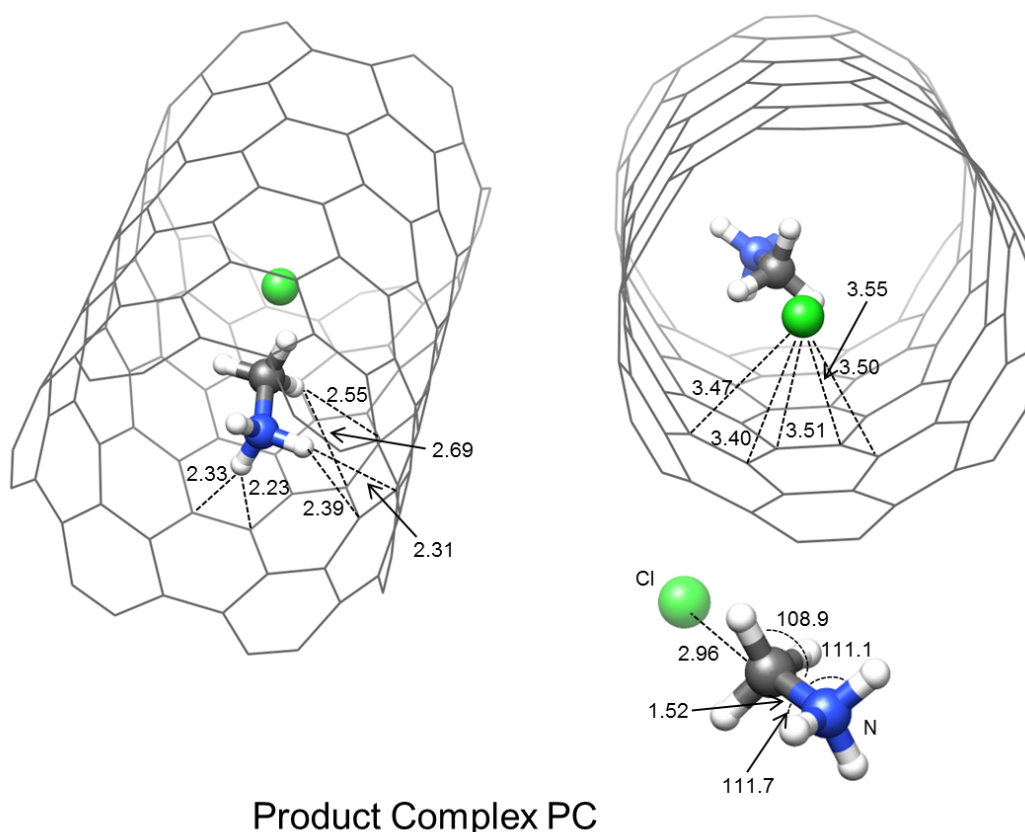


**Figure 3.4**

CNT-confined Menshutkin  $S_N2$  reaction: a schematic representation of the final product complex **PC** computed at the M06-2X level. At the bottom of the figure we have hidden the tube structure and we have represented only the reacting system. Geometrical parameters are given in Å and degrees.

According to the augmented ammonium character of nitrogen, the positive charges on the N-bonded hydrogens further increase (the average charge of the three hydrogens becomes 0.50), causing the increase of the stabilizing NH... $\pi$  interactions: this is confirmed by the average NH...CNT distances of the three NH bonds, that become 2.53, 3.90 and 2.60 Å (all three values are shorter with respect to those of **TS** and two of them significantly shorter with respect to **RC**). The trend observed for the CH... $\pi$  and Cl... $\pi$  interactions on passing from **RC** to **PC** is similar to that evidenced in the **RC-TS** comparison: the C-H...CNT distances of the three carbon-bonded H atoms are 2.99, 2.68 and 3.56 Å while the average Cl...CNT distance is 3.49 Å suggesting again that on the whole their effect does not change significantly (Figure 3.4).

### 3.2.2 CNT confined reaction using hybrid methods

Taking into account the results of our previous work where we showed that a hybrid QM/MM (MM = UFF force-field) is able to provide a reliable description of a prototype  $S_N2$  reaction ( $Cl^{(-)} + H_3CCl = H_3CCl + Cl^{(-)}$ ) occurring within a nanotube, we used the same computational approach to study the CNT-confined Menshukin reaction. We obtained an activation barrier  $E_a$  of 25.8 kcal mol<sup>-1</sup> and an endothermicity value  $\Delta E$  of 18.1 kcal mol<sup>-1</sup>. While the activation barrier is in very good agreement with the value obtained in the full QM computation for the same model-system (25.7 kcal mol<sup>-1</sup>), the endothermicity  $\Delta E$  is rather overestimated (18.1 vs. 13.5 kcal mol<sup>-1</sup>). This result could be ascribed to the fact that, since the UFF force-field includes only van der Waals interactions (in the Lennard-Jones-type form), to take partially into account the electronic polarizability of the nanotube we used a charge equilibration approach (as implemented in the Gaussian09 package) based on the QM charges of the reacting system and the MM charges of the tube. Our results clearly show that this approach is unsatisfactory and probably underestimates the tube polarization: actually, the major discrepancy between the full QM and the QM/MM computations was found in the energy of the final complex **PC** (and the consequent endothermicity  $\Delta E$ ) where the polarization effects become more important because of the net charge separation occurring in the product.

To correct the lack of our QM/MM approach we carried out single-point QM/MM computations with PCM corrections on the previously optimized QM/MM structures. Since in the PCM approach the system is placed inside a cavity embedded in a polarizable continuum characterized by a fixed dielectric constant, it is reasonable to expect that part of the stabilizing effect due to the polarizability of the nanotube (and that was missed because of the absence of

explicit  $\pi$  electron orbitals) can be recovered in this way. The results of these computations (using the benzene dielectric constant) confirm the accuracy of this model: the activation barrier changes slightly (from 25.8 to 24.5 kcal mol<sup>-1</sup>) while a more significant variation was found for reaction energy  $\Delta E$  that becomes 13.1 kcal mol<sup>-1</sup>, a value in good agreement with the full QM computations (13.5 kcal mol<sup>-1</sup>). In our previous discussion we showed that a rather complex interplay of non-bonded interactions (Cl... $\pi$ , C-H... $\pi$  and especially N-H... $\pi$  interactions) is the key-factor determining the catalytic effect of the nanotube (decrease of activation barrier  $E_a$ ) and reaction energy  $\Delta E$  with respect to the gas-phase. Since it is conceivable that the relative importance of these interactions in **RC**, **TS** and **PC** can be significantly affected by a change of the tube radius, in principle, different CNT diameters could lead to an increase/decrease of the catalytic effect. To elucidate the actual effect of the tube diameter on the reaction energetics, we examined at the M06-2X/UFF level (followed by single-point PCM computations in benzene) various CNT model-systems with different radii: (4,4), (5,5), (6,6), (7,7), (8,8), (9,9), (10,10), (12,12), (14,14) and, as a limit case, a graphene sheet. Taking into account the results of our previous work<sup>181</sup> on S<sub>N</sub>2 reactions, where we demonstrated that a change in the length of the tube for values larger than 24.4 Å does not significantly affect the activation barrier (the barrier reached an asymptotic value), we fixed the tube length at 24 Å.

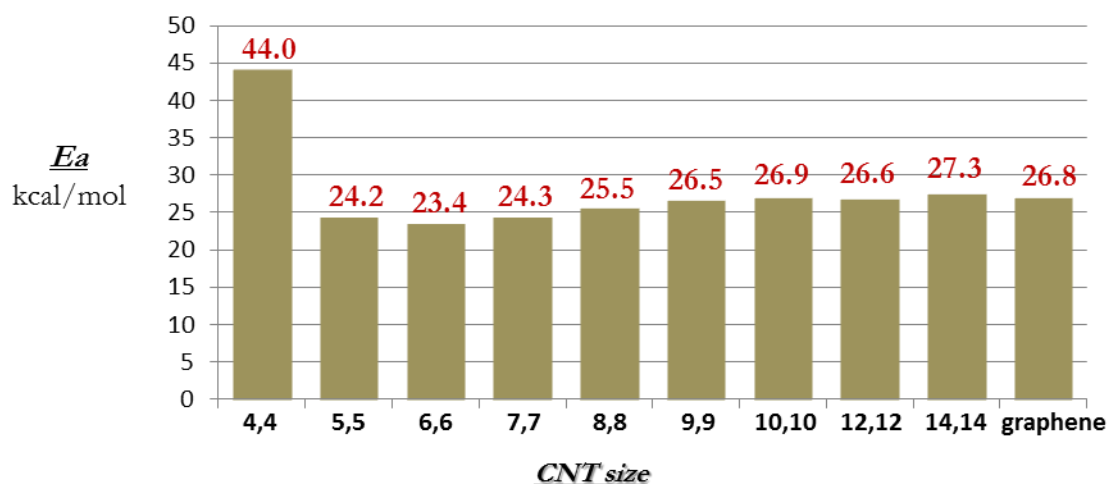


**Figure 3.5**

Diagram showing the variation of the activation barrier  $E_a$  (kcal mol<sup>-1</sup>) as a function of the tube radius.



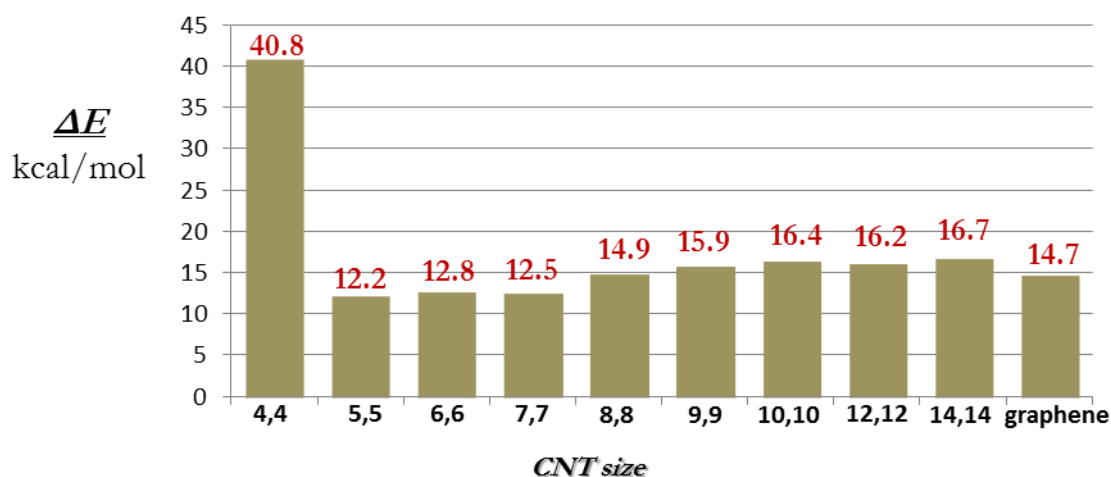


**Figure 3.6**

Diagram showing the variation of the reaction energy  $\Delta E$  ( $\text{kcal mol}^{-1}$ ) as a function of the tube radius.

We have summarized the results for the various CNTs in Figure 3.5 and 3.6 where the trends of the activation barrier  $E_a$  and reaction energy  $\Delta E$  are reported as a function of the tube size. In the two figures we show that both  $E_a$  and  $\Delta E$  values are very large for narrow tubes (44.0 and 40.8  $\text{kcal mol}^{-1}$  in the (4,4) case), they suddenly decrease (24.2 and 12.2  $\text{kcal mol}^{-1}$ ) for a (5,5) tube and do not change significantly with the growing tube radius ((6,6) and (7,7)) until the (8,8) case (25.5 and 14.9  $\text{kcal mol}^{-1}$ ). A further increase of  $E_a$  and  $\Delta E$  is observed for larger tubes. For a (9,9) tube these quantities become 26.5 and 15.9  $\text{kcal mol}^{-1}$  and remain almost constant for larger tubes: 27.3 and 16.7  $\text{kcal mol}^{-1}$  are the values computed for a (14,14) CNT and 26.8 and 14.7  $\text{kcal mol}^{-1}$  in the limit case of an infinite radius represented by a graphene sheet. The lowest activation energy (23.4  $\text{kcal mol}^{-1}$ ) was found in the (6,6) case. This value is a little lower than that computed in the benchmark QM/MM computation for a tube length of 12 Å (24.5  $\text{kcal mol}^{-1}$ ), suggesting that the longer tube provides a more complete description of non-bonded interactions.

These results can be easily understood. The arrangement and the structure of the reacting endohedral system are strongly affected by the tube radius and the associated augmented (or reduced) volume inside the tube. Since the available volume is reduced for small (4,4) tubes, in order to avoid too short distances between the hydrogen atoms and the tube wall (which could make the non-bonded N-H... $\pi$  and C-H... $\pi$  interactions repulsive), the structure of the transition state changes dramatically: the axis of the  $\text{NH}_3$  group and that of the  $\text{CH}_3$  group are not collinear with the tube axis, but point in the direction of the tube wall (Figure 3.7).

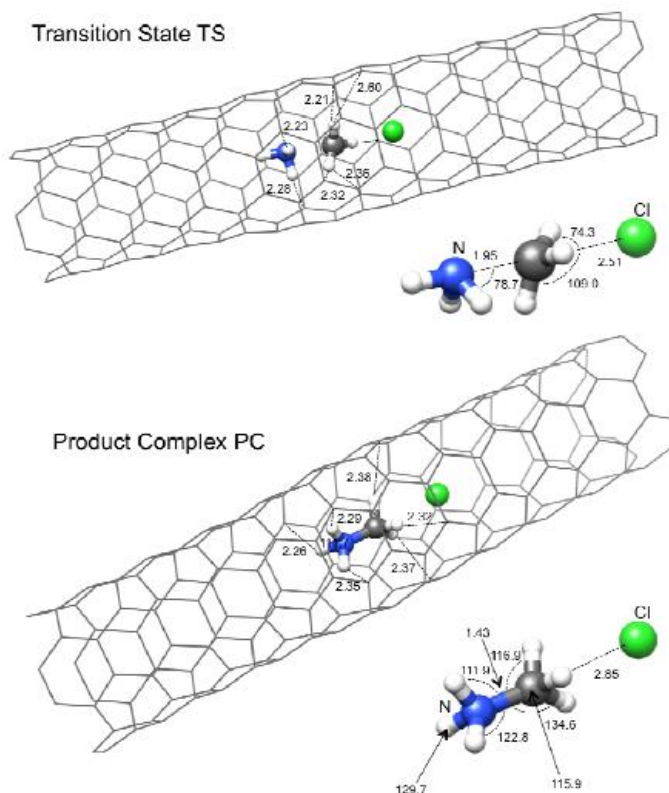


**Figure 3.7**

CNT-confined Menshutkin SN<sub>2</sub> reaction: a schematic representation of transition state **TS** and product complex **PC** computed at the M062X/UFF level in a (4,4) tube. The pictures highlight the strong structural distortion caused by confinement. Geometrical parameters are given in Å and degrees.

As a consequence the central carbon does not attain the usual planar structure approximately orthogonal to the reaction coordinate N...C...Cl and the breaking C-Cl bond becomes significantly longer (2.51 Å) than in the reference (6,6) case. This structural distortion causes a strong destabilization of **TS** and a consequent very large activation barrier (44.0 kcal mol<sup>-1</sup>). A similar argument can be used to explain the high ΔE value (40.8 kcal mol<sup>-1</sup>). Because of the vicinity of the tube wall the ammonium species is characterized by HNC and HCN angles significantly larger (<HNC = 111.9°, 122.8°, 129.7° and <HCN = 116.9°, 115.9°, 134.6) than those found in the (6,6) tube where they are much closer to the “ideal” value of 109.5°. These “unnatural” angles are certainly responsible for the destabilization of the product complex.

The sudden decrease of E<sub>a</sub> and ΔE observed for a (5,5) tube (24.2 and 12.2 kcal mol<sup>-1</sup>, respectively) occurs because the augmented volume allows an arrangement of the reacting system similar to that previously described for the (6,6) case (reaction coordinate N...C...Cl collinear with the tube axis). Since no significant structural changes are observed in the (7,7) CNT case, where the reaction coordinate only slightly deviates from the direction of the tube axis, E<sub>a</sub> and ΔE remain almost constant.

When the volume inside the tube further grows ((8,8), (9,9) and (10,10) tubes) various structural arrangements of the reacting system with respect to the tube wall become possible.

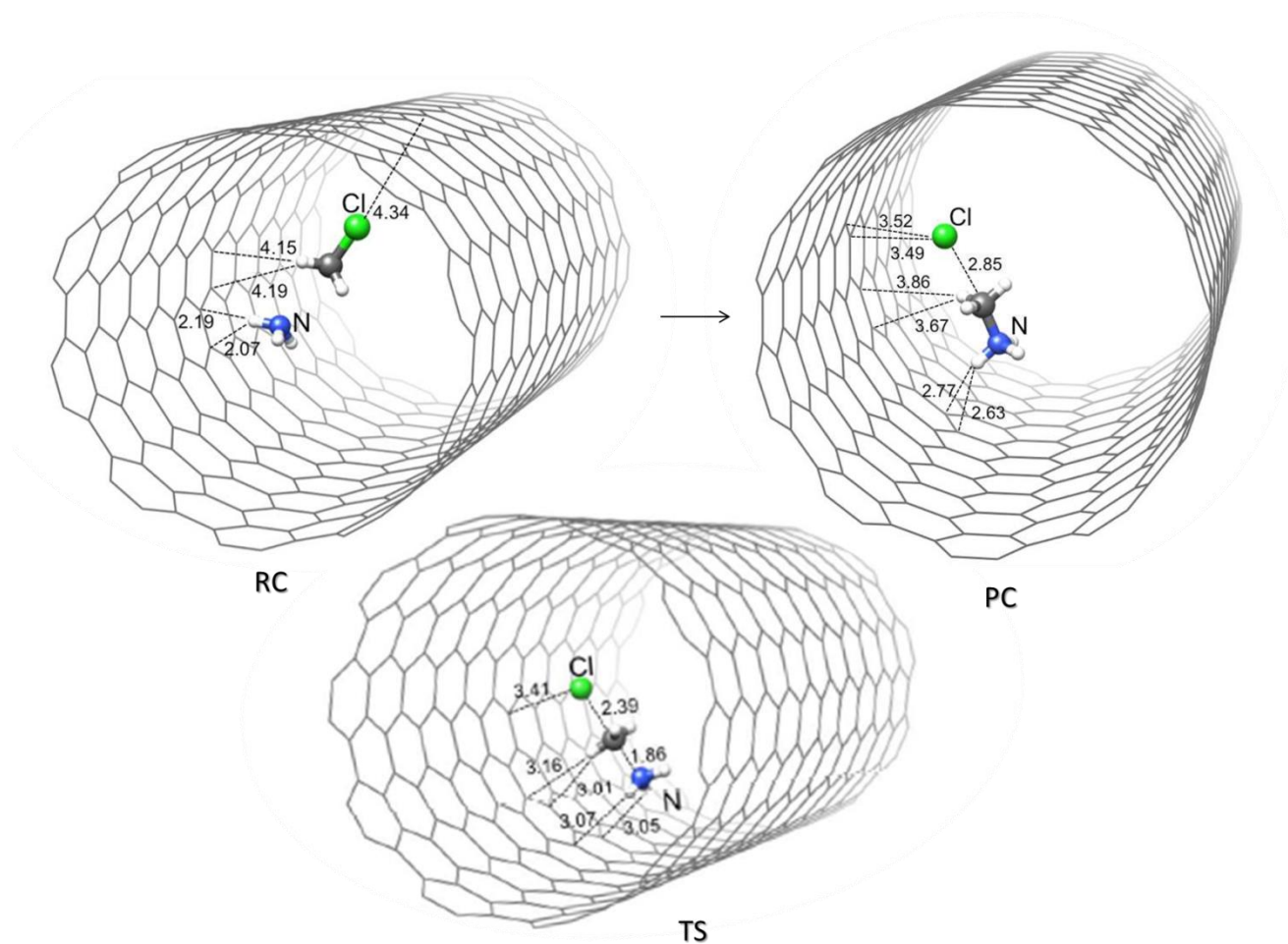


**Figure 3.8**

CNT-confined Menshutkin  $S_N2$  reaction: a schematic representation of the preliminary complex **I** and transition state **TS** computed at the M06-2X/UFF level in a (14,14) tube. In the transition state the reaction coordinate is orthogonal to a plane cutting the tube along the main axis. Geometrical parameters are given in Å and degrees.

The minimum energy arrangements of **RC**, **TS** and **PC** found for a (10,10) CNT are shown in Figure 3.8. The Cl... $\pi$ , C-H... $\pi$  and N-H... $\pi$  interactions fasten the reacting system to the tube wall in such a way that the reaction coordinate becomes approximately orthogonal to a plane cutting the tube along the axis. In **RC** the dominant interaction of the reacting system with the tube wall involves only one NH bond as shown in Figure 3.8 (the two shortest N-H...CNT distances are 2.07 and 2.19 Å), while the two remaining hydrogens are significantly more distant from the tube frame. Also the Cl... $\pi$  and C-H... $\pi$  contacts are rather weak: the shortest Cl...CNT distance is 4.34 Å and the shortest C-H...CNT distances are 4.15 and 4.19 Å. In **TS** the system appears to be more strictly

pasted to the CNT wall. We observed a significant increase of Cl... $\pi$  and C-H... $\pi$  interactions, as suggested by the shorter Cl...CNT and C-H...CNT distances, while the single strong N-H... $\pi$  contact found in **RC** is replaced by two average N-H... $\pi$  contacts (N-H...CNT = 3.07 and 3.05 Å). On the whole the various stabilizing interactions in **TS**, characterized by a developing charge separation, appear more important than in **RC** and contribute to maintain the activation barrier lower with respect to the gas phase. Our results suggest that the differential stabilization from **RC** to **TS** is lower than that found in smaller CNTs where the reduced available space forces stronger contacts between the reacting system and the carbon wall. In the product complex **PC** the position of the reacting system is similar to that found in **TS**, i.e. it adheres to the CNT wall. In this case, as a consequence of the net charge separation, N-H... $\pi$  and Cl... $\pi$  become the dominant stabilizing interactions. Only one of the three ammonium hydrogens significantly interacts with the carbon wall, the two shortest N-H...CNT distances being 2.63 and 2.77 Å. The two shortest distances featuring the contact between Cl and the wall are 3.49 and 3.52 Å. The structural arrangement of the reacting system remains approximately the same for larger tubes and for the graphene sheet in agreement with the almost constant value of the barrier.

### 3.3 Computational Details

Nanotubes were built using the Nanotube Builder plugin, as implemented in VMD.<sup>189</sup> Carbon atoms at the two far ends of the tube were hydrogen-terminated. All the computations were carried out with the Gaussian09<sup>4</sup> series of programs. In the full QM calculations we used the DFT M06-2X<sup>24,25</sup> functional. The 3-21G\*<sup>190</sup> and the 6-31+G\*<sup>191</sup> basis sets were chosen to describe the nanotube and the endohedral reactive system, respectively. ONIOM calculations<sup>41</sup> were performed considering mechanical and electrostatic embedding. The inner layer (high-level layer) consisted of the reacting system, i.e.  $\text{H}_3\text{N} + \text{H}_3\text{CCl} = \text{H}_3\text{NCH}_3^{(+)} + \text{Cl}^{(-)}$ . This was described at the DFT level using the M06-2X functional and the 6-31+G\* basis set. The outer layer (low-level layer) was formed by the nanotube and was described at the molecular mechanics (MM) level using the UFF<sup>29</sup> force field. In the MM calculations, partial atomic (point) charges were calculated using the QEq formalism.<sup>195</sup> The structure of the various critical points (minima and saddle points) was fully optimized. Frequency calculations were carried out at the same level of theory to check the nature of critical points. The solvent effect was evaluated with the Polarizable Continuum Model (PCM),<sup>100</sup> as implemented in Gaussian 09.

### 3.4 Conclusions

In this second work about chemistry inside Carbon Nanotubes we investigated the effects of CNT confinement on the model Menshutkin reaction  $\text{H}_3\text{N} + \text{H}_3\text{CCl} = \text{H}_3\text{NCH}_3^{(+)} + \text{Cl}^{(-)}$  using either a full QM approach or a hybrid QM/MM approach. This prototype reaction is representative of chemical processes involving developing of charge separation along the reaction pathway. Our aim was to carry out an accurate benchmark on the features of the hybrid QM/MM method required for an accurate description of this type of reactions occurring inside a nanotube. In agreement with previous Schlegel results,<sup>200</sup> we found that the CNT speeds up the reaction with respect to the gas-phase and this “catalytic” effect is similar to that of a non-polar solvent. The CNT causes a significant decrease of both activation barrier  $E_a$  (from 34.6 in gas-phase to 25.7 kcal mol<sup>-1</sup>) and endothermicity  $\Delta E$  (from 31.2 in gas-phase to 13.5 kcal mol<sup>-1</sup>). Our analysis of the structure of the reactant complex **RC**, transition state **TS** and product complex **PC** showed that the lower barrier and lower endothermicity can be ascribed to a complex interplay between C-H $\cdots\pi$ , N-H $\cdots\pi$  and Cl $\cdots\pi$  non-bonded interactions of the endohedral system with the electron cloud of the CNT wall. Because of the increasing charge separation occurring along the reaction coordinate **RC**→**TS**→**PC**, the N-H $\cdots\pi$  contacts play a dominant role in determining the reaction speedup and the  $\Delta E$  decrease: they are significantly more stabilizing in **TS** and **PC** with respect to **RC**, while the effect of the C-H $\cdots\pi$  and Cl $\cdots\pi$  contacts remain approximately constant along the reaction coordinate. We compared the results of the full QM approach (DFT using the M06-2X functional) to those obtained with a QM/MM approach (same DFT functional and MM=UFF force field). This was the same hybrid method that we previous demonstrated to provide reliable results in the case of the prototype chloride exchange  $S_N2$  reaction of methyl chloride. Contrary to what found in that case, for the Menshutkin reaction we found that, in the presence of a net charge separation such as that featuring the product complex **PC**, the simple QEq formalism (included in the MM potential) was not able to describe properly the effect of CNT polarization that was clearly underestimated: accordingly, a significant discrepancy between the two approaches was found in the computation of reaction energy  $\Delta E$  (18.1 and 13.5 kcal mol<sup>-1</sup> at the QM and QM/MM level, respectively), while the activation barrier was satisfactorily reproduced by the QM/MM approach (25.8 vs. 25.7 kcal mol<sup>-1</sup>). We demonstrated that a more accurate estimate of the tube polarization can be obtained with single-point QM/MM computations with PCM corrections (using the benzene dielectric constant) on the

QM/MM optimized structures. In our opinion this approach partially recovers the absence, in the MM treatment, of explicit  $\pi$  electron orbitals of the tube wall. According to our model we observed a small change of activation barrier (from 25.8 to 24.5 kcal mol<sup>-1</sup>) and a more significant variation of  $\Delta E$  that becomes 13.1 kcal mol<sup>-1</sup>, in rather good agreement with the full QM computations. We suggest this level of theory (QM/MM with PCM correction, MM = UFF) as a more general approach capable of describing CNT-confined chemical processes involving significant charge separation. To examine the effects on reaction energetics of the change of the CNT diameter and to obtain a more exhaustive description of the confinement effects, we extended our computational approach (QM/MM followed by PCM computations) to CNTs of different radii: (4,4), (5,5), (6,6), (7,7), (8,8), (9,9), (10,10), (12,12), (14,14) CNTs and, as a limit case, a graphene sheet. The lack of space available in small tubes (4,4) causes a strong structural distortion and a consequent destabilization of transition state **TS** and product complex **PC**: both activation barrier and reaction energy strongly increase to become 40.8 kcal mol<sup>-1</sup> and 44.0 kcal mol<sup>-1</sup>. The augmented volume inside the tube in the (5,5) case determines a sudden decrease of these quantities: the arrangement of the reacting system becomes similar to that observed for a (6,6) tube, which is characterized by the lowest value of  $E_a$  (23.4 kcal mol<sup>-1</sup>). A growth of the volume inside the tube ((8,8), (9,9) and (10,10)) determines a weak increase of  $E_a$  and  $\Delta E$  (26.5 and 15.9 kcal mol<sup>-1</sup> for a (9,9) tube). These values remain almost constant for larger tubes until the limiting case of graphene. This increase is associated with different structural arrangements of the endohedral system. A detailed analysis of the (10,10) case shows that the Cl $\cdots\pi$ , C-H $\cdots\pi$  and N-H $\cdots\pi$  interactions fasten the reacting system to the tube wall and the reaction coordinate becomes approximately orthogonal to a plane cutting the tube along the axis. In this case all non-bonded interactions seem to contribute to maintain the activation barrier lower with respect to the gas phase, even if the catalytic effect is less pronounced than that found in smaller CNTs.

## 4. Regioselective control of CNT confined aromatic halogenation reactions:<sup>206</sup> a computational study

### 4.1 Introduction

The examples presented above opened a new scenario in the field of catalysis by carbon nanostructures. However, up to date, in the majority of examples of CNT-based catalysis reported in literature, the active phase was the external wall interacting with the reacting species.<sup>207,208</sup> Experimental results for important industrial processes carried out in the presence of CNTs are available in literature. For instance, it was shown that, thanks to the presence of surface oxygens, MWCNTs effectively catalyse the oxidative dehydrogenation of ethylbenzene to styrene.<sup>207</sup> Other recent experimental data showed that defective MWCNTs are active in the benzene hydroxylation to phenol, thus avoiding a multistep process involving cumene and cumene hydroperoxide.<sup>208</sup> A further interesting example of an industrially relevant reaction, where CNTs behave as metal-free catalysts, is the catalytic oxidation of cyclohexane to cyclohexanol and cyclohexanone.<sup>208</sup>

The use of carbon nanotubes as nanocontainers now appears an alternative and admittedly challenging way to promote catalysis, manipulate reaction pathways and govern the outcome of chemical reactions.<sup>208,209</sup> Various experiments demonstrated that the CNT confinement can lead to significant modifications on structure and distribution of encapsulated molecules which, in principle, can assume properties rather different from those found in the bulk.<sup>210</sup> For instance, when water molecules are confined inside a nanotube they form layered cylindrical structures.<sup>210a</sup> In the case of a (10,10) tube these structures consist of hydrogen-bonded heptagonal rings that are not found in the bulk phase. Studies on confined metal catalysts inside CNTs showed that, in addition to the effect of spatial restriction on the metal particles and local concentration of reactants inside the tube, the interaction between the encapsulated molecules and the inner tube surface modifies the redox properties of metal catalysts.<sup>210c</sup> Other examples of confinement of different molecules within nanotubes are reported in the literature suggesting in general that a nanotube is not only a passive nanocontainer but, since it can affect structures and properties of confined molecules, it can work as an effective nanoreactor.<sup>209b,210</sup> Unfortunately, in spite of the large number of papers concerning CNTs and their catalytic role in reactions, a clear experimental evidence of catalysis involving the internal surface is not yet widely documented. This is partly due to the difficulties in

discriminating the molecules inside and outside CNTs and determining the corresponding concentration. Nevertheless, a few examples have already appeared in literature.<sup>206,211</sup>

## 4.2 Aromatic halogenation reactions in single-walled carbon nanoreactors

Recently Khlobystov and co-workers demonstrated that single-wall CNTs can be used as effective nanoreactors for preparative chemical reactions. They found that the spatial confinement of reactant molecules inside the tube drastically affects both the regioselectivity and kinetics of aromatic halogenation reactions.<sup>206</sup> The bromination of N-phenylacetamide was taken as the model system to study the effect of the confinement on regioselectivity. The authors carried out the bromination reaction in the absence of nanotubes and inside several SWNT differing in diameter at room temperature.

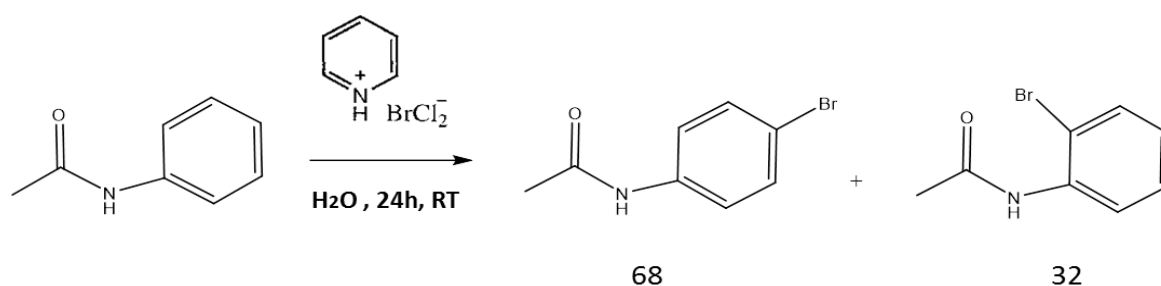


**Figure 4.1**

Schematic representation of the model bromination reaction<sup>206</sup>

The bromination reaction readily occurred in water solution in the absence of nanotubes, reliably and reproducibly forming an unselective 68:32 mixture of N-(4-bromophenyl)acetamide (para-regioisomer) and N-(2-bromophenyl)acetamide (ortho-regioisomer) respectively (Figure 4.1).<sup>206</sup> Subsequently, in order to prove selectivity, the model substrates were reacted in the presence to various nanotube of suitable diameter which can successfully discriminate between the formation of para- and ortho-products. Three SWNT family groups, divided according to the average diameter of production, were employed (Figure 4.2). Among these SWNT produced by Arc Discharge (AD) (figure 4.2c) and by supported cobalt and molybdenum catalysis (CoMoCAT<sup>®</sup>) processes (figure 4.2a) have average diameters respectively wider and narrower than that produced by HiPco<sup>®</sup> (high pressure carbon monoxide method)<sup>212</sup> process (figure 4.2b). Geometric constrain



showed single-walled carbon nanotubes produced by the HiPco<sup>®</sup> process to have the most suitable diameters for this purpose.

To be sure that the reaction can take place successfully within the CNT it is necessary that the substrate and the reagent are encapsulated before their use. The authors tested a cunning methods of reactant encapsulation by immersing the open nanotubes in molten N-phenylacetamide; the capillary forces provided to fill spontaneously nanotubes with the reactant. The excess of N-phenylacetamide adsorbed on SWNT outer wall is removed prior to the reaction by means of a fractional distillation procedure.<sup>206,213</sup>

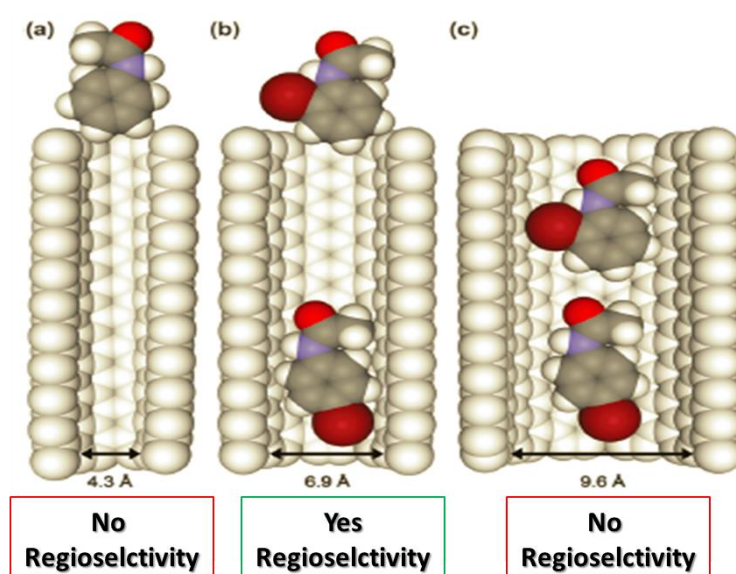


**Figure 4.2**

Van der Waals diameter of three types of nanotubes. (a) CoMoCAT SWNT too narrow to allow confinement of the reactant; (b) HiPCO SWNT, allowing the formation of para- but not ortho-product and (c) wider AD SWNT freely allowing the formation of both products.

In the table 4.1 the effect of the CNTs confinement on the regioselective bromination of N-phenylacetamide is reported. The use of HiPco SWNT (entry 2) points out a significant improvement in para-selectivity of the reaction compared to the reaction in solution without SWNT (entry 1). The use of wider AD and narrower CoMoCAT SWNT resulted in no change toward para-selectivity with respect to the reaction in solution without SWNT (entry 1). The AD nanotube diameter is large enough to get the product with no size discrimination. CoMoCAT Van Der Waals diameter is insufficient to encapsulate N-phenylacetamide reactant molecules (figure 4.2).

<i>Entry</i>	Carbon nanotube presence	Halogenation agent	Product ratio/%	
			Para	Ortho
1	<i>None</i>	BrCl	68	32
2	<i>HiPCO® SWNT</i>	BrCl	97	3
3	<i>CoMoCAT® SWNT</i>	BrCl	70	30
4	<i>AD SWNT</i>	BrCl	69	31

**Table 4.1**

Effect of confinement in nanotubes on the regioselective halogenation of N-phenylacetamide

Strikingly the authors as well as showing a strong increase in regioselectivity, also observed a kinetic improvement. Indeed theoretical product ratios based on calculated SWNT capacity, for the confined reaction, showed that the selectivity for the para-product is higher than is expected (Table 4.2).<sup>206</sup>

	Product Ratio / %	
	<i>para</i>	<i>ortho</i>
<b>Calculated</b>	71.5	28.5
<b>Experimental</b>	97	3

**Table 4.2**

Theoretical product ratios based on calculated SWNT capacity.

The authors tried to rationalize the discrepancy between calculated and experimental product ratios assuming that it can depend by diffusion into the nanotube combined with an accelerated confined reaction rate compared to the bulk. However to have a detailed view is necessary to evaluate the mechanism and the activation barriers of the reaction. In conjunction with our research interests focused on CNT confined reactions, a computational study on the mechanism of this bromination reactions we carried out attempting to rationalize these important experimental results. The reported results can be useful in searching for a predictive tool to design the best host to control a chemical reaction inside a carbon nanotube.

## 4.3 Results and discussion

### 4.3.1 Computed reaction without CNT

As a basal point we had to identify the bromination reaction mechanism with no CNT employing a full QM approach. As brominating agent was experimentally used pyridinium dichlorobromate, (Figure 4.1) considered as a safe source of bromine chloride BrCl.<sup>214</sup>

The reaction taken into account is a classical Aromatic Electrophilic Substitution ( $S_{EAr}$ ), considered the most characteristic reactions of aromatic systems. The  $S_{EAr}$  are typically described by the two-stage mechanism process depicted in Figure 4.3. However is well documented in literature<sup>215</sup> that this traditional interpretations for the  $S_{EAr}$  mechanism is not always the most advantageous path. Indeed the experimental reaction conditions strongly affected the substitution yields often optimized by using highly polar media, Lewis acid or zeolite catalysts, strong electrophiles, and by the choice of substituents.

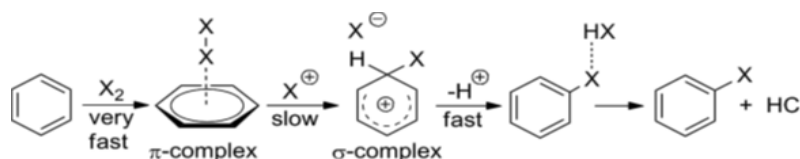


**Figure 4.3**

Typical mechanism for  $S_{EAr}$  reactions via arenium ion ( $\sigma$ -complex) formation.

In the light of these experimental considerations Schleyer et al.<sup>216</sup> have been demonstrated that the  $S_{EAr}$  mechanisms, for bromination and chlorination reactions on different aromatic substrates, may also involve several different pathways. Among these a direct substitution with a single concerted transition state following the barrierless formation of a products  $\pi$ -complex seems to be kinetically favored.<sup>215,216</sup> This is especially true in gas-phase and in non-polar solvents where the conventional arenium ion ( $\sigma$ -complex) intermediate is unstable due to the presence of the strong charge separation unsupported in a non-polar medium and obviously in gas-phase. Moreover Keefer et al.<sup>217</sup> have experimentally established a specific catalytic role of one of the reaction product, hydrogen chloride, in non-polar environments. Therefore in our studies we had to take into account also the catalytic effect of HCl.<sup>215</sup>

In order to model exhaustively the mechanism we preliminarily studied the gas-phase reaction with no CNT. The energies of the optimized critical structures along the Para(A) and

Ortho(B) reaction pathways, for gas phase bromination of N-phenylacetamide, are summarized in Figure 4.5. Among the pathway Para is observed the direct substitution as the favored reaction channel associated with an activation barrier of 54.3 kcal mol<sup>-1</sup>. However, the non-bonding interaction between the N-H of the amide and the chlorine, stabilizes the intermediate I-O (NH...Cl 1.78 Å CH...Cl 2.46 Å Figure 4.4) which is 8.9 kcal mol<sup>-1</sup> above the reactant complex C1 in the ortho reaction pathway. Because of this, the gas phase Ortho bromination proceeds via arenium ion (σ-complex I-O) intermediate (two-step mechanism) and in contrast to the usual knowledge, results kinetically favored on the Para position (Figure 4.5).

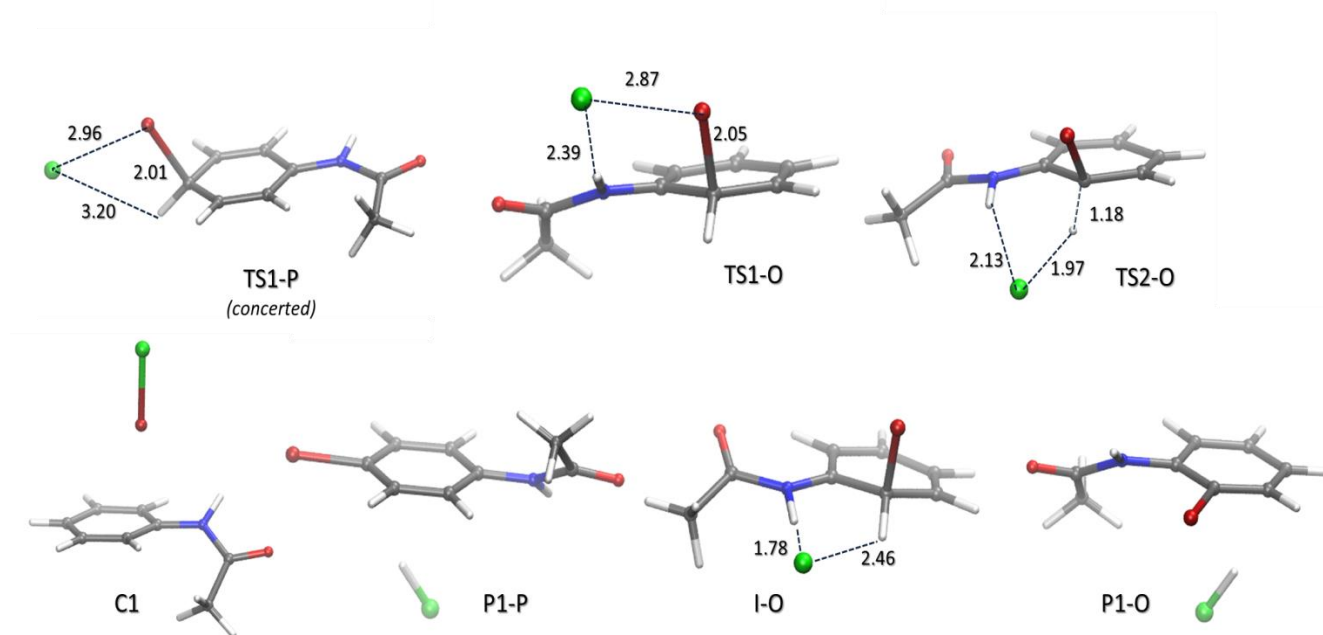


**Figure 4.4**

Three dimensional representation of critical points for the uncatalyzed gas-phase bromination of N-phenylacetamide computed at the M06-2x/6-31+G(2d) level (bond lengths in Å).

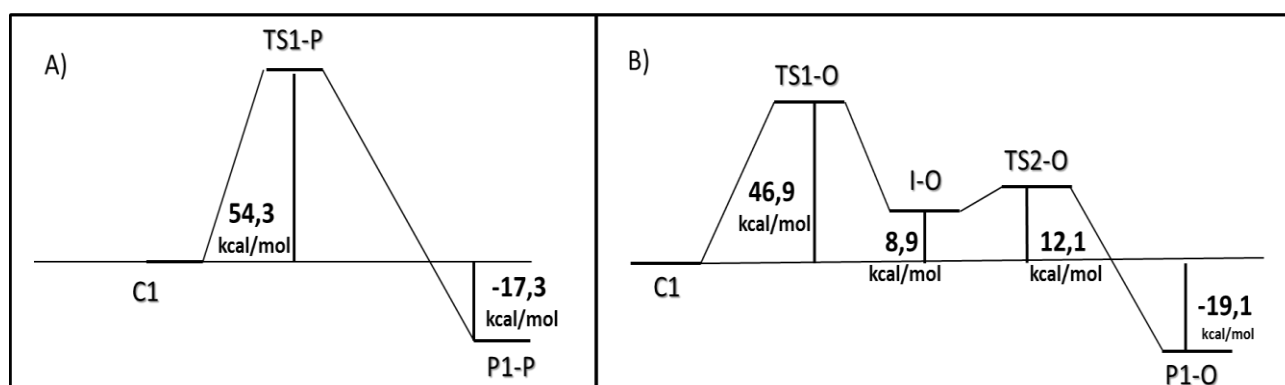


**Figure 4.5**

The Para A) (concerted single step mechanism) and Ortho B) (classical two step via arenium ion intermediate mechanism) computed reaction profiles for the uncatalyzed gas-phase bromination of N-phenylacetamide. The total energy values are in kcalmol<sup>-1</sup>

The **TS1-O**, which is the rate determining step along the Ortho profile, is 7.4 kcal mol<sup>-1</sup> lower than **TS1-P** (54.3 kcal mol<sup>-1</sup>). The structures of the stationary points along the PES of the gas-phase bromination reaction are illustrated in Figure 4.4.

In addition the catalytic effect of HCl on the gas-phase N-phenylacetamide bromination we have evaluated. The Ortho and Para profiles for the HCl catalysed reactions are reported in Figure 4.7. The effectiveness of the catalysis by HCl is revealed by the considerably lowered activation barriers. The N-H of the amide plays an active role also in the ortho catalyzed process making it once again favored compared to the Para direct substitution (Figure 4.7). In the Figure 4.6 the three dimensional structure of the critical points for the HCl-catalyzed reaction are reported.

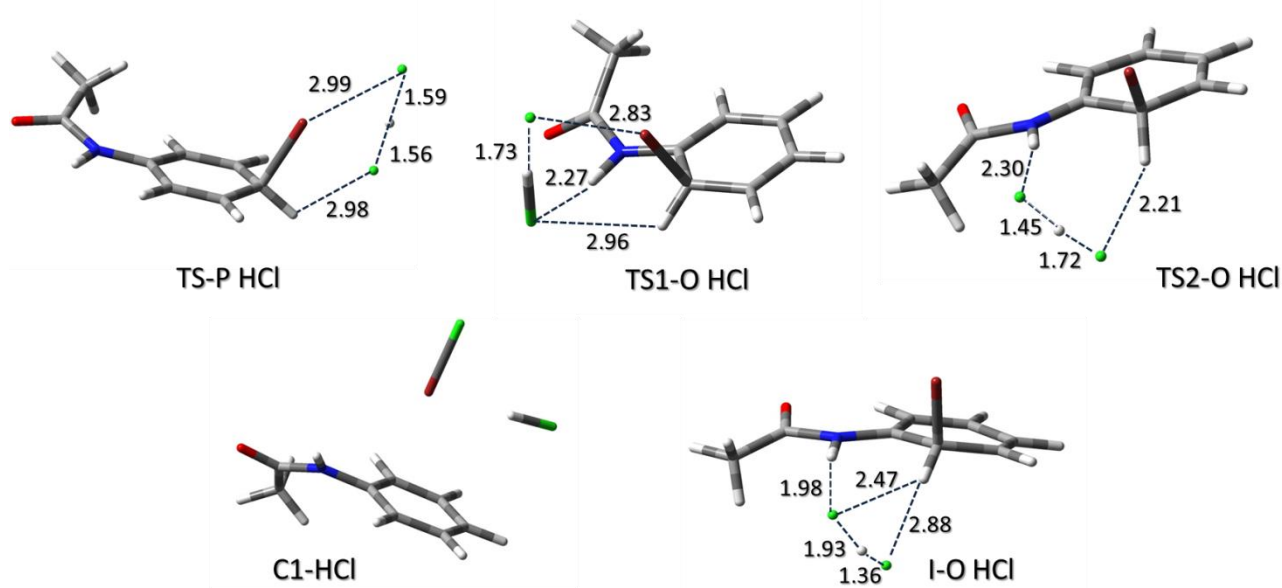


**Figure 4.6**

Three dimensional representation of critical points for the HCl-catalyzed gas-phase bromination of N-phenylacetamide. computed at the M06-2x/6-31+G(2d) level (bond lengths in Å).

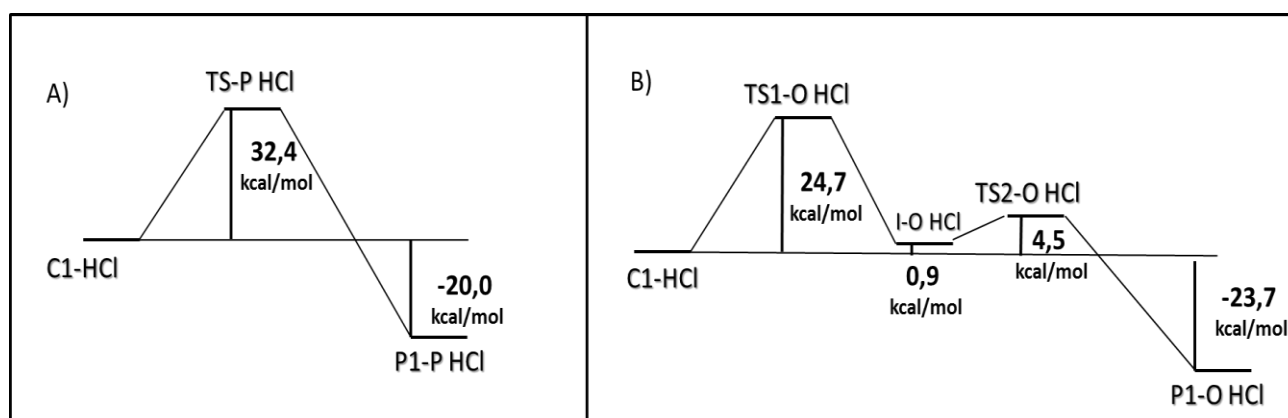


**Figure 4.7**

The Para A) (concerted single step mechanism) and Ortho B) (classical two step via arenium ion intermediate mechanism) computed reaction profiles for the HCl-catalyzed gas-phase bromination of N-phenylacetamide. The total energy values are in kcalmol<sup>-1</sup>

The arenium ion intermediate **I-O HCl** (0.9 kcal mol<sup>-1</sup> above the reactant complex **C1-HCl**) is obtained overcoming the transition state **TS1-O HCl** (24.7 kcal mol<sup>-1</sup>) which is 22.2 kcal mol<sup>-1</sup> lower than **TS1-O**. The Para direct substitution has an activation barrier of 32.4 kcal mol<sup>-1</sup> (**TS1-P HCl**), 21,9 kcal mol<sup>-1</sup> less of the uncatalysed substitution (**TS1-P** 54.3 kcal mol<sup>-1</sup>).

In Table 4.3 the general framework of the gas-phase bromination process is summarized. The first emerging result is the marked efficacy of the HCl catalyst which is able to significantly stabilize the energies of the critical points.

REACTION OCCURRING IN <i><b>GAS-PHASE</b></i>	
Entry	
1. <b>Concerted</b>	<b>Para;</b> TS: 54.3
2. <b>Non-concerted path (Wheland intermediate)</b>	<b>Ortho;</b> TS1: 46.9; TS2: 12.1
3. <b>HCl catalysis</b>	<b>Para;</b> (concerted) TS: 32.4 <b>Ortho;</b> (non-concerted) TS1: 24.7 ; TS2: 4.5

**Table 4.3**

Energy summary table of the gas-phase reaction

According to experimental conditions used by the authors (Figure 4.1), we re-computed the Ortho and Para reaction profiles in water using an implicit PCM approach.<sup>100</sup> Our computations revealed a classical two-step mechanism involving arenium ion ( $\sigma$ -complex) intermediate for both Ortho and Para substitutions (see Figure 4.9 and 4.11). This is allowed by the strong stabilization of the intermediate performed by the high polarity of the aqueous medium.

In Figure 4.9 and Figure 4.11 the energetic profiles of the Para and Ortho pathways are respectively reported. The transition state along the Para profile **TS1-Pw** (9.6 kcal mol<sup>-1</sup> above the reactant complex C1-w), corresponding to formation of the  $\sigma$ -complex **I-Pw** (6.7 kcal mol<sup>-1</sup> above the reactant complex C1-w), is 3.4 kcal mol<sup>-1</sup> lower than **TS1-Ow** along the Ortho path (13.0 kcal mol<sup>-1</sup> above the reactant complex C1-w).

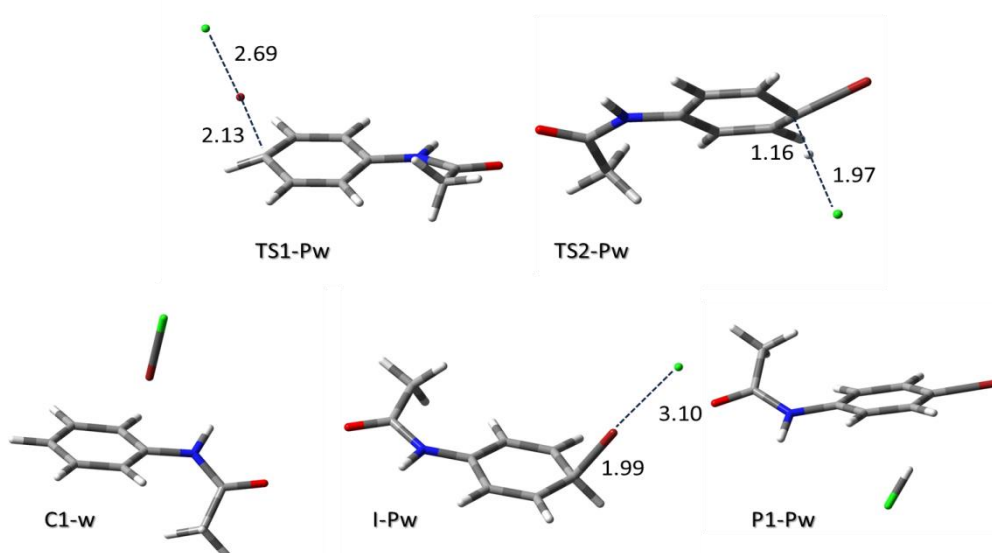


**Figure 4.8**  
 Three dimensional representation of critical points for the Para bromination of N-phenylacetamide computed at the M06-2x/6-31+G(2d) level in simulated water solvent (bond lengths in Å).

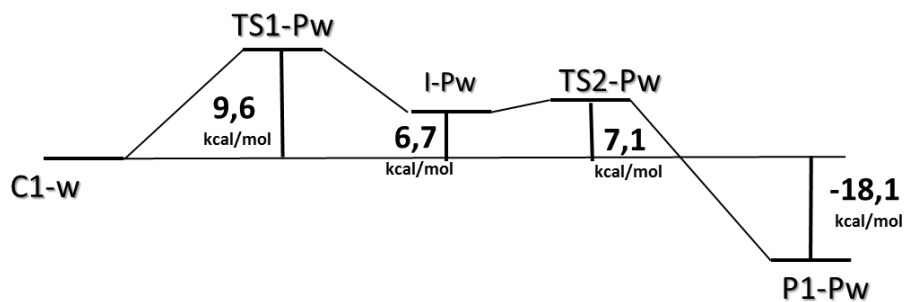


**Figure 4.9**  
 The Para computed reaction profile for bromination of N-phenylacetamide in water solvent. The total energy values are in  $\text{kcal}\cdot\text{mol}^{-1}$

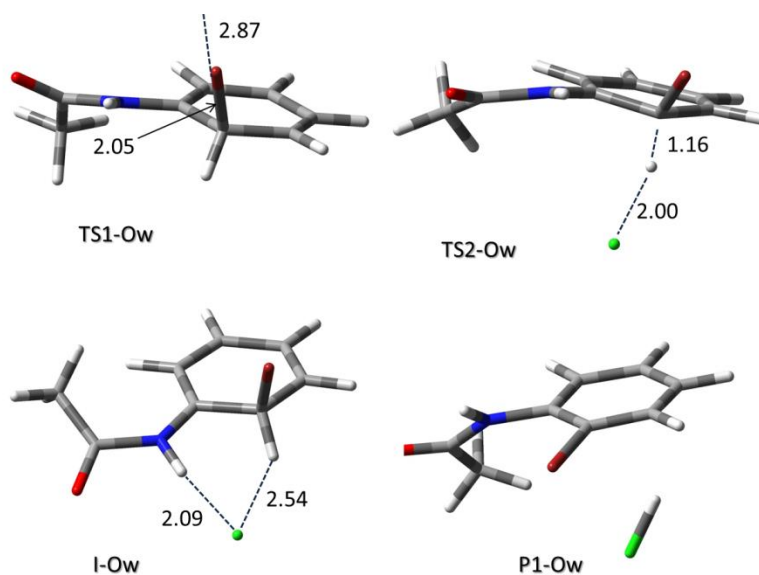


**Figure 4.10**  
 Three dimensional representation of critical points for the Ortho bromination of N-phenylacetamide. computed at the M06-2x/6-31+G(2d) level in simulated water solvent (bond lengths in Å).

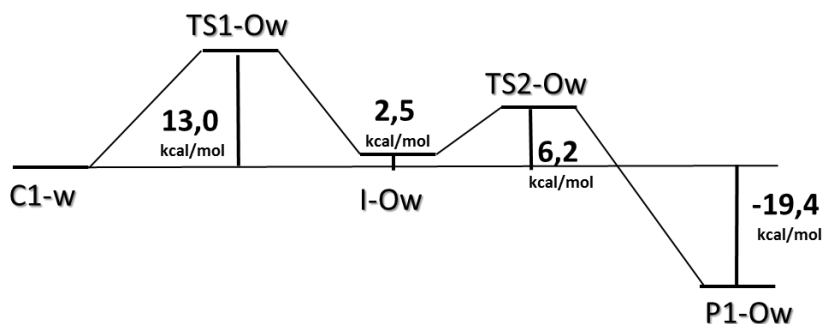


**Figure 4.11**

The Ortho computed reaction profile for bromination of N-phenylacetamide in water solvent. The total energy values are in kcal·mol<sup>-1</sup>

The energy values of **TS1-Pw** and **TS1-Ow** (rate determining step in both cases) clearly indicates that in aqueous solution the Para substitution is favoured respect to the Ortho position. This is consistent with the experimental data of Table 4.1, in which the Para product is slightly favored than Ortho ones providing a product ratio% 68:32 respectively. It is interesting to note that the  $\sigma$ -complex **I-Pw** is less stabilized comparing with **I-Ow** (2.5 kcal mol<sup>-1</sup> above the reactant complex C1-w) in which the N-H...Cl interaction (2.09 Å Figure 4.10) cause a significant decrease of the energy. A three dimensional representations of the structures identified along the energy profiles are shown in Figure 4.8 for the Para and Figure 4.10 for the Ortho pathways. Since in aqueous solution the strongly acid HCl results largely dissociated the catalytic effect of the HCl on the bromination reaction in water solvent may be negligible, therefore, it was not considered by us.

The Table 4.4 summarize the general framework of the bromination process in water solvent. A much more linear situation respect to the gas-phase is obtained. The unique favored channel for the bromination reaction remains the classical two-step substitution for both of the Ortho and Para positions.

REACTION OCCURRING IN WATER SOLUTION	
entry	<b>H<sub>2</sub>O</b>
1. <b>Non-concerted path</b> (Wheland intermediate)	<b>Para;</b> TS1: 9.6, TS2: 7.1
	<b>Ortho;</b> TS1: 13.0, TS2: 6.2

**Table 4.4**

Energy summary table of reaction in water solvent



### 4.3.2 The CNT Confined Reaction

We reinvestigate the bromination of N-phenylacetamide inside selective carbon nanotubes using the hybrid QM/MM (MM = UFF force-field) method tested to be able to provide a reliable description of two prototype  $S_N2$  reaction ( $Cl^{(-)} + H_3CCl = H_3CCl + Cl^{(-)}$  and the Menshutkin  $S_N2$  reaction) occurring within a nanotube. The armchair (8,8) CNT, which has a diameter of 10.8 Å, was chosen as the best suitable CNT to reproduce the selective CNTs (Figure 4.2b) used in the experimental process (the average diameter of the CNT produced by HiPCO is about 10Å). The length of the model-CNT(8,8) used was 12.08 Å as in our previous work.

First we studied the CNT confined bromination in the gas-phase to have an initial basis of comparison with the previous results on the same gas-phase reaction without CNT. The computed Para and Ortho energetic profiles of the gas-phase bromination are grouped together in the figure 4.12 in which are also present the reaction profiles for the Para and Ortho HCl catalysed reaction (Figure 4.12b).

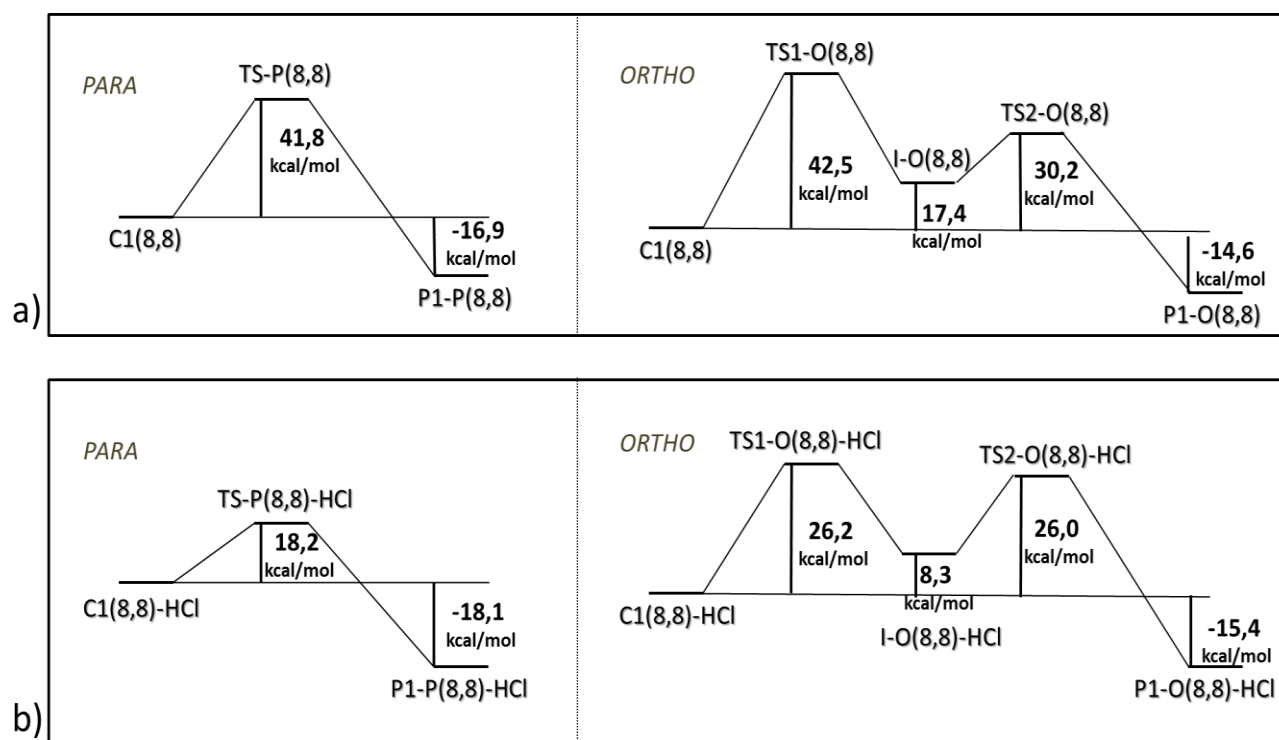


**Figure 4.12**

- a) Para and Ortho computed reaction profiles for CNT-confined bromination of N-phenylacetamide in gas-phase.  
 b) Para and Ortho computed reaction profiles for CNT-confined bromination of N-phenylacetamide in gas-phase catalysed by HCl. The total energy values are in kcal·mol<sup>-1</sup>

The reaction mechanisms remains broadly unchanged from the non-confined reaction (Figure 4.5) for both Para and Ortho substitution. Our computations confirmed the single-step (direct concerted substitution) mechanism for the Para substitution and the classical two-step mechanism in the Ortho. The effect of the CNT on the relative energy of the critical points is evident. As regards the uncatalysed process (Figure 4.12a) in the Para concerted mechanism the activation barrier decreases to 41.8 kcal·mol<sup>-1</sup> (**TS-P(8,8)**), and becomes slightly lower than the Ortho rate determining transition state **TS1-O(8,8)** (42.5 kcal·mol<sup>-1</sup>). On the contrary the energy of the second Ortho transition state increases (**TS2-O(8,8)** 30.2 kcal·mol<sup>-1</sup>) and the intermediate **I-O(8,8)** appears to be strongly destabilized (17.4 kcal·mol<sup>-1</sup> above the reactant  $\pi$ -complex **C1(8,8)**).

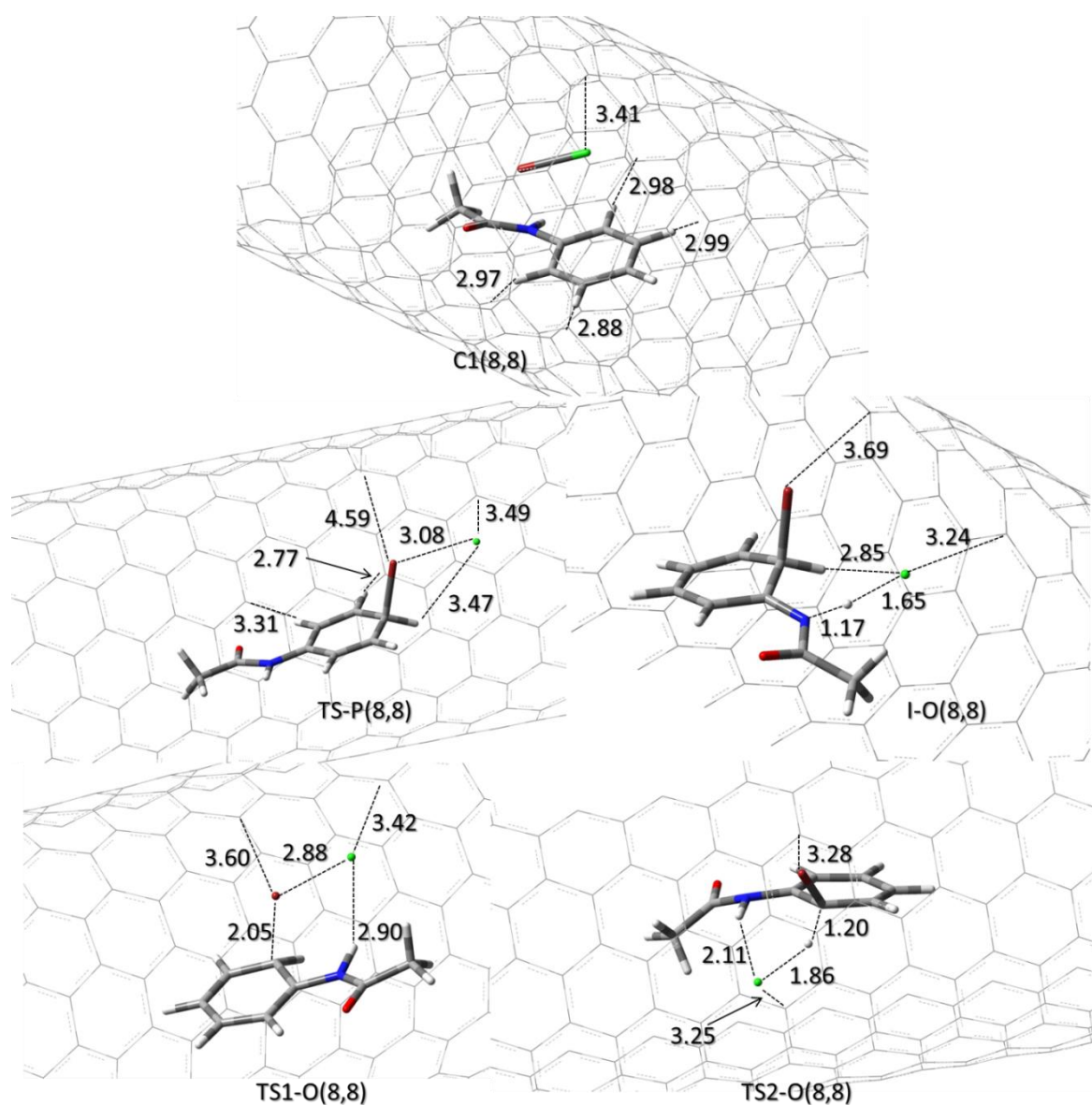


**Figure 4.13**

Three dimensional representation of the main critical points for the Para and Ortho CNT-confined bromination of N-phenylacetamide, computed at the M06-2x(6-31+G(2d))/UFF level (bond lengths in Å).

The general reduced activation barriers observed may depend by the non-conventional weak interactions between the endohedral system and the electron cloud of the surrounding nanotube. However, the geometric constraints imposed by the CNT(8,8), which has an internal Van der Waals diameter (about 6.9 Å) comparable with the critical van der Waals diameter of the reactant (6.9 Å)<sup>206</sup>, causes structural changes in the transition states and intermediate leading to the Ortho product. In the figure 4.13 three dimensional representation of the critical points for the gas-phase confined reaction with the main geometrical parameter are reported. The available volume, inside the CNT, is lacking to both sides corresponding to the Ortho positions of the N-phenylacetamide, therefore, the transition states **TS1-O(8,8)** and **TS2-O(8,8)** and the intermediate **I-O(8,8)** needs to adapt their geometry to avoid too short distances between the halogens Cl and Br and the tube wall. Actually, as evidenced by the values of the Br...C(wall) in Figure 4.13 (3.60Å for **TS1-O(8,8)**, 3.28Å for **TS2-O(8,8)** and 3.69Å for **I-O(8,8)**), the massive bromine atom is too close to the CNT wall making the non-bonded Br...π interactions repulsive especially in **TS2-O(8,8)**. In the **TS1-O(8,8)** the distance NH-Cl (2.90Å) is very stretched with respect to NH-Cl of the **TS1-O** (2.39Å Figure 4.4) thus its stabilization inner phase is lower than to that observed for the transition state Para.

The same observations can be made for the HCl catalyzed reaction (Figure 4.12b). The concerted single step mechanism is observed for the Para substitution whereas the classical two-step mechanism for the Ortho.

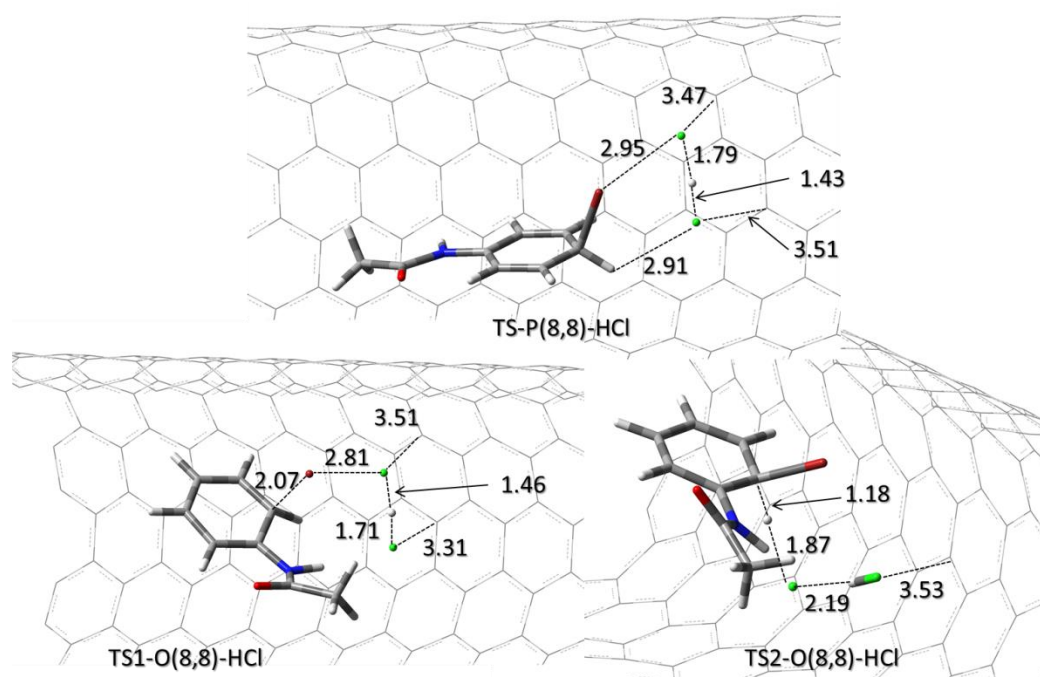


**Figure 4.14**

Three dimensional representation of the transition states for the Para and Ortho CNT-confined bromination of N-phenylacetamide. computed at the M06-2x(6-31+G(2d))/UFF level (bond lengths in Å).

The difference between the Para and Ortho catalyzed profiles is more evident due to the presence of the HCl molecule that even more cluttered the already too lacking space around the Ortho positions (see figure 4.14). This leads to a structural distortion to the two Ortho transition states that become isoenergetic ( $26.2 \text{ kcal}\cdot\text{mol}^{-1}$  **TS1-O(8,8)-HCl**  $26.0 \text{ kcal}\cdot\text{mol}^{-1}$  **TS2-O(8,8)-HCl**). The Para transition state **TS-P(8,8)-HCl** decreases until  $18.2 \text{ kcal}\cdot\text{mol}^{-1}$ .

The above results demonstrated a slight increase in regioselectivity towards the para-product in the gas-phase, confirming that confinement in SWNT can promote the formation of the para-product. However, only on the HCl catalyzed reaction differences in activation barriers are relevant to explain the selectivity towards the para-product.

As well as considered for the unconfined reaction we re-computed the bromination reaction trying to simulate the same reaction conditions experimentally used. In this context some interesting aspects should be taken into account. In the experimental procedure SWNT filled with the reagent were added to the aqueous solution of pyridinium dichlorobromate. Since N-phenylacetamide is very slightly soluble in water at room temperature the reaction could proceed in the same N-phenylacetamide as solvent inner phase. The reaction could start at the ends of the CNT and gradually proceed by diffusion into the nanotube catalyzed by the HCl *in-situ* produced. Therefore we reinvestigate the CNT confined bromination in ethylbenzene to better simulate N-phenylacetamide as solvent ( $\epsilon$  (Ethylbenzene) = 2.5  $\epsilon$  (N-phenylacetamide) = 2.9) using an implicit PCM approach.<sup>100</sup>. The computed energetic profiles for the uncatalyzed and catalyzed process in ethylbenzene are reported in figure 4.15. The same remarks for the gas-phase confined reaction can be made for the reaction CNT-confined in ethylbenzene, indeed, the same unchanged mechanisms remained for both profiles Para and Ortho. However, along the uncatalyzed pathway (Figure 4.15a), although the energy barrier of the Para concerted transition state (**TS-P(8,8)-Et**) is slightly lower ( $29.9 \text{ kcal}\cdot\text{mol}^{-1}$ ) compared to the rate determining Ortho transition state (**TS1-O(8,8)-Et**) ( $34.2 \text{ kcal}\cdot\text{mol}^{-1}$ ) they are too close to explain the pronounced regioselectivity experimentally observed. In the catalyzed process (Figure 4.15b), which remains the energetically favored channel of the CNT-confined reaction, the lowered activation barrier provided for the Para concerted substitution ( $10.3 \text{ kcal}\cdot\text{mol}^{-1}$ ) generates a marked difference compared to the Ortho transition states (**TS1-O(8,8)-HCl-Et** and **TS2-O(8,8)-HCl-Et**) that have a rather high activation barriers ( $24.6 \text{ kcal}\cdot\text{mol}^{-1}$  and  $25.5 \text{ kcal}\cdot\text{mol}^{-1}$  respectively) contributing to increasing the product ratio in favor of the Para-product.

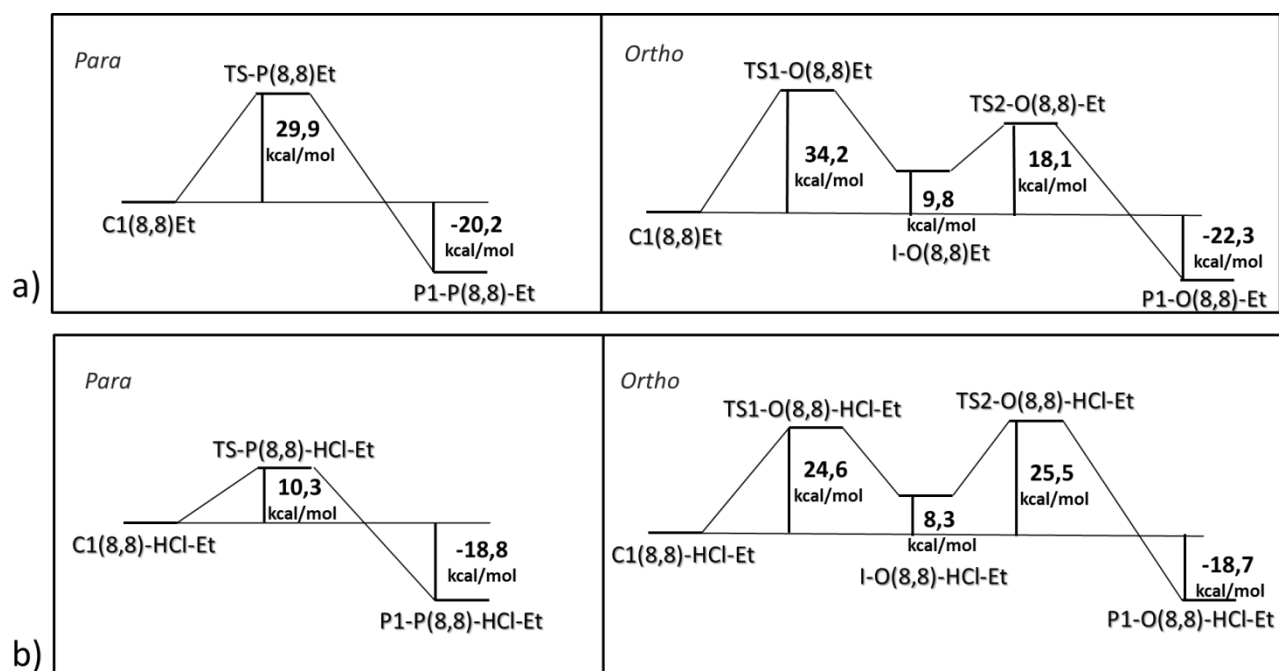


**Figure 4.15**

a) Para and Ortho computed reaction profiles for CNT-confined bromination of N-phenylacetamide in simulated ethylbenzene solvent. b) Para and Ortho computed reaction profiles for CNT-confined bromination of N-phenylacetamide catalysed by HCl in simulated ethylbenzene solvent. The total energy values are in kcal·mol<sup>-1</sup>

The large increase in the Ortho activation barriers in the catalysed confined reaction (ethylbenzene solvent) can successfully explain the regioselectivity observed by the authors in the experimental work (see Table 4.1). Indeed, in the water reaction without CNT (Figures 4.9 and 4.11) the energy difference between the two rate determining step (**TS1-Pw** 9.6 kcal·mol<sup>-1</sup> and **TS1-Ow** 13.0 kcal·mol<sup>-1</sup>) is just 3.4 kcal·mol<sup>-1</sup> contrasted with the more conspicuous 15.2 kcal·mol<sup>-1</sup> between **TS-P(8,8)-HCl-Et** and **TS2-O(8,8)-HCl-Et** along the confined reaction in ethylbenzene solvent (see Figure 14.b), this can easily explain the augmented Para-selectivity in the confined reaction reported in the experimental data (97:3 in favour of Para table 4.1). However, the closeness energy between **TS1-Pw** (9.6 kcal·mol<sup>-1</sup>) and **TS-P(8,8)-HCl-Et** (10.3 kcal·mol<sup>-1</sup>) does not indicate a clear kinetic improvement experimentally observed in the confined reaction. To rationalize this experimental evidence, we must consider that in the internal phase, the reactants are contained in a fairly small space, therefore, this amplified proximity effect increases the probability of favorable bumps resulting in a kinetic improvement.

#### 4.4 Computational details

Single-Walled Carbon Nanotubes were built using the Nanotube Builder plugin, as implemented in VMD.<sup>189</sup> All reported computations were carried out with the Gaussian09<sup>4</sup> series of programs. ONIOM calculations<sup>41</sup> were performed considering mechanical and electrostatic embedding. The inner layer (high-level layer), consisted of the reacting system, N-phenylacetamide, Br-Cl and H-Cl, were described at DFT level using the M06-2X functional<sup>24,25</sup> and the 6-31+G\* basis set.<sup>191</sup> The outer layer (low-level layer) was formed by the nanotube and was described using molecular mechanics (MM) UFF,<sup>29</sup> method. In the MM calculations partial atomic (point) charges were used to compute the electrostatic interactions. These charges were calculated using the QEq formalism.<sup>195</sup> The structure of the various critical points (minima and saddle points) was fully optimized. Frequency calculations were carried out at the same level of theory to check the nature of critical points. The solvent effects were taken into account during optimization using the polarizable continuum model (PCM) approach.<sup>100</sup>

#### 4.5 Conclusions

In this work a computational study on preparative aromatic halogenation reactions in carbon nanotube we carried out. We used a full QM and a previously tested hybrid QM/MM (MM = UFF force-field) approach to rationalize the effects of CNT confinement on the kinetic and regioselectivity of the reaction.

We first analyzed the reaction without CNT in the gas phase and in the bulk water solvent using a PCM approach. In the gas-phase the catalytic role of the hydrogen chloride (byproduct of the reaction) was also taken into account. We identified a single-step (direct concerted substitution) mechanism for the Para substitution and a classical two-step mechanism toward the Ortho position for both uncatalyzed and HCl-catalysed processes. The gas phase results showed a slight increase in regioselectivity towards the ortho-product due to the active role played by the N-H of the amide (next to the Ortho position) which stabilizes the Ortho intermediate and the transition states. Moreover we recorded a net effect of the HCl catalysis which stabilize all the critical point along the PES. Subsequently, according to experimental conditions used by the authors (Figure 4.1), we computed the Ortho and Para reaction in water solvent. Our computations revealed a classical two-step mechanism involving arenium ion ( $\sigma$ -complex) intermediate for both Ortho and Para

substitutions (see Figure 4.9 and 4.11). The energy values for **TS1-Pw** (9.6 kcal mol<sup>-1</sup> above the reactant complex C1-w) and **TS1-Ow** (13.0 kcal mol<sup>-1</sup> above the reactant complex C1-w), rate determining step in both cases, clearly indicated that in aqueous solution the Para substitution is favoured respect to the Ortho position. This is consistent with the experimental data in which the Para product is slightly favored than Ortho ones providing a product ratio% 68:32 respectively.

The CNT(8,8) as the best suitable nanocontainer to reproduce the selective nanotubes used in the experimental process were used to model the CNT-confined reaction. The computed gas-phase (Para and Ortho) energetic profiles confirmed the reaction mechanisms already seen for the not confined gas-phase reaction. A slight increase in regioselectivity towards the para-product is obtained, however, differences in activation barriers are significant only on the HCl catalyzed reaction to explain the experimentally observed regioselectivity. In this regard analyzing the experimental conditions and considering the poor solubility of the N-phenylacetamide in water we assumed that the reaction could gradually proceed by diffusion into the nanotube in the same N-phenylacetamide as solvent catalyzed by the HCl *in-situ* produced. Therefore we reinvestigate the CNT confined bromination in ethylbenzene which is the best available solvent in simulating N-phenylacetamide. Comparison of the computed energetic profiles in the bulk (water solvent) and inside CNT catalysed by HCl (ethylbenzene solvent) clearly indicate the strong increase in regioselectivity towards the para-product in the CNT-confined reaction, confirming the augmented selectivity observed in the experimental data (97:3 in favour of Para, table 4.1). However, these activation barriers (**TS1-Pw** 9.6 kcal mol<sup>-1</sup> and **TS-P(8,8)-HCl-Et** 10.3 kcal mol<sup>-1</sup>) are too close to explain the kinetic improvement observed by the authors which can be rationalized by an augmented proximity effect due to the reduced space in which are stored the encapsulated reactants.

# Part IV

## Bio-Catalysis



# 1. A computational investigation on the catalytic mechanism of Tyrosylprotein Sulfotransferases<sup>218</sup>

## 1.1 Introduction

The sulfonation of biomolecules has been known<sup>219</sup> for a long time to occur in organisms ranging from prokaryotes to multicellular species and the biotransformation of molecules by sulfonation is a basic metabolic route of primary importance.

The sulfonation is catalyzed by a broad class of enzymes called sulfotransferases (STs): these enzymes are responsible for catalyzing the transfer of a sulfonyl group ( $\text{SO}_3^-$ ) from an activated donor to a substrate compound containing hydroxyl or amino group which act as a nucleophile. The universal sulfate donor is 3'-phosphoadenosine-5'-phosphosulfate (PAPS). The process was originally indicated as *sulfation*, but a more appropriate definition would be *sulfonation* (or sulfonylation), because the group that is transferred is a sulfonyl ( $\text{SO}_3^-$ ) and not a sulfate ( $\text{SO}_4^{2-}$ ). However, the term *O*-sulfation is still used and refers to the transfer of  $\text{SO}_3^-$  to a substrate ( $\text{R-OH}$  or  $\text{R-NH}_2$ ) to obtain a sulfonated product ( $\text{R-OSO}_3^-$  or  $\text{R-NH-SO}_3^-$ ).<sup>220</sup>

There are two vast classes of STs: cytosolic and membrane-associated sulfotransferases. The first ones are involved in hormone regulation, drug metabolism and detoxification, while the membrane-associated sulfotransferases are responsible for the sulfonation of carbohydrates and proteins and play a key role in biochemical signaling pathway and molecular-recognition.

The first studies of STs have been carried out on cytosolic proteins and in 1998<sup>221</sup> the first cytosolic sulfotransferase crystal structure has been published. Membrane-associated sulfotransferases did not receive the same interest and only recently their important role in biological processes has been uncovered. Membrane-associated sulfotransferases include tyrosylprotein sulfotransferases (TPSTs), a particular group of sulfotransferases that transfer a sulfonyl group from the active donor 3'-phosphoadenosine-5'-phosphosulfate (PAPS) to the hydroxyl group of a protein bound tyrosine to form a *O*-sulfated tyrosine and 3'-phosphoadenosine-5'-phosphate (PAP) (Figure 1.1).

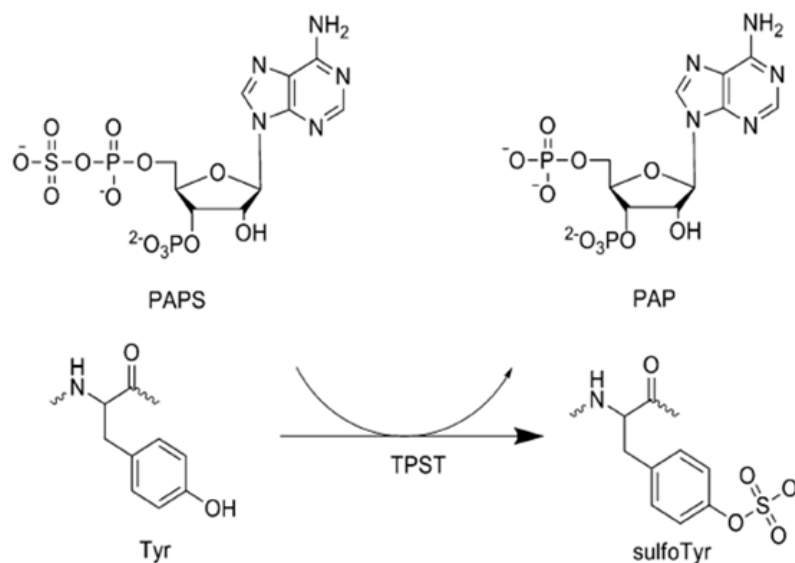


**Figure 1.1**

A schematic representation of the TPST catalyzed tyrosine O-sulfonation reaction.

## 1.2 Tyrosylprotein Sulfotransferases

Tyrosine *O*-sulfonation was firstly observed in 1954 by Bettelheim in bovine fibrinopeptide B4 and was considered to be very rare and confined to fibrogen and a few other proteins until 1982, when Huttner demonstrated that every tissue in rats contained proteins with tyrosine *O*-sulfated residues.<sup>222</sup> Afterwards many mammalian tissues and cells were described to undergo tyrosine sulfonation reaction. A greater interest in tyrosine *O*-sulfonated peptides began in the second half of nineties, when Farzan reported that chemokine receptor CCR5 (a G-protein coupled receptor belonging to the cytokine receptor class, important in cell signaling) served as coreceptor for immunodeficiency viruses (HIV viruses) and was tyrosine *O*-sulfonated.<sup>223</sup> At the beginning of the XXI century, tyrosine sulfonation was shown to be involved in inflammation processes, such as asthma and chronic pulmonary diseases.<sup>224</sup> Also, sulfonation of tyrosine residues was revealed to be critical in atherosclerosis progression.<sup>225</sup>

A significant advance in understanding TPST operating principles was made possible by the molecular cloning in 1998 of two TPST isoforms (TPST-1 and TPST-2)<sup>226</sup> from mouse and human. TPST-1 and TPST-2, which are probably coexpressed in all mammalian cells, have a similar size, consisting of a sequence of 370 and 377 amino acids, respectively, and sharing 64% amino acid sequence identity. Each TPST gene encodes a protein with a short eightresidue cytosolic region that

contains the N-terminus of the protein, a single ~17 residue transmembrane region (TM), a putative ~40 residue stem region, and a catalytic region that is located on the luminal side of the membrane. Since no X-ray diffraction data were available until 2013, information on TPSTs were based on sequence comparison with other STs of known structure. Further information were obtained from mass spectroscopy, sulfonation inhibition, metabolic labeling and amino acid analysis.<sup>227</sup> The prediction of the tyrosine sulfonation site has been one of the central points in the study of TPSTs. An interesting tool was developed under the name of “Sulfinator”, an online software which predicts tyrosine sulfonation sites in protein sequences with 98% of correct predictions of validated tyrosine sulfonation sites. Only very recently, after crystallization of the human TPST-2, the X-ray diffraction data become available.<sup>228</sup>

### 1.3 Human Tyrosylprotein Sulfotransferase-2

The crystallization of the core domain of human TPST-2 (Gly43-Leu359), usually denoted as TPST2 $\Delta$ C18, has proven that TPST-2 is a homodimer consisting of two protomers, denoted as protomer A and protomer B. The existence of TPST-2 as a dimer has been further supported by gel filtration chromatography: in that experiment TPST2 $\Delta$ C18 was eluted with a mass of 77 kDa, a result consistent with the dimeric structure.<sup>228</sup> In the present study we have decided to use the crystal structure under accession number *3API* because, among the three available structures, it is that with the best resolution and includes both substrates i.e. PAP and C4P5Y3. At the beginning of 1990 complement component 4 (C4), a blood protein involved in the complement system was shown to bind TPST-2 and undergo specific tyrosine sulfonation reaction.<sup>229</sup> Later kinetic studies, aimed at differentiate enzymatic characteristics and tissue-specific expression of human TPST-1 and TPST-2, reported that a sequence of protein C4 was specific for TPST-2.<sup>230</sup> The sequence involved in tyrosine *O*-sulfonation reaction is: Glu–Asp–Tyr–Glu–Asp–Tyr–Glu–Tyr–Asp–Glu, which has three suitable sulfonation sites.

The peptidic sequence chosen by Teramoto for the crystallization of TPST-2 system was a 9 peptidic sequence based on the complement C4 including only one sulfonation site. This peptide, named C4P5Y3, presents the sequence: Asp–Phe–Glu–Tyr<sup>1006</sup>–Asp–Glu–Phe–Asp–Glu where Tyr<sup>1006</sup> is the sulfonation site.

Even if there is no consensus yet on the mechanism of tyrosine *O*-sulfonation, during the few last years two hypotheses have been proposed. In 2010, on the basis of mass spectroscopy and

kinetics analysis, Danan proposed a ping-pong mechanism,<sup>231</sup> in which a histidine residue behaves as a sulfuryl group carrier. More recently Teramoto has suggested an alternative mechanistic hypothesis (SN2-like mechanism) where Arg<sup>78</sup> and Glu<sup>99</sup> act as a catalytic acid and base, respectively. Moreover, he hypothesized that Lys<sup>158</sup> and Ser<sup>285</sup> residues play a key role in stabilizing the transition state. A schematic representation of Teramoto's mechanism is given in Figure 1.2. While the recognition/binding of human TPST-2 has been recently investigated,<sup>232</sup> as far as we know to date no studies are available to clarify its catalytic mechanism. Since the knowledge of the crystal structure of this enzyme makes it now possible to build reliable model-systems, in the present work we carried out a detailed DFT computational investigation of the mechanism of tyrosine O-sulfonation catalyzed by the human TPST-2 enzyme.

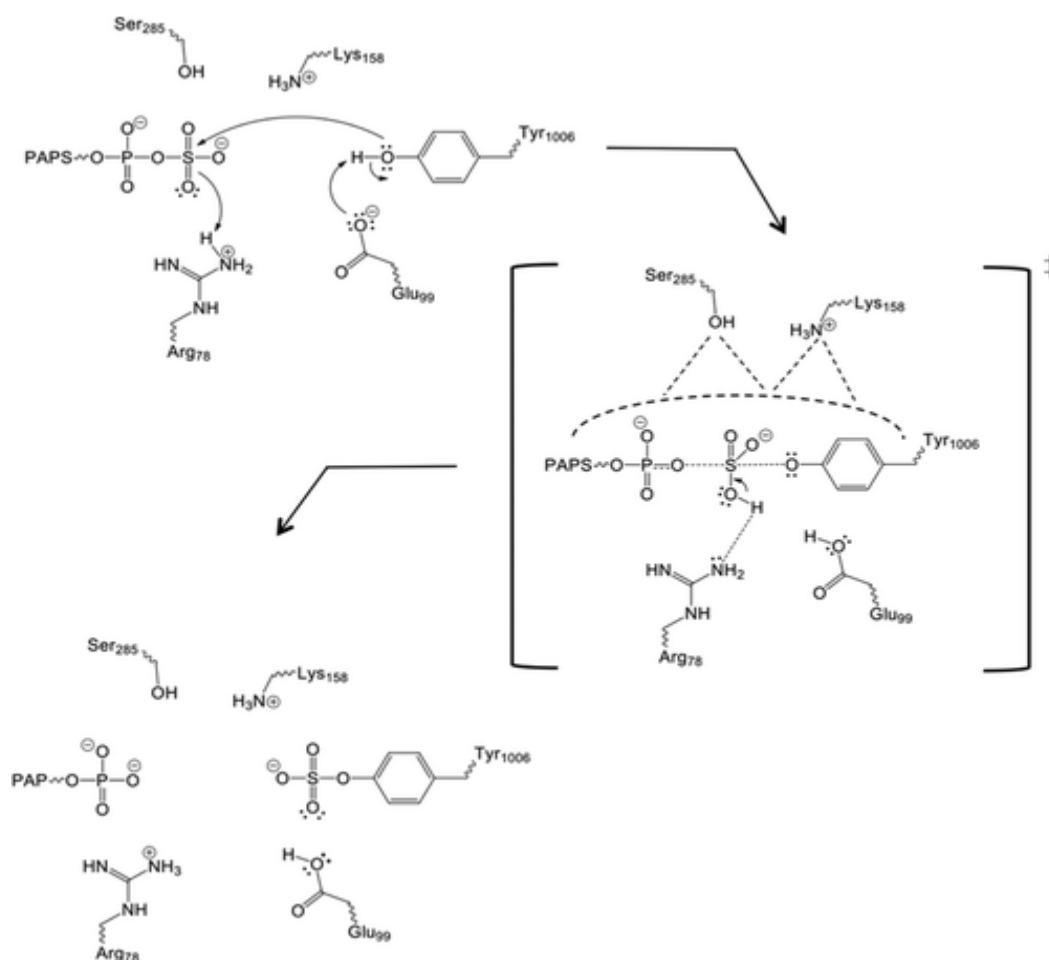


**Figure 1.2**

A schematic representation of Teramoto's mechanistic hypothesis.

Our goal is to outline the mechanistic scheme of the TPST-2 catalyzed reaction to understand the role of various residues in the catalysis and the possible involvement of an histidine residue as a sulfuryl group carrier.

## 1.4 Results and discussion

### 1.4.1 Danan mechanism

In the ping-pong<sup>231</sup> mechanism proposed by Danan, the His<sup>91</sup> residue is assumed to act as a carrier for the sulfuryl group; to check the reliability of this hypothesis we evaluated the distance between His<sup>91</sup> ( $\tau$  nitrogen) and the sulfuryl group (S<sup>212</sup>) of PAPS in the *3API* structure. We found a value of 22.7 Å, which is evidently too large to allow the histidine residue to clasp the SO<sub>3</sub><sup>(-)</sup> group. Moreover, to evaluate the possibility that other histidine residues in the vicinity of the active site could be involved as a possible carrier, we examined in various cases the distance between the histidine  $\tau$  nitrogen and the S<sup>212</sup> atom of the 5'PS moiety of PAPS. These distances are in all cases very large (in the range 8–22.5 Å) suggesting that none of the examined histidine residues are in a suitable position to behave as a sulfuryl carrier. These values are reported in Table 1.1.

histidine residue	His <sup>91</sup>	His <sup>148</sup>	His <sup>190</sup>	His <sup>244</sup>	His <sup>266</sup>	His <sup>267</sup>	His <sup>304</sup>
Distance S <sup>212</sup> – $\tau$ nitrogen atom	20.2	22.5	13.6	17.3	16.5	7.9	18.4

**Table 1.1**

Distance between the S<sup>212</sup> atom of the 5'PS moiety of PAPS and the  $\tau$  nitrogen of various Histidine residues. Values in Ångstrom.

### 1.4.2 Teramoto mechanism

The mechanism of the sulfuryl group transfer in human TPST-2 involves the PAPS cofactor which donates the sulfuryl group to the hydroxyl group of tyrosine (Tyr<sup>1006</sup>) in the substrate C4P5Y3. The products are the O-sulfonylated tyrosine and PAP. The computed energy profile indicates that the reaction proceeds through a concerted mechanism. The corresponding critical points are the starting enzyme–substrate complex (ES), the transition state (TS) and the final enzyme–product complex

(EP). A schematic representation of the three critical points, including only the closest atoms around PAPS, is given in Figure 1.3.

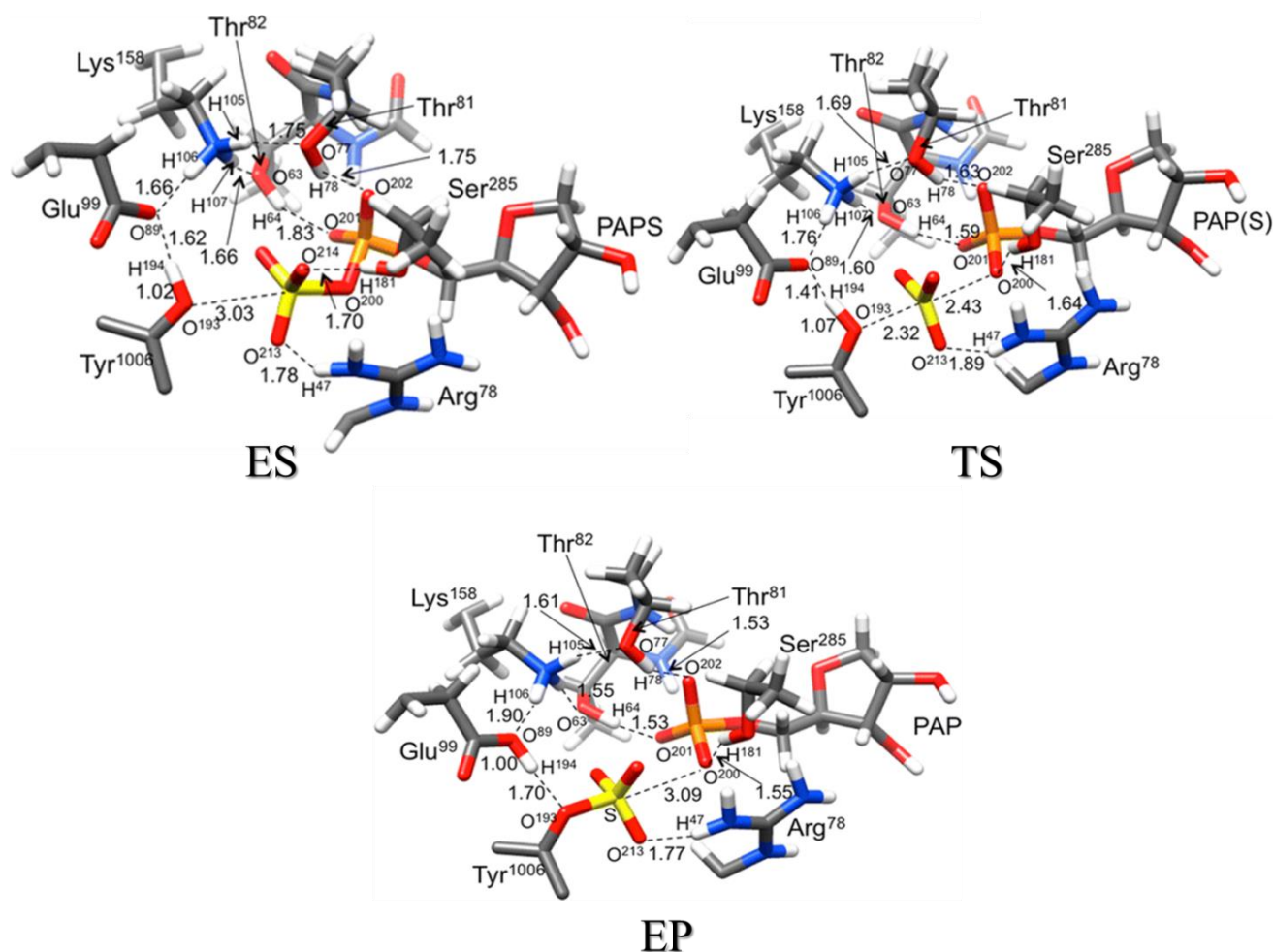


**Figure 1.3**

A schematic representation (including only the closest atoms around PAPS) of the starting enzyme–substrate complex ES. The reported energy value ( $\text{kcal mol}^{-1}$ ) is relative to ES. Bond lengths are in Å.

The computations carried out at the 6-31+G\*/3-21G\* level show that an activation barrier of  $18.5 \text{ kcal mol}^{-1}$  must be surmounted to reach EP, which is  $5.7 \text{ kcal mol}^{-1}$  above the starting complex. These values do not change significantly at the TZVP level: they become 20.8 and  $7.7 \text{ kcal mol}^{-1}$ , respectively, suggesting the 6-31+G\*/3-21G\* basis is as a reliable level of accuracy to describe the model-system. It is reasonable to believe that the difference found between the two accuracy levels could be further reduced after geometry optimization. The hydrogen transfer between the Tyr<sup>1006</sup> hydroxyl group to the Glu<sup>99</sup> carboxylate group (H<sup>194</sup> moving from O<sup>193</sup> to O<sup>89</sup>)

is crucial in the reaction scheme proposed by Teramoto because it generates the nucleophilic oxygen ( $O^{193}$  belonging to Tyr<sup>1006</sup>) that attacks the sulfuryl group. Interestingly, in the ES starting complex H<sup>194</sup> already forms a strong hydrogen bond with O<sup>89</sup> (H<sup>194</sup>...O<sup>89</sup> distance is 1.62 Å). This interaction anticipates the subsequent proton transfer that activates O<sup>193</sup> as a nucleophile. Lys<sup>158</sup> and Ser<sup>285</sup>, which are hypothesized to stabilize the transition state in the Teramoto's reaction scheme, are involved in rather important interactions. In particular the three hydrogen atoms of the protonated Lys<sup>158</sup> form strong hydrogen bonds with Glu<sup>99</sup>, Thr<sup>81</sup>, and Thr<sup>82</sup>: the H<sup>106</sup>...O<sup>89</sup>(Glu99), H<sup>105</sup>...O<sup>77</sup>(Thr<sup>81</sup>) and H<sup>107</sup>...O<sup>63</sup>(Thr<sup>82</sup>) distances are 1.66, 1.75, and 1.66 Å, respectively. Similarly, the hydroxyl hydrogen of Ser<sup>285</sup> strongly interacts with the SO<sub>3</sub> group bonded to PAPS (the H<sup>181</sup>(Ser<sup>285</sup>)...O<sup>214</sup>(SO<sub>3</sub>) distance is 1.70 Å).

Additional significant interactions help to maintain atoms in the ES complex in a suitable position for reactions. These are (i) interaction between Arg<sup>78</sup> and the sulfuryl group of PAPS (H<sup>47</sup>(Arg<sup>78</sup>)...O<sup>213</sup> = 1.78 Å); (ii) interaction between Thr<sup>81</sup> hydroxyl group and the 5'-phosphate of PAPS (H<sup>78</sup>...O<sup>202</sup> = 1.75 Å); (iii) a similar interaction involving Thr<sup>82</sup> and the 5'-phosphate group (H<sup>64</sup>...O<sup>201</sup> = 1.83 Å). In the transition state a planar sulfuryl moiety is moving from O<sup>200</sup> to O<sup>193</sup>. The SO<sub>3</sub><sup>(-)</sup> group is approximately halfway between the two oxygen atoms, the O<sup>193</sup>...S<sup>212</sup> and O<sup>200</sup>...S<sup>212</sup> distances being 2.32 and 2.44 Å, respectively. The TS structure clearly shows that Glu<sup>99</sup> behaves as a base catalyst, as suggested by Teramoto: H<sup>194</sup> is now closer to O<sup>89</sup>(Glu<sup>99</sup>) (H<sup>194</sup>...O<sup>89</sup> distance is 1.41 Å) with a consequent weakening of the O<sup>193</sup>-H<sup>194</sup> bond (from 1.02 Å in ES to 1.07 Å in TS). Thus, TS is a concerted highly asynchronous transition state where the approach of SO<sub>3</sub> to tyrosine oxygen triggers the tyrosine deprotonation. This is confirmed by the shape of the transition vector obtained in the frequency computation. Interestingly, SO<sub>3</sub><sup>(-)</sup> remains anchored to Arg<sup>78</sup> by means of the strong interaction with the sulfuryl oxygen O<sup>213</sup> (the H<sup>47</sup>...O<sup>213</sup> distance is 1.89 Å) suggesting that the arginine residue does not behave as an acid catalyst by donating a proton to the migrating sulfuryl group (as hypothesized in Teramoto's scheme) but acts as a shuttle for SO<sub>3</sub><sup>(-)</sup> following its "travel" along the reaction path. The interactions involving Lys<sup>158</sup> and the two residues Thr<sup>81</sup> and Thr<sup>82</sup> become more important in the TS as suggested by the decrease of the two distances H<sup>105</sup>...O<sup>77</sup>(Thr<sup>81</sup>) and H<sup>107</sup>...O<sup>63</sup>(Thr<sup>82</sup>) (1.69 and 1.60 Å, respectively). Furthermore, a strong stabilizing interaction (made possible by the transfer of the SO<sub>3</sub><sup>(-)</sup> group) is established between the hydroxyl hydrogen of Ser<sup>285</sup> and the oxygen O<sup>200</sup> of PAPS, which is losing the sulfuryl group (H<sup>181</sup>(Ser<sup>285</sup>)...O<sup>200</sup>(PAPS) distance is 1.64 Å). A significant increase of the stabilizing effect is also observed for the interaction between the Thr<sup>81</sup> hydroxyl group and the 5'- phosphate of PAPS

(the  $\text{H}^{78}(\text{Thr}^{81})\cdots\text{O}^{202}(\text{PAPS})$  distance varies from 1.75 Å in ES to 1.63 Å in TS). A further stabilization of TS is provided by the interaction of  $\text{Thr}^{82}$  with the 5'-phosphate of PAPS. In this case the  $\text{H}^{64}(\text{Thr}^{82})\cdots\text{O}^{201}(\text{PAPS})$  distance varies from 1.83 Å in ES to 1.59 Å in TS. Furthermore, we examined the possibility of an alternative mechanism where the proton transfer (from  $\text{O}^{193}$  to  $\text{O}^{89}$ ) and the attack of the tyrosine oxygen  $\text{O}^{193}$  on the  $\text{SO}_3$  group occur in two separate kinetic steps. In spite of an extensive search we could not locate any intermediate corresponding to deprotonated tyrosine, and we discarded the possibility of a two-step nonconcerted mechanism. In the final complex EP the sulfuryl group is definitively bonded to the tyrosine residue  $\text{Tyr}^{1006}$ , and the hydrogen  $\text{H}^{194}$  has been completely transferred to  $\text{Glu}^{99}$  ( $\text{O}^{89}-\text{H}^{194}$  distance is 1.00 Å). A strong hydrogen bond involving  $\text{O}^{193}$  of tyrosine persists, the  $\text{O}^{193}\cdots\text{H}^{194}$  distance being 1.70 Å. Furthermore, the  $\text{SO}_3$  group is still anchored to  $\text{Arg}^{78}$  ( $\text{H}^{47}\cdots\text{O}^{213}$  distance = 1.77Å), which confirms the role played by the arginine residue in “accompanying” the sulfuryl group (shuttle) along the reaction pathway. On the whole the remaining part of the structure does not significantly differ from that of the ES complex. The most important exceptions are represented by (a) the hydrogen bond between the serine hydroxyl hydrogen ( $\text{H}^{181}$ ) and  $\text{O}^{200}$  ( $\text{H}^{181}\cdots\text{O}^{200}$  distance = 1.55 Å) and (b) the two hydrogen bonds involving  $\text{Thr}^{81}$  ( $\text{H}^{78}\cdots\text{O}^{202}$ ) and  $\text{Thr}^{82}$  ( $\text{H}^{64}\cdots\text{O}^{201}$ ) that become stronger in EP, the corresponding distances being 1.53Å in both cases (1.75 and 1.83 Å in ES, respectively). These three hydrogen interactions certainly contribute to stabilize the product complex, which remains nevertheless 5.7 kcal mol<sup>-1</sup> above ES.

### 1.4.3 The virtual mutagenesis experiment

To quantify the catalytic effect of the residues playing a key role in the sulfuryl exchange reaction ( $\text{Lys}^{158}$  and  $\text{Ser}^{285}$ , as suggested by Teramoto,  $\text{Arg}^{78}$ ,  $\text{Thr}^{81}$ , and  $\text{Thr}^{82}$ ), we carried out a virtual mutagenesis experiment by alanine scanning: thus, we replaced each of these residues with alanine, and we recomputed the energy barrier<sup>233</sup> at the 6-31+G\*/3-21G\* level. In these computations we neglected the ZPE corrections, but we included the solvent effects. Thus, these barriers must be compared with the value of 18.2 kcal mol<sup>-1</sup>, which is the barrier obtained for the non-mutated enzyme without ZPE corrections. The results (collected in Table 1.2) clearly demonstrate the stabilizing effects exerted by the various residues. The effect on the barrier is significant in all cases (in the range 4.0–5.5 kcal mol<sup>-1</sup>) except for  $\text{Lys}^{158}$ : for this residue the increase is only 0.6 kcal mol<sup>-1</sup> and can be ascribed to the trend of the three H-bonds involving



Lys<sup>158</sup> (H<sup>105</sup>...O<sup>77</sup>, H<sup>106</sup>...O<sup>89</sup> and H<sup>107</sup>...O<sup>63</sup>) that do not change significantly on passing from ES to TS. We can conclude that Lys<sup>158</sup>, even if not interacting with the groups directly involved in the reaction, plays an important role in keeping close the residues participating to the overall H-bond network that stabilizes TS. In particular, the above analysis confirms that the stabilization of TS via strong hydrogen interactions can be ascribed to Ser<sup>285</sup> (as suggested by Teramoto) and to other residues such as Thr<sup>81</sup> and Thr<sup>82</sup>. These residues exert in ES a sort of “kicking effect” on the sulfuryl group, since they facilitate its detachment by stabilizing the incipient negative charge on the phosphate group of PAPS. The stabilizing effect on TS of Arg<sup>78</sup> (that anchors SO<sub>3</sub><sup>(-)</sup> along the whole reaction path and acts as a shuttle following the sulfuryl “travel”) is due to a salt bridge, dominated by electrostatic interactions between the negative charge of sulfuryl and the positive charge of arginine. To obtain a more complete picture of the stabilizing effect of the various residues we have estimated the total charge of the SO<sub>3</sub> group in the reactant complex ES and transition state TS for the non-mutated enzyme and each mutated forms of Table 1.2. In the non-mutated enzyme the net SO<sub>3</sub> charge is -0.98 in ES and -0.50 in TS: this significant decrease of the charge is further evidence for the stabilizing effect of the various interactions that delocalize the SO<sub>3</sub> charge on passing from reactants to transition state. Interestingly, the charge variation is much less significant when the various residues are replaced by alanine and the corresponding delocalizing interactions partly disappear.

Mutated residue	Interaction	Activation barrier E <sub>a</sub>	ΔE <sub>a</sub>	Mulliken charge on SO <sub>3</sub>
Arg <sup>78</sup>	H <sup>47</sup> ...O <sup>213</sup> H-bond	22.3	4.1	ES: -0.58 TS: -0.38
Lys <sup>158</sup>	H <sup>105</sup> ...O <sup>77</sup> , H <sup>106</sup> ...O <sup>89</sup> and H <sup>107</sup> ...O <sup>63</sup> H-bonds	18.8	0.6	ES: -0.47 TS: -0.43
Ser <sup>285</sup>	H <sup>181</sup> ...O <sup>200</sup> (SO <sub>3</sub> ) and H <sup>181</sup> ...O <sup>202</sup> (PAP) H-bonds	22.9	4.7	ES: -0.72 TS: -0.55
Thr <sup>81</sup>	H <sup>78</sup> ...O <sup>202</sup> (PAP) H-bonds	22.7	4.0	ES: -0.43 TS: -0.36
Thr <sup>82</sup>	H <sup>64</sup> ...O <sup>201</sup> (PAP) H-bonds	23.7	5.5	ES: -0.51 TS: -0.40

**Table 1.2**

Activation barrier E<sub>a</sub> (kcal mol<sup>-1</sup>) computed after replacement of each residue reported on the left column with alanine. For each residue a short description of the main interactions is reported. ΔE<sub>a</sub> (kcal mol<sup>-1</sup>) is the variation with respect to the non-mutated enzyme.

## 2.1 Computational details

All reported DFT computations were carried out with the Gaussian 09 series of programs<sup>4</sup> on the model-system obtained from the crystal structure. The M06-2X functional was employed.<sup>24,25</sup> The geometries of the various critical points on the potential surface were optimized with the gradient method available in Gaussian 09, and harmonic vibrational frequencies were computed to evaluate the nature of all critical points. The system was partitioned into two regions, which were assigned basis sets of different accuracy. The atoms of one region were those directly involved in the reaction (i.e., Tyr<sup>1006</sup> side-chain, Glu<sup>99</sup> side-chain, and 5'-phosphosulfate moiety) or in the formation of hydrogen bonds with the reacting core (i.e., Lys<sup>158</sup> side-chain): for these atoms we used the 6-31+G\* basis set.<sup>191</sup> The other region included all remaining atoms which were described by the 3-21G\* basis set.<sup>191</sup> This basis set (denoted as 6-31+G\*/3-21G\*) corresponds to a total of 1462 basis functions. ZPE corrections were taken into account. In our experience this approach can provide an accurate description of enzymatic reactions at a reasonable computational cost.<sup>234</sup> However, to check the accuracy of this basis we carried out single point computations on the optimized geometries with the TZVP basis set<sup>191</sup> (corresponding to a total of 2858 basis functions). Furthermore, we considered ZPE corrections obtained at the lower level of accuracy.

To model the active site of human TPST-2 we used the X-ray crystal structure 3AP1 (TPST2ΔC18, C4 peptide and PAP),<sup>218</sup> to which we added manually the sulfuryl group SO<sub>3</sub><sup>(-)</sup>. The hydrogen atoms were included in the 3AP1 structure at pH 7.4 using the H++ online program.<sup>235</sup> The choice of a suitable model-system is crucial in the investigation of an enzymatic reaction mechanism. It should include the groups that are supposed to play a key-role in the reaction within the active site, but the number of atoms ( $N$ ) cannot be too large to make the QM calculation unfeasible within a reasonable computational time. Thus, to examine in detail the SN2-like mechanism proposed by Teramoto,<sup>218</sup> starting from the X-ray crystal structure 3AP1, we built a model-system including Glu<sup>99</sup> and Arg<sup>78</sup> that are postulated to behave as a catalytic base and acid, respectively. Also, we added Ser<sup>285</sup> and Lys<sup>158</sup> that are supposed to stabilize the transition state. Furthermore, we considered initially all long-range interactions between TPST2ΔC18, C4P5Y3, and PAPS. Then, to reduce the size of the resulting model-system we cut off the residues farther than 8 Å from the sulfonation site, i.e., the hydroxylic oxygen (O<sup>193</sup>) of the Tyr<sup>1006</sup> side-chain. Finally, to reduce further the number of atoms, we discarded those parts of PAPS and C4P5Y3 that were not directly involved in the reaction, i.e., the adenine ring and the 3'-phosphate of PAPS and

all residues of C4P5Y3 except Tyr<sup>1006</sup>. The cut bonds were replaced by bonds with hydrogen atoms. In summary, in addition to Tyr<sup>1006</sup> and the cut PAPS, our model-system includes (a) the four critical residues Glu<sup>99</sup>, Arg<sup>78</sup>, Ser<sup>285</sup>, Lys<sup>158</sup>; (b) Pro<sup>77</sup>, Thr<sup>81</sup>, Thr<sup>82</sup> that interact specifically with Tyr<sup>1006</sup> and the 5'PS group of PAPS; (c) Val<sup>76</sup>, Ile<sup>199</sup>, Asp<sup>159</sup>, Phe<sup>161</sup>, Pro<sup>160</sup>, Val<sup>197</sup>, Gly<sup>80</sup>, and Asp<sup>159</sup> which surround the reaction site. The size of all these residues was reduced by an appropriate cut of conveniently chosen chemical bonds (in particular, the bonds involving the  $\alpha$  carbons). The cut bonds were again replaced by bonds with hydrogen atoms. The resulting model-system finally used in DFT computations is schematically represented in Figure 1.4. It involves 241 atoms and the total charge is  $-1$ .

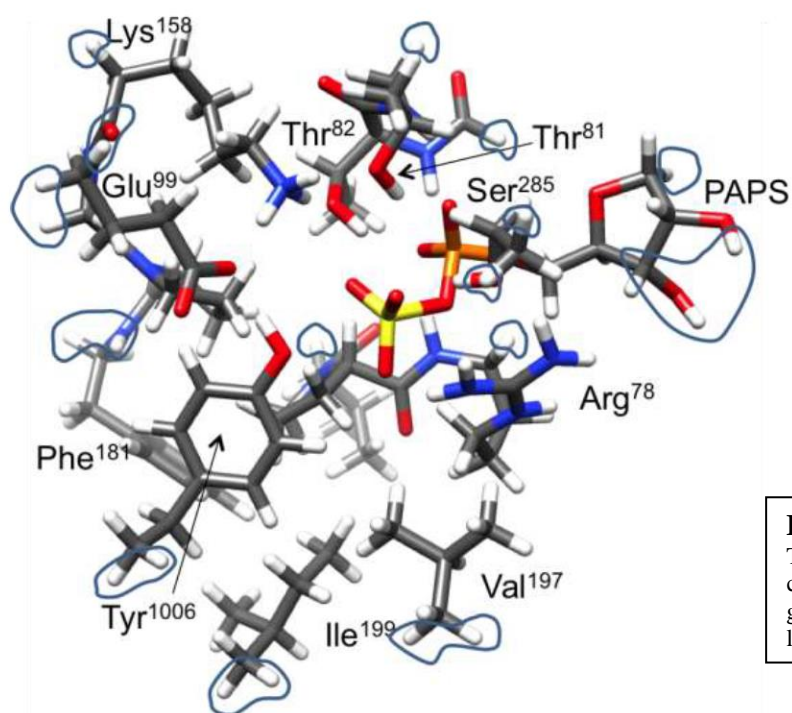


**Figure 1.4**

The full model-system used in our computations. Atoms kept “frozen” during geometry optimization are marked by contour lines.

To emulate the partially constraining effect of the protein environment, during the geometry optimization process we kept “frozen” to their crystallographic coordinates the positions of appropriately chosen atoms: these were mainly the hydrogens added in place of the cut bonds and the atoms near the border of the model-system and not directly involved in the reaction or in hydrogen bond formation. This approach preserves the geometry of the active-site cavity and avoids the possibility that the TPST-2 active site secondary structure will run into unwanted conformational changes. Furthermore, the effect of the entire protein environment was evaluated with the polarizable continuum model (PCM),<sup>100</sup> as implemented in Gaussian 09. We used a value of 4.24 (corresponding to diethyl ether) for the dielectric constant  $\epsilon$ .<sup>236</sup> This value is close to 4.0,

which is the value generally chosen to describe the surrounding protein and to account for the simultaneous presence of hydrophilic and hydrophobic groups around the active site.<sup>237</sup>

## 2.2 Conclusions

In this paper we have examined the mechanism of tyrosine O-sulfonation catalyzed by human TPST-2. Our DFT computations have confirmed in outline Teramoto's general scheme, i.e., a concerted highly asynchronous SN2-like reaction (with an activation barrier of 18.5 kcal mol<sup>-1</sup>) where the tyrosine oxygen is deprotonated by Glu<sup>99</sup> (that acts as a base catalyst as suggested by Teramoto) and simultaneously attacks as a nucleophile the sulfuryl group. Arg<sup>78</sup> plays a different role from that proposed by Teramoto. A strong hydrogen interaction involving the sulfuryl oxygen and Arg<sup>78</sup> allows this group to anchor SO<sub>3</sub><sup>(-)</sup> along the whole reaction path, acting as a shuttle that follows the sulfuryl "travel" from PAPS to threonine. After a careful analysis of the structural features of the reactant-complex (ES) and TS and using a QM protocol of "alanine scanning", we could identify unequivocally the role of the amino acids involved in the catalysis. In addition to the "assistance" of Arg<sup>78</sup> toward the sulfuryl group moving from PAPS to threonine, we found that (i) the stabilizing effect of Arg<sup>78</sup> on TS is due to a salt bridge, dominated by electrostatic interactions between the negative charge of sulfuryl and the positive charge of arginine; (ii) Ser<sup>285</sup>, Thr<sup>81</sup>, and Thr<sup>82</sup> stabilize TS via strong hydrogen interactions (in particular, these three residues exert a sort of "kicking effect" in the starting reactant complex, since they facilitate the detachment of sulfuryl group by stabilizing the incipient negative charge on the phosphate group of PAPS); (iii) the role of Lys<sup>158</sup> is that of keeping close the residues participating to the overall H-bond network that stabilizes TS. A careful analysis of the structure of enzyme and MD simulations helped us to exclude the Danan's ping-pong mechanism where the His<sup>91</sup> residue is proposed to act as a carrier for the sulfuryl group. This group and His<sup>91</sup> are too far away to make possible a mutual significant interaction. Similarly, too large distances have been evidenced for other histidine residues around SO<sub>3</sub><sup>(-)</sup> that in principle could act as a carrier. However, we cannot exclude, in principle, the possibility of secondary reaction channels leading to the formation of covalent intermediates congruent with Danan's experimental evidence and where another residue replaces the histidine residue suggested by Danan. We believe that all these results can be extremely useful in the design of mutated forms of the enzyme and in the synthesis of possible antagonists to enhance or decrease the tyrosine O-sulfonation of the target substrate.

## References

1. (a) Green S., *Industrial Catalysis, Macmillan Company, New York, 1928*. (b) Lindström B., Pettersson L. J., A Brief History of Catalysis, *CATTECH*, **2003**, 7, 130-138.
2. (a) Leach, A. R. *Molecular Modelling: Principles and Applications; second ed.; Pearson Education EMA: UK, 2001*. (b) Cramer, C. J. *Essentials of Computational Chemistry: Theories and Models; Second ed., 2004*. (c) Jensen, F. *Introduction to Computational Chemistry; first ed.; John Wiley & Sons: UK, 1999*.
3. Born, M.; Oppenheimer, R. *Ann. Physic.* **1927**, 84, 457-484.
4. Frisch, M. J.; Trucks, G. W.; Schlegel, H. B.; Scuseria, G. E.; Robb, M. A.; Cheeseman, J. R.; Scalmani, G.; Barone, V.; Mennucci, B.; Petersson, G. A.; et al. *Gaussian 09, revision B.01*; Gaussian, Inc.: Wallingford CT, **2009**.
5. Young, D. C. *Computational Chemistry: A Practical Guide for Applying Techniques to Real-World Problems*; Wiley: New York, **2001**.
6. Dykstra, C. E. *Quantum Chemistry & Molecular Spectroscopy*; Prentice Hall: Englewood Cliffs, **1992**.
7. McQuarrie, D. A. *Quantum Chemistry*; University Science Books: Mill Valley, **1983**.
8. Atkins, P. W.; Friedman, R. S. *Molecular Quantum Mechanics*; Oxford: Oxford, **1997**.
9. Boys, S.F. *Proc. Roy.Soc. (London)*, **1950**, 200, 542.
10. Szabo, A.; Ostlund, N. S. *Modern Quantum Chemistry*; Dover Publications, INC: New York, **1996**.
11. Shavitt, I. *J. Chem. Phys.*, **1962**, 36, 550.
12. Roothaan, C. C. *J. Reviews of Modern Physics* **1951**, 23, 69-89.
13. (a) Hehre, W.J.; Ditchfield, R.; Pople, J.A., *J.Chem. Phys.* **1972**, 56, 2257. (b) Hariharam, P.C.; Pople, J.A., *Theor. Chim. Acta* **1973**, 28, 213 (). (c) Binkley, J. S.; Pople J.A. *J.Chem. Phys.* 1977, 66, 879 . (d) Francl, M.M. ; Pietro W.J. ; Hehre W.J. ; Binkley, J.S.; Gordon M.S.; Defrees, D.J.; Pople, J.A. ; *Ibid.* 1982, 77, 3654.
14. Szabo, A.; Ostlund, N. S. *Modern Quantum Chemistry*; Dover Publications, INC: New York, **1996**.
15. Møller, C.; Plesset, M. S. *Phys. Rev.* **1934**, 46, 618-622.
16. Hohenberg P., Kohn W. P. *Phis. Rev.*, **1964**, B136, 864.
17. Kohn W., Sham L.J., *Phis. Rev.*, **1965**, A140, 1133.
18. Becke A.D. *Phis Rev.*, **1988**, A38, 3098.

19. Vosko S.H., Wilk L., Nusair M. *J. Phys.*, **1980**, 58, 1200;
20. Lee, C. Yang W., Parr R.G. *Phys Rev.*, **1988**, B37, 785;
21. Becke, A.D. *J. Chem. Phys.*, **1993**, 98, 5648.
22. (a) Grimme, S. *J. Comput. Chem.* **2004**, 25, 1463-1473. (b) Grimme, S. *J. Comput. Chem.* **2006**, 27, 1787-1799.
23. Harvey, J. N. *Annu. Rep. Prog. Chem., Sect. C: Phys. Chem.* **2006**, 102, 203-226.
24. Zhao, Y., Truhlar, D.G. *J. Phys. Chem.A*, **2006**, 110, 13126.
25. Zhao, Y., Truhlar, D.G. *Theor Chem Account*, **2008**, 120, 215–241.
26. (a) Case, D.A. *AMBER12*, **2010**, University of California, San Francisco; (b) Duan, Y.; Wu, C.; Chowdhury, S.; Lee, M. C.; Xiong, G.; Zhang, W.; Yang, R.; Cieplak, P.; Luo, R.; Lee, T.; Caldwell, J.; Wang, J.; Kollman, P. *J. Comput. Chem.* **2003**, 24, 1999-2012.
27. (a) Ponder, J. W.; Case, D. A.; Valerie, D. *In Advances in Protein Chemistry*; Academic Press: **2003**; Vol. Volume 66, p 27-85. (b) Dudek, M. J.; Ponder, J. W. *J. Comput. Chem.* **1995**, 16, 791-816.
28. Cheatham, T. E. I.; Young, M. A. *Biopolymers* **2000**, 56, 232-256.
29. Rappe, A. K.; Casewit, C. J.; Colwell, K. S.; Goddard, W. A. III; Skiff, W. M.; *J Am Chem Soc*, **1992** v. 114, 10024-10039.
30. Mayo S. L., Olafson B. D., and Goddard III W. A. *J. Phys. Chem.* **1990**, 94, 8897-8909.
31. Van Der Spoel, D.; Lindahl, E.; Hess, B.; Groenhof, G.; Mark, A. E.; Berendsen, H. J. C. *J. Comput. Chem.* **2005**, 26, 1701-1718.
32. (a) Brooks, B. R.; Bruccoleri, R. E.; Olafson, B. D.; States, D. J.; Swaminathan, S.; Karplus, M. *J. Comput. Chem.* **1983**, 4, 187-217. (b) MacKerell, A. D.; Brooks, B.; Brooks, C. L.; Nilsson, L.; Roux, B.; Won, Y.; Karplus, M. *In The Encyclopedia of Computational Chemistry*; al., P. v. R. S. e., Ed.; John Wiley & Sons: Chichester, **1998**, p 271-277.
33. (a) Warshel, A. & Levitt, M. *Journal of Molecular Biology*, **1976**, 103, 227-249. (b) Lin, H. & Truhlar, D.G. *Theoretical Chemistry Accounts*, **2007**, 2, 117. (c) Bakowies, D. & Thiel, W. *J. Phys. Chem.*, **1996**, 100, 10580-10594. (d) Gao, J.; Lipkowitz, K.B. & Boyd, D.B. *Reviews in Computational Chemistry*, **1995**, 7, 119-185. (e) Sherwood, P. & J Grotendorst *NIC series*, **2000**, 3, 285-305.
34. (a) Senn, H. M.; Thiel, W. *Angew. Chem., Int. Ed.* **2009**, 48, 1198. (b) Senn, H. M.; Thiel, W. *In Atomistic Approaches in Modern Biology: From Quantum Chemistry to Molecular Simulations*; Reiher, M., Ed.; Springer: New York, **2007**; Vol. 268.
35. Cornell, W. D.; Cieplak, P.; Bayly, C. I.; Gould, I. R.; Merz, K. M.; Ferguson, D. M.; Spellmeyer, D. C.; Fox, T.; Caldwell, J. W.; Kollman, P. A. *J. Am. Chem. Soc.* **1995**, 117, 5179.
36. (a) Chung, L. W.; Sameera, W. M. C.; Ramozzi, R.; Page, A. J.; Hatanaka, M.; Petrova, G. P.; Harris, T. V.; Li, X.; Ke, Z.; Liu, F.; Li, H.-B.; Ding, L.; Morokuma, K. *Chem. Rev.* **2015**, 115, 5678–5796 (b) Maseras, F. & Morokuma, K. *Journal of Computational Chemistry*, **1995**, 16, 1170-1179. (c) Svensson,

- M.; Humbel, S.; Froese, R.D.J.; Matsubara, T.; Sieber, S. & Morokuma, K. *J. Phys. Chem.* ,**1996**,100, 19357-19363.
37. (a) Maseras, F.; Morokuma, K. *J. Comput. Chem.* **1995**, 16, 1170. (b) Matsubara, T.; Sieber, S.; Morokuma, K. *Int. J. Quantum Chem.***1996**, 60, 1101.
38. Svensson, M.; Humbel, S.; Froese, R. D. J.; Matsubara, T.; Sieber, S.; Morokuma, K. *J. Phys. Chem.* **1996**, 100, 19357.
39. Politzer, P.; Truhlar, D. G. *Chemical Applications of Atomic and Molecular Electrostatic Potentials. Reactivity, Structure, Scattering, and Energetics of Organic, Inorganic, and Biological Systems*; Eds.; Plenum: New York, **1981**.
40. (a) Sherwood, P. & J Grotendorst *NIC series* ,**2000**,3, 285-305. (b) Stanton, R. V.; Hartsough, D. S.; Merz, K. M., Jr. *J. Comput. Chem.***1995**, 16, 113.
41. (a) Vreven, T.; Morokuma, K.; Farkas, O.; Schlegel, H. B.; Frisch, M. J., *J. Comput. Chem.***2003**, 24, 60. (b) Vreven, T.; Morokuma, K. *Theor. Chem. Acc.***2003**, 109, 125.
42. (a) Lin, H.; Truhlar, D. G. *Theor. Chem. Acc.* **2006**, 117, 185-199. (b) Field, M. J.; Bash, P. A.; Karplus, M. *J. Comput. Chem.* **1990**, 11, 700-733. (c) Singh, U. C.; Kollman, P. A. *J. Comput. Chem.* **1986**, 7, 718-730. (d) Ferre, N.; Olivucci, M. *J. Mol. Struct.* **2003**, 632, 71-82.
43. (a) Warshel, A.; Levitt, M. *J. Mol. Biol.* **1976**, 103, 227-249. Pu, J.; (b) Gao, J.; Truhlar, D. G. *J. Phys. Chem. A* **2004**, 108, 632-650. (c) Gao, J.; Amara, P.; Alhambra, C.; Field, M. J. *J. Phys. Chem. A* **1998**, 102, 4714-4721. (d) Théry, V.; Rinaldi, D.; Rivail, J.-L.; Maignet, B.; Ferenczy, G. G. *J. Comput. Chem.* **1994**, 15, 269-282.
44. (a) Vreven, T.; Byun, K. S.; Komáromi, I.; Dapprich, S.; Montgomery, J. A., Jr.; Morokuma, K.; Frisch, J. *J. Chem. Theory Comput.* **2006**, 2,815. (b) Dapprich, S.; Komáromi, I.; Byun, K. S.; Morokuma, K.; Frisch, M. J. *J. Mol. Struct. (THEOCHEM)* **1999**, 461, 1.
45. (a) Singh, U. C.; Kollman, P. A. *J. Comput. Chem.* **1986**, 7, 718. (b) Field, M. J.; Bash, P. A.; Karplus, M. *J. Comput. Chem.* **1990**, 11,700.
46. Bell R. P.; *Trans. Faraday Soc.* **1931**, 27, 797.
47. Kirkwood J.G.; *J. Chem. Phys.* **1934**, 2,351.
48. Onsager L.; *J. Am. Chem. Soc.* **1936**, 58, 1486.
49. (a) B. Mennucci , R. Cammi, J. Tomasi. *J. Chem. Phys.* **1999**, 110 6858. (b) R. Cammi, B. Mennucci, J. Tomasi, *J. Chem. Phys.* **1999**,110 7627.
50. Angyan J. G.; *J. Math. Chem.* **1992**, 10, 93.
51. Tapia O.; *J. Math. Chem.* **1992**, 10, 139.
52. Lee B. and Richards F. M. *J. Mol. Biol.*, **1971**, 55.
53. Richards F. M. *151. Ann. Rev. Biophys. Eng.*, **1977**, 6.
54. Miertus S., Scrocco E. Tomasi J. ; *J. Chem. Phys.* **1981**, 55, 117.

55. Ulig H. H., *J. Phys. Chem.*, **1937**,41,1215.
56. Pierotti R. A., *Chem. Rev*, **1976**,76 712.
57. Vigne'-Maeder, F. and Claverie P., *J. Am. Chem. Soc.* **1987**, 109, 24.
58. H. Schmidbaur, *Naturwiss. Rundsch.* **1995**, 48, 443– 451.
59. M. Haruta, T. Kobayashi, H. Sano, N. Yamada, *Chem. Lett.* **1987**, 16, 405 – 408.
60. G. J. Hutchings, *J. Catal.* **1985**, 96, 292 – 295.
61. A. S. K. Hashmi and G. J. Hutchings *Angew. Chem. Int. Ed.* **2006**, 45, 7896 – 7936.
62. (a) A. Furstner, O. D. Davies, *Angew. Chem.* **2007**, 119, 3478; *Angew. Chem. Int. Ed.* **2007**, 46, 4310; (d) H. C. Shen, *Tetrahedron* **2008**, 64, 3885; (b) R. Skouta, C.-J. Li, *Tetrahedron* **2008**, 64, 4917; (c) A. Arcadi, *Chem. Rev.* **2008**, 108, 3266; (d) D. J. Gorin, B. D. Sherry, F. D. Toste, *Chem. Rev.* **2008**, 108, 3351; (e) P. Belmont, E. Parker, *Eur. J. Org. Chem.* **2009**, 6075; (f) N. D. Shapiro, F. D. Toste, *Synlett* **2010**, 675; (g) S. Wang, G. Zhang, L. Zhang, *Synlett* **2010**, 692.
63. (a) A. S. K. Hashmi, *Angew. Chem.* 2005, 117, 7150; *Angew.Chem. Int. Ed.* 2005, 44, 6990; (b) A. S. K. Hashmi, *Chem. Rev.* 2007, 107, 3180; (c)
64. Bond, G. C.; Louis, C.; Thompson, D. T. *Catalysis by Gold*; Imperial College Press: London, **2006**.
65. Nolan, P. S. *Nature* **2007**, 445, 496.
66. (a) Hutchings, G. *J. Catal. Today* **2007**, 122, 196. (b) *CatGoldNews*, Gold Bull. **2007**, 40/2, C1.
67. (a) J.P. Collman, L.S. Hegedus, J.R. Norton and R.G. Finke, *Principles and Applications of Organotransition Metal Chemistry*, University Science Books, Mill Valley, California, **1987**, p 42 and p 156 (b) G.G. Melikyan and K.M. Nicholas in *Modern Acetylene Chemistry* (Eds.: P.J. Stang and F. Diederich), VCH, Weinheim, **1995**, p 99.
68. (a) Gorin, D. J.; Toste, F. D. *Nature* **2007**, 446, 395-403. (b) Pyykkö, P.; Desclaux, J. P. *Acc. Chem. Res.* **1979**, 12, 276-281
69. P. Giacinto, G. Cera, A. Bottoni, M. Bandini, and G. P. Miscione; *ChemCatChem* **2015**, 7, 2480 – 2484.
70. P. Ertl, S. Jelfs, J. Mhlbacher, A. Schuffenhauer, P. Selzer, *J. Med. Chem.* **2006**, 49, 4568.
71. (a) Marti, C.; Carreira, E. M. *Eur. J. Org. Chem.***2003**, 2209–2219; (b) Sundberg,R. J. *The Chemistry of Indoles*; Academic Press: New York, **1970**; (c) *Indoles (Parts I–III)*; Houlihan, W. J., Ed.; Wiley Interscience: New York, **1979**; (d) Cordell, G.A. *Introduction to Alkaloids*; Wiley-Interscience: New York, **1981**; (e) Trost, B. M.; Brennan, M. K. *Synthesis* **2009**, 3003.
72. (a) L. Angenot, O. Diberg, L. Dupont, *Tetrahedron Lett.* **1975**, 16,1357; (b) G. Massiot, P. Thpenier, M. J. Jacquier, C. Delaude, L.Le Men-Olivier, R. Verpoorte, *Tetrahedron Lett.***1985**, 26, 2441; (c) M. Chbani, M. Pas, *J. Nat. Prod.* **1993**, 56, 99; (d) J. Kraxner,H. Hbner, P. Gmeiner, *Arch. Pharm. Pharm. Med. Chem.* **2000**,333, 287. (e) P. M. Barbour, L. J. Marholz, L. Chang, W. Xu, X. Wang, *Chem. Lett.* **2014**, 43, 572, and references therein.



73. (a) M.H.Powdrill, J. A. Bernatchez and M. Gotte, *Viruses*, **2010**,2, 2169–2195; (b) L.Beaulieu, *Expert Opin. Ther. Pat.*, **2009**,19, 145–164; (c) E. Tramontano, *Mini-Rev. Med. Chem.*, **2008**,8, 1298–1310.
74. a) T. W. Hudyma, X. Zheng, F. He, M. Ding, C. P. Bergstrom, P. Hewawasam,S. W. Martin,R. G. Gentles, *WO2007/092000A1*, **2007**; b) M. Ding, F.He, M. A. Poss, K. L. Rigat, Y.-K. Wang, S. B. Roberts, D. Qiu, R. A. Fridell, M. Gao, R. G. Gentles, *Org. Biomol. Chem.* **2011**, 9, 6654;
75. (a) Isaac, M. *Drugs Future* **2001**,26, 383. (b) Roth, B. L.; Shapiro, D. A. *Exp. Opin. Ther. Targets* **2001**,5, 685. (c) Fitzgerald, L. W.; Ennis, M. D. *Annu. Rep. Med. Chem.* **2002**,37, 21.
76. M. D. Ennis, R. L. Hoffman, N. B. Ghazal, R. M. Olson, C. S. Knauer, C. L. Chio, D. K. Hyslop, J. E. Campbell, L. W. Fitzgerald, N. F. Nichols, K. A. Svensson, R. B. McCall, C. L. Haber, M. L. Kagey, D. M. Dinh, *Bioorg. Med. Chem. Lett.* **2003**, 13, 2369.
77. (a) H. Kusama, Y. Suzuki, J. Takaya, N. Iwasawa, *Org. Lett.* **2006**, 8, 895; (b) K. Cariou, B. Ronan, S. Mignani, L. Fensterbank, M. Malacria, *Angew. Chem. Int. Ed.* **2007**, 46, 1881; *Angew. Chem.* 2007, 119, 1913.
78. (a) V. Aureggi, M. Davoust, K. M. Gericke, M. Lautens, *Synlett* **2009**, 1004; (b) S. Pozzi, J. Habermann, M. de R. Rico Ferreira, F. Narjes, *Synlett* **2009**, 1395; (c) P. A. Suryavanshi, V. Sridharan, J. Carlos Menendez, *Org. Biomol. Chem.* **2010**, 8, 3426; (d) L. Huang, M. Shi, *Chem. Commun.* **2012**, 48, 4501.
79. J. Barluenga, F. Rodriguez, F. J. FaÇans, *Chem. Asian J.* 2009, 4, 1036.
80. For some recent leading examples using [Au], see: (a) M. Alfonsi, A. Arcadi, M. Aschi, G. Bianchi, F. Marinelli, *J. Org. Chem.* **2005**, 70, 2265; (b) C. Praveen, K. Karthikeyan, P. T. Perumal, *Tetrahedron* **2009**, 65, 9244; (c) X. Zeng, R. Kinjo, B. Donnadieu, G. Bertrand, *Angew. Chem.* **2010**, 122, 954; *Angew. Chem. Int. Ed.* **2010**, 49, 942; (d) A. Wetzol, F. Gagosz, *Angew. Chem.* **2011**, 123, 7492; *Angew. Chem. Int. Ed.* **2011**, 50, 7354; (e) B. Lu, Y. Luo, L. Liu, L. Ye, Y. Wang, L. Zhang, *Angew. Chem.* **2011**, 123, 8508; *Angew. Chem. Int. Ed.* **2011**, 50, 8358; (f) J. P. Brand, C. Chevalley, J. Waser, Beilstein *J. Org. Chem.* **2011**, 7, 565; (g) P. Kothandaraman, S. Reddy Mothe, S. Si Min Toh, P.W. H. Chan, *J. Org. Chem.* **2011**, 76, 7633; for [Ag], see: (h) S. R. Mothe, P. Kothandaraman, S. J. L. Lauw, S. M.-W. Chin, P.W. H. Chan, *Chem. Eur. J.* **2012**, 18, 6133; (i) for [Pd], see ; (j) Z. Hu, D. Liang, J. Zhao, J. Huang, Q. Zhu, *Chem. Commun.* 2012, 48, 7371.
81. (a) D. Bouyssi, N. Monteiro, G. Balme, Beilstein *J. Org. Chem.* **2011**, 7, 1387, and references therein; (b) Y. Oda, N. Matsuyama, K. Hirano, T. Satoh, M. Miura, *Synthesis* **2012**, 1515. (c) R. Vicente, *Org. Biomol. Chem.* **2011**, 9, 6469.
82. (a) S. Diez-Gonzalez, N. Marion, S. P. Nolan, *Chem. Rev.* **2009**, 109, 3612; (b) S. P. Nolan, *Acc. Chem. Res.* **2011**, 44, 91; (c) S. Gaillard, C. S. J. Cazin, S. P. Nolan, *Acc. Chem. Res.* **2012**, 45, 778.
83. a) H. Kusama, Y. Suzuki, J. Takaya, N. Iwasawa, *Org. Lett.* **2006**, 8, 895; (b) K. Cariou, B. Ronan, S. Mignani, L. Fensterbank, M. Malacria, *Angew. Chem.* **2007**, 119, 1913; *Angew. Chem. Int. Ed.* **2007**, 46, 1881.

84. (a) V. Aureggi, M. Davoust, K. M. Gericke, M. Lautens, *Synlett* **2009**, 1004; (b) S. Pozzi, J. Habermann, M. de R. Rico Ferreira, F. Narjes, *Synlett* **2009**, 1395; (c) P. A. Suryavanshi, V. Sridharan, J. Carlos Mendez, *Org. Biomol. Chem.* **2010**, 8, 3426; (d) L. Huang, M. Shi, *Chem. Commun.* **2012**, 48, 4501.
85. G. Cera, S. Piscitelli, M. Chiarucci, G. Fabrizi, A. Goggiamani, R. S. Ramûn, S. P. Nolan, M. Bandini, *Angew. Chem. Int. Ed.* **2012**, 51, 9891; *Angew. Chem.* **2012**, 124, 10029.
86. For previous studies on gold-catalyzed functionalization of indoles with p-alcohols, see: (a) M. Bandini, A. Eichholzer, *Angew. Chem. Int. Ed.* **2009**, 48, 9533; *Angew. Chem.* **2009**, 121, 9697; (b) M. Bandini, A. Gualandi, M. Monari, A. Romaniello, D. Savoia, M. Tragni, *J. Organomet. Chem.* **2011**, 696, 338; (c) G. Cera, P. Crispino, M. Monari, M. Bandini, *Chem. Commun.* **2011**, 47, 7803; (d) G. Cera, M. Chiarucci, A. Mazzanti, M. Mancinelli, M. Bandini, *Org. Lett.* **2012**, 14, 1350; (e) M. Chiarucci, E. Matteucci, G. Cera, G. Fabrizi, M. Bandini, *Chem. Asian J.* **2013**, 8, 1776; (f) M. Chiarucci, R. Mocchi, L.-D. Syntrivanis, G. Cera, A. Mazzanti, M. Bandini, *Angew. Chem. Int. Ed.* **2013**, 52, 10850; *Angew. Chem.* **2013**, 125, 11050.
87. J. S. Mahanty, M. De, P. Das, N. G. Kundu, *Tetrahedron* **1997**, 53, 13397.
88. G. Abbiati, F. Marinelli, E. Rossi, A. Arcadi, *Isr. J. Chem.* **2013**, 53, 856.
89. A. S. K. Hashmi, T. D. Ramamurthi, F. Rominger, *Adv. Synth. Catal.* **2010**, 352, 971.
90. C. Obradors, A. M. Echavarren, *Chem. Commun.* **2014**, 50, 16.
91. Characterization data and/or use of nucleophilic alkenyl-gold species in organic transformations, see: (a) E. Jimenez-Nunez, C. K. Claverie, C. Nieto-Oberhuber, A. M. Echavarren, *Angew. Chem. Int. Ed.* **2006**, 45, 5452; *Angew. Chem.* **2006**, 118, 5578; (b) C. Kim, H. J. Bae, J. H. Lee, W. Jeong, H. Kim, V. Sampath, Y. H. Rhee, *J. Am. Chem. Soc.* **2009**, 131, 14660; (c) A. Escribano-Cuesta, V. Lúpez-Carrillo, D. Janssen, A. M. Echavarren, *Chem. Eur. J.* **2009**, 15, 5646; (d) A. S. K. Hashmi, A. M. Schuster, S. Gaillard, L. Cavallo, A. Poater, S. P. Nolan, *Organometallics* **2011**, 30, 6328; (e) M. C. Blanco Jaimes, A. Ahrens, D. Pflasterer, M. Rudolph, A. S. K. Hashmi, *Chem. Eur. J.* **2015**, 21, 427.
92. (a) A. R. Jagdale, J. H. Park, S. W. Youn, *J. Org. Chem.* **2011**, 76, 7204; (b) M. Zhang, Y. Wang, Y. Yang, X. Hu, *Adv. Synth. Catal.* **2012**, 354, 981.
93. (a) D. Zuccaccia, L. Belpassi, A. Macchioni, F. Tarantelli, *Eur. J. Inorg. Chem.* **2013**, 4121; (b) M. Jia, M. Bandini, *ACS Catal.* **2015**, 5, 1638; (c) D. J. Gorin, F. D. Toste, *Nature* **2007**, 446, 395; (d) D. Zuccaccia, L. Belpassi, F. Tarantelli, A. Macchioni, *J. Am. Chem. Soc.* **2009**, 131, 3170; (e) N. Salvi, L. Belpassi, D. Zuccaccia, F. Tarantelli, A. Macchioni, *J. Organomet. Chem.* **2010**, 695, 2679; (f) A. Zhdanko, M. E. Maier, *ACS Catal.* **2014**, 4, 2770; (g) G. Ciancaleoni, L. Belpassi, D. Zuccaccia, F. Tarantelli, P. Belanzoni, *ACS Catal.* **2015**, 5, 803; (h) L. Biasiolo, G. Ciancaleoni, L. Belpassi, G. Bistoni, A. Macchioni, F. Tarantelli, D. Zuccaccia, *Catal. Sci. Technol.* **2015**, 5, 1558.
94. (a) H. M. J. Wang, C. S. Vasam, T. Y. R. Tsai, S.-H. Chen, A. H. H. Chang, I. J. B. Lin, *Organometallics* **2005**, 24, 486; (b) C. Nieto-Oberhuber, S. Lúpez, A. M. Echavarren, *J. Am. Chem. Soc.*

- 2005**, 127, 6178; (c) C. Nieto- Oberhuber, M. Paz Munoz, S. Lopez, E. Jimenez-NfflÇez, C. Nevado, E. Herrero-Gòmez, M. Raducan, A. M. Echavarren, *Chem. Eur. J.* **2006**, 12, 1677; (d) J. delPozo, J. A. Casares, P. Espinet, *Chem. Commun.* **2013**, 49, 7246.
95. (a) T. J. Brown, M. G. Dickens, R. A. Widenhoefer, *J. Am. Chem. Soc.* **2009**, 131, 6350; (b) T. J. Brown, M. G. Dickens, R. A. Widenhoefer, *Chem. Commun.* **2009**, 6451.
96. M. Bandini, A. Bottoni, M. Chiarucci, G. Cera, G. P. Miscione, *J. Am. Chem. Soc.* **2012**, 134, 20690.
97. A. Bottoni, M. Calvaresi, A. Ciogli, B. Cosimelli, G. Mazzeo, L. Pisani, E. Severi, D. Spinelli, S. Superchi, *Adv. Synth. Catal.* **2013**, 355, 191.
98. N. Godbout, D. R. Salahub, J. Andzelm, E. Wimmer, *Can. J. Chem.* **1992**, 70, 560.
99. (a) P. J. Hay, W. R. Wadt, *J. Chem. Phys.* **1985**, 82, 270; (b) W. R. Wadt, P. J. Hay, *J. Chem. Phys.* **1985**, 82, 284; (c) P. J. Hay, W. R. Wadt, *J. Chem. Phys.* **1985**, 82, 299C.
100. J. Tomasi, B. Mennucci, R. Cammi, *Chem. Rev.* **2005**, 105, 2999.
101. M. M. Mastandrea, N. Mellonie, P. Giacinto, A. Collado, S. P. Nolan, G. Miscione, A. Bottoni and M. Bandini; *Angew. Chem. Int. Ed.* **2015**, 54, 14885-14889; *Angew. Chem.* **2015**, 127, 15098-15102.
102. L. Zhang, *Acc. Chem. Res.* **2014**, 47, 877-888.
103. (a) S. Wang, G. Zhang, L. Zhang, *Synlett* **2010**, 692-706; (b) R. Kazem Shiroodi, V. Gevorgyan, *Chem. Soc. Rev.* **2013**, 42, 4991-5001, and references therein; (c) R. Dorel, A. M. Echavarren, *Chem. Rev.* **2015**, 115, 9028-9072.
104. (a) G. Zhang, Y. Peng, L. Cui, L. Zhang, *Angew. Chem. Int. Ed.* **2009**, 48, 3112-3115; *Angew. Chem.* **2009**, 121, 3158-3161; (b) Y. Peng, L. Cui, G. Zhang, L. Zhang, *J. Am. Chem. Soc.* **2009**, 131, 5062-5063; (c) L. Cui, G. Zhang, L. Zhang, *Bioorg. Med. Chem. Lett.* **2009**, 19, 3884-3887; (d) M. Yu, G. Zhang, L. Zhang, *Org. Lett.* **2007**, 9, 2147-2150.
105. O. N. Faza, C. S. López, *J. Org. Chem.* **2013**, 78, 4929-4939.
106. M. Jia, G. Cera, D. Perrotta, M. Monari, M. Bandini, *Chem. Eur. J.* **2014**, 20, 9875-9878.
107. Allenamides in organic synthesis, see: (a) L.-L. Wei, H. Xiong, R. P. Hsung, *Acc. Chem. Res.* **2003**, 36, 773-782; (b) T. Lu, Z. Lu, Z.-X. Ma, Y. Zhang, R. P. Hsung, *Chem. Rev.* **2013**, 113, 4862-4904, and references therein.
108. L. Rocchigiani, M. Jia, M. Bandini, A. Macchioni, *ACS Catal.* **2015**, 5, 3911-3915.
109. Y. Yu, W. Yang, F. Rominger, A. S. K. Hashmi, *Angew. Chem. Int. Ed.* **2013**, 52, 7586-7589; *Angew. Chem.* **2013**, 125, 7735-7738.
110. Use of  $\pi$ -alcohols in catalytic synthetic applications, see: (a) J. Muzart, *Tetrahedron* **2005**, 61, 4179-4212; (b) Y. Tamaru, *Eur. J. Org. Chem.* **2005**, 2647-2656; (c) J. Muzart, *Eur. J. Org. Chem.* **2007**, 3077-3089; (d) M. Bandini, M. Tragni, *Org. Biomol. Chem.* **2009**, 7, 1501-1507; (e) E. Emer, R. Sinisi, M. G. Capdevila, D. Petruzzello, F. D. Vincentiis, P. G. Cozzi, *Eur. J. Org. Chem.* **2011**, 647-666; (f) B.

- Biannic, A. Aponick, *Eur. J. Org. Chem.* **2011**, 6605–6617; (g) M. Bandini, G. Cera, M. Chiarucci, *Synthesis* **2012**, 504–512.
111. (a) N. Krause, C. Winter, *Chem. Rev.* **2011**, 111, 1994–2009; (b) W. Yang, A. S. K. Hashmi, *Chem. Soc. Rev.* **2014**, 43, 2941–2955.
112. Electrophilic gold activation of allenamides, see: (a) M. C. Kimber, *Org. Lett.* **2010**, 12, 1128–1131; (b) S. Singh, M. R. J. Elsegood, M. C. Kimber, *Synlett* **2012**, 565–568; (c) Z.-X. Ma, S. He, W. Song, R. P. Hsung, *Org. Lett.* **2012**, 14, 5736–5739; (d) S. Montserrat, H. Faustino, A. Lledýs, J. L. Mascareñas, F. López, G. Ujaque, *Chem. Eur. J.* **2013**, 19, 15248–15260; (e) V. Pirovano, L. Decataldo, E. Rossi, R. Vicente, *Chem. Commun.* **2013**, 49, 3594–3596; (f) N. H. Slater, N. J. Brown, *Org. Lett.* **2014**, 16, 4606–4609; (g) P. Bernal-Albert, H. Faustino, A. Gimeno, G. A. Sensio, J. L. Mascareñas, F. López, *Org. Lett.* **2014**, 16, 6196–6199; (h) H. Faustino, I. Varela, J. L. Mascareñas, F. López, *Chem. Sci.* **2015**, 6, 2903–2908; (i) Y. Wang, P. Zhang, Y. Liu, F. Xia, J. Zhang, *Chem. Sci.* **2015**, 6, 5564–5570.
113. (a) N. Marion, S. P. Nolan, *Chem. Soc. Rev.* **2008**, 37, 1776–1782; (b) J. C. Y. Lin, R. T. W. Huang, C. S. Lee, A. Bhattacharyya, W. S. Hwang, I. J. B. Lin, *Chem. Rev.* **2009**, 109, 3561–3598; (c) S. Diez-Gonzalez, N. Marion, S. P. Nolan, *Chem. Rev.* **2009**, 109, 3612–3676; (d) S. P. Nolan, *Acc. Chem. Res.* **2011**, 44, 91–100; (e) S. Gaillard, C. S. J. Cazin, S. P. Nolan, *Acc. Chem. Res.* **2012**, 45, 778–787.
114. (a) H. Li, R. A. Widenhoefer, *Org. Lett.* **2009**, 11, 2671–2674; (b) D. Wang, R. Cai, S. Sharma, J. Jirak, S. K. Thummanapelli, N. G. Akhmedov, H. Zhang, X. Liu, J. L. Petersen, X. Shi, *J. Am. Chem. Soc.* **2012**, 134, 9012–9019; (c) A. Homs, I. Escofet, A. M. Echavarren, *Org. Lett.* **2013**, 15, 5782–5785.
115. (a) M. Jia, M. Bandini, *ACS Catal.* **2015**, 5, 1638–1652; (b) B. Ranieri, I. Escofet, A. M. Echavarren, *Org. Biomol. Chem.* **2015**, 13, 7103–7118.
116. (a) A. S. K. Hashmi, C. Lothschütz, R. Dçpp, M. Ackermann, J. De Buck Becker, M. Rudolph, C. Scholz, F. Rominger, *Adv. Synth. Catal.* **2012**, 354, 133–147; (b) A. S. K. Hashmi, K. Graf, M. Ackermann, F. Rominger, *ChemCatChem* **2013**, 5, 1200 – 1204; (c) M. Ackermann, J. Bucher, M. Rappold, K. Graf, F. Rominger, A. S. K. Hashmi, *Chem. Asian J.* **2013**, 8, 1786–1794.
117. J. Wang, W. Huang, Z. Zhang, X. Xiang, R. Liu, X. Zhou, *J. Org. Chem.* **2009**, 74, 3299–3304.
118. K. Troshin, C. Schindele, H. Mayr, *J. Org. Chem.* **2011**, 76, 9391 – 9408.
119. D. Basavaiah, G. Veeraraghavaiah, *Chem. Soc. Rev.* **2012**, 41, 68–78, and references therein.
120. R. Ocello, A. De Nisi, M. Jia, Q.-Q. Yang, M. Monari, P. Giacinto, A. Bottoni, G. P. Miscione and M. Bandini; *Chem. Eur. J.* **2015**, 21, 18445 – 18453.
121. (a) Wei L -L, Xiong H, Hsung RP; *Acc. Chem. Res.* **2003**, 36 ;773. (b) T. Lu, Z. Lu, Z.-X. Ma, Yu Zhang, R. P. Hsung; *Chem.Rev.* **2013**, 113, 4862 –4904
122. Shen L, Hsung RP, Highly; *Org. Lett.* **2005**, 7, 775.

123. (a) Berry CR, Hsung RP, Antoline JE, Petersen ME, Challeppan R, Nielson JA; *J. Org. Chem.* **2005**, 70 4038. (b) Navarro-Vazquez A, Rodriguez D, Martinez-Esperon MF, A. Garcia, Saa C, Dominguez D: Acid; *Tet. Letts.* **2007**, 48 :2741.
124. (a) Beccalli EM, Broggin G, Clerici F, Galli S, Kammerer C, Rigamonti M, Sottocornola S; *Org. Lett.* **2009**, 11:1563. (b) Fuwa H, Sasaki M; *Org. Biomol. Chem.* **2007**, 5:2214. (c) Chen G, Li Y, Fu C, Ma S ; *Tetrahedron* **2009**, 65:4547.
125. Broggin G, Galli S, Rigamonti M, Sottocornola S, Zecchi G; *Tet. Letts.* **2009**, 50; 1447.
126. (a) Hyland CJT, Hegedus LS: . *J. Org. Chem.* **2006**, 71; 8658. (b) Watanabe T, Oishi S, Fujii N, Ohno H; *Org. Lett.* **2007**, 9:4821.
127. (a) Skucas E, Zbieg JR, Krische MJ; *J. Am. Chem. Soc.* **2009**, 131; 5054. (b) Zbieg JR, McInturff EL, Krische MJ; *Org. Lett.* **2010**, 12:2514.
128. Saalfrank, R. W.; Lurz, C. J. *In Methoden Der Organischen Chemie(Houben-Weyl)*; Kropf, H., Schaumann, E., Eds.; Georg ThiemeVerlag: Stuttgart, **1993**; pp 3093–3102.
129. Chemistry of allenol ethers: (a) Brasholz, M.; Reissig, H.-U.; Zimmer, R. *Acc. Chem. Res.* **2009**, 42, 45.(b) Zimmer, R. *Synthesis* **1993**, 165.
130. Chemistry of allenyl sulfides: Hayashi, Y.; Narasaka, K. *In Advances in Cycloaddition*; Lautens, M., Ed.; JAI Press Ltd.: London, **1997**; pp 41–86.
131. Krause, N.; Hashmi, A. S. K. *Modern Allene Chemistry*; Wiley-VCH Verlag GmbH & Co. KGaA: Wein-heim, **2004**; Vols. 1 and 2.
132. (a) R. Dal Pozzo, *Chem. Soc. Rev.* **2015**, 44, 742; (b) S. P. Roche, J.-J. Y. Tendoung, B. TrÀguier, *Tetrahedron* **2015**, 71, 3549; and references therein; (c) H. Wu, Y.-P. He, F. Shi, *Synthesis* **2015**, 1990.
133. (a) F. Lúpez Ortiz, M. J. Iglesias, I. Fernandez, C. M. Andfflljar Sanchez, G. R. Gúmez, *Chem. Rev.* **2007**, 107, 1580; (b) L. Pouys'igu, D. Deffieux, S. Quideau, *Tetrahedron* **2010**, 66, 2235; (c) S. P. Roche, J. A. Porco, Jr., *Angew. Chem. Int. Ed.* **2011**, 50, 4068; *Angew. Chem.* **2011**, 123, 4154; (d) C.-X. Zhuo, W. Zhang, S.-L. You, *Angew. Chem. Int. Ed.* **2012**, 51, 12662; *Angew. Chem.* **2012**, 124, 12834; (f) C. C. Loh, D. J. Enders, *Angew. Chem. Int. Ed.* **2012**, 51, 46; *Angew. Chem.* **2012**, 124, 46; (g) C.-X. Zhuo, C. Zheng, S.-L. You, *Acc. Chem. Res.* **2014**, 47, 2558; (h) Q. Ding, X. Zhou, R. Fan, *Org. Biomol. Chem.* **2014**, 12, 4807; (i) W. Zi, Z. Zuo, D. Ma, *Acc. Chem. Res.* **2015**, 48, 702.
134. J. Barluenga, E. Tudela, A. Ballesteros, M. Tomas, *J. Am. Chem. Soc.* **2009**, 131, 2096.
135. L. M. Repka, J. Ni, S. E. Reisman, *J. Am. Chem. Soc.* **2010**, 132, 14418.
136. Y. Lian, L. Davies, *J. Am. Chem. Soc.* **2010**, 132, 440.
137. (a) G.-J. Duan, J.-B. Ling, W.-P. Wang, Y.-C. Luo, P.-F. Xu, *Chem. Commun.* **2013**, 49, 4625; (b) W. R. Gutekunst, P. S. Baran, *J. Org. Chem.* **2014**, 79, 2430.
138. (a) L. Zhang, *J. Am. Chem. Soc.* **2005**, 127, 16804; (b) H. Faustino, P. Bernal, L. Castedo, F. Lopez, J. L. MascareÇas, *Adv. Synth. Catal.* **2012**, 354, 1658.

139. D. Zhao, J. Zhang, Z. Xie, *J. Am. Chem. Soc.* **2015**, 137, 9423.
140. (a) N. Bongers, N. Krause, *Angew. Chem. Int. Ed.* **2008**, 47, 2178; *Angew. Chem.* **2008**, 120, 2208; (b) R. A. Widenhoefer, *Chem. Eur. J.* **2008**, 14, 5382; (c) S. Sengupta, X. Shi, *ChemCatChem* **2010**, 2, 609; (d) R. L. La-Londe, W. E. Brenzovich, Jr., D. Benitez, E. Tkatchouk, K. Kelley, W. A. Goddard III, F. D. Toste, *Chem. Sci.* **2010**, 1, 226; (e) T. de Haro, C. Nevado, *Synthesis* **2011**, 2530; (f) M. Bandini, *Chem. Soc. Rev.* **2011**, 40, 1358; (g) A. Pradal, P. Y. Toullec, V. Michelet, *Synthesis* **2011**, 1501; (h) M. Rudolph, A. S. K. Hashmi, *Chem. Soc. Rev.* **2012**, 41, 2448; (i) M. Livendahl, A. M. Echavarren, *Chim. Oggi-Chem. Today* **2012**, 30, 19; (k) N. T. Patil, *Chem. Asian J.* **2012**, 7, 2186; (j) E. M. Barreiro, L. A. Adrio, K. K. Hii, J. B. Brazier, *Eur. J. Org. Chem.* **2013**, 1027; (l) G. Cera, M. Bandini, *Isr. J. Chem.* **2013**, 53, 848; (m) G. Abbiati, F. Marinelli, E. Rossi, A. Arcadi, *Isr. J. Chem.* **2013**, 53, 856; (n) A. Firstner, *Acc. Chem. Res.* **2014**, 47, 925; (o) C. Obradors, A. S. K. Echavarren, *Acc. Chem. Res.* **2014**, 47, 902; (p) Y.-M. Wang, D. Lackner, A. D. Toste, *Acc. Chem. Res.* **2014**, 47, 889; (q) W. Yang, A. S. K. Hashmi, *Chem. Soc. Rev.* **2014**, 43, 2941; (r) R. Dorel, R. A. Echavarren, *Chem. Rev.* **2015**, 115, 9028; (s) P. M. Barbour, L. J. Marholz, L. Chang, W. Xu, X. Wang, *Chem. Lett.* **2014**, 43, 572.
141. Reviews on the topic: (a) B. Alcaide, P. Almendros, C. Aragoncillo, *Chem. Soc. Rev.* **2010**, 39, 783; (b) F. Lúpez, J. L. Mascareñas, *Beilstein J. Org. Chem.* **2011**, 7, 1075; (c) F. Lúpez, J. L. Mascareñas, *Beilstein J. Org. Chem.* **2013**, 9, 2250.
142. Examples of gold-catalyzed [2+2]-cycloaddition reactions see: (a) M. R. Luzung, P. Mauleûn, F. D. Toste, *J. Am. Chem. Soc.* **2007**, 129, 12402; (b) H. Teller, S. Flügge, R. Goddard, A. Firstner, *Angew. Chem. Int. Ed.* **2010**, 49, 1949; *Angew. Chem.* **2010**, 122, 1993; (c) A. Z. Gonzalez, D. Benitez, E. Tkatchouk, W. A. Goddard III, F. D. Toste, *J. Am. Chem. Soc.* **2011**, 133, 5500; (d) S. Suarez-Pantiga, C. Hernandez-Diaz, E. Rubio and J. M. Gonzalez, *Angew. Chem. Int. Ed.* **2012**, 51, 11552; *Angew. Chem.* **2012**, 124, 11720; (e) H. Teller, M. Corbet, L. Mantilli, G. Gopakumar, R. Goddard, W. Thiel, A. Firstner, *J. Am. Chem. Soc.* **2012**, 134, 15331; (f) S. Suarez-Pantiga, C. Hernandez-Diaz, M. Piedrafita, E. Rubio, J. M. Gonzalez, *Adv. Synth. Catal.* **2012**, 354, 1651; (g) P. Maulûn, *ChemCatChem* **2013**, 5, 2149; (h) R. E. M. Brooner, T. J. Brown, R. A. Widenhoefer, *Angew. Chem. Int. Ed.* **2013**, 52, 6259; *Angew. Chem.* **2013**, 125, 6379; (i) X.-X. Li, L.-L. Zhu, W. Zhou, Z. Chen, *Org. Lett.* **2012**, 14, 436; (j) C. Obradors, D. Leboeuf, J. Aydin, A. M. Echavarren, *Org. Lett.* **2013**, 15, 1576; (k) H. Zheng, R. J. Felix, M. R. Gagné, *Org. Lett.* **2014**, 16, 2272; (l) A. Homs, C. Obradors, D. Leboeuf, A. M. Echavarren, *Adv. Synth. Catal.* **2014**, 356, 221; (m) Y. Su, Y. Zhang, N. G. Akhmedov, J. L. Petersen, X. Shi, *Org. Lett.* **2014**, 16, 2478; (n) D. Li, W. Rao, G. Liang Tay, B. J. Ayers, P. W. H. Chan, *J. Org. Chem.* **2014**, 79, 11301; (o) P. Bernal-Albert, H. Faustino, A. Gimeno, G. Asensio, J. L. Mascareñas, F. López, *Org. Lett.* **2014**, 16, 6196; (p) B. D. Robertson, R. E. M. Brooner, R. A. Widenhoefer, *Chem. Eur. J.* **2015**, 21, 5714.
143. M. Jia, M. Monari, Q.-Q. Yang, M. Bandini, *Chem. Commun.* **2015**, 51, 2320.

144. (a) C. Nieto-Oberhuber, S. Lúpez, A. M. Echavarren, *J. Am. Chem. Soc.* **2005**, 127, 6178; (b) E. Herrero-Gúmez, C. N. Oberhuber, S. Lúpez, J. Benet-Buchholz, A. M. Echavarren, *Angew. Chem. Int. Ed.* **2006**, 45, 5455; *Angew. Chem.* **2006**, 118, 5581.
145. (a) V. Pirovano, L. Decataldo, E. Rossi, R. Vicente, *Chem. Commun.* **2013**, 49, 3594; (b) Y. Wang, P. Zhang, Y. Liu, F. Xia, J. Zhang, *Chem. Sci.* **2015**, 6, 5564.
146. R. Zimmer, H.-U. Reissig, *Chem. Soc. Rev.* **2014**, 43, 2888, and references therein.
147. S. Montserrat, H. Faustino, A. Lledùs, J. L. Mascarenas, F. Lòpez, G. Ujaque, *Chem. Eur. J.* **2013**, 19, 15248.
148. (a) O. Lozano, G. Blessley, T. Martinez del Campo, A. L. Thompson, G. T. Giuffredi, M. Bettati, M. Walker, R. Borman, V. Gouverneur, *Angew. Chem. Int. Ed.* **2011**, 50, 8105; *Angew. Chem.* **2011**, 123, 8255; (b) Q. Cai, C. Zheng, J.-W. Zhang, S.-L. You, *Angew. Chem. Int. Ed.* **2011**, 50, 8665; *Angew. Chem.* **2011**, 123, 8824; (c) Q. Cai, S.-L. You, *Org. Lett.* **2012**, 14, 3040; (d) Q. Cai, C. Liu, X.-W. Liang, S.-L. You, *Org. Lett.* **2012**, 14, 4588; (e) W. Xie, G. Jiang, H. Liu, J. Hu, X. Pan, H. Zhang, X. Wan, Y. Lai, D. Ma, *Angew. Chem. Int. Ed.* **2013**, 52, 12924; *Angew. Chem.* **2013**, 125, 13162; (f) M. E. Kieffer, K. V. Chuang, S. E. Reisman, *J. Am. Chem. Soc.* **2013**, 135, 5557; (g) H. Liu, G. Jiang, X. Pan, X. Wan, Y. Lai, D. Ma, W. Xie, *Org. Lett.* **2014**, 16, 1908; (h) Y.-C. Zhang, J.-J. Zhao, F. Jiang, S.-B. Sun, F. Shi, *Angew. Chem. Int. Ed.* **2014**, 53, 13912; *Angew. Chem.* **2014**, 126, 14132; (i) L. Han, C. Liu, W. Zhang, X.-X. Shi, S.-L. You, *Chem. Commun.* **2014**, 50, 1231; (j) W. Zi, H. Wu, F. D. Toste, *J. Am. Chem. Soc.* **2015**, 137, 3225.
149. (a) M. Jia, M. Bandini, *ACS Catal.* **2015**, 5, 1638; (b) L. Rocchigiani, M. Jia, M. Bandini, A. Macchioni, *ACS Catal.* **2015**, 5, 3911; (c) B. Ranieri, I. Escofet, A. E. Echavarren, *Org. Biomol. Chem.* **2015**, 13, 7103.
150. (a) T. Akiyama, *Chem. Rev.* **2007**, 107, 5744. (b) M. Terada, *Synthesis* **2010**, 1929.
151. T. Akiyama, J. Itoh, K. Yokota, K. Fuchibe, *Angew. Chem. Int. Ed.* **2004**, 43, 1566.
152. D. Uraguchi, M. Terada, *J. Am. Chem. Soc.* **2004**, 126, 5356.
153. (a) T. Akiyama, J. Itoh, K. Fuchibe, *Adv. Synth. Catal.* **2006**, 348, 999 – 1010; (b) M. S. Taylor, E. N. Jacobsen, *Angew. Chem. Int. Ed.* **2006**, 45, 1520 – 1543; *Angew. Chem.* **2006**, 118, 1550 – 1573; (c) T. Akiyama, *Chem. Rev.* **2007**, 107, 5744 – 5758; (d) M. Terada, *Chem. Commun.* **2008**, 4097 – 4112; (e) M. Terada, *Synthesis* **2010**, 1929 – 1982; (f) M. Terada, *Bull. Chem. Soc. Jpn.* **2010**, 83, 101 – 119; (g) A. Zamfir, S. Schenker, M. Freund, S. B. Tsogoeva, *Org. Biomol. Chem.* **2010**, 8, 5262 – 5276; (h) D. Kampen, C. M. Reisinger, *B. List, Top. Curr. Chem.* **2010**, 291, 395 – 456; (i) M. Rueping, A. Kuenkel, I. Atodiresei, *Chem. Soc. Rev.* **2011**, 40, 4539 – 4549; (j) M. Rueping, B. J. Nachtsheim, W. Ieawsuwan, I. Atodiresei, *Angew. Chem. Int. Ed.* **2011**, 50, 6706 – 6720; *Angew. Chem.* **2011**, 123, 6838 – 6853; (k) R. J. Phipps, G. L. Hamilton, F. D. Toste, *Nat. Chem.* **2012**, 4, 603 – 612; (l) M. Mahlau, B. List, *Angew.*

- Chem. Int. Ed.* **2013**, 52, 518 – 533; *Angew. Chem.* **2013**, 125, 540 – 556; (m) K. Brak, E. N. Jacobsen, *Angew. Chem. Int. Ed.* **2013**, 52, 534 – 561; *Angew. Chem.* **2013**, 125, 558 – 588.
154. N. D. Shapiro, V. Rauniyar, G. L. Hamilton, J. Wu, F. D. Toste, *Nature* **2011**, 470, 245 – 249.
155. (a) M. Terada, K. Sorimachi, *J. Am. Chem. Soc.* **2007**, 129, 292 – 293; (b) M. Terada, K. Moriya, K. Kanomata, K. Sorimachi, *Angew. Chem. Int. Ed.* **2011**, 50, 12586 – 12590; *Angew. Chem.* **2011**, 123, 12794 – 12798.
156. C. Romano, M. Jia, M. Monari, E. Manoni, and M. Bandini; *Angew. Chem. Int. Ed.* **2014**, 53, 1 – 5.
157. (a) L.-L. Wei, H. Xiong, R. P. Hsung, *Acc. Chem. Res.* **2003**, 36, 773 – 782; (b) T. Lu, Z. Lu, Z.-X. Ma, Y. Zhang, R. P. Hsung, *Chem. Rev.* **2013**, 113, 4862 – 4904, and references therein.
158. (a) F. Lopez, J. L. Mascarenas, Beilstein *J. Org. Chem.* **2011**, 7, 1075 – 1094; (b) F. Lopez, J. L. Mascarenas, Beilstein *J. Org. Chem.* **2013**, 9, 2250 – 2264.
159. H. G. Raubenheimer, H. Schmidbaur, *Organometallics* **2012**, 31, 2507 – 2522.
160. (a) S. Preciado Gallego, A. Perez Perarnau, J. Gil Santano, F. Albericio Palomera, R. La Villa Grifols, *WO 2013079754A1 20130606*, **2013**; (b) M. Panigrahi, S. Dash, S. Patel, B. K. Mishra, *Tetrahedron* **2012**, 68, 781 – 805; (c) N. Norouzi, *Synlett* **2013**, 1307 – 1308, and references therein.
161. M. Jia, G. Cera, D. Perrotta, M. Monari, M. Bandini, *Chem. Eur. J.* **2014**, 20, 9875 – 9878.
162. (a) T. Akiyama, Y. Honma, J. Itoh, K. Fuchibe, *Adv. Synth. Catal.* **2008**, 350, 399 – 402; (b) V. Rauniyar, A. D. Lackner, G. L. Hamilton, F. D. Toste, *Science* **2011**, 334, 1681 – 1684; (c) S. Harada, S. Kuwano, Y. Yamaoka, K. Yamada, K. Takasu, *Angew. Chem. Int. Ed.* **2013**, 52, 10227 – 10230; *Angew. Chem.* **2013**, 125, 10417 – 10420; (d) W.-W. Zi, Y.-M. Wang, F. D. Toste, *J. Am. Chem. Soc.* **2014**, 136, 12864 – 12867.
163. A. D. Lackner, A. V. Samant, F. D. Toste, *J. Am. Chem. Soc.* **2013**, 135, 14090 – 14093.
164. Z. Sun, G. A. Winschel, P. M. Zimmerman, P. Nagorny, *Angew. Chem. Int. Ed.* **2014**, 53, 11194 – 11198; *Angew. Chem.* **2014**, 126, 11376 – 1380.
165. (a) Stratakis, M.; Garcia, H. *Chem. Rev.* **2012**, 112, 4469. (b) Chinchilla, R.; Najera, C. *Chem. Rev.* **2007**, 107, 874. (c) Jana, R.; Pathak, T. P.; Sigman, M. S. *Chem. Rev.* **2011**, 111, 1417.
166. (a) Punniyamurthy, T.; Velusamy, S.; Iqbal, J. *Chem. Rev.* **2005**, 105, 2329. (b) Sherry, B. D.; Furstner, A. *Acc. Chem. Res.* **2008**, 41, 1500.
167. S. Navalon, A. Dhakshinamoorthy, M. Alvaro, H. Garcia, *Chem. Rev.* **2014**, 114, 6179–6212.
168. (a) E. Auer, A. Freund, J. Pietsch and T. Tacke, *Appl. Catal., A*, **1998**, 173, 259–271. (b) F. Rodriguez-Reinoso, *Carbon*, **1998**, 36, 159–175. (c) V. Meille, *Appl. Catal. A*, **2006**, 315, 1–17. (d) P. Ehrburger, *Carbon*, **1991**, 29, 763–768.
169. (a) A. Kutzelnigg, *Ber. Dtsch. Chem. Ges. B*, **1930**, 63, 1753–1758. (b) I. M. Kolthoff, *J. Am. Chem. Soc.*, **1932**, 54, 4473–4480.
170. D.S. Su, S. Perathoner, G. Centi, *Chem. Rev.* **2013**, 113, 5782–5816.



171. (a) Vilatela, J. J.; Eder, D. *ChemSusChem* **2012**, 5, 456. (b) D'Souza, F.; Ito, O. *Chem. Soc. Rev.* **2012**, 41, 86. (c) Rahman, A.; Ali, I.; Al Zahrani, S. M.; Eleithy, R. H. *NANO* **2011**, 6, 185. (d) Roth, S.; Park, H. *Chem. Soc. Rev.* **2010**, 39, 2477. (e) Su, D. S.; Schlogl, R. *ChemSusChem* **2010**, 3, 136. (f) Komatsu, N. *J. Jpn. Petrol. Inst.* **2009**, 52, 73.
172. *Molecular Encapsulation: Organic Reactions in Constrained Systems*; Brinker, U. H., Miesusset, J.-L., Eds.; Wiley: New York, **2010**.
173. Santiso, E. E.; George, A. M.; Turner, C. H.; Kostov, M. K.; Gubbins, K. E.; Buongiorno-Nardelli, M.; Sliwinska-Bartkowiak, M. *Appl. Surf. Sci.* **2005**, 252, 766–777.
174. (a) Pederson, M. R.; Broughton, J. Q. *Phys. Rev. Lett.* **1992**, 69, 2689–2692. (b) Khlobystov, A. N.; Britz, D. A.; Briggs, G. A. D. *Acc. Chem. Res.* **2005**, 38, 901–909. (c) Khlobystov, A. N. Carbon. *ACS Nano* **2011**, 5, 9306–9312. (d) Britz, D. A.; Khlobystov, A. N. *Chem. Soc. Rev.* **2006**, 35, 637–659. (e) Troche, K. S.; Coluci, V. R.; Braga, S. F.; Chinellato, D. D.; Sato, F.; Legoas, S. B.; Rurali, R.; Galvao, D. S. *NanoLett.* **2005**, 5, 349–355. (f) Guan, L.; Suenaga, K.; Shi, Z.; Gu, Z.; Iijima, S. *Nano Lett.* **2007**, 7, 1532–1535. (g) Takenobu, T.; Takano, T.; Shiraishi, M.; Murakami, Y.; Ata, M.; Kataura, H.; Achiba, Y.; Iwasa, Y. *Nat. Mater.* **2003**, 2, 683–688. (h) Plank, W.; Pfeiffer, R.; Schaman, C.; Kuzmany, H.; Calvaresi, M.; Zerbetto, F.; Meyer, J. *ACS Nano* **2010**, 4, 4515–4522. (i) Liu, X.; Kuzmany, H.; Ayala, P.; Calvaresi, M.; Zerbetto, F.; Pichler, T. *Adv. Funct. Mater.* **2012**, 22, 3202–3208.
175. Wang, W.; Wang, D.; Zhang, Y.; Ji, B.; Tian, A. *J. Chem. Phys.* **2011**, 134, 054317.
176. (a) Santiso, E. E.; Buongiorno Nardelli, M.; Gubbins, K. E. *J. Chem. Phys.* **2008**, 128, 034704. (b) Feng, H.; Qian, Z.; Wang, C.; Chen, C.; Chen, J. *Dalton Trans.* **2011**, 40, 4183–4189. (c) Wang, L.; Yi, C.; Zou, H.; Gan, H.; Xu, J.; Xu, W. *J. Mol. Model.* **2011**, 17, 2751–2758. (d) Wang, L.; Yi, C.; Zou, H.; Xu, J.; Xu, W. *Mater. Chem. Phys.* **2011**, 127, 232–238.
177. (a) Mann, D. J.; Halls, M. D. *Phys. Rev. Lett.* **2003**, 90, 195503. (b) Zoete, V.; Meuwly, M. *J. Chem. Phys.* **2004**, 120, 7085–7094.
178. (a) Santiso, E. E.; George, A. M.; Gubbins, K. E.; Buongiorno Nardelli, M. *J. Chem. Phys.* **2006**, 125, 084711. (b) Trzaskowski, B.; Adamowicz, L. *Theor. Chem. Acc.* **2009**, 124, 95–103. (c) Wang, L.; Yi, C.; Zou, H.; Xu, J.; Xu, W. *Chem. Phys.* **2010**, 367, 120–126. (d) Wang, L.; Xu, J.; Yi, C.; Zou, H.; Xu, W. *J. Mol. Struct. (Theochem)* **2010**, 940, 76–81.
179. (a) Halls, M. D.; Raghavachari, K. *Nano Lett.* **2005**, 5, 1861–1866. (b) Lu, T.; Goldfield, E. M.; Gray, S. K. *J. Phys. Chem. C* **2008**, 112, 2654–2659. (c) Lu, T.; Goldfield, E. M.; Gray, S. K. *J. Phys. Chem. C* **2008**, 112, 15260–15266. (d) Lu, T.; Goldfield, E. M.; Gray, S. K. *J. Phys. Chem. C* **2010**, 114, 9030–9040. (e) Ravinder, P.; Subramanian, V. *J. Phys. Chem. C* **2013**, 117, 5095–5100.
180. (a) Pan, X.; Fan, Z.; Chen, W.; Ding, Y.; Luo, H.; Bao, X. *Nat. Mater.* **2007**, 6, 507–511. (b) Pan, X.; Bao, X. *Chem. Commun.* **2008**, 47, 6271–6281. (c) Serp, P.; Castillejos, E. *ChemCatChem* **2010**, 2, 41–47. (d) Pan, X.; Bao, X. *Acc. Chem. Res.* **2011**, 44, 553–562.

181. P. Giacinto, A. Bottoni, M. Calvaresi, F. Zerbetto *J. Phys. Chem. C* **2014**, 118, 5032–5040
182. Chen, Z.; Nagase, S.; Hirsch, A.; Haddon, R. C.; Thiel, W.; Schleyer, P. van R. *Angew. Chem., Int. Ed.* **2004**, 43, 1552–1554.
183. (a) Barlow, S. E.; van Doren, J. M.; Bierbaum, V. M. *J. Am. Chem. Soc.* **1988**, 110, 7240–7242. (b) Li, C.; Ross, P.; Szulejko, J. E.; McMahon, T. B. *J. Am. Chem. Soc.* **1996**, 118, 9360–9367. (c) Parthiban, S.; de Oliveira, G.; Martin, J. M. L. *J. Phys. Chem. A* **2001**, 105, 895–904.
184. (a) Glukhovtsev, M. N.; Bach, R. B.; Pross, A.; Radom, L. *Chem. Phys. Lett.* **1996**, 260, 558–564. (b) Bento, A. P.; Solà, M.; Bickelhaupt, F. M. *J. Comput. Chem.* **2005**, 26, 1497–1504.
185. (a) Zhao, Y.; Truhlar, D. G. *Acc. Chem. Res.* **2008**, 41, 157–167. (b) Karthikeyan, S.; Ramanathan, V.; Mishra, B. K. *J. Phys. Chem. A* **2013**, 117 (30), 6687–6694.
186. Forni, A.; Pieraccini, S.; Rendine, S.; Sironi, M. *J. Comput. Chem.* **2014**, 35, 386–394.
187. (a) Janowsky, T.; Pulay, P. *High Chem. Phys. Lett.* **2007**, 447, 27–32. (b) Pitoňák, M.; Neogrády, P.; Rěžáč, J.; Jurečka, P.; Urban, M.; Hobza, P. *J. Chem. Theory Comput.* **2008**, 4, 1829–1834. (c) Sinnokrot, M. O.; Sherill, C. D. *J. Phys. Chem. A* **2006**, 110, 10656–10668.
188. (a) Prasanna, M. D.; Guru Row, T. N. *Cryst. Eng.* **2000**, 3, 135–154. (b) Saraogi, I.; Vijay, V. G.; Soma, D.; Sekar, K.; Guru Row, T. N. *Cryst. Eng.* **2003**, 6, 69–77. (c) Imai, Y. N.; Inoue, Y.; Nakanishi, I.; Kitaura, K. *Protein Sci.* **2008**, 17, 1129–1137.
189. Humphrey, W.; Dalke, A.; Schulten, K. VMD - Visual Molecular Dynamics. *J. Mol. Graphics* 1996, 14, 33–38.
190. Binkley, J. S.; Pople, J. A.; Hehre, W. J. *J. Am. Chem. Soc.* **1980**, 102, 939–947.
191. Ditchfield, R.; Hehre, W. J.; Pople, J. *J. Chem. Phys.* **1971**, 54, 724–728.
192. Dewar, M. J. S.; Zoebisch, E. G.; Healy, E. F. *J. Am. Chem. Soc.* **1985**, 107, 3902–3909.
193. Stewart, J. J. P. *J. Comput. Chem.* **1989**, 10, 209–220.
194. Stewart, J. J. P. *J. Mol. Model.* **2007**, 13, 1173–1213.
195. Rappé, A. K.; Goddard, W. A., *J. Phys. Chem.* **1991**, 95, 3358–3363.
196. Sola, M.; Lledos, A.; Duran, M.; Bertran, J.; Abboud J-L. M. *J. Am. Chem. Soc.* **1991**, 113, 2873–2879.
197. Gao, J. *J. Am. Chem. Soc.* **1991**, 113, 7796–7797.
198. Castejon, H.; Wiberg, K. B. *J. Am. Chem. Soc.* **1999**, 121, 2139–2146.
199. Webb, S. P.; Gordon, M. S. *J. Phys. Chem.* **1999**, 103, 1265–1273.
200. Halls, M. D.; Schlegel, H. B. *J. Phys. Chem. B* **2002**, 106, 1921–1925.
201. Meyer, E. A.; Castellano, R. K.; Diederick, F. *Angew. Chem. Int. Ed.* **2003**, 42, 1210–1250.
202. (a) Janowsky, T.; Pulay, P. *Chem. Phys. Lett.* **2007**, 447, 27–32. (b) Pitoňák, M.; Neogrády, P.; Rěžáč, J.; Jurečka, P.; Urban, M.; Hobza, P. *J. Chem. Theory Comput.* **2008**, 4, 1829–1834. (c) Sinnokrot, M. O.; Sherill, C. D. *J. Phys. Chem. A* **2006**, 110, 10656–10668.

203. (a) Prasanna, M. D.; Guru Row, T. N. *Crystal. Eng.* **2000**, *3*, 135-154. (b) Saraogi, I.; Vijay, V. G.; Soma, D.; Sekar, K.; Guru Row, T. N. *Crystal. Eng.* **2003**, *6*, 69-77. (c) Imai, Y.N.; Inoue, Y.; Nakanishi, I; Kitaura, K. *Protein Sci.* **2008**, *17*, 1129-1137.
204. (a) Zhao, Y.; Truhlar, D. G. *Acc. Chem. Res.* **2008**, *41*, 157–167. (b) Karthikeyan, S.; Ramanathan, V.; Mishra, B. K. *J. Phys. Chem. A* **2013**, *117* (30), pp 6687–6694. (c) Forni, A.; Pieraccini, S.; Rendine, S.; Sironi, M. *J. Comput. Chem.* **2014**, *35*, 386–394. (d) Ottiger, P.; Pfaffen, C.; Leist, R.; Leutwyler, S.; Bachorz, R. A.; Klopffer, W. *J. Phys. Chem. B* **2009**, *113*, 2937-2943.
205. (a) Bradley, K.; Briman, M.; Star, A.; Gruner, G. *Nano Lett.* **2004**, *4*, 253–256. (b) Calvaresi, M.; Hoefinger, S.; Zerbetto, F. *Chem. Eur. J.* **2012**, *18*, 4308-4313. (c) Calvaresi, M.; Zerbetto, F. *Acc. Chem. Res.* **2013**, *46*, 2454-2463.
206. Miners, S. A.; Rance, G. A.; Khlobystov, A. N. *Chem. Commun.*, **2013**, *49*, 5586-5588.
207. Mestl, G.; Maksimova, N. K.; Roddatis, V. V.; Schlogl, R. *Angew. Chem. Int. Ed.* **2001**, *40*, 2066-2068.
208. Su, D. S.; Perathoner, S.; Centi, G. *Chem. Rev.* **2013**, *113*, 5782–5816.
209. (a) Khlobystov, A. N.; Britz, D. A.; Briggs, G. A. D. *Acc. Chem. Res.* **2005**, *38*, 901-909. (b) Khlobystov, A. N. *ACS Nano*, **2011**, *5*, 9306–9312. (c) Pan, X.; Bao, X. *Acc. Chem. Res.* **2011**, *44*, 553-562.
210. (a) Kondratyuk, P.; Yatesw, J. T. *Acc. Chem. Res.* **2007**, *40*, 995-1004. (b) Pan, X.; Fan, Z.; Chen, W.; Ding, Y.; Luo, H.; Bao, X. *Nat. Mater.* **2007**, *6*, 507-511. (c) Pan, X.; Bao, X. *Chem. Commun.* **2008**, *47*, 6271–6281. (d) Serp, P.; Castillejos, E. *ChemCatChem* **2010**, *2*, 41–47. (e) Pan, X.; Bao, X. *Acc. Chem. Res.* **2011**, *44*, 553-562. (f) Takaiwa, D.; Hatano, I.; Koga, K.; Tanaka, H. *PNAS* **2008**, *105*, 39-43. (g) Paineau, E.; Albouy, P-A.; Rouziere, S.; Orecchini, A.; Rols, S.; Launois, P. *Nano Lett.* **2013**, *23*, 1751-1756. (h) Calvaresi, M.; Zerbetto, F. *J. Mater. Chem. A*, **2014**, *2*, 12123-12135.
211. (a) Zhang, H.; Pan, X.; Han, X.; Liu, X.; Wang, X.; Shen, W.; Bao, X. *Chem. Sci.* **2013**, *4*, 1075-1078. (b) Solomosz, W. A.; Rance, G. A.; Suyetin M.; La Torre, A.; Bichoutskaia, E.; Khlobystov, A. N. *Chem. Eur. J.* **2012**, *18*, 13180-13187. (c) Xiao, J.; Pan, X.; Guo, S.; Ren, P.; Bao, X. *J. A. Chem. Soc.* **2015**, *137*, 477-482.
212. P. Nikolaev, M. J. Bronikowski, R. K. Bradley, F. Rohmund, D. T. Colbert, K. A. Smith and R. E. Smalley, *Chem. Phys. Lett.*, **1999**, *313*, 91.

213. (a) E. Dujardin, T. W. Ebbesen, H. Hiura and K. Tanigaki, *Science*, **1994**, 265, 1850. (b) K. Koga, G. T. Gao, H. Tanaka and X. C. Zeng, *Nature*, **2001**, 412, 802. (c) V. V. Chaban and O. V. Prezhdo, *ACS Nano*, **2011**, 5, 5647.
214. H.A. Muathen. *Synthesis*, **2002**, No. 2, 169–171.
215. B. Galabov, G. Koleva, J. Kong, H. F. Schaefer III, and P.v.R. Schleyer, *Eur. J. Org. Chem.* **2014**, 6918–6924.
216. J. Kong, B. Galabov, G. Koleva, J. Zou, H. F. Schaefer III, and P.v.R. Schleyer, *Angew. Chem. Int. Ed.* **2011**, 50, 6809 –6813.
217. (a) L. J. Andrews, R. M. Keefer, *J. Am. Chem. Soc.* **1957**, 79, 5169–5174. (b) L. J. Andrews, R. M. Keefer, *J. Am. Chem. Soc.* **1959**, 81, 1063–1069. (c) R. M. Keefer, L. J. Andrews, *J. Am. Chem. Soc.* **1960**, 82, 14547–4553.
218. T. D. Marforio, P. Giacinto, A. Bottoni, M. Calvaresi, *Biochemistry* **2015**, 54, 4404–4410.
219. E. Baumann, *Ber. Dtsch. Chem. Ges.*, **1876**, 9, 54-58.
220. E. Chapman , M. D. Best., S. R., Hanson, C. H. Wong, *Angew. Chem. Int. Ed.* **2004**, 43, 3526–3548.
221. Y., Kakuta, , L. G., Pedersen, C. W., Carter, M., Negishi, L. C. Pedersen, *Nat. Struct. Biol.* **1997**, 4, 904–908.
222. W. B. Huttner, *Nature* 1982,299, 273–276.
223. M., Farzan, T., Mirzabekov, P., Kolchinsky, R., Wyatt, M., Cayabyab, N. P., Gerard, C., Gerard, J., Sodrosky, H. Choe, *Cell.* **1999**, 96, 667–676.
224. J., Liu, S., Louie, W., Hsu, K .M., Yu, B. N., Hugh, Jr., G. L. Rosenquist, *Am. J. Respir. Cell Mol. Biol.* 2008, 38, 738–743.
225. E., Koltsova, K. Ley, *Arterioscler., Thromb., Vasc. Biol.* **2009**, 29, 1709–1711.
226. (a) K. L. Moore, *J. Biol. Chem.*, **2003**, 278, 24243-24246; (b) A.S. Tait, *Blood*, **2002**, 99, 4422-442;
227. Stone, M. J., Chuang, S., Hou, X., Shoham, M., and Zhu, J. Z. (2009) *New Biotechnol.* 25, 299–317.
228. T., Teramoto, Y., Fujikawa, Y., Kawaguchi, K., Kurogi, M., Soejima, R., Adachi, Y., Nakanishi, E., Mishiro-Sato, M., Liu, Y., Sakakibara, M., Suiko, M., Kimura, Y.Kakuta, *Nat. Commun.* 2013, 4, 1572.
229. A., Leyte, H. B., van Schijndel, C., Niehrs, W. B., Huttner, M. P., Verbeet, K., Mertens, J. A. van Mourik, *J. Biol. Chem.* **1991**, 266, 740–746.
230. E., Mishiro, Y., Sakakibara, M. C., Liu, M. Suiko, *J. Biochem.* **2006**, 140, 731–737.
231. L. M., Danan, Z., Yu, P. J., Ludden, W., Jia, K. L., Moore, J. A. Learty, *J. Am. Soc. Mass Spectrom.* 2010, 21, 1633–1642.
232. P.,Nedumpully-Govindan, L., Li, E. G., Alexov, M. A., Blenner, F. Ding, *Bioinformatics* **2014**, 30, 2302–2309.

233. (a) M., Stenta, M., Calvaresi, P., Altoe, D., Spinelli, M., Garavelli, A. Bottoni, *J. Phys. Chem. B* **2008**, 112, 1057–1059. (b) M., Stenta, M., Calvaresi, P., Altoe, D., Spinelli, M., Garavelli, R., Galeazzi, A. Bottoni, *J. Chem. Theory. Comput.* **2009**, 5, 1915–1930. (c) M., Calvaresi, M., Stenta, M., Garavelli, P., Altoe, A. Bottoni, *ACS Catal.* **2012**, 2, 280–286.
234. (a) M., Calvaresi, A., Bottoni, M. Garavelli, *J. Phys. Chem. B* **2007**, 111, 6557–6570. (b) M., Calvaresi, M., Garavelli, A. Bottoni, *Proteins: Struct., Funct., Genet.* **2008**, 73, 527–538. (c) A., Bottoni, G. P., Miscione, M. Calvaresi, *Phys. Chem. Chem. Phys.* **2011**, 20, 9568–9577.
235. R., Anandakrishnan, B., Aguilar, A. V. Onufriev, H++ 3.0: automating pK prediction and the preparation of biomolecular structures for atomistic molecular modeling and simulations. *Nucleic Acids Res.* **2012**, 40, W537–W541.
236. R., Prabhakar, K., Morokuma, D. G. Musaev, *Biochemistry* **2006**, 45, 6967–6977.
237. T., Borowski, P. E. M. Siegbahn, *J. Am. Chem. Soc.* **2006**, 128, 12941–12953.

# *Publications*

Some of the work presented here has been published in the following papers:

## **Part II : Metal- and Organo-Catalysis**

### **Chapter 3**

P. Giacinto, G. Cera, A. Bottoni, M. Bandini, and G. P. Miscione. A DFT mechanistic investigation of the gold(I) catalyzed synthesis of Azepino [1,2a] Indoles. *ChemCatChem* **2015**, 7, 2480 – 2484.

### **Chapter 4**

M. Mastandrea, N. Mellonie, P. Giacinto, A. Collado, S. P. Nolan, G. Miscione, A. Bottoni and M. Bandini. [Au(I)]-assisted  $\alpha$ -Allylation of Enals and Enones with Alcohols. *Angew. Chem. Int. Ed* **2015**, 54, 14885-14889.

### **Chapter 5**

R. Ocello, A. Di Nisi, M. Jia, Q. Zhang, M. Monari, P. Giacinto, A. Bottoni, G.P. Miscione and M. Bandini. Gold(I)-Catalyzed Dearomative [2+2]-Cycloaddition of Indoles with Activated Allenes: A Combined Experimental–Computational Study. *Chem. Eur. J.* **2015**, 21, 18445-18453.

## **Part III : Carbo-Catalysis**

### **Chapter 2**

P. Giacinto, A. Bottoni, M. Calvaresi, F. Zerbetto. Cl(–) Exchange SN2 Reaction inside Carbon Nanotubes: C–H $\cdots\pi$  and Cl $\cdots\pi$  Interactions Govern the Course of the Reaction. *J. Phys. Chem. C*, **2014**, 118, 5032–5040.

## **Part IV: Bio-Catalysis**

### **Chapter 1**

T. D. Marforio, P. Giacinto, A. Bottoni and M. Calvaresi; Computational evidence for the catalytic mechanism of Tyrosylprotein Sulfotransferases (TPST): a DFT investigation *Biochemistry* **2015**, 54, 4404–4410.

## RINGRAZIAMENTI

*Il presente lavoro di tesi è stato condotto grazie al Prof. Andrea Bottoni che ha creduto in me, concedendomi la possibilità di svolgere il dottorato presso il suo prestigioso gruppo di ricerca. Desidero ringraziarlo di vero cuore. Insieme a Lui desidero ringraziare anche il Dr. Gian Pietro Miscione ed il Dr. Matteo Calvaresi i quali mi hanno sostenuto durante tutto il periodo del dottorato e mi hanno sempre generosamente fornito preziosi consigli. Grazie per i loro insegnamenti, per il tempo dedicatomi a volte anche in mezzo a mille difficoltà. La loro disponibilità è stata sempre aperta e gentile e la loro professionalità sempre ineccepibile. Un grazie sentito va anche a Tainah per la sua collaborazione ed il suo supporto.*

*Questo lavoro è dedicato a mio padre che mi ha mostrato, con la sua vita, la strada dell'onestà, del lavoro e del rispetto per gli altri. Tutto ciò che sono e che ho lo devo a lui ed a mia madre. Grazie.*

*Grazie speciale a Maria ed alla mia famiglia Paola, Licia, Roberto e Francy.*